MAX–DOAS measurements of bromine explosion events in McMurdo Sound, Antarctica.

A thesis
submitted in partial fulfilment
of the requirements for the Degree
of
Doctor of Philosophy in Physics
at the
University of Canterbury

by

Timothy Hay

University of Canterbury
2010

Abstract

Reactive halogen species (RHS) are responsible for ozone depletion and oxidation of gaseous elemental mercury and dimethyl sulphide in the polar boundary layer, but the sources and mechanisms controlling their catalytic reaction cycles are still not completely understood. To further investigate these processes, ground–based Multi–Axis Differential Optical Absorption Spectroscopy (MAX–DOAS) observations of boundary layer BrO and IO were made from a portable instrument platform in McMurdo Sound during the Antarctic spring of 2006 and 2007. Measurements of surface ozone, temperature, pressure, humidity, and wind speed and direction were also made, along with fourteen tethersonde soundings and the collection of snow samples for mercury analysis.

A spherical multiple scattering Monte Carlo radiative transfer model (RTM) was developed for the simulation of box–air–mass–factors (box–AMFs), which are used to determine the weighting functions and forward model differential slant column densities (DSCDs) required for optimal estimation. The RTM employed the backward adjoint simulation technique for the fast calculation of box-AMFs for specific solar zenith angles (SZA) and MAX–DOAS measurement geometries. Rayleigh and Henyey–Greenstein scattering, ground topography and reflection, refraction, and molecular absorption by multiple species were included. Radiance and box–AMF simulations for MAX–DOAS measurements were compared with nine other RTMs and showed good agreement.

A maximum *a posteriori* (MAP) optimal estimation algorithm was developed to retrieve trace gas concentration profiles from the DSCDs derived from the DOAS analysis of the measured absorption spectra. The retrieval algorithm was validated by performing an inversion of artificial DSCDs, simulated from known NO_2 profiles. Profiles with a maximum concentration near the ground were generally well reproduced, but the retrieval of elevated layers was less accurate. Retrieved partial vertical column densities (VCDs) were similar to the known values, and investigation of the averaging kernels indicated that these were the most reliable retrieval product. NO_2 profiles were also retrieved from measurements made at an NO_2 measurement and profiling intercomparison campaign in Cabauw, Netherlands in July 2009.

Boundary layer BrO was observed on several days throughout both measurement periods in McMurdo Sound, with a maximum retrieved surface mixing ratio of 14.4±0.3 ppt. The median partial VCDs up to 3 km were $9.7\pm0.07 \times 10^{12}$ molec cm^{-2} in 2007, with a maximum of $2.3\pm0.07 \times 10^{13}$ molec cm^{-2}, and $7.4\pm0.06 \times 10^{12}$ molec cm^{-2} in 2006, with a maximum of $1.05 \pm 0.07 \times 10^{13}$ molec cm^{-2}. The median mixing ratio of 7.5±0.5 ppt for 2007 was significantly higher than the median of 5.2±0.5 ppt observed in 2006, which may be related to the more extensive first year sea ice in 2007. These values are consistent with, though lower than estimated boundary layer BrO concentrations at other polar coastal sites.

Four out of five observed partial ozone depletion events (ODEs) occurred during strong winds and blowing snow, while BrO was present in the boundary layer in both stormy and calm conditions, consistent with the activation of RHS in these two weather extremes. Air mass back trajectories, modelled using the Hybrid Single–Particle Lagrangian Integrated Trajectory (HYSPLIT) model, indicated that the events were locally produced rather than transported from other sea ice zones. Boundary layer IO mixing ratios of 0.5–2.5$\pm$0.2 ppt were observed on several days. These values are low compared to measurements at Halley and Neumayer Stations, as well as mid–latitudes. Significantly higher total mercury concentrations observed in 2007 may be related to the higher boundary layer BrO concentrations, but further measurements are required to verify this.

Acknowledgements

I wish to thank my supervisors Karin Kreher and Robyn Schofield for their excellent support and invaluable advice and encouragement, and Adrian McDonald for his guidance and supervision.

I wish to thank Paul Johnston for his great support and his major role in the development of the spectrometer and DOAS software as well as many helpful discussions on DOAS analysis and radiative transfer. I would also like to thank Alan Thomas for all his excellent work building the instrument system for Antarctica, and Jill Scott for her help with computer and technical problems. I wish to thank Hamish Chisholm for his invaluable help with the ozonesondes and for his encouragement during the final stages of my thesis preparation. I would like thank all the staff and students at the National Institute of Water and Atmospheric Research (NIWA) at Lauder for their friendly support. I wish to thank my flatmates Birgit Hassler, Stefanie Kremser and Martin Brabec for their support and encouragement.

I wish to thank Katja Riedel for her great company and support during both Antarctic measurement campaigns and I am also grateful to Selami Yilmaz for his support during the first half of the 2007 campaign. I would also like to thank Antarctica NZ, in particular Paul Woodgate, Kevin Rigarslford, Peter Cleary, Blake McDavitt, Mark Hay and all the Scott Base staff of 2006 and 2007 for their support.

I would like to thank Greg Bodeker for writing the original NIMO Monte Carlo ray tracing algorithm, which was further developed in this work, as well as Ben Liley for his help with spherical geometry and aerosol scattering problems. I wish to thank Martin Scherer for his previous input into NIMO and for proof–reading the NIMO paper manuscript.

I wish to thank Rod Krempasky at Able Solar and Jon Maunsell at Solar Selectives for helpful discussions on batteries, wind and solar power. I would like to thank Stephane Baguette from the British Antarctic Survey for loaning the 2B–205 ozone monitor in 2007, and Steve Brooks for supplying the mercury sampling vials and for the total mercury analysis of the snow samples. I am also grateful to Thomas Wagner for supplying the radiative transfer model intercomparison data, and to Jen Mercer for providing McMurdo ozonesonde data. I would like to thank Katrijn Clemer and Folkard Wittrock for providing the NO_2 simulation data and Bremen measurements from Cabauw. I am also grateful to Martyn Chipperfield for SLIMCAT BrO model data, Xin Yang for TOMCAT BrO model data, and Luca Di Liberto for McMurdo LIDAR data.

Finally, I would like to thank NIWA for providing my funding and the Christchurch City Council for an Antarctic Scholarship.

Contents

List of Figures

List of Abbreviations

AERONET	AErosol RObotic NETwork
AGM	Absorbed Glass Mat
AMAX-DOAS	Aircraft Multi-AXis Differential Optical Absorption Spectroscopy
AMF	Air-Mass Factor
AOD	Aerosol Optical Depth
BOC	Brominated Organic Compound
Br_2	Bromine dimer
BrCl	Bromine Chloride
BrO	Bromine oxide
CCD	Charged Couple Device
CCN	Cloud Condensation Nuclei
CDF	Cumulative Distribution Function
CH_3Br	Methyl Bromide
$CHBr_3$	Bromoform
CINDI	Cabauw Intercomparison Campaign of Nitrogen Dioxide Measuring Instruments
ClO	Chlorine Monoxide
DFS	Degrees of Freedom for Signal
DMS	Dimethyl sulphide
DOAS	Differential Optical Absorption Spectroscopy
DSCD	Differential Slant Column Density
ECC	Electrochemical Concentration Cell
FOV	Field Of View
FWHM	Full Width at Half Maximum
GEM	Gaseous Elemental Mercury
GOME	Global Ozone Monitoring Experiment
Hg	Mercury
HO_2	Hydroperoxyl radical
HOBr	Hypobromous acid
HYSPLIT	Hybrid Single-Particle Lagrangian Integrated Trajectory model
I_2	Iodine dimer
IDL	Interactive Data Language
IO	Iodine monoxide
LIDAR	Light Detection and Ranging
LOS	Line Of Sight
LP-DOAS	Long Path DOAS
MAP	Maximum *a Posteriori*
MAX-DOAS	Multi-AXis Differential Optical Absorption Spectroscopy
MBL	Marine Boundary Layer
MC	Monte Carlo

MCRTM	Monte Carlo Radiative Transfer Model
MODIS	MODerate resolution Imaging Spectroradiometer
NDACC	Network for the Detection of Atmospheric Composition Change
NIMO	NIwa MOnte carlo model
NIWA	National Institute of Water and Atmospheric research
NO_2	Nitrogen Dioxide
NZST	New Zealand Standard Time
O_3	Ozone
O_4	Oxygen Dimer
OClO	Chlorine Dioxide
ODE	Ozone Depletion Event
OH	Hydroxyl radical
OSIRIS	Optical Spectrograph and InfraRed Imager System
PDF	Probability Density Function
PSC	Polar Stratospheric Cloud
ppb	Parts Per Billion
ppt	Parts Per Trillion
PV	PhotoVoltaic
RAA	Relative Azimuth Angle
RGM	Reactive Gaseous Mercury
RHS	Reactive Halogen Species
RMS	Root Mean Square
RRS	Rotational Raman Scattering
RT	Radiative Transfer
RTE	Radiative Transfer Equation
RTM	Radiative Transfer Model
SAA	Solar Azimuth Angle
SCD	Slant Column Density
SCIAMACHY	SCanning Imaging Absorption spectroMeter for Atmospheric CartograpHY
SZA	Solar Zenith Angle
TARDIS	Transportable Antarctic Remote DOAS Instrument System
TOA	Top Of Atmosphere
UT	Universal Time
UTC	Coordinated Universal Time
UV	Ultra-Violet
VCD	Vertical Column Density
VOD	Vertical Optical Depth

Chapter 1

Introduction

Enhanced concentrations of reactive halogen species (RHS), including bromine monoxide (BrO) and iodine monoxide (IO) radicals, in the polar marine boundary layer (MBL) are responsible for very efficient photocatalytic ozone destruction (Hausmann and Platt, 1994; Frieß et al., 2001; Simpson et al., 2007b), as well as oxidation of gaseous elemental mercury (Schroeder et al., 1998; Temme et al., 2003) and dimethyl sulphide (Boucher et al., 2003; Breider et al., 2010), but many key processes involving RHS remain poorly understood. Although enhanced BrO concentrations in the polar MBL are naturally occurring phenomena, areas covered by elevated BrO columns, as measured by the Global Ozone Monitoring Experiment (GOME) satellite instrument, have been expanding, possibly due to anthropogenic influences on climate and bromine source gases (Hollwedel et al., 2004).

Tropospheric BrO has been observed by Kreher et al. (1997) at Arrival Heights (77.8°S, 166.7°E) in McMurdo Sound using ground–based zenith–sky Differential Optical Absorption Spectroscopy (DOAS) and by Schofield et al. (2006) using combined direct–sun and zenith–sky DOAS measurements. Multi–Axis DOAS (MAX–DOAS) measurements have been conducted at Arrival Heights since 1998 and bromine explosion events have been observed each spring, though in about 20% of cases corresponding ozone depletion is not observed at the site. The MAX–DOAS instrument is sensitive to light absorption by BrO on a scale of several kilometers both above and below the instrument, whereas ozone is measured by sampling the air at Arrival Heights, located at $\sim$185 m above the sea ice. Therefore, it was thought that the observed BrO enhancements and depleted ozone might frequently be contained under a temperature inversion layer over the sea ice, but below Arrival Heights, or in some cases, concentrated in an elevated layer above Arrival Heights, as has been observed by Frieß et al. (2004) at Neumayer Station. To further investigate these bromine explosion events, a portable MAX–DOAS system was deployed on the sea ice at three sites in McMurdo Sound, at 2 km, 22 km and 68 km north of Arrival Heights in the spring of 2006 and 2007.

The quantity derived from DOAS measurements is a differential slant column density (DSCD) that is the difference between the integrated column of molecules for the ensemble of atmospheric light paths observed in the viewing direction

relative to the column in a reference (usually zenith) direction. As DSCDs depend on numerous variables, including the measurement geometry, the solar zenith angle (SZA), aerosols and the surface albedo, more useful quantities for interpretation and comparison are the vertical column density (VCD) and the vertical concentration profile. Brewer et al. (1973) was the first to derive vertical trace gas profile information from UV–visible spectroscopic measurements, using the ratio of solar intensities at three wavelengths to estimate NO_2 concentrations in the stratosphere and near the ground. Noxon (1975) derived NO_2 profile information from DSCDs and later McKenzie et al. (1991) used the iterative Chahine inversion method to retrieve NO_2 and O_3 profiles. Preston et al. (1997) was the first to implement optimal estimation (Rodgers, 1976, 2000) to retrieve NO_2 profiles from zenith–sky DSCD measurements at different SZA. A non–linear maximum *a posteriori* (MAP) inversion (Rodgers, 2000) was implemented by Hoogen et al. (1999) for the retrieval of O_3 profiles from the nadir–viewing Global Ozone Monitoring Experiment (GOME) satellite–based instrument, and by Haley et al. (2004) to retrieve profiles of O_3 and NO_2 from Optical Spectrograph and Infrared Imager System (OSIRIS) limb–scattered sunlight measurements.

Schofield et al. (2004) applied formal optimal estimation to retrieve BrO altitude information from ground–based UV–visible measurements at different SZA, by combining direct–sun and zenith–sky DSCDs. The sensitivity of both these measurement geometries is highest at twilight when the mean scattering altitudes and air–mass factors (AMFs) change rapidly with SZA. This presents a problem for the observation of photochemically active radical species such as BrO, IO, OClO and NO_2, since their concentrations vary with the changing SZA along the long stratospheric light paths at twilight, due to different photolysis rates. Therefore, Schofield et al. (2004) simultaneously retrieved information on the diurnal variation along with the vertical distribution of the trace gas, avoiding the uncertainties that would be introduced by treating diurnal variation as a forward model parameter. In contrast, Hendrick et al. (2004) used optimal estimation to retrieve stratospheric NO_2 profiles from zenith–sky DSCDs, by coupling the radiative transfer model (RTM) with a stacked box photochemical model, PSCBOX (Errera and Fonteyn, 2001), to reproduce the rapid variation of NO_2 concentration at twilight.

The treatment of diurnal variation is less important for the retrieval of boundary layer trace gas profiles from MAX–DOAS measurements, as the DSCDs are obtained from the ratio of observation and reference spectra measured at similar SZA. Also, the sensitivity of MAX–DOAS does not rely on the changing AMFs that occur at twilight, so measurements can be made throughout the day, with a temporal resolution of a few minutes (usually less than 30 min). Therefore, photochemistry was not included in the RTM calculations for this study. The first optimal estimation retrieval for MAX–DOAS was done by Bruns et al. (2004) for aircraft MAX–DOAS measurements (AMAX–DOAS) of NO_2. Theys et al. (2007) applied a linear multiple regression retrieval algorithm to MAX–DOAS BrO DSCDs, separating the AMFs into a stratospheric and a tropospheric component, making use of the different variation of these two AMFs with SZA.

Photochemistry was included in the forward model for high SZA, as done by Hendrick et al. (2004), and five profiles, describing the stratospheric variation of BrO were retrieved, in addition to the independent retrieval of tropospheric profiles from the off–axis measurements. Frieß et al. (2006) retrieved aerosol properties from O_4 DSCDs using the Gauss–Newtonian iterative method to converge on a non–linear MAP solution. The time–consuming weighting function calculations must be performed for each iteration, and a positive constraint must be applied, for example by inverting the natural logarithm of the state profile (Haley et al., 2004), as the negative trace gas densities that often arise from the direct inversion of the state vector cannot be dealt with in RTMs. In this study, the focus is on boundary layer BrO and IO with very low optical depths, so a linear MAP solution is used for efficiency, and the risk of any potential bias introduced by putting a positive constraint on the state vector, is thus avoided.

An introduction to the current knowledge of halogen chemistry in the polar marine boundary layer is given in Chap. 2. Then, Chap. 3 describes the measurement campaigns and study sites in McMurdo Sound, the instrumental platform that was developed for the measurements on the sea ice, and the DOAS measurement and spectral retrieval technique. The Monte Carlo RTM, which was developed for the simulation of weighting functions and forward model DSCDs, required for optimal estimation, is described in Chap. 4, and the results from a series of intercomparison and validation exercises are presented. Chap. 5 introduces optimal estimation retrieval theory and describes the retrieval algorithm developed in this work. A validation of the retrieval algorithm for the Cabauw Intercomparison Campaign of Nitrogen Dioxide measuring Instruments (CINDI), using artificial DSCDs simulated from known NO_2 profiles, is also presented along with retrieved profiles from NO_2 measurements made during CINDI at Cabauw, Netherlands in June 2009. The BrO and IO DSCD measurements, made during the two campaigns in McMurdo Sound in the spring of 2006 and 2007, are presented along with the retrieved profiles and VCDs in Chap. 6. The tethersonde, snow mercury, and back trajectory modelling results are also discussed. Conclusions and recommendations for further development and investigation are outlined in Chap. 7.

Chapter 2

Halogen chemistry in the polar marine boundary layer

This chapter discusses the importance of bromine and iodine in the polar boundary layer and describes the chemistry of bromine explosion events. For a comprehensive review of halogen chemistry in the polar boundary layer and their role in ozone depletion events see Simpson et al. (2007b).

2.1 Historical background

Ozone depletion events in the polar marine boundary layer have been reported since the mid–1980s (Bottenheim et al., 1986; Oltmans and Komhyr, 1986; Barrie et al., 1988; Platt, 1994; Kreher et al., 1997; Stutz and Platt, 1997; Wagner et al., 1998; Wittrock et al., 2000). Sudden disappearances of ozone in air at ground level were first observed at Alert, in the Canadian high Arctic in 1985, where mixing ratios dropped from the normal 30 to 40 parts per billion (ppb) to almost zero ppb within a few hours (Bottenheim et al., 1986). Further study by Barrie et al. (1988) confirmed that this was a regular occurrence during the transition from the dark winter to the sunlit spring. A strong anti–correlation between daily mean concentrations of surface ozone and filterable bromine was also observed. Large reductions and variations in boundary layer ozone during polar sunrise were also evident from 10 years of surface ozone observations at Barrow, Alaska (Oltmans and Komhyr, 1986).

These measurements of atmospheric composition at high latitudes resulted in the discovery of tropospheric ozone depletion events (ODEs). Gaseous bromine–containing species had already been recognized as catalysts for stratospheric ozone depletion as early as 1975. The potential of bromine to act more efficiently than and also synergistically with chlorine was also recognized (Wofsy et al., 1975; Yung et al., 1980; Rasmussen and Khalil, 1984). The photolysis rate for BrO is two to three orders of magnitude faster than that for ClO (Yung et al., 1980). The involvement of bromine compounds in polar tropospheric ozone depletion was confirmed by observations of BrO in the Arctic (Hausmann and Platt, 1994; Wagner et al., 1998), as well as in the Antarctic boundary layer (Kreher et al.,

1997; Wagner et al., 1998; Wessel et al., 1998; Frieß et al., 2004).

Though it is now widely accepted that the mechanism for these sudden depletion events involves autocatalytic release of halogens by heterogeneous reactions on sea–salt surfaces, referred to as a 'bromine explosion' (Fan and Jacob, 1992; Mozurkewich, 1995; Tang and McConnell, 1996; Sander et al., 1997; Fickert et al., 1999; Michalowski et al., 2000; Platt and Honninger, 2003), many aspects of the chemistry involved in this process are not fully understood. For example, how sea salt and bromine reach the snow surface and how they become activated to undergo the necessary reactions.

The proposed mechanism of ozone depletion in the boundary layer is as follows. Persistently throughout the winter and early spring, a cold surface boundary layer over the sea ice is isolated from the free tropospheric reservoir of O_3 by a strong radiation inversion. Simultaneously, the low levels of OH in winter allow tropospheric organic bromine to build up. During the dark polar winter there is virtually no production of hydroxyl radicals, which is initiated by the photolysis of ozone and completed by the presence of water vapour. With tropospheric OH sharply reduced, the normal removal of brominated organic species by OH is also shut down in the polar atmosphere (Berg et al., 1984). Production of filterable bromine, principally from $CHBr_3$, and ozone destruction are induced by sunlight at polar sunrise and the strong inversion inhibits both replenishment of O_3 and dilution of filterable bromine from above. The sea ice covered regions around Antarctica extend to much lower latitudes and are thus exposed to solar radiation much earlier compared to the Arctic, so ozone minima tend to occur one to two months earlier in the year (Wessel et al., 1998).

2.2 Importance of bromine in the troposphere

Although a polar phenomenon, it is still an open question as to how much impact bromine explosion events have on global tropospheric chemistry. Additionally, it is not yet clear what impact climate change and potential change in sea ice cover could have on the bromine activation. We are also still not able to predict the spatial or temporal distribution of the depletion events, nor are we able to simulate the processes. The surprising magnitude of the effect points to a weakness in our understanding of tropospheric ozone chemistry. This needs to be addressed given the central role ozone plays with respect to the atmosphere's oxidizing capacity and its significant contribution to radiative forcing.

During spring there are frequent episodic depletions of boundary layer mercury vapour that are very similar to and coincide with surface ozone depletion events (Schroeder et al., 1998). BrO is involved with this oxidation of gaseous mercury in the boundary layer, resulting in deposition of harmful water–soluble mercury on the sea ice and subsequent release into the sea during the spring melt. Together with increasing amounts of anthropogenic mercury in the polar atmosphere, these processes could have a negative impact on the ecology of Antarctica and the Arctic

(Lindberg et al., 2002; Calvert and Lindberg, 2003).

Atmospheric bromine is important, not only in polar marine boundary layer chemistry but also in the overlying free troposphere. McElroy et al. (1999) suggested that BrO, along with ice crystals and water droplets, are lifted well above the boundary layer by convective transport over wide ice leads. Thus surfaces are provided in the free troposphere that can recycle BrO from less reactive forms and thereby maintain its activity in the free troposphere. If ozone loss in the free troposphere is sustained from mixing with boundary layer air, a slight cooling could occur in the free troposphere due to the reduced greenhouse effect (Roscoe et al., 2001; Frieß et al., 2004).

Bromine can potentially influence global climate by removing ozone (which absorbs solar radiation), by oxidation of greenhouse gases such as methane, and by altering the production of cloud condensation nuclei through oxidation of dimethyl sulphide (Boucher et al., 2003; Breider et al., 2010). Conversely, the potential impact of climate change on the chemistry of bromine, ozone and mercury by altering the extent of sea ice cover through warmer temperatures is uncertain and needs further investigation. It is likely that a reduction in spring and early summer sea ice areas would result in a significant increase in boundary layer ozone (Voulgarakis et al., 2009).

2.3 Bromine explosion events

Satellite remote sensing by GOME (Global Ozone Monitoring Experiment) and SCIAMACHY (Scanning Imaging Spectrometer for Atmospheric Cartography) reveals that during polar spring large areas of BrO enriched air masses form, which are clearly associated with certain sea ice zones (Richter et al., 1998; Wagner et al., 1998, 2001; Hollwedel et al., 2004). These often coincide with ozone depletion events measured by ground–based instruments. The conditions that lead to the initial bromine release, as well as the influence of transport and chemical processes on the enhanced BrO, are not yet fully understood, but the presence of first–year sea ice and an inversion layer, which acts as a barrier against exchange with the air above, are known to be important (Berg et al., 1984; Hansen and Rosen, 1984; Barrie et al., 1988; Wessel et al., 1998; Lehrer et al., 2004).

Begoin et al. (2010) studied BrO measurements from GOME–2 together with model calculations to investigate an Arctic bromine explosion event in March 2007, which they observed over a large area for several days. This event was linked to a cyclone with very high surface wind speeds, which could have been involved in the production and lifting of aerosols or blowing snow. Uplifted and transported aerosols or snow can also provide the surface for BrO recycling within the plume for several days. Backward trajectories from the area of BrO initialisation indeed showed upward lifting from the surface up to 3 km. The evolution of the BrO plume was reproduced by model simulations of a passive tracer indicating that the activated air mass was transported all the way from

Siberia to Hudson Bay.

Begoin et al. (2010) concluded that these observations are consistent with a scenario in which bromine in the air mass was activated on the surface within the cyclone, lifted upwards and transported over several thousand kilometres to Hudson Bay. They also considered the influence of changes in tropopause height on the measured BrO values and state that in spite of the low tropopause heights present during the event, no indication was found for a stratospheric intrusion bringing BrO rich stratospheric air into the troposphere.

Salawitch (2010), however, came to a somewhat different conclusion when they studied airborne measurements of BrO and ozone within the Arctic boundary layer during the Arctic Research of the Composition of the Troposphere from Aircraft and Satellites (ARCTAS) and Aerosol, Radiation, and Cloud Processes affecting Arctic Climate (ARCPAC) field campaigns in April 2008. They conclude from their investigations that there was much less association between satellite BrO "hotspots" (defined as regions where total column BrO is elevated by 2 to 3×10^{13} molec cm^{-2} relative to the zonal mean), and elevated boundary layer BrO and depleted ozone than expected. The authors agree that ODEs are certainly real and caused by bromine enhancements near the surface during polar spring, but might have been overestimated in geographic extent by associating all satellite "hotspots" with enhancements of boundary layer BrO. The location of numerous satellite BrO "hotspots" during Arctic spring is consistent with observations of total column ozone and tropopause height, suggesting a stratospheric origin to elevated BrO. Another interesting result from this study is that tropospheric enhancements of BrO large enough to affect the column abundance were observed, with important contributions originating from above the boundary layer. These findings lead to the overall conclusion that the interpretation of the BrO distribution in the atmosphere is more complicated than previously assumed and that more studies of the altitude distribution are needed, especially in the polar regions.

2.3.1 Dynamics of ozone depleted air masses

Elevated bromine should generally coincide with measurements of low ozone during bromine explosions, although various causes, such as pollution and transport of air masses from other regions can sometimes negate this relationship. An important factor is the origin of the air that is sampled, since air masses passing over sea ice are more likely to carry ozone depleted air from a bromine explosion event than air masses arriving from inland (Hopper et al., 1998). However, ozone depleted air masses can sometimes travel for several days and several hundred kilometres before normal ozone levels are restored through mixing with ozone rich air (Roscoe et al., 2001; Bottenheim and Chan, 2006). Barrie et al. (1988) suggested that the high variability in daily average concentrations of O_3 and filterable bromine result from the alternating presence of below–inversion air off the icecap and of above–inversion air mixed to the surface in winds coming off rougher

terrain. Thus, the observed variation could be a meteorological modulation which alternately brings to the sampling location boundary layer air, depleted in ozone and enriched in filterable bromine, and free tropospheric air with abundant ozone and few bromine compounds (Bottenheim et al., 1990; Finlayson-Pitts et al., 1990).

Monthly mean GOME and SCIAMACHY measurements frequently show a ring of high BrO around Antarctica in the spring (Richter et al., 1998; Wagner et al., 1998, 2001). This suggests that surface ozone loss occurs throughout the sea ice covered region, unobserved because there are no ground–based measurement sites on the sea ice and satellite measurements of changes in tropospheric ozone are difficult due to the large amounts of ozone intervening in the stratosphere (Roscoe et al., 2001). Also, frequent storms probably mix ozone–poor air over hundreds of kilometres horizontally and several kilometres vertically, rendering the ozone loss unobservable. This idea is also supported by the low wind speeds in the trajectories during measured events. Furthermore, most trajectories arriving at the surface at Neumayer and McMurdo originate over the plateau and rarely over the sea ice (Kottmeier and Fay, 1998; Roscoe et al., 2001).

However, depleted air masses can also be transported to lower latitudes or over land. A ground–based observation of depleted ozone could thus indicate either advection of ozone–depleted air masses to the site, local chemical ozone depletion, or a combination of the two (Simpson et al., 2007b). Meteorology–controlled ozone depletion events can have a very rapid onset (Morin et al., 2005; Jones et al., 2006) on a timescale of minutes, while locally–originating chemically–controlled ozone depletion events normally arise more gradually and are not as intense (Jones et al., 2006). Efficient chemical ozone loss can sometimes occur over a period of a few hours where bromide concentrations are very high, during formation of new ice under a stable boundary layer (Jacobi et al., 2006).

In the Arctic the ozone–poor layer generally develops from the surface up to a temperature inversion, whereas in the Antarctic, ozone–depleted air masses are sometimes observed above the boundary layer due to uplifting by cold katabatic surface winds from the continental ice cap (Wessel et al., 1998) or by cyclonic advection processes (Frieß et al., 2004). This uplift of marine air masses depleted in ozone, can lead to ozone minima not appearing at the ground, but at several hundred or thousand metres up (Kreher et al., 1997; Wessel et al., 1998; Frieß et al., 2004; Jones et al., 2010). These higher–level inversions are characteristic of air masses of different origin and calculation of back trajectories often reveals a surface origin from sea ice zones. Roscoe et al. (2001) found that ozone depletion events at McMurdo and Neumayer correlated with trajectories which sampled the boundary layer near the sea ice edge between three and five days previously, with varying degrees of mixing from continental or non–boundary layer air. The horizontal extent of ozone–depleted layers was estimated, using local wind data and the duration of the ozone minimum, to be roughly 800±300 km for the Arctic and 1000±400 km for the Antarctic (Hausmann and Platt, 1994; Wessel et al., 1998).

Jones et al. (2010) investigated low and high altitude features of ozone depletion events in the Antarctic using two different profiling methods (tethered and free–flying ozonesondes) at Halley Bay (76°S, 27°W). The tethersonde data set showed that low altitude ODEs were highly constrained by the complex layering within the troposphere and were often confined within an extremely shallow lowest layer. Satellite images of BrO at the time of the tethersonde launches show no significant enhancement to the BrO column, which suggests that the impact on the wider atmosphere from Antarctic ODEs generated under low wind speeds and quiescent conditions is limited.

The results from the 1987 free–flying ozonesonde observations suggest that in Antarctica, profiles of ozone depletion to significant altitudes are associated with high wind speeds, low pressure systems and enhanced BrO. Their analyses strongly suggest that, when considering the wider implications of Antarctic tropospheric ODEs, it is the large, energetic low pressure systems that appear to be able to both process larger air masses and export them to lower latitudes. Such events are thus likely to drive the regional (or wider) impact of ODEs around Antarctica. The degree to which the free troposphere is altered by ODE chemistry in the future will therefore also be strongly influenced by any changes that may occur to such meteorological systems.

In pristine regions like Antarctica, tropospheric ozone is of stratospheric origin and variations in surface ozone can be interpreted in terms of transport processes (Wyputta, 1997). A possible forcing mechanism for the annual surface ozone variations is the intensity and frequency of synoptic scale disturbances moving from sub–polar latitudes into Antarctica (Oltmans and Komhyr, 1986; Wyputta, 1997). There is often a strong positive correlation between the surface temperature and surface ozone concentrations, though this wasn't observed at Neumayer (Bottenheim et al., 1990; Solberg et al., 1996; Wessel et al., 1998). Relative humidity is high inside the ozone depleted layer and in Antarctica ozone depleted air parcels are often transported by marine cyclones (Yurganov, 1990; Wessel et al., 1998). Lower levels of ozone are associated with cold Antarctic air masses within cyclones and higher levels with warm sectors of cyclones which are regions of influx of mid–latitude air. However, Wyputta (1997) found that at Neumayer cyclones accounted for 66% of increases in ozone partial pressure and suggested that a decrease in ozone and sea salt concentrations is observed in spring due to a decrease in cyclonic activity.

In Antarctic coastal areas, there is generally less complete ozone loss in the free troposphere than in the boundary layer events in the Arctic (Kreher et al., 1997; Wessel et al., 1998). Unlike the Arctic, the sea ice edge is far from most observing sites in Antarctica and katabatic winds from the interior carry air masses which are unlikely to be depleted in ozone (Roscoe et al., 2001). Hence few boundary layer ozone depletion events are observed at coastal sites, but many may be observed offshore, within and downwind of sea salt surfaces on ice or aerosols. Multi–axis DOAS measurements of tropospheric BrO were carried out aboard the German research vessel Polarstern during the Antarctic winter of 2006 (Wagner

et al., 2007b). For the period when the ship was inside the first year ice belt, enhanced BrO concentrations were almost continuously observed, beginning one month earlier than detected by satellite measurements. Ship–based measurements have also been performed in marginal ice zones in the Arctic, where fast chemical ozone loss was observed (Jacobi et al., 2006), and Pöhler et al. (2010) recently observed high BrO concentrations on the sea ice several kilometres from the coast in the Amundsen Gulf using active long–path DOAS (LP–DOAS) measurements.

2.3.2 Bromine sources

The two hypotheses that have been proposed for the primary mechanism that renders the salts accessible to the atmosphere are frost flowers and saline snow (Kaleschke et al., 2004; Simpson et al., 2007a). Frost flowers are fragile crystals that usually form on the surface in the early stages of sea ice formation, except where winds are too strong. They have been proposed as the surface from which bromine is released because they are highly saline and fractionated in sea–salt ions and provide a high surface area for bromine activation (Rankin et al., 2002; Kaleschke et al., 2004). Alternatively, they are very fragile and can be windblown onto the snow surface where they constitute a source of bromine (Wolff et al., 2003). Bromide ions are present in frost flowers and associated surface brine with concentrations typically two to three times those found in seawater (Perovich and Richtermenge, 1994; Rankin et al., 2002). Kaleschke et al. (2004) analysed tropospheric BrO and sea ice coverage, both measured from satellite remote sensing, and found that young ice areas potentially covered in frost flowers were correlated with high tropospheric BrO. Ozone depletion events at Halley Bay, Antarctica were correlated with air mass trajectories that had recent contact with a large coastal polynya that often produces frost flowers (Jones et al., 2006).

Snow and ice surfaces contaminated with salts, which are prevalent on first–year sea ice, have also been proposed as a primary surface for bromine release to the atmosphere (Foster et al., 2001; Simpson et al., 2005). Many recent studies have shown that snow and ice play an important role in photochemical production of a variety of important atmospheric species (Grannas et al., 2007). Laboratory experiments have shown that the uptake of HOBr on frozen sea–salt surfaces leads to efficient release of Br_2 and BrCl to the atmosphere (Adams et al., 2002). Br_2 and BrCl can reach high mixing ratios close to the snow surface and down to depths of 20 cm, even in the absence of sunlight or in twilight conditions (Foster et al., 2001; Spicer et al., 2002). There are several possible sources of the elevated bromine levels on pack ice and snow. Freezing sea water separates ice from brine, and some of this concentrated salt solution is forced to the new ice surface. Surface snow becomes impregnated with salts when brine wicks up the snow or wind scours the snow to re–expose saline surfaces, or sea salt aerosols are deposited on the snow (Domine et al., 2004). Sea spray is continually deposited on the snow pack throughout the polar night, from open oceans at the ice edge and from leads and polynyas within the sea ice zone. Additionally, sea salt can be moved by several mechanisms through the thick sea ice cracks and fissures

into the snow pack (McConnell et al., 1992).

The majority of the bromine atoms responsible for ozone depletion and mercury deposition come from salts containing bromide ions (Br^-) that originate from the ocean (McConnell et al., 1992) and are oxidized to bromine radicals by an autocatalytic pathway known as the bromine explosion (Fan and Jacob, 1992; Lehrer et al., 2004). The primary source of the bromine compounds is not yet clarified, but some indications point to brominated organic compounds (BOCs) like bromoform (Barrie et al., 1988; Sturges et al., 1993), or sea salt aerosols which can release reactive inorganic bromine by reactions with nitric oxides (Finlayson-Pitts et al., 1990), HSO_5^- or HO_2 radicals (Mozurkewich, 1995), and by photoinduced conversion of Br^- to Br_2 involving dissolved organic materials or transition metals (McConnell et al., 1992).

The peak in annual filterable bromine shortly after the Arctic sunrise is attributed to photochemically induced conversion of gaseous organobromine compounds (Barrie et al., 1988). Total alkanobromine concentrations were found to be a factor of 3.6 higher in the Arctic than in Antarctica, with 57% of the alkanobromine as bromoform versus only 15% in the Antarctic. Bromoform ($CHBr_3$) is the most easily photolysed of the alkanobromine gases (Berg et al., 1984; Barrie et al., 1988). Bromoform is produced from ice algae, macroalgae such as kelp, phytoplankton and decay of marine algae such as red benthic algae (Dyrssen and Fogelqvist, 1981; Sturges et al., 1993; Cota and Sturges, 1997; Quack and Wallace, 2003; Warwick et al., 2006b). The most rapid decrease in bromoform is observed during polar sunrise, suggesting photochemical activity of this gas (Barrie et al., 1988).

Methyl bromide (CH_3Br) is the most abundant species containing bromine in the free troposphere as well as the stratosphere, but there are currently large uncertainties in the strengths of CH_3Br sources (Yung et al., 1980; Yokouchi et al., 2000, 2002; Warwick et al., 2006a). The largest source of CH_3Br is likely to be agricultural chemical fumigation, followed by terrestrial ecosystems and biomass burning. The oceans are believed to be a net sink for CH_3Br, although future changes in sea surface temperature or marine organisms could make the oceans a net source. There is a negative flux from surface waters under–saturated in CH_3Br in tropical ($>20°C$) and cold regions ($<12°C$), while temperate waters are often supersaturated in CH_3Br and are a net CH_3Br source (Warwick et al., 2006a). CH_3Br is also the longest lived bromine containing species in the free troposphere besides the halons, which are used in fire extinguishers (Warwick et al., 2006b).

The sea salt aerosol has been suggested as a source of bromine to the atmosphere (Finlayson-Pitts et al., 1990; Mozurkewich, 1995). In most cases, observations of air masses originating from the sea ice are characterized by strong tropospheric light path enhancement in zenith–sky spectra, as the BrO slant column densities are amplified due to multiple scattering. It is likely that the light path enhancements are at least partially caused by transport of sea–salt aerosols inland

(Frieß et al., 2004). However, the bromide from aerosols alone is not sufficient to account for the high levels of reactive gas phase bromine species (including Br, Br_2, BrO, HOBr, $BrNO_2$, and $BrONO_2$) necessary for fast ozone depletion (Tang and McConnell, 1996; Lehrer et al., 2004). However, the aerosol efficiently recycles less reactive bromine species (e.g. HBr) and feeds them back into the ozone destruction cycle (Lehrer et al., 2004). Outside the polar regions, the main source of bromine is sea salt aerosol generated by breaking waves on the ocean surface (Tang and McConnell, 1996; Sander et al., 2003). Whereas, the process in sea ice covered regions appears to be largely modulated by air temperature (Frieß et al., 2004; Piot and von Glasow, 2008) or blowing snow and ice (Jones et al., 2009; Yang et al., 2008, 2010).

From observations at Neumayer Station in the Weddell Sea, Wyputta (1997) suggested that atmospheric sea salt production is dependent on wind speed over the ice–free ocean and on sea ice cover. Outside sea ice–covered regions, sea salt aerosols are produced by the wind–induced bursting of bubbles at the ocean surface and most of the sea salt particles are found in the lowest 1.5 km of the atmosphere. Strong winds with cyclonic activity and low sea ice cover produce high sea salt concentrations in autumn. Wyputta (1997) suggested that in winter, the extent of sea ice cover is too large for transport of sea salt aerosols from their open–water source to the Antarctic coast, so the sea salt concentration is at a minimum. Deposition of sea salt onto the sea ice and snow pack occurs closer to the areas of open ocean away from the coast. Slightly higher levels of sea salt in the spring are due to polynyas that open up at the coast, while the summer minimum is due to anticyclonic activity transporting clean continental air (Wyputta, 1997).

Meanwhile, clear evidence has emerged that the primary source of sea salt aerosol in winter for coastal Antarctic sites is not open water, but the sea ice surface (Wagenbach et al., 1998; Rankin et al., 2002; Wolff et al., 2003). Because mirabilite (sodium sulphate decahydrate) starts to precipitate below -8°C, the aerosol formed from young sea ice is strongly depleted in sulphate (Rankin et al., 2002). Measurements of aerosol and snow, as well as air masses coming from fresh sea ice covered in frost flowers, show high salt concentrations and negative non–sea salt SO_4^{2-}. This means that they are depleted in sulphate ions relative to sodium ions when compared to the ratio in sea water and can thus be distinguished from the direct open water source (Rankin et al., 2002). Small BrO concentrations over the open oceans indicate that activated bromine has a short atmospheric lifetime without contact with first–year sea ice (Wagner et al., 2007b).

2.3.3 Bromine explosion chemistry

The sea–salt is exposed to the atmosphere via heterogeneous reactions on young sea ice surfaces, frost flowers (fragile ice crystals), the snow pack, sea water and marine aerosols. To produce the amount of gaseous BrO_x required for the observed rapid ozone destruction, a production time of one month would be

required if it came from $CHBr_3$ photolysis alone (Barrie et al., 1988; McConnell et al., 1992). The source of this extra BrO_x is from heterogeneous reactions on ice surfaces. A likely possibility is that sea salt Br^- reaches high concentrations on the snow pack during the long polar night and is released to the atmosphere as Br_2 at polar sunrise (McConnell et al., 1992; Tang and McConnell, 1996). Normally, gas–phase photochemical reactions of Br_2 with species such as HO_2, HCHO, and C_2H_2 rapidly produce relatively inactive HBr, HOBr, $BrNO_3$ and other BOCs, with consequently little destruction of boundary layer ozone. However, in the polar boundary layer these less reactive species are scavenged by aerosols and ice crystals, and heterogeneous reactions then release Br_2 and BrO back into the atmosphere (see Eq. 2.4 below) (Fan and Jacob, 1992; McConnell et al., 1992; McElroy et al., 1999). Photolysis of Br_2 rapidly forms Br, which can then destroy O_3 through the catalytic cycle:

$$\begin{aligned} 2(Br + O_3) &\longrightarrow 2(BrO + O_2) && (2.1)\\ BrO + BrO &\longrightarrow 2Br + O_2 && (2.2)\\ \hline \text{Net}: \quad 2O_3 &\longrightarrow 3O_2 \end{aligned}$$

As the solar flux becomes more intense, more Br_2 is released from the snow pack and aerosols, until either the snow is depleted or the boundary inversion layer breaks down, diluting the high bromine levels with free tropospheric air. There is also a diurnal cycle for gas–phase reactive bromine during the period before the onset of 24–hour sunlight. The gas–phase Br_2 is rapidly photolysed during daytime, but high concentrations may accumulate at night through the reaction

$$BrO + BrO \longrightarrow Br_2 + O_2 \qquad (2.3)$$

During the night HBr, and probably many of the BOCs, are scavenged by the aerosols and ice crystals. Heterogeneous reactions, such as the reaction of HOBr with Br^- in acid solution then release Br_2 back to the atmosphere:

$$HOBr_{(aq)} + Br^- + H^+ \longrightarrow Br_{2(aq)} + H_2O \qquad (2.4)$$

where the subscript (aq) denotes aqueous phase heterogeneous reactions on sea salt surfaces. This reaction is expected to be rapid in first–year sea ice zones due to the high concentration of bromine, and the high solubilities of HBr and HOBr, and may be further facilitated in the Arctic by the abundance of sulphuric acid aerosol. The production of $Br_{2(aq)}$ by this reaction is probably limited only by the rate of uptake of either HBr or HOBr by the aerosol. As $Br_{2(aq)}$ is produced it volatizes to the gas phase much more rapidly than the hydrolysis, which is the reverse of the above reaction (Fan and Jacob, 1992). The recycling of bromine maintains high levels of Br atoms and BrO radicals to destroy ozone (Fan and Jacob, 1992; McConnell et al., 1992; Roscoe et al., 2001). Model studies by Piot and von Glasow (2008) found that recycling of bromine on snow is the most important process to sustain high boundary layer bromine levels and ozone

depletion. The heterogeneous recycling of bromine appears to be a process which self–terminates once ozone depletes to low levels (Tang and McConnell, 1996). The bromine explosion reaction sequence is then (Simpson et al., 2007b):

$$\begin{aligned} \mathrm{HOBr} + \mathrm{Br}^- + \mathrm{H}^+ &\longrightarrow \mathrm{H_2O} + \mathrm{Br_2} && (2.5)\\ \mathrm{Br_2} &\xrightarrow{h\nu} 2\mathrm{Br} && (2.6)\\ \mathrm{Br} + \mathrm{O_3} &\longrightarrow \mathrm{BrO} + \mathrm{O_2} && (2.7)\\ \mathrm{BrO} + \mathrm{HO_2} &\longrightarrow \mathrm{HOBr} + \mathrm{O_2} && (2.8)\\ \hline \text{Net}: \quad \mathrm{H}^+ + \mathrm{Br}^- + \mathrm{HO_2} + \mathrm{O_3} &\longrightarrow \mathrm{Br} + \mathrm{H_2O} + 2\mathrm{O_2} \end{aligned}$$

Low concentrations of NO_x are observed during ozone depletion events due to the rapid formation of $BrNO_3$ through the reaction (Bottenheim et al., 1990; Fan and Jacob, 1992):

$$\mathrm{BrO} + \mathrm{NO_2} \longrightarrow \mathrm{BrNO_3} \qquad (2.9)$$

This is rapidly scavenged by the aerosol and ice surfaces and hydrolyzed to HOBr through the reaction:

$$\mathrm{BrNO_{3(g)}} + \mathrm{H_2O} \longrightarrow \mathrm{HOBr_{(aq)}} + \mathrm{HNO_3} \qquad (2.10)$$

where the subscript (g) denotes gas phase reactions. The Antarctic snow pack is known to be a source of NO_x in summer (Jones et al., 2000), but it is small in spring when sunlight is low. In the low NO_x environment, the typical ozone production rate is less than 0.55 ppb per day in summer, and even less in spring when UV levels are lower (Ayers et al., 1997). Production at 0.55 ppb per day corresponds to twenty days to recover to normal levels (Roscoe et al., 2001). Since some BrO can also still be present in the ozone–poor air masses, ozone loss will continue in transit. A long lifetime for BrO, through recycling together with a long recovery time for NO_x suggests that an ozone deficit may continue for a month or more and be mixed into the free troposphere (McElroy et al., 1999; Roscoe et al., 2001). Several recent studies investigating snow photochemistry, have found evidence that halogen chemistry may influence HO_x and NO_x cycling in coastal Antarctica during the summer (outside of the severe ozone depletion season) (Grannas et al., 2007).

A still unresolved question is the explanation how the acid–catalysed bromine explosion reaction cycle is triggered on particles derived from alkaline sea water. The key trigger might be precipitation of calcium carbonate from brine on the surface of sea ice and frost flowers at sufficiently low temperatures (Sander et al., 2006; Piot and von Glasow, 2008). Halogen activation is limited by both salt content and acidity. There is a trade–off between the amount of available sea salt, which provides bromide but is alkaline, and the required acidity. The fastest modelled ozone depletion rate occurs at medium aerosol levels where bromide concentrations are moderately high, but the available acids are still able to neutralize the sea–water alkalinity (Sander et al., 2006).

2.4 Other halogens

2.4.1 Iodine

The atmospheric chemistry of iodine is important for several reasons, including the influence on the oxidising capacity of the troposphere, the formation of new particles, and the enrichment of iodine in marine aerosols (Saiz-Lopez and Plane, 2004). Modelling studies of boundary layer iodine chemistry have shown that, even at very low mixing ratios, IO can have a major impact on the ozone concentration (Alicke et al., 1999; Vogt et al., 1999; McFiggans et al., 2000; Calvert and Lindberg, 2004; Saiz-Lopez et al., 2006a). At low iodine concentrations the ozone destruction pathway involving HOI is the most important:

$$\mathrm{I} + \mathrm{O_3} \longrightarrow \mathrm{IO} + \mathrm{O_2} \tag{2.11}$$
$$\mathrm{IO} + \mathrm{HO_2} \longrightarrow \mathrm{HOI} + \mathrm{O_2} \tag{2.12}$$
$$\mathrm{HOI} + \xrightarrow{h\nu} \mathrm{OH} + \mathrm{I} \tag{2.13}$$

At higher iodine concentrations the reaction cycle involving the IO self–reaction becomes dominant:

$$2(\mathrm{I} + \mathrm{O_3}) \longrightarrow 2(\mathrm{IO} + \mathrm{O_2}) \tag{2.14}$$
$$\mathrm{IO} + \mathrm{IO} \longrightarrow 2\mathrm{I} + \mathrm{O_2} \tag{2.15}$$
$$\mathrm{IO} + \mathrm{IO} + \mathrm{M} \longrightarrow \mathrm{I_2O_2} + \mathrm{M} \tag{2.16}$$
$$\mathrm{I_2O_2} \xrightarrow{h\nu} 2\mathrm{I} + \mathrm{O_2} \tag{2.17}$$

However, this has recently been thrown into question with IO concentrations measured in the ppb range inside the snow pack by Frieß et al. (2010). These high amounts cannot be explained on the basis of the current knowledge of iodine chemistry, which predicts that IO concentrations should be limited by the self reaction.

The addition of iodine chemistry to models has the effect of accelerating photochemical release of Br and Cl from sea salt (Vogt et al., 1999). Depending on the concentration of BrO the following cross–reaction cycle becomes important (Solomon et al., 1994a):

$$\mathrm{I} + \mathrm{O_3} \longrightarrow \mathrm{IO} + \mathrm{O_2} \tag{2.18}$$
$$\mathrm{Br} + \mathrm{O_3} \longrightarrow \mathrm{BrO} + \mathrm{O_2} \tag{2.19}$$
$$\mathrm{IO} + \mathrm{BrO} \longrightarrow \mathrm{I} + \mathrm{Br} + \mathrm{O_2} \tag{2.20}$$

There is also a corresponding IO plus ClO cycle but it is much less important because of the lower ClO mixing ratio and reaction coefficient (Vogt et al., 1999).

The main source of iodine in the marine boundary layer is from photodegradation of iodinated organic compounds produced by macroalgae and phytoplankton (Carpenter et al., 1999; Saiz-Lopez and Plane, 2004; Saiz-Lopez et al., 2006a). Measurements indicate that IO is present at low levels in much of the coastal and open ocean boundary layer at mid–latitudes (Allan et al., 2000), but so far tropospheric IO in the Arctic has only been observed by Wittrock et al. (2000), but with some uncertainty. Observations at Mace Head, Ireland showed that I_2 was the main precursor of ultra–fine aerosol particle formation when macroalgae are exposed to the atmosphere at low tide (Saiz-Lopez and Plane, 2004; Saiz-Lopez et al., 2006b).

Recent measurements at Neumayer (Frieß et al., 2001, 2010) and Halley (Saiz-Lopez et al., 2007a) showed substantial amounts of reactive iodine, which could play an important role in boundary layer ozone depletion in Antarctica, mainly through coupling with bromine chemistry. These high levels of IO observed in coastal Antarctica might lead to the formation of fine aerosol particles. Nadir measurements made by the SCIAMACHY satellite instrument (Schönhardt et al., 2007, 2008; Saiz-Lopez et al., 2007a) provide a global picture of the distribution of IO columns. The largest amounts are found in the Antarctic with the highest monthly values of 8×10^{12} molec cm^2 detected in a widespread area close to the Antarctic continent. A seasonal variation in the Antarctic region is observed with low values in winter (in the regions accessible to the satellite measurements), and a maximum IO column density during October and March (springtime and autumn). This is in good accordance, for this seasonal evolution of IO amounts, with ground–based measurements at Halley (Saiz-Lopez et al., 2007a) where peak IO concentrations of 20 ppt were reported. No enhanced amounts of IO were observed by SCIAMACHY for the Arctic region, which indicates systematic differences in the availability of precursor substances between the northern and southern polar regions. Potential release mechanisms include both a direct inorganic release of iodine from the mineral phase and the photolysis of organic iodocarbon compounds, for example, from the biosphere below and around the sea ice. Enhanced IO amounts are also detected on the Antarctic continent, which is noteworthy as this means that IO is detected some distance from suspected sources of iodine and the most likely explanation includes transport processes from neighbouring sea ice regions.

2.4.2 Chlorine

As chlorine is present only in small concentrations in the polar boundary layer, its direct effect on ozone depletion is probably only minor. But chlorine does play an important role in oxidation of volatile organic compounds (VOCs) and indirectly influences bromine chemistry (Simpson et al., 2007b). During a bromine explosion event the production of chloride ions from Cl_2 is small; most of the

chloride originates from the photolysis of BrCl. Bromine is activated first and chlorine activation only occurs once the particles have lost all of their bromide (Foster et al., 2001; Sander et al., 2006). The chemistry of chlorine atoms and their precursors in the boundary layer is not well understood and further research is required to develop the understanding of their role in ozone depletion events.

2.5 Mercury

Each spring at high latitudes, oxidation of gas–phase elemental mercury (GEM) occurs in concert with ozone depletion events (Lu et al., 2001). BrO and Br are thought to play essential roles in these oxidation reactions of mercury (Hg^0) vapour to water soluble mercury, Hg^{2+}, as indicated by observations of gaseous and particulate mercury in the Arctic (Barrie and Platt, 1997; Schroeder et al., 1998) and Antarctica (Temme et al., 2003). Thus, BrO enhancements can have an impact on the polar environment by increasing the deposition of mercury, a toxic compound, which then accumulates on the snow pack. Mercury exists in the atmosphere predominantly in its elemental gaseous state, with atmospheric residence times of 6–24 months (Schroeder et al., 1998). Thus, mercury can undergo long range atmospheric transport from industrial source areas to the polar regions. Surface measurements at Alert, Canada show that, during three months in spring, there are frequent episodic depletions in mercury vapour concentrations resembling surface ODEs (Schroeder et al., 1998).

Recent research (Calvert and Lindberg, 2003; Ariya et al., 2004) has elucidated the following series of photochemically initiated reactions to convert GEM to reactive gaseous mercury (RGM), which can subsequently deposit onto snow and ice surfaces:

$$\mathrm{Br} + \mathrm{Hg}^0 \longrightarrow \mathrm{HgBr} \tag{2.21}$$

$$\mathrm{BrO} + \mathrm{Hg}^0 \longrightarrow \mathrm{HgO} + \mathrm{Br} \tag{2.22}$$

$$\mathrm{BrO} + \mathrm{Hg}^0 \longrightarrow \mathrm{HgBrO} \tag{2.23}$$

$$\mathrm{BrO} + \mathrm{Hg}^0 \longrightarrow \mathrm{HgBr} + \mathrm{O} \tag{2.24}$$

The rapid melting of snow and ice during spring can result in massive inputs of mercury into the ecosystems and biogeochemistry in Antarctica (Ebinghaus et al., 2002). This introduction of mercury into marine and terrestrial ecosystems occurs at the beginning of the season of peak activity and breeding for most of the region's biota. Together with the increasing anthropogenic mercury release in the atmosphere (Fitzgerald et al., 1998; Martinez-Cortizas et al., 1999), these processes are likely to have a negative impact on the biosphere in polar regions. A better understanding of the mechanisms leading to the increased deposition of toxic mercury during bromine explosion events could be achieved by simultaneous measurements of BrO together with mercury in the gas phase, in aerosols and in the snow pack.

Chapter 3

Measurements in McMurdo Sound, Antarctica

This chapter describes the measurement sites in McMurdo Sound, Antarctica and the TARDIS (Transportable Antarctic Remote DOAS Instrument System) measurement platform comprising the MAX–DOAS system, in situ ozone analysers and a weather station. Some background is given on absorption spectroscopy and the DOAS spectral retrieval technique used to convert the radiance measurements into trace gas slant column densities (SCDs).

3.1 Measurement sites

Two springtime measurement campaigns were conducted close to Ross Island in McMurdo Sound, Antarctica (see Fig. 3.1); the first from 26$^{\text{th}}$ August to 28$^{\text{th}}$ November 2006 and the second from 20$^{\text{th}}$ August to 1$^{\text{st}}$ December 2007. Measurements were made at four sites, shown in Fig. 3.2: Arrival Heights observatory (AH), multi–year sea ice north of McMurdo Station (M), first–year sea ice between Inaccessible Island and Cape Evans (CE), and active new sea ice at Cape Bird (CB).

3.1.1 Arrival Heights

Zenith sky DOAS measurements of BrO have been made at the New Zealand observatory at Arrival Heights (77.83° S, 166.66° E) since 1995 and MAX–DOAS measurements have been made since 1998. Arrival Heights is located 185 m above the sea ice on Ross Island, close to McMurdo Station and it is one of the primary NDACC (Network for Detection of Atmospheric Composition Change) measurement sites. The primary reason for making measurements with the TARDIS at Arrival Heights was to calibrate the surface ozone analysers, the Aeroqual S500 and the 2B 205, with the TEI 49C surface ozone analyser there. In 2006, the TARDIS was tested at Arrival Heights from 5$^{\text{th}}$ to 16$^{\text{th}}$ September, then Aeroqual measurements were made on the 23$^{\text{rd}}$ September and 16$^{\text{th}}$ October and 25$^{\text{th}}$ of November. In 2007, the initial testing and comparison of the 2B–205 and

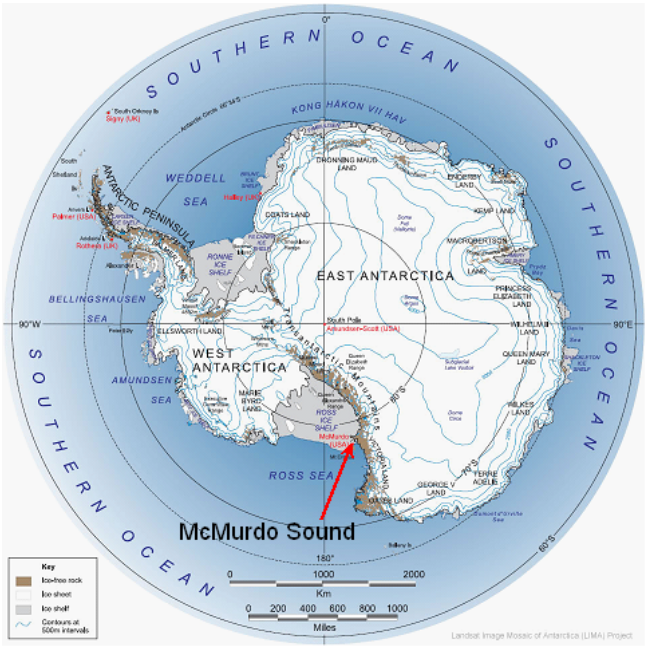

Figure 3.1: The location of Ross Island and McMurdo Sound on the edge of the Ross Ice Shelf with the Ross Sea to the north.

Aeroqual with the TEI as conducted at Arrival Heights from 25th to 27th August, and further comparisons were made on 16th October and 26th to 16th November.

3.1.2 McMurdo

Measurements were made at the McMurdo site (77.82° S, 166.58° E) on multi–year sea ice 2 km north–west of Arrival Heights from 25th September to 14th October 2006 (left–hand picture in Fig. 3.3). This site was chosen for its proximity to Scott Base during the initial instrument testing period, and also because of limited availability of transport. Without a wind generator in 2006, it was necessary to visit the instrument every second day to recharge the batteries. Located approximately 25 km from open water, with the prevailing wind coming from inland (south–east), concentrations of sea salt in the snow pack and ice surface, and thus the expected likelihood of observing locally–produced BrO, were likely to be lower than on first year sea ice. However, the location allowed a more direct comparison of BrO and ozone measurements on the sea ice with the nearby elevated site of Arrival Heights.

3.1.3 Cape Evans

From 25th August to 15th October 2007, measurements were made 22 km north of Arrival Heights, between Inaccessible Island and Cape Evans (77.64° S, 166.38° E, right–hand pictures in Figs. 3.3 and 3.4). In the previous summer the multi–

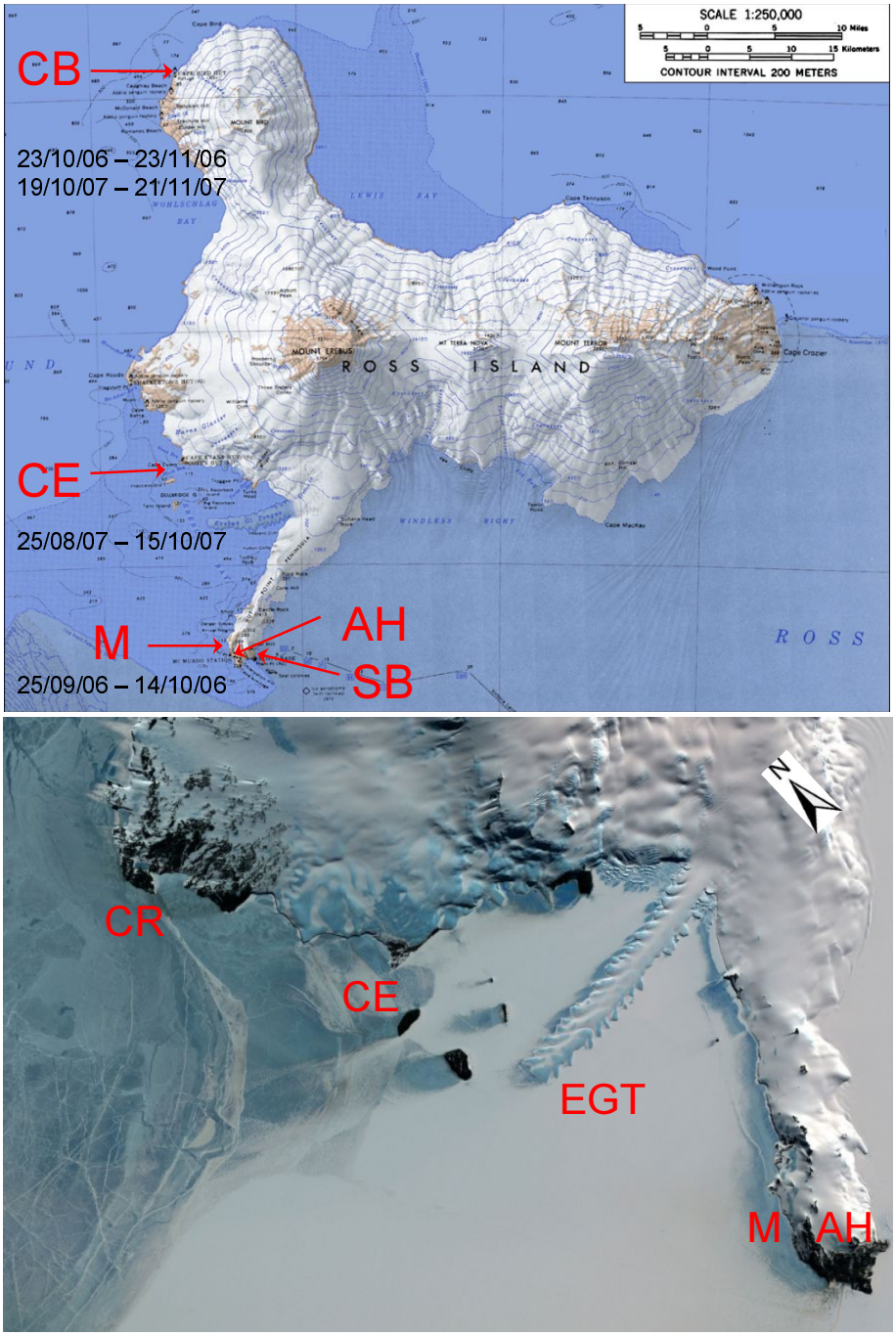

Figure 3.2: Locations of the measurement sites around Ross Island (USGS map) showing the corresponding measurement dates (top). The red dotted line indicates the approximate boundary of the first year sea ice above the line and multi–year ice below the line in 2007. The MODIS (Moderate Resolution Imaging Spectrometer) satellite image of Erebus Bay, McMurdo Sound (bottom) clearly shows the first year sea ice north–west of Cape Evans and the snow–covered multi–year sea ice to the south. CB=Cape Bird, CE=Cape Evans, M=McMurdo, AH=Arrival Heights, SB=Scott Base, CR=Cape Royds and EGT=Erebus Glacier Tongue.

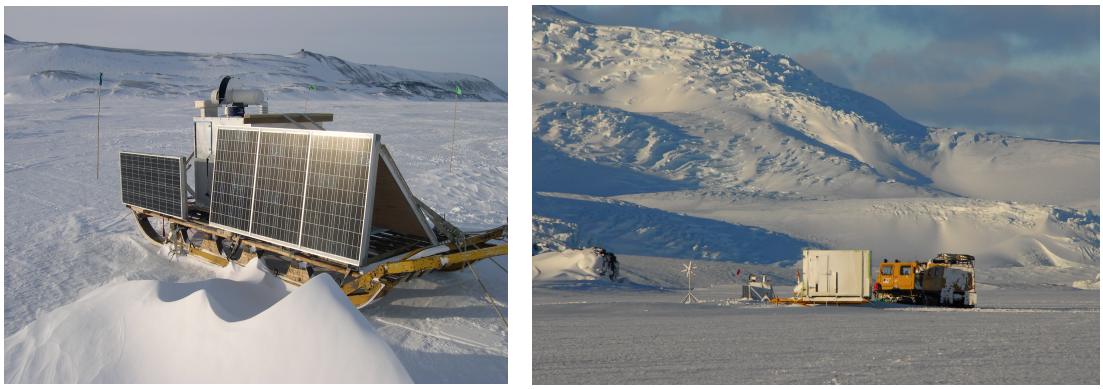

Figure 3.3: Left: The TARDIS on the sea ice near McMurdo Station, with Arrival Heights observatory on the hill directly above the tracker. Right: The TARDIS with the wind generator, Wannigan day shelter, and Hägglunds at Inaccessible Island. Cape Evans and the Pakaru Icefalls of Mount Erebus in the background.

year ice had broken out as far back as the Erebus Glacier Tongue, which meant that this site was on first year sea ice approximately 8 km beyond the edge of the multi year ice and about 5 km from open water. The sea ice was approximately 1.5 metres thick at the site. The prevailing wind at Inaccessible Island, as at McMurdo, was from the Ross Ice Shelf (south–easterly).

3.1.4 Cape Bird

Two measurement campaigns were conducted at Cape Bird (77.22° S, 166.43° E, left–hand picture in Fig. 3.4) 68 km north of Arrival Heights near the northern tip of Ross Island from 23rd October to 23rd November 2006 and from 19th October to 21st November 2007. This was expected to be an ideal site for observing halogens since it is well inside the first year sea ice zone where open leads frequently form and refreeze. Cape Bird can only be reached by helicopter so access was not possible until mid–October, when helicopter operations begin at McMurdo Station.

3.2 The instrument platform

The TARDIS is a portable instrument platform which contains a spectrometer, two in situ ozone analysers, a weather monitor to measure temperature, pressure, wind speed, wind direction, and relative humidity. The TARDIS was designed to survive in extreme cold, below −40° C, and high winds over 100 km hr^{-}1, and to operate semi–autonomously at remote sites. It was also designed to withstand vibration and movement during transportation by vehicle, sledge and helicopter, without requiring extensive reassembly at the field sites. The primary external components of the TARDIS are displayed in Fig. 3.5 and the internal layout is shown in Fig. 3.6.

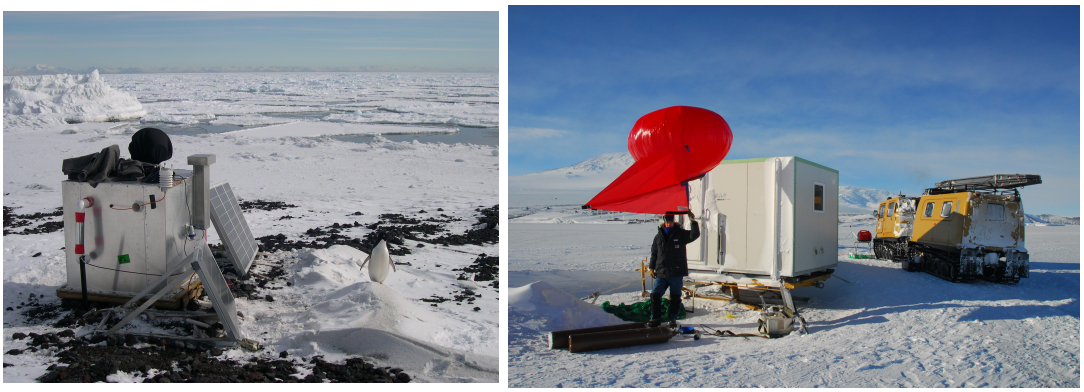

Figure 3.4: The left–hand picture shows the TARDIS at Cape Bird in 2006 with the original chimney system for the Aeroqual and the short cooling tube, which is open in the picture. The tracker head is covered for a dark measurement. Note, the broken condition of the sea ice typical for much of the time at Cape Bird. The right–hand picture shows the Helikite, Wannigan day shelter and Hägglunds at Inaccessible Island.

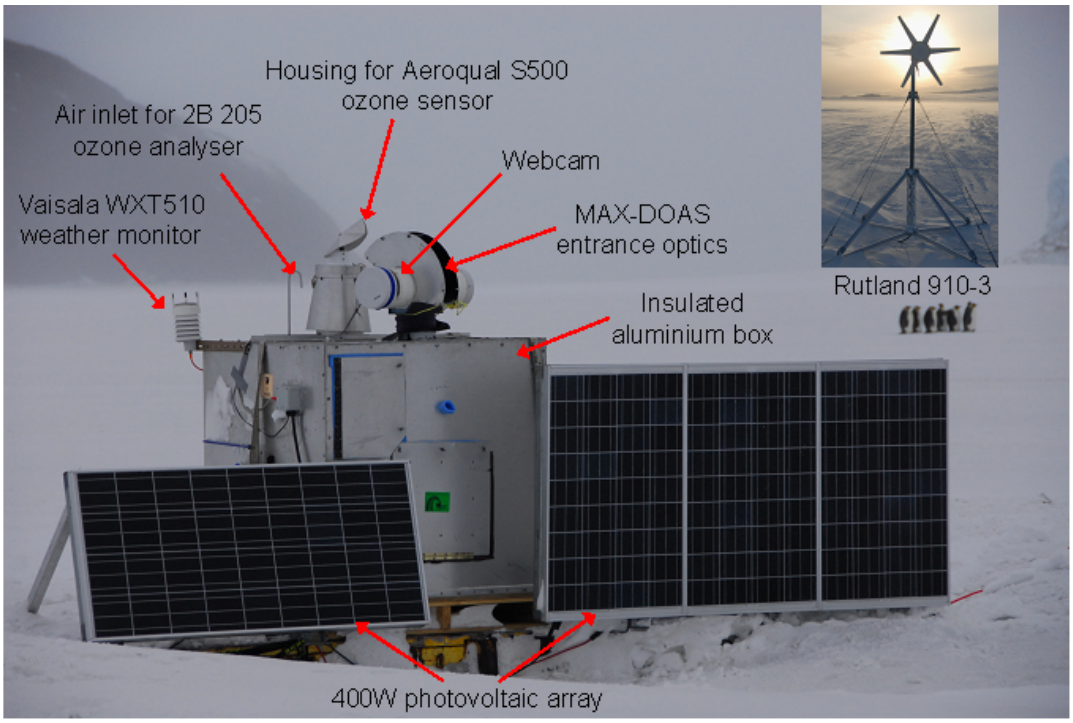

Figure 3.5: The TARDIS instrument platform at Cape Evans with Inaccessible Island in the background and the wind generator in the inset picture.

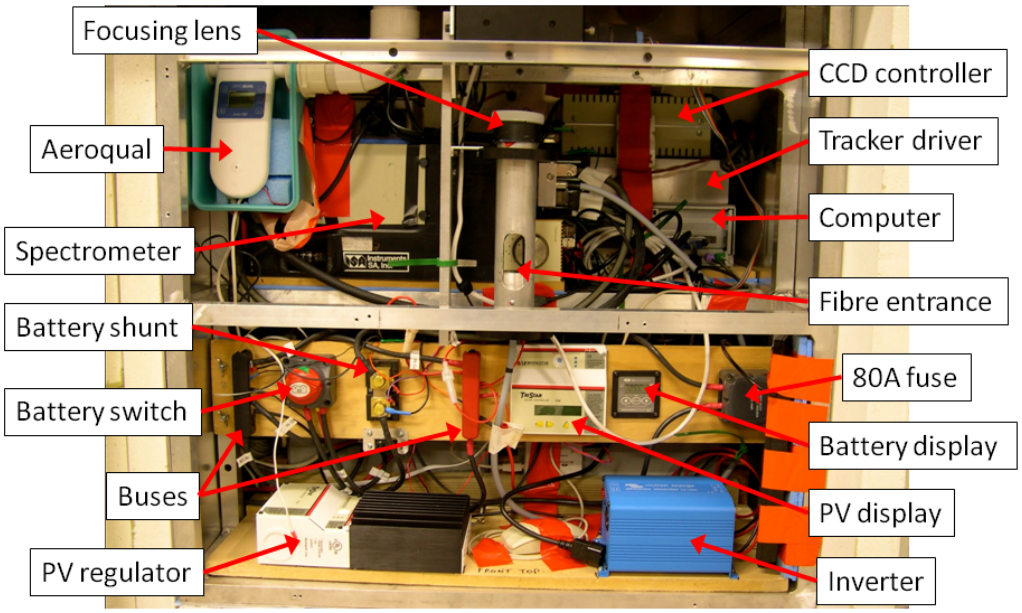

Figure 3.6: The internal layout of the TARDIS. The batteries are located out of sight behind the inverter and PV regulator.

3.2.1 The spectrometer and entrance optics

The BrO and IO measurements were made using a Czerny–Turner type ISA HR320 flat–field spectrograph with a focal length of 320 mm, an aperture ratio of f/4 and a field of view of $\sim 0.5°$. The 1200 g/mm grating had a wavelength range of 330–452 nm with a resolution, measured with a mercury line lamp, of 0.61 nm FWHM at 334.15 nm and 0.58 nm FWHM at 435.8 nm. The array detector was a Hamamatsu C7042 detector head with S7032–1007 sensor chip. The chip is back–thinned, allowing light to enter from the rear of the silicon substrate, which substantially increases the quantum efficiency over the whole spectral range, especially in the UV range (<400 nm). The sensitivity in the UV region is important in order to obtain a good signal–to–noise ratio for BrO measurements. This charge coupled device (CCD) device has 1044 horizontal by 128 vertical pixels each 24 microns square. In the fast frame transfer (FFT) mode used, the 128 vertical pixels are clocked into a horizontal bin of 1044 storage wells, which are read out serially by the electronics once every integration period (with a range of 0.016 to 20 seconds). The electron capacity of the storage wells (600,000) that are shielded from the light, is twice the capacity of the photo–active pixels, which therefore operate well below saturation. The detector signal is then passed to the computer via a 16–bit analogue to digital converter card. The detector was cooled to -20°C

using a Peltier cooler to minimise the dark current noise caused by thermally excited electrons. The dark current approximately doubles for every 7°C increase in temperature and becomes important in low light conditions. Cooling to -20°C achieves acceptable noise reduction, while further cooling would require too much power. Regular dark current measurements were made, with an exposure time of 20 s and an integration time of 20 min, after capping the fibre entrance lens and covering the tracker with a dark cloth.

The entrance optics, shown in Fig. 3.7, consisted of a rotating flat mirror and an angled telescope mirror that reflected light down through a focusing lens onto the entrance of a quartz fibre optic bundle inside the TARDIS. Grating spectrometers have different transmittances as a function of wavelength depending on whether the incident light is polarised parallel to or normal to the grating. The fibre optic cable overcomes this problem by depolarising the incoming light, while the polarising effect of the spectrometer mirrors is canceled out when the spectra are ratioed with the reference spectra. The mirrors were contained inside a sealed plastic tube with a UV–transmitting acrylic (Perspex) window. Silicon desiccant was placed inside the tube to reduce moisture and frosting on the mirrors and windows. Aluminium flanges, painted black on the inside, were mounted on the outside of the tube to shade the telescope from direct sunlight. A Schott band pass BG–24 coloured glass filter with a maximum transmittance at 350 nm (transmittance range: $\sim$ 330–450 nm) was placed just above the fibre optic cable to reduce stray light. A webcam, also housed in the tube with a small rotating mirror, recorded images of the sky in the spectrometer viewing direction at two minute intervals.

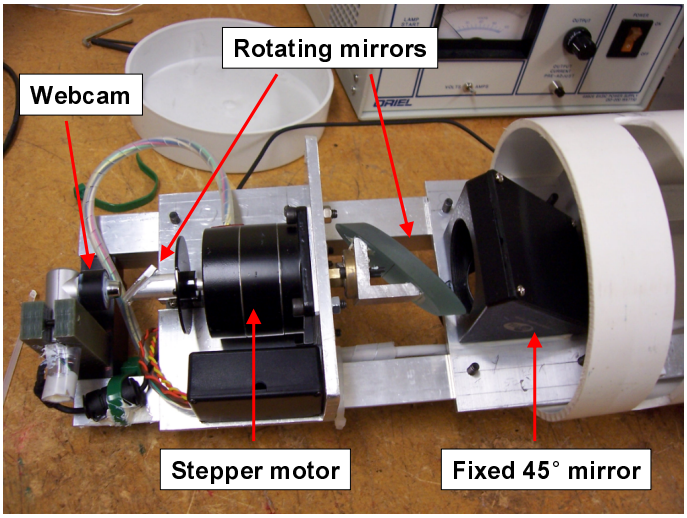

Figure 3.7: The inside of the tracker head.

The elevation angles used were 0°, 1°, 3°, 5°, 10°, 45°, and 90° with the addition of 20° from the 3rd to 22nd November 2007. Most of the information about the lowermost $\sim$500 m of the atmosphere is provided by the lowest elevation angles

up to 5°, while the 10° and 45° can provide some extra information about the overlying layers up to ∼2 km (see Chap. 5). The elevation and azimuth of the tracker were controlled by a stepper motor and an optical position sensor was used to reset the tracker elevation to 0° at the beginning of each scan sequence. The tracker azimuth was fixed in various directions during the measurement campaigns, with an unobstructed view across first year and fresh sea ice. An integration time of three minutes for each elevation angle was chosen to provide a good signal–to–noise ratio.

At low viewing elevation angles, the air–mass traversed by the scattered light entering the narrow field of view of the telescope is sensitive to small changes in elevation angle (see Chap. 4). The elevation angle, therefore, must be accurate so that the forward modelled DSCDs in the retrieval are consistent with the measurements and the retrieved state profile is meaningful (see Chap. 5). The tracker elevation angle on the TARDIS was calibrated in the dark at Scott Base by directing a light into the horizontal telescope from several metres away on a level concrete floor, moving the light up and down on a graduated pole until a maximum signal was observed on the detector. The height of the light was then compared with the height of the centre of the telescope above the floor and they were found to be equal, so no adjustments to the tracker were required. The level of the TARDIS was then checked in the field using a spirit level.

3.2.2 The measurement software

The spectrometer control and logging software used in this work was developed in Labview by Paul Johnston at the National Institute of Water and Atmospheric Research (NIWA), Lauder, New Zealand. The program controls the signal saturation, sample and integration times, the stepper motors for telescope elevation and azimuth and the Peltier temperature, displays the spectra and saves them to a daily data file after each integration.

3.2.3 The power supply

The power consumption of the TARDIS ranged from approximately 140–180 W in 2006 and 110–160 W in 2007, for approximately seven hours per day at the start of the season to twenty four hours per day at the end. The minimum requirement was to supply power for two to three days at a time, as a fully autonomous power supply would have been too costly and too large to transport. All components of the power system were supplied, along with excellent advice, by Able Solar Ltd. (www.ablesolar.co.nz) in Auckland, and Solar Selectives Ltd. (www.solarselectives.co.nz) in Nelson.

Batteries

The energy was stored in six Concorde Sun–Xtender (www.concordebattery.com) 12 V 104 Ah (ampere–hours, charge storage capacity) valve–regulated lead–acid, absorbed glass mat (AGM) deep cycle batteries. Battery specialists recommended either Concorde AGMs or Sonneschein high performance gel cells, but the AGMs were chosen for several reasons. They are sealed, non–spillable and recombinant, which means that greater than 99% of the hydrogen and oxygen released by electrolysis is reconverted to water during charging, so they are safe for transport on aircraft and for installation in poorly ventilated spaces together with electrical equipment. This was an important requirement because battery capacity is severely reduced at cold temperatures (see left–hand plot in Fig. 3.8) and even AGM batteries freeze below -30°C when more than 50% discharged, though this does not destroy them. The boron–silicate glass fibre between the plates is not completely saturated, so unlike gel cells, AGM batteries will not burst if frozen. By housing the batteries together with the instruments, they were kept in the temperature range of 10° to 25°. A primary advantage of AGM batteries over gelled electrolyte batteries is that they can be recharged at much higher currents. Gel cells must be recharged slowly and at a lower voltage than other lead–acid batteries, generally at an ampere rate of 0.05C (one twentieth of the capacity in ampere–hours) or 0.1C, which means that a 100 Ah battery should only be charged at 5–10 A, or there is a risk of destroying or bursting the battery due to excess gas production. Concorde Sun–Xtender AGMs have a very high charge acceptance rate up to 5C due to their low impedance, and a bulk charging rate of 0.2C, which is 120 A for this 600 Ah battery bank, is recommended for repetitive deep cycling (www.sunxtender.com, 2009), so they can be recharged very quickly. The final consideration was to maximise energy density in order to keep the dimensions of the TARDIS within reasonable limits for transportation. The Concorde AGMs have one of the highest capacities for their volume compared to other lead–acid batteries, and a gel cell typically has only 80% of the capacity of a similar sized AGM. It was also important to use true deep–cycle batteries that can handle repeated depths of discharge of up to 80%, in order to maximize the running time of the instruments between charges.

It is preferable to connect several batteries in series where possible, as over time the battery voltages can become uneven and the voltage of the battery bank falls to that of the battery with the lowest voltage. Therefore, the preference was to use 6 V batteries connected in three parallel pairs, rather than 12 V batteries all in parallel, but there were none available in time for the campaign.

A TBS E–xpert 501 (www.tbs–electronics.nl) battery monitor was used to measure the battery voltage, current and state of charge. The battery monitor measures current using a very low resistance accurate resistor, called a shunt, on the negative lead close to the battery. The battery monitor had an alarm circuit, which was set to open when the state of charge dropped below 40%, thus switching the detector and tracker off via a Labjack U12 (labjack.com)

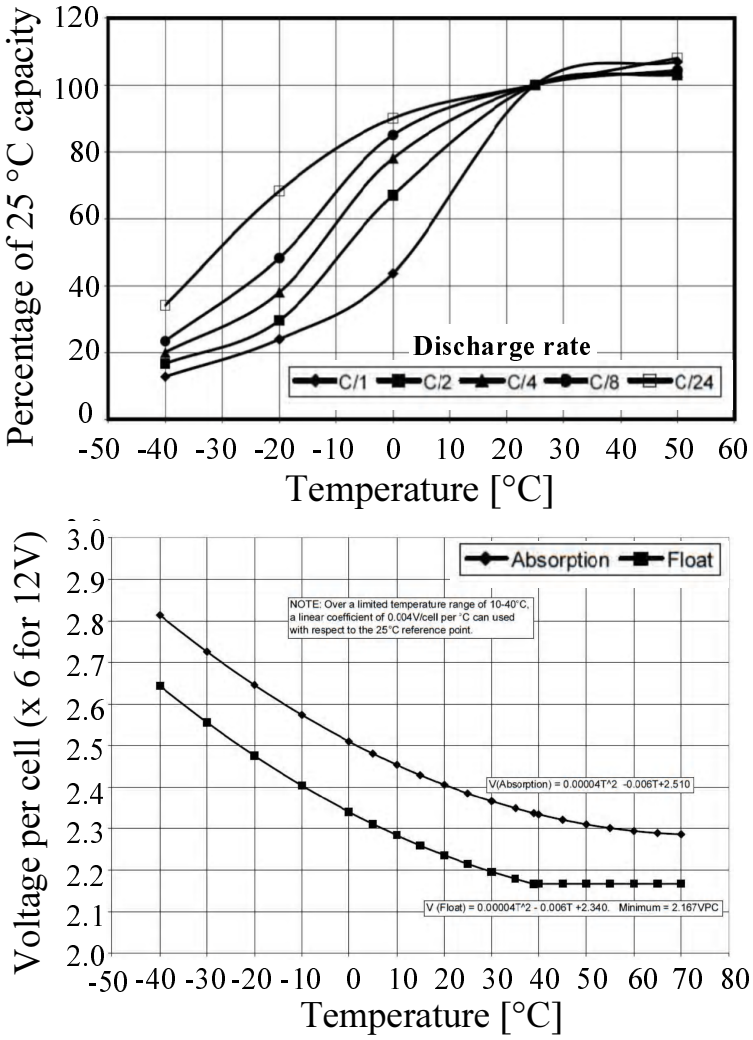

Figure 3.8: Percentage capacity at different discharge rates versus temperature (top) and recommended charging voltage per cell (multiply by six for a 12 V battery) versus temperature (bottom) for a Concorde Sun–Xtender battery (www.concordebattery.com, 2009).

USB interface to the spectometer controller software. This served to protect the batteries from excessive discharge, which reduces their lifetime and performance (see Fig. 3.9), and to maintain power to the computer for as long as possible in the event of low battery charge. The detector and tracker were also switched off at SZA greater than 92° to conserve power early in the spring when daylight hours were short, and also when the temperature in the box reached 30°C, to prevent overheating. After the computer (∼40 W), the detector controller (∼35 W) was the second largest consumer of power because of the energy required for Peltier cooling, followed by the tracker (∼20 W).

The computer, detector controller, and Aeroqual required AC power, which was converted from 12 V DC using a Victron Phoenix 220 W sinewave inverter (www.victronenergy.com). All other components operated on 12 V DC. An inverter is typically only 85–90% efficient, depending on the load, and computer power supplies are generally about 70-75% efficient. In addition, the inverter efficiency dropped to 75% when used with the computer, due to the low power factor of the switched mode computer power supply. Thus, choosing components that run on DC would considerably reduce the power consumption. Since the Antarctic campaigns, a DC computer and a more efficient tracker stepper motor driver have been used for this MAX–DOAS system.

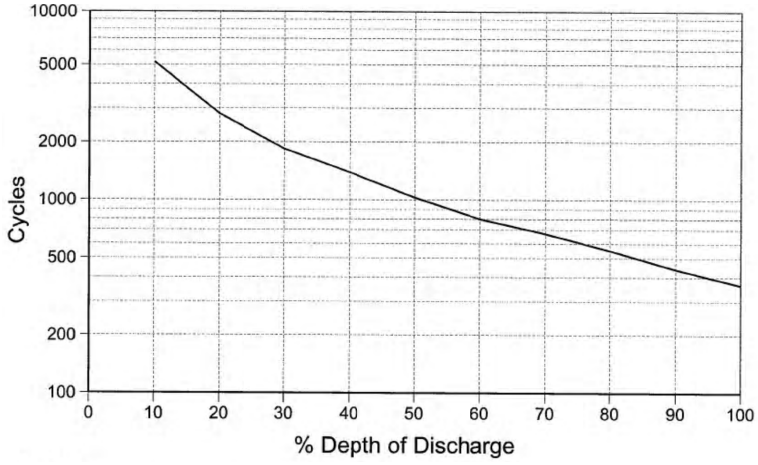

Figure 3.9: The typical lifetime for a Concorde Sun–Xtender battery, defined as the number of cycles achieved before the capacity drops to 80% of the original, versus depth of discharge for each cycle (www.concordebattery.com, 2009).

The battery bank was fully recharged every two to three days using a small 1 kVA petrol generator. For long–term maintenance of battery capacity, a full recharge is recommended at least every tenth cycle, but preferably more often. A Xantrex XC 50 A (www.xantrex.com) battery charger was housed inside the TARDIS and the generator was connected via a weatherproof caravan socket on the side of the TARDIS. Due to the high charge current, and to reduce resistance losses, short thick cables (6 mm^2 cross–sectional area) were used to connect the batteries together. The Tristar solar controller and the Xantrex battery charger

were both equipped with battery temperature and voltage sensors to regulate the charging voltage and current (see right–hand plot in Fig. 3.8).

Solar power

A 400 W photovoltaic (PV) array was connected to the battery bank via a Tristar 12 V 45 A (www.morningstarcorp.com) solar controller and a 45 A circuit breaker. Kyocera polycrystalline solar panels were chosen for their high energy conversion efficiency of 16% and relatively strong construction. These were mounted on a steel frame, constructed at Scott Base, with an adjustable tilt angle and designed to fit on the Maudheim sledge. A vertical panel orientation was chosen to maximize the energy received from the low sun and to shed snow more easily. The high snow albedo also significantly increases the intensity of incident sunlight on vertically oriented panels. During September and early October, the Sun is in the northern half of the sky, so vertically oriented north–facing panels collect the most energy. Conversely, during the 24-hour daylight of mid–summer, horizontally oriented panels would receive the most energy. The panels were tilted progressively further back as the season progressed, down to approximately 60° from the horizontal, to orient them towards the higher Sun. Despite the near vertical orientation of the panels, snow up to ∼10 cm thick often adhered to them, and had to be scraped off, although it sometimes fell off under its own weight or when the Sun heated the black surface of the panels. The presence of snow on the surface of the panels reduced their efficiency to some degree, whereas any shading by solid objects on any part of a panel severely reduced the output from the whole array. Therefore, care was taken to mount the panels slightly forward of the TARDIS and to avoid shading by the strops that secured the TARDIS to the ice. Low–temperature 6 mm^2 cable, rated to -40 °C, was used for the PV connections as the insulation on standard cable becomes rigid and brittle at low temperatures.

Fig. 3.10 displays the charge output of the photovoltaic array in ampere–hours (Ah) for each site and year. The average solar charging for 50 days in 2006 was 127.7 $Ah\,day^{-1}$ (1.46 $kWh\,day^{-1}$). The average solar charging for 82 days in 2007 was 76.0 $Ah\,day^{-1}$ (0.87 $kWh\,day^{-1}$), but the solar panels were installed one month earlier in 2007, with short days and low Sun elevations, reducing the daily average. The average for the same period in 2007 as in 2006 was 97.7 $Ah\,day^{-1}$. The average solar charging per day is a good proxy for sunshine hours and is consistent with qualitative observations of cloudiness. The 2006 season was notable for many cloudless days at Cape Bird in particular, while there were very few clear days in 2007.

In the extreme low humidity and windy conditions of Antarctica there is a risk of static electricity buildup, which could harm the electronics. The TARDIS and solar panels were earthed by attaching an electrical wire to a stake hammered 0.5 m into the sea ice where the salt content, and therefore the conductance, should be higher than at the surface. This was also done on the beach at Cape

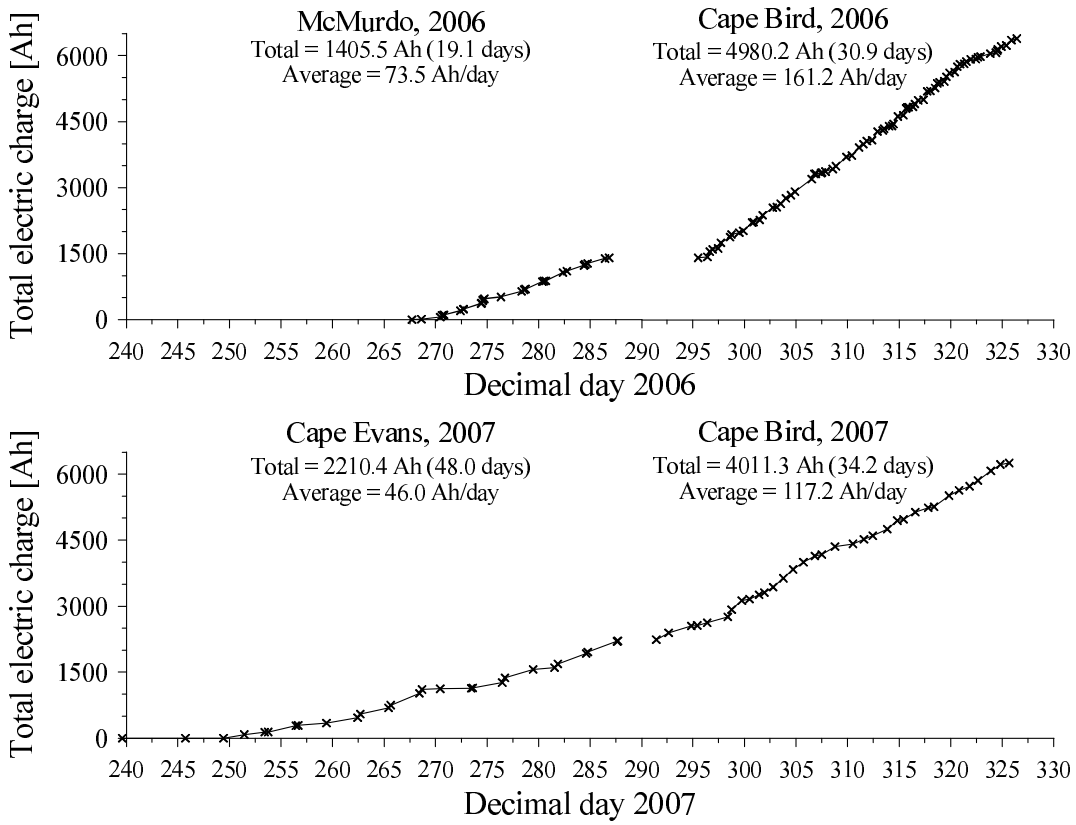

Figure 3.10: Battery charging in ampere–hours (Ah) from the 400 W photovoltaic array for 2006 and 2007.

Bird, although the frozen volcanic rock debris is a poor conductor.

Wind power

Although it is a cheap, lightweight and seemingly simple power source, reliable wind power generation in extreme environments has proven to be difficult to master. Some of the many problems encountered include rime icing on blades, uneven ice shedding leading to blade imbalance, debris impact, regulator failure, over speed and gyroscopic vibration failure. One of the problems is that wind generators built heavy and rugged enough to survive the most severe conditions often produce insufficient power during periods of prevailing light winds. Lubricants, greases and bearings must also be capable of retaining their properties in the extreme cold and under low humidity conditions. Only a handful of wind turbine designs have been used successfully in Antarctica, and two of these are the Rutland FM910–3 and the Ampair Pacific 100.

In 2007, a Rutland Furlmatic 910–3 (www.marlec.co.uk) wind generator was used during the measurements at Cape Evans. This provided the extra energy required to keep the system powered for three days at a time while the solar energy input

was low. The wind generator also maintained enough charge on the batteries to keep the system running and warm during severe weather when it was not possible to visit the instrument. The Rutland FM910–3 has six fibre-reinforced blades with a diameter of 910 mm. Some efficiency is lost by having more than three blades as each blade operates partly in the wake of the other blades. Turbines with a larger number of smaller blades operate at a lower Reynolds number, which makes them less efficient, but it also decreases vibration intensity making them more robust in high or gusty winds. The Rutland FM910–3 has a low startup wind speed of $2.6\,\mathrm{m\,s^{-1}}$ and a high inertia alternator that acts like a flywheel maintaining momentum between gusts, which increases efficiency (see Fig. 3.11). The Rutland FM910–3 automatically furls out of the wind flow, due the aerodynamic tail fin design, when the wind speed reaches $16\,\mathrm{m\,s^{-1}}$, causing the sudden drop in power seen in Fig. 3.11. The Rutland HRS913 voltage regulator progressively slowed the turbine down when the batteries became full.

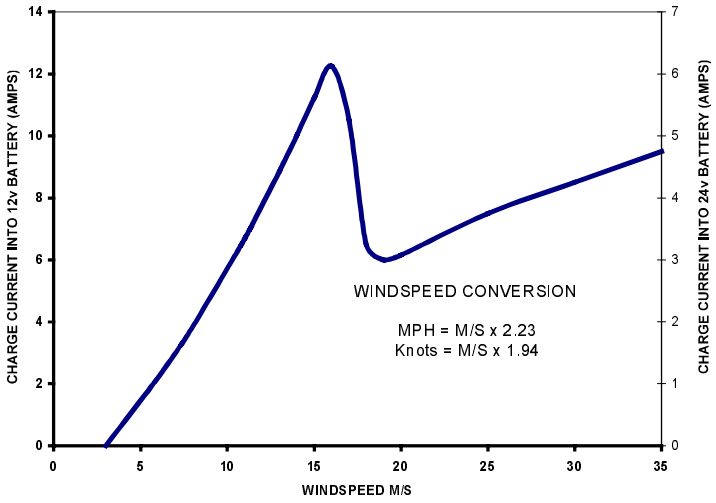

Figure 3.11: Rutland FM910–3 charge current output versus wind speed (www.marlec.co.uk, 2007).

The energy input from the wind generator was not monitored, but there was a steady wind on most days at Cape Evans, and the battery charge generally remained above 40% for three days at a time, whereas in 2006, without the wind generator, the batteries required recharging every second day. This was despite the lower average solar charging of $61.7\,\mathrm{Ah\,day^{-1}}$ from 25$^{\mathrm{th}}$ September to 14$^{\mathrm{th}}$ October in 2007, compared with $73.5\,\mathrm{Ah\,day^{-1}}$ for the same period in 2006. The lower PV charging in 2007 was roughly balanced by the lower power consumption, which was 80–90% of that in 2006, so the increased autonomy time in 2007 can be mostly attributed to the wind generator.

In order to keep the wind generator above the ground turbulence, the blades should normally be over three metres from the ground. The main reason for failure is from wind rotor and debris impact due to the turbine not being high

enough off the ground. Wind speeds are higher at greater altitudes because of the drag of the surface and the viscosity of the air. The variation in velocity with altitude, called wind shear, is most dramatic near the surface. Typically, in daytime the variation follows the $1/7^{\text{th}}$ power law, which predicts that wind speed rises proportionally to the seventh root of altitude. Doubling the altitude of a turbine increases the expected wind speeds by 10% and the expected power by 34%. However, doubling the tower height generally requires doubling the pole diameter as well due to the increase in thrust and torque, thus increasing the amount of material by a factor of eight. The stand used in this work had to be small and light enough to easily transport and to secure on the sea ice.

The wind generator stand, constructed by Nick Key in the Department of Geography at the University of Canterbury, Christchurch, was a two metre high structure with four legs (see inset in Fig. 3.5). The poles were made of aircraft strength aluminium, with guy wires from the mast to each foot, and the collapsible structure was easy to transport and quick to assemble. The foot pads contained holes through which they could be firmly secured to the sea ice using ice screws. For safety, the wind generator was erected approximately 20 m from the TARDIS, away from the prevailing wind direction, and the power cable was buried under the snow.

The wind generator was not required at Cape Bird as the instrument was close to the hut, so the batteries could be charged whenever necessary and in most weather conditions, using the petrol generator. In addition, although the spectrometer was running continuously at Cape Bird, the PV input was high due to the high Sun elevations and long daylight hours. In addition, it would have been very difficult to securely anchor the wind generator stand on the frozen volcanic rock debris there.

3.2.4 Ozone analysers

Two instruments were used to measure the ozone concentration at the TARDIS. An Aeroqual (www.aeroqual.com) S–500 ozone monitor was used in both 2006 and 2007, but there were several problems with noisy measurements and keeping it running continuously. The Aeroqual ozone measurement is based on a tungsten oxide semiconductor heated to $\sim 500°$C to evacuate oxygen atoms from the oxide lattice. Ozone quickly reacts with the surface and fills these vacancies, creating electron traps and thus increasing the resistivity of the sensor (Hansford et al., 2005). A small fan in the sensor head draws air over the sensor at a constant calibrated flow rate so that the ozone concentration can be determined. In the initial configuration, the sensor was attached directly to the monitor inside the TARDIS with a 10 cm long non–reactive PTFE (polytetrafluoroethylene) tube passing from the sensor head to the outside. A chimney (see Fig. 3.4) prevented snow from blowing inside the tube and provided wind shielding, but the Venturi effect created by wind blowing across the entrance, altered the air flow rate though the sensor resulting in noisy, unusable measurements except during calm

conditions. In 2007, the Aeroqual sensor was mounted in the centre of a large conical aluminium housing on top of the TARDIS (see Fig. 3.5) and connected via an extension cable to the Aeroqual monitor inside the TARDIS. Air entered the bottom of the housing, circulated and exited through a fan at the top, so changes in wind speed were balanced at either end of the sensor head, keeping the flow rate relatively stable. However, the connection to the sensor often failed due to the cold temperatures and corrosion in the salty air.

In addition to the Aeroqual, in 2007 a 2B–205 ozone analyser (www.twobtech.com) was loaned by the British Antarctic Survey. The measurement principle of the 2B–205 is similar to the TEI 49–C at Arrival Heights. A pump draws air through a teflon tube into the instrument at a flow rate of approximately 1.5 $\mathrm{L\,min^{-1}}$ and a pair of solenoid valves alternately send ozone–scrubbed and unscrubbed air through the two UV absorption cells. Photodiodes measure the intensity of UV light at 254 nm passing through the 15 cm long cells from a low–pressure mercury lamp at the opposite end. The ozone concentration is calculated based on the relative intensities between the two cells using the Beer–Lambert–Bouguer law and the flow rate. The 2B–205 performed well, though there was a gradual downward drift in the measured ozone relative to the TEI at Arrival Heights. This was attributed to the instrument rather than true changes in ozone, and a correction was made using the calibrations with the TEI at Arrival Heights.

Care was taken to keep the petrol generator downwind of the instrument when recharging the batteries, as the fumes affected the ozone measurements.

When the wind speed was below about $6\,\mathrm{m\,s^{-1}}$, boundary layer ozone, temperature, pressure and humidity were measured using a 2Z Electrochemical Concentration Cell (ECC) ozonesonde and a Vaisala RS–80 radiosonde, lifted by a tethered helium–filled helikite (www.allsopp.co.uk). This is a balloon with a kite on the base (see Fig. 3.4). The ozonesonde was placed in a standard polystyrene ozonesonde container with the teflon intake tube to the outside. The ozonesonde and radiosonde package weighed 820 g and the maximum altitude reached ranged from approximately 100–250 m. The ozonesonde chemical preparation was done at the Crary Laboratory at McMurdo Station, but at Cape Bird the two ozonesondes were reused without conditioning them between flights.

An Aeroqual SM–50 sensor, which operates on the same principle as the Aeroqual S–500, was also trialled as a possible alternative to the 2Z sonde. The SM–50 was connected to the radiosonde to transmit the data. Although the SM–50 sampled air using a small pump rather than a fan, the flow rate was sensitive to airflow past the entrance tube and thus the measurements were too noisy to be of any use. Some improvement was made in the quality of the measurements by making a space under the lid for the pumped air to flow out of the box. With further testing and development these solid state sensors would be very convenient for remote measurements as they do not require pre-launch conditioning with chemical solutions and they are much smaller and lighter than an ECC sonde.

3.2.5 Weather monitor

A Vaisala WXT510 (www.vaisala.com) electronic weather monitor, mounted on the TARDIS, recorded temperature, pressure, relative humidity, wind speed and wind direction at 15 s intervals. The WXT510 determines wind speed and direction by measuring the transit times in both directions along each of the paths between three equally spaced ultrasonic transducers. The temperature, pressure and humidity sensors are based on an Resistance-Capacitance oscillator circuit with two reference capacitors against which the capacitance of the sensors is continuously measured. A microprocessor compensates for the temperature dependence of the pressure and humidity sensors. The accuracies specified by Vaisala are ±2% for wind speed and direction, ±1 hPa for pressure, ±0.3° C for temperature, and ±3% for relative humidity. The data was transmitted to the computer via an RS–232 port and logged using the Vaisala software. Power consumption was less than 0.05 W.

3.2.6 Housing

The instrument housing consisted of a strong welded aluminium frame, with the batteries on the bottom and the instruments and computer on a shelf above the batteries. The walls and top were insulated with two layers of 50 mm thick Formathane polyurethane sheet. The standard density (32 kg m^{-2}) Formathane is light–weight, relatively cheap and has a very low thermal conductivity of 0.02 W m^{-2} °C^{-1}, but it is fragile and dusty, so a higher density foam is recommended for future campaigns. A second aluminium frame, on the outside of the insulation, was clad in aluminium sheet and with no attachment to the inner frame, in order to minimise thermal conduction. The box was mounted on a 10 cm thick closed cell foam pad, and thin closed–cell foam was put under and between the instruments, which were securely mounted to the frame to prevent vibration and movement during transport.

The key challenge was to keep the batteries and electronics warm during the power–saving (∼40–60 W) periods, while avoiding overheating during normal operation (∼120–160 W). The thickness of insulation required was estimated for the two different power regimes over a temperature range of $^{-}$50–$^{+}$5°C using Fourier's law of Heat Conduction. The key was to optimise the insulation thickness in order to minimise the heating or cooling requirements and associated power demands. There is no single optimal thickness of insulation suitable for the large variations in ambient temperature and power output, but this problem was solved by having two layers of removable insulation panels, each 50 mm thick, and using the extremely cold outside air for efficient cooling. The 100 m total thickness was chosen for protection of the instruments and batteries against extreme cold in case of severe weather for several days preventing access to the instrument site.

Cooling was provided by external pipes that passed through an aluminium heat–exchanger and back into the instrument box. Initially, in 2006, a single cross

pipe was used, but the cooling rate was inadequate, so the cooling system was extended for the 2007 campaign. Early in the campaign, when the instruments were only operating for part of the day and ambient temperatures were low, insulating plugs were pushed into the cooling pipes to reduce heat–loss. These were removed during battery charging, as the battery charger and, to a lesser extent the batteries, produced considerable heat during charging. A thermostatically–controlled fan was set to turn on at 20°C to increase the air flow from the box into the cooling pipes. A high–powered fan, which switched on when the temperature reached 28°C, was added in 2007 to improve the cooling efficiency. Sections of Formathane were progressively removed from the walls and roof as the season progressed, to cope with increasing ambient temperatures and the extra heat generated by the instruments and battery chargers that were running for longer each day, matching the increasing day length.

Fig. 3.12 displays the temperature of the spectrometer housing and the batteries along with the ambient air temperature measured by the WXT510. The battery temperature was measured by the TBS E–xpert 501 temperature sensor taped to the side of a battery in the centre of the battery bank and insulated on the outside with closed–cell foam. The temperature inside the TARDIS was more stable in 2007 than in 2006 due to the extended external cooling pipes and the high–powered fan. In 2006, there is a slight correlation between the internal temperature and the ambient temperature, but the internal temperature is not affected by variations in the ambient temperature in 2007. The dips in temperature are mainly due to the spectrometer switching off at night time, while the peaks occur during battery charging, usually every second day in 2006 and every third day in 2007. The Tristar also heated up when the photovoltaic charge current was high. The low temperature near the beginning of the McMurdo period in 2006, was due to the battery charge dropping below 40%, as a storm prevented access to the site, so only the computer was running. The low temperature at the start of the Cape Bird measurements was due to cooling during the helicopter flight from Scott Base, and the short, sharp dip in temperature seen at Cape Evans on day 251 in 2007 was a result of removing the front panel of the TARDIS to fix a connection.

There were two small doors on the lee side from the prevailing wind for access to the instruments and power supply in most weather conditions. The TARDIS computer was accessed from a laptop via a weatherproof network cable socket on the side of the box. The box was carefully sealed to prevent the entry of fine blowing snow, which is often a problem in Antarctica as it can pass through very fine cracks and holes.

3.3 Differential optical absorption spectroscopy

Spectroscopy is the study of the interaction between radiation and matter as a function of wavelength or frequency. UV, Visible and infrared radiation is partly

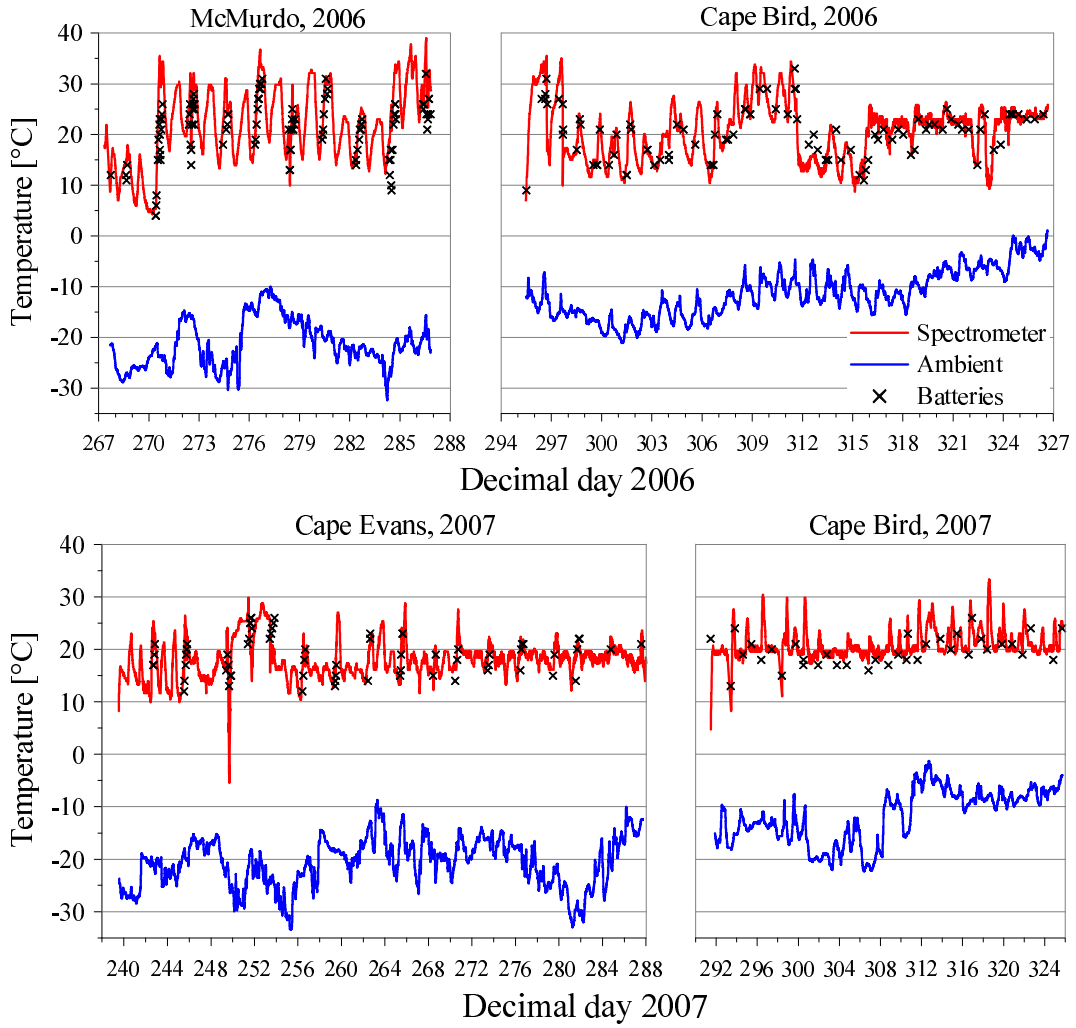

Figure 3.12: Temperature of the spectrometer housing and batteries, and the ambient temperature measured by the Vaisala WXT510.

absorbed by gas molecules under certain conditions, leading to the formation of absorption lines or narrow band features in the observed spectra. The internal energy of a gas molecule is a combination of the orbital energy of electrons in the atoms, the vibrational and rotational state of the molecule, and the translational or kinetic energy associated with random molecular motions. Quantum mechanical laws predict that only certain discrete configurations of electron orbits, and only certain vibrational frequencies and amplitudes, and rotation rates are permitted for a given molecular species. Low energy transitions occur in the microwave region of the spectrum and involve changes in the rotational state of gas molecules. In the infrared region, transitions involve changes in vibrational states as well as rotational states. Electronic orbital transitions extend from the near infrared to the ultraviolet region and are normally accompanied by a change in the vibrational state and the associated rotational state. The atmospheric absorption features produced by various molecules are based on their molecular

structure (Liou, 2002). The absorption lines of molecules are of finite width due to the inherent uncertainty in quantising their energy levels, but this 'natural broadening' is minor in comparison to the broadening caused by the motions and collisions of the gas molecules. Doppler broadening is caused by the Doppler effect from the relative velocities of gas atoms or molecules towards or away from the light source. Pressure broadening is associated with molecular collisions, so it is dependent on the density of air. Below an altitude of ∼20 km, pressure broadening is the dominant factor in determining line width, while above 50 km, where molecular collisions are less frequent, Doppler broadening is dominant. Between these altitudes the line shape is a convolution of the Doppler and Lorentz (due to pressure broadening) line shapes (Wallace and Hobbs, 2006).

Among the many spectroscopic techniques, differential optical absorption spectroscopy is one of the most powerful and widely used methods to measure atmospheric composition (Platt et al., 1979; Perner and Platt, 1979; Platt, 1994; Platt and Stutz, 2008). Many remote sensing measurements of trace gases in the troposphere and stratosphere, from the surface, from airborne platforms and from satellites, employ this technique, which measures the wavelength dependent absorption of light by atoms and molecules using artificial or natural light sources. The ability to separate broad and narrow absorption features in the atmosphere is the foundation of DOAS, but restricts DOAS to species with distinct narrow band absorption structures less than about 10 nm in width. There are nevertheless many detectable species with unique narrow band absorption features in the UV–visible wavelength region, including O_3, NO_2, NO_3, NO, NH_3, HONO, SO_2, CS_2, HCHO, CHOCHO, BrO, OBrO, OClO, IO, OIO, I_2, OH and O_4.

A major advantage of the DOAS technique is the ability to detect extremely weak absorption with optical depths around 10^{-4} (Platt and Stutz, 2008), which means it is sensitive enough to detect trace gases at typical atmospheric mixing ratios from as low as 0.1 parts per trillion (ppt) to several parts per billion (ppb). As long as the wavelength region is carefully chosen, other trace gas species present in the sampled air mass do not influence the measurement (Platt, 1994). Another primary advantage of DOAS, is the ability to measure absolute trace gas concentrations without any in–situ calibration, once the absorption cross–section of the species is known. Additionally, DOAS measures the trace gases without chemical interference so it is particularly useful for the measurement of highly reactive species such as the free radicals BrO, IO, OIO, OClO, OH and NO_3. The simultaneous measurement of several trace gas species, by analysing the sum of their absorptions in one wavelength interval, provides information on the actual chemical composition of one air mass, typically in a few minutes (Stutz and Platt, 1996). Finally, DOAS instruments are relatively simple, low–cost, portable, and capable of real–time, unattended operation.

Active DOAS techniques, such as long–path DOAS (LP–DOAS), folded–path DOAS and tomographic DOAS, use an artificial light source often combined with retro–reflectors (Platt, 1994), and LP–DOAS has been widely used, especially for pollution studies (CamyPeyret et al., 1996; Stutz and Platt, 1997; Veitel et al.,

2002; Lee et al., 2005; Pundt et al., 2005; Saiz-Lopez et al., 2006a,c; Pöhler et al., 2010). The advantage of this technique is that the light path is precisely known and, with long light paths, active DOAS is highly accurate and sensitive for measurements of trace gases near the ground. In addition, measurements can also be made at night and at wavelengths below 300 nm, but active DOAS instruments require a much more complicated optical setup, more power, and higher maintenance than passive instruments (Hönninger et al., 2004b). Passive DOAS uses light from the sun, moon or stars, so the instrumental setup is simpler than active DOAS, but since the light traverses an ensemble of paths through the whole atmosphere, the direct calculation of concentrations from absorptions is not possible. Thus radiative transfer calculations or geometric approximations are required in order to retrieve vertical column densities (VCD) or concentration profiles from the measurements. The range of passive DOAS geometries include ground–based and balloon–borne direct sunlight DOAS, zenith scattered light DOAS (ZSL–DOAS), multi–axis DOAS (MAX–DOAS), airborne multi–axis DOAS (AMAX–DOAS), imaging DOAS, and satellite–borne occultation, nadir and limb DOAS (Platt and Stutz, 2008).

3.3.1 MAX–DOAS

ZSL–DOAS has been used extensively since the 1970's and is a valuable tool for the measurement of several trace gas species, including O_3, NO_2, NO_3, OClO, BrO and O_4 (Noxon, 1975; Noxon et al., 1979; Perner and Platt, 1979; Platt et al., 1979; Carroll et al., 1989; Johnston and McKenzie, 1989; Johnston et al., 1992; McKenzie and Johnston, 1984; Sanders et al., 1987; Solomon et al., 1989; McKenzie et al., 1991; Arpag et al., 1994; Solomon et al., 1994b; Van Roozendael et al., 1994; Kreher et al., 1996, 1997; Otten et al., 1998; Frieß et al., 2001; Tornkvist et al., 2002; Frieß et al., 2005). The first "off–axis" (viewing in directions other than the zenith) measurements were made by Sanders et al. (1993) using an off–axis zenith angle of 80° in the direction of the Sun in order to observe stratospheric OClO for longer into the "polar night". As the sky is brighter in the direction of the Sun compared to the zenith at high SZA, this viewing direction improved the signal–to–noise ratio of the measurements. They also concluded that this approach enhanced absorption by tropospheric species, while absorptions for stratospheric species are comparable to the zenith observations (Perliski and Solomon, 1993; Solomon et al., 1987). Arpag et al. (1994) used twilight off–axis observations to measure stratospheric BrO for the first time at mid–latitudes and Miller et al. (1997) used observations made at off–axis angles of 87° and 85° to measure tropospheric BrO and OClO related to polar sunrise boundary layer ozone depletion events (ODEs) in Greenland.

The use of multiple off–axis observation angles to obtain increased information about the vertical distribution of trace gases in the vicinity of the instrument, was recently developed, and became known as Multi–Axis Differential Optical Absorption Spectroscopy (MAX–DOAS) (Hönninger and Platt, 2002; Leser et al., 2003; Hönninger et al., 2004a,b; Wagner et al., 2004; Wittrock et al., 2004; Sin-

reich et al., 2005; Heckel et al., 2005). Measurements made with a telescope aimed at multiple elevation angles close to the horizon observe scattered sunlight that has traversed different paths through the atmosphere, with lower elevation angles typically observing light from longer absorption paths through the lowest layers relative to higher elevation angles. Thus, the slant column densities (see Sect. 3.3.2) measured at low telescope elevation angles are enhanced for trace gases close to the instrument. In particular, this technique is highly sensitive only to trace gas abundance in the lowest 1–2 km of the atmosphere for ground–based instruments, which is the typical upper range of the marine boundary layer height (Leser et al., 2003), and the ideal range for pollution studies.

For illustration of the MAX–DOAS measurement geometry, consider the geometric approximation of the SCD for single scattering given by

$$SCD \approx \left[a\frac{1}{\sin\,\alpha} + (1-a)\frac{1}{\cos \mathrm{SZA}} \right] \tag{3.1}$$

where a is the fraction of the total vertical trace gas column that resides below the scattering altitude and α is the elevation angle of the telescope. An absorber below the scattering altitude (e.g. in the boundary layer) enhances the air–mass factor (AMF) by a factor of approximately $1/\sin\alpha$, demonstrating the strong effect of elevation angle on the tropospheric light path. For telescope elevation angles close to the horizontal, the light path through a low altitude trace gas layer is increased relative to the light path for higher viewing angles. Conversely, when the trace gas layer is above the scattering altitude (e.g. in the stratosphere), the AMF strongly depends on the SZA, approximated by $1/\cos\mathrm{SZA}$ (Hönninger and Platt, 2002; Hönninger et al., 2004b; Sinreich et al., 2005). Thus, under the assumption of single scattering in the free troposphere, the AMF of the boundary layer is approximated by $1/\sin\alpha$ and the contribution from the rest of the atmosphere is approximately $1/\cos\mathrm{SZA}$.

To be able to correctly interpret the MAX–DOAS absorption measurements and retrieve vertical profile information, the distribution of light paths observed at each viewing geometry must be well understood (Marquard et al., 2000; Hönninger et al., 2004b; Wittrock et al., 2004). Therefore, it is crucial to have an accurate multiple scattering radiative transfer model along with a knowledge of the altitude profiles of temperature and pressure, strong absorbers such as ozone, and aerosols, and the surface albedo and topography. The radiative transfer model used in this work, and the influence of these parameters on the radiative transfer is discussed in detail in Chap. 4. Given that clouds have a complex, inhomogeneous, rapidly changing structure, with variable particle sizes, clouds are not included in the radiative transfer model. MAX–DOAS measurements made on cloudy days are generally treated as qualitative observations of the presence or absence of the trace gas in the boundary layer, though O_4 measurements are used to investigate the radiative transfer in the lowermost troposphere on cloudy days (Wagner et al., 2004). Thus, in addition to the ideal cloudless days, profiles are also retrieved for days with visibility similar to clear sky conditions, as indicated by the O_4 measurements (see Chaps. 5 and 6).

One disadvantage of the MAX–DOAS technique is that a complete scan sequence comprising the different viewing elevation angles may take several minutes, in which time the profile of the trace gas being measured may change. Simultaneous measurements can be made with multiple instruments or using a two–dimensional detector with one dimension for dispersion into wavelengths and the other dimension for the different elevations. However, this adds to the instrumental cost and development, and can introduce errors because spectra are ratioed from instruments with different instrument functions (Platt and Stutz, 2008).

3.3.2 The DOAS principle

Absorption spectroscopy techniques make use of the absorption of electromagnetic radiation by matter, which is quantitatively expressed by the Beer–Lambert–Bouguer law (often referred to as the Lambert–Beer law) that describes the exponential decrease in the intensity of light along a path of length, l, passing through an absorber, i, of concentration, c_i:

$$I(\lambda) = I_0(\lambda) \cdot \exp\left(-\int_0^l \sigma_i(\lambda, P, T) c_i \, dl\right) \tag{3.2}$$

where $\sigma(\lambda, P, T)$ is the wavelength dependent absorption cross section of the species, I(λ) is the intensity, at wavelength λ at the end of the path and $I_0(\lambda)$ is the intensity at the start of the path. If the temperature and pressure dependency of the absorption cross sections σ_i are negligible, the optical depth, τ, of the medium, which is the sum of the optical depths of n absorbers, can be expressed by:

$$\tau(\lambda) = \ln\left(\frac{I_0(\lambda)}{I(\lambda)}\right) = \sum_{i=1}^{n} \int_0^l \sigma_i(\lambda)\, c_i \, dl = \sum_{i=1}^{n} \sigma_i \cdot S_i \tag{3.3}$$

where S_i, the slant column density (SCD), is the integrated concentration along a given light path or the ensemble of all the observed light paths through the atmosphere, and the units are in molecules per unit cross–sectional area of the observed column. Once the path length is determined, usually trivial for active DOAS geometries, the average concentration of the trace gas species i along the light path is given by:

$$c_i = \frac{\tau(\lambda)}{\sigma_i(\lambda)\, l} \tag{3.4}$$

In addition to molecular absorption, Rayleigh scattering, $\epsilon_R(\lambda)$, and Mie Scattering, $\epsilon_M(\lambda)$, also reduce the intensity of light along the path, so the Beer–Lambert–Bouguer law can be expanded to:

$$I(\lambda) = I_0(\lambda) \cdot \exp\left[-\int_0^l \left(\sum_{i=1}^{n} \sigma_i(\lambda)\, c_i + \epsilon_R(\lambda) + \epsilon_M(\lambda)\right) dl\right] \tag{3.5}$$

In the atmosphere, Rayleigh and Mie scattering are important in the UV-visible region and most trace gas species are continuously present, so it is not possible to determine $I_0(\lambda)$ or to quantify all the factors influencing the intensity, $I(\lambda)$. Instead, DOAS makes use of the fact that extinction due to scattering and many trace gas absorptions exhibit very broad or smooth spectral features, while some species have very distinct absorption structure within a narrow wavelength range. The broadband absorption spectrum is then taken as the intensity with the species of interest removed, $I'_0(\lambda)$, and the absolute cross–section $\sigma_i(\lambda)$ is considered to be the sum of $\sigma'_i(\lambda)$, which varies rapidly with wavelength, and $\sigma^s_i(\lambda)$, which changes slowly with wavelength (Platt, 1994; Stutz and Platt, 1996). The differential cross section is much smaller than the absolute cross section but the fine structure is sufficient for fitting to atmospheric spectra if the intensity is measured over a range of wavelengths. Intensity measurements for multiple wavelengths are also necessary for the absorption features of the species of interest to be unique and separable from other absorbers. These absorption lines or bands can be separated from the broadband absorption using a filtering procedure or by fitting a polynomial representing $\sigma^s_i(\lambda)$ (Platt, 1994; Stutz and Platt, 1996; Hönninger et al., 2004b). The definition of the separation between slowly–varying and rapidly–varying absorption cross sections depends on the observed wavelength interval and the width of the absorption bands to be detected (Stutz and Platt, 1996; Marquard et al., 2000). Calibration is not necessary since the trace gas concentrations are determined solely from the modified source intensity $I'_0(\lambda)$ and the differential absorption cross section $\sigma'_i(\lambda)$. Substituting these cross section components into Equation 3.5 and averaging over the optical path length, l, yields (Platt, 1994):

$$\begin{aligned} I(\lambda) &= I_0(\lambda) \cdot \exp\left(-l \cdot \sum_{i=1}^{n} (\sigma'_i(\lambda)\, \bar{c_i})\right) \\ &\cdot \quad \exp\left(-l \cdot \sum_{i=1}^{n} (\sigma^s_i(\lambda) \bar{c_i} + \bar{\epsilon_R}(\lambda) + \bar{\epsilon_M}(\lambda))\right) \end{aligned} \tag{3.6}$$

where the first exponential function describes light extinction by the narrow band features of the trace gas of interest, while the second exponential term characterises the slowly varying absorption by other species and the extinction due to Rayleigh and Mie scattering. Thus, the SCDs of individual absorbers can be estimated by separating these differential intensities without knowledge of the original light intensity, $I_0(\lambda)$ before passing through the absorber:

$$S_i = \frac{\tau_i(\lambda)}{\sigma_i(\lambda)} = \frac{\tau'_i(\lambda)}{\sigma'_i(\lambda)} = \frac{l \cdot \sum_{i=1}^{n} \sigma'_i(\lambda)\, \bar{c_i}}{\sigma'_i(\lambda)} \tag{3.7}$$

3.4 The spectral retrieval

A brief background of the DOAS spectral fitting technique is described. For detailed descriptions of the technique see Platt (1994) and Platt and Stutz (2008). The DOAS analysis package used in this work was developed by Paul Johnston at NIWA, Lauder. The analysis package and Lauder spectrometers have been validated in Network for Detection of Atmospheric Composition Change (NDACC) intercomparisons in 1992, 1996, 2003 (Vandaele et al., 2005) and recently in the CINDI MAX–DOAS campaign in Cabauw, Netherlands (in preparation, see Chap. 5).

DOAS spectral fitting methods employ linear or non–linear least squares fitting to minimise the difference between the measured spectral radiances and the differential cross–sections of the relevant absorbers that are predicted to be present. The wavelength region chosen for spectral fitting must be wide enough to contain distinctive fine absorption features, but avoid the interference of spectral features of other absorbers as much as possible. Additionally, the differential absorption must be strong enough to give a high signal–to–noise ratio, but the absolute absorption must be weak enough to avoid high optical depths. The strong, temperature–dependent Huggins bands of ozone absorption in the UV region, the Chappuis bands in the visible region, and water vapour bands, pose a particular challenge for absorption spectroscopy (Arpag et al., 1994). In the UV region from 220–290 nm, the optical transmission of the atmosphere is limited by extinction due to Rayleigh scattering and absorption by O_2, and the Hartley bands of O_3. While, in the infrared region, optical transmission is limited by strong absorption by molecules such as H_2O, CO_2 and O_3 (Plane and Saiz-Lopez, 2006). Aliwell et al. (2002) found that the wavelength interval selected for fitting was a source of significant differences in SCDs retrieved from zenith sky measurements.

The solar radiation spectrum is approximately described as the continuous emission of a black body with T≈5780 K. However, due to absorption and re–emission of radiation by gaseous species in the outer solar photosphere, this continuum is overlaid by a large number of strong absorption lines called Fraunhofer lines. The strongest of these lines are produced by H, Mg, Fe, Ca, and Si as well as singly ionized Ca and Mg. Fraunhofer lines are substantially stronger than the absorption lines of most constituents of the terrestrial atmosphere and must be carefully removed in the DOAS analysis procedure (Hönninger et al., 2004b). Atmospheric trace gases have optical depths in the order of less than 10^{-3} compared to Fraunhofer lines with up to 30% absorption at typical DOAS spectral resolution.

The Fraunhofer features were eliminated by ratioing the spectra with a reference spectrum (usually a zenith measurement) before applying the numerical fitting which for MAX–DOAS, was the zenith measurement (a high elevation angle measurement could also be used) in each sequence of viewing elevation observations. The reference spectrum was first aligned with the Fraunhofer spectrum using non–linear least squares fitting (Aliwell et al., 2002) and then the reference was aligned

with the observation spectrum before being subtracted from the observation. When two spectra are ratioed, interpolation errors can be introduced as a result of spectral shape differences that arise from the interpolation required to shift and stretch each spectrum in wavelength to correctly align them. To calculate a spectrum's value at a wavelength between the known values at each CCD pixel, an interpolation technique is used and this introduces (usually small) errors.

Background spectral features that vary slowly with wavelength, including broad-band absorption, as well as Rayleigh and aerosol scattering, which are treated as "pseudo–absorptions", were approximated by low-order polynomials to separate them from the fine spectral structures (high–pass filtering). A non–linear least squares fitting procedure (Aliwell et al., 2002) was then applied to fit the measured spectra to the differential cross–sections of each absorber expected to be present, with wavelength shift and stretch applied between iterations to account for non–linearity from changes in the instrumental wavelength alignment, and to minimise the residual.

The errors in the retrieved differential slant column densities (DSCDs) are derived from one standard deviation of the residual errors from the least squares fitting. A detailed description of error analysis is given in Stutz and Platt (1996). A useful summary of error sources is given by Aliwell et al. (2002). The most significant sources of error include the wavelength calibration, the shape of the fitted absorption cross sections and the measured spectra, the wavelength interval chosen for spectral fitting, misalignment of the cross sections, the temperature dependence of O_3 absorption cross sections, failure to adequately account for the I_0 effect, inadequate offset correction, and inadequate measurement of the instrumental resolution functions.

Examples of cross section fits and residuals are displayed for spectral retrievals of BrO with a wide fitting window containing four absorption lines (337–361.9 nm) in Fig. 3.13 and for a smaller fitting window (341.5–357.6 nm), with three absorption lines, used for the retrieval of zenith sky measurements in Fig. 3.14. The smaller wavelength region was used for the zenith sky retrievals of stratospheric BrO to avoid two O_3 absorption bands between 337 nm and 341.5 nm. The fitted cross sections for a spectral retrieval of IO are shown in Fig. 3.15.

3.4.1 Absorption cross–sections

Systematic errors arising from inaccuracies in the shape and wavelength alignment of absorption cross–sections are one of the greatest sources of uncertainty in the retrieved DSCDs, and there are significant differences between experimentally–determined cross–sections. In addition, the temperature dependence of absorption cross sections leads to errors in the retrieved SCDs when using a single cross section typical of one temperature, since stratospheric trace gases experience temperatures in the 230–250 K range while tropospheric absorbers experience temperatures in the range 230–298 K (Wahner et al., 1988; Aliwell et al., 1997; Wilmouth et al., 1999; Schofield, 2003; Fleischmann et al., 2004).

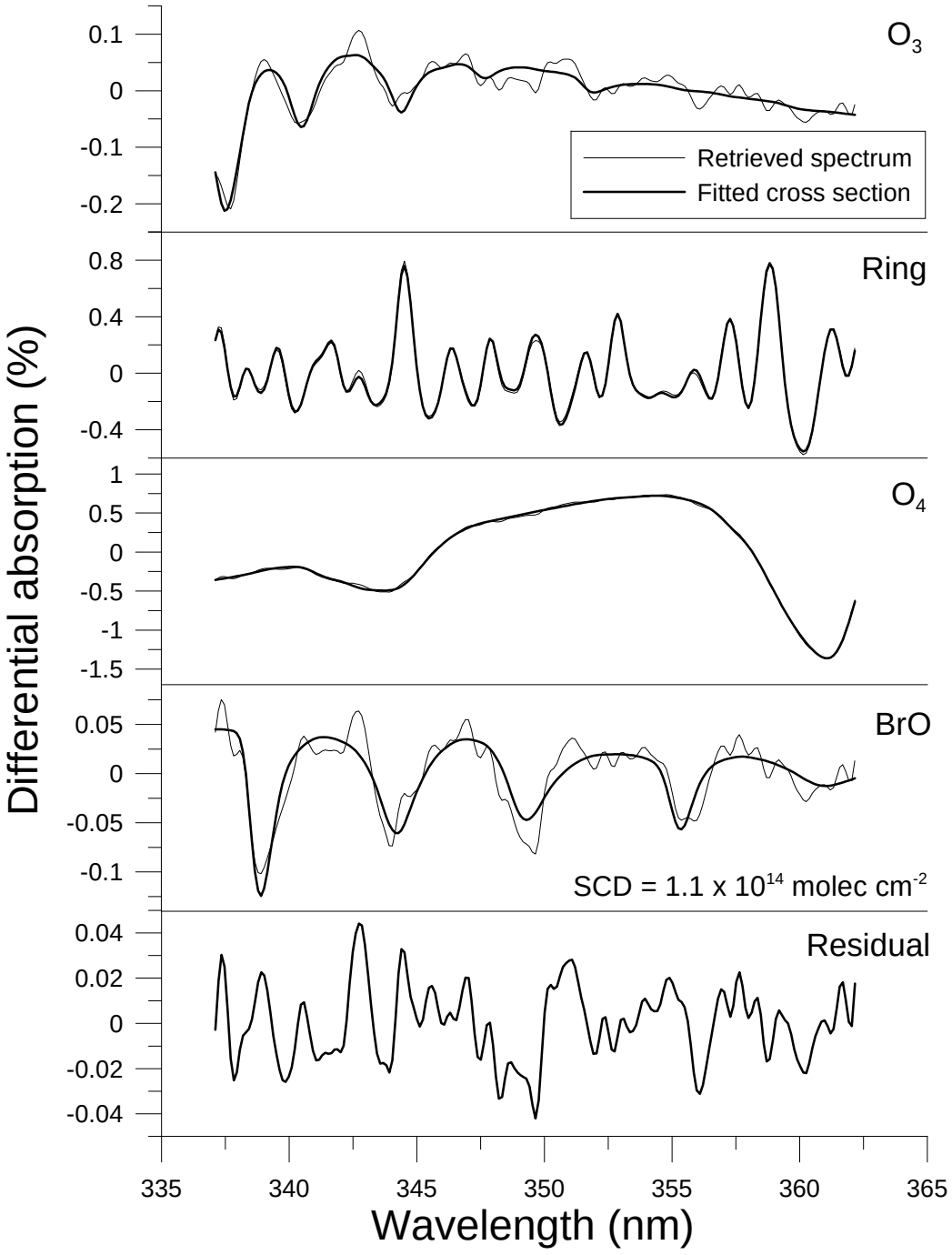

Figure 3.13: A spectral retrieval of BrO with the 337–362 nm fitting window for a 0° elevation angle measurement at 86° SZA, on 31st October, 2007. The reference spectrum, measured in the zenith, was recorded during the three minute integration interval immediately preceding the observation.

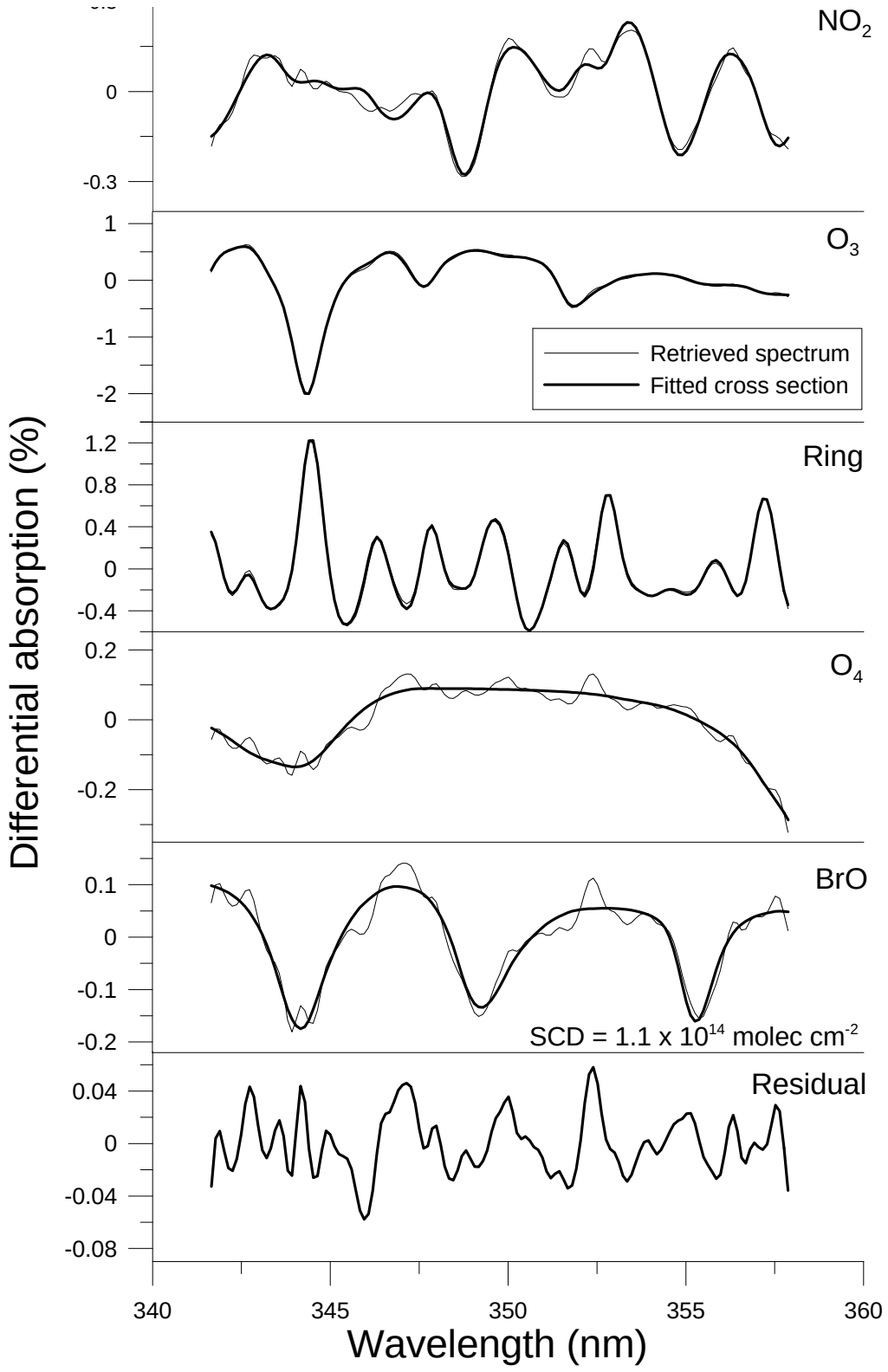

Figure 3.14: A spectral retrieval of BrO with the 341.5–357.6 nm fitting window for a 0° elevation angle measurement at 86° SZA on 31st October, 2007. The reference spectrum, measured in the zenith, was recorded at SZA 67°.

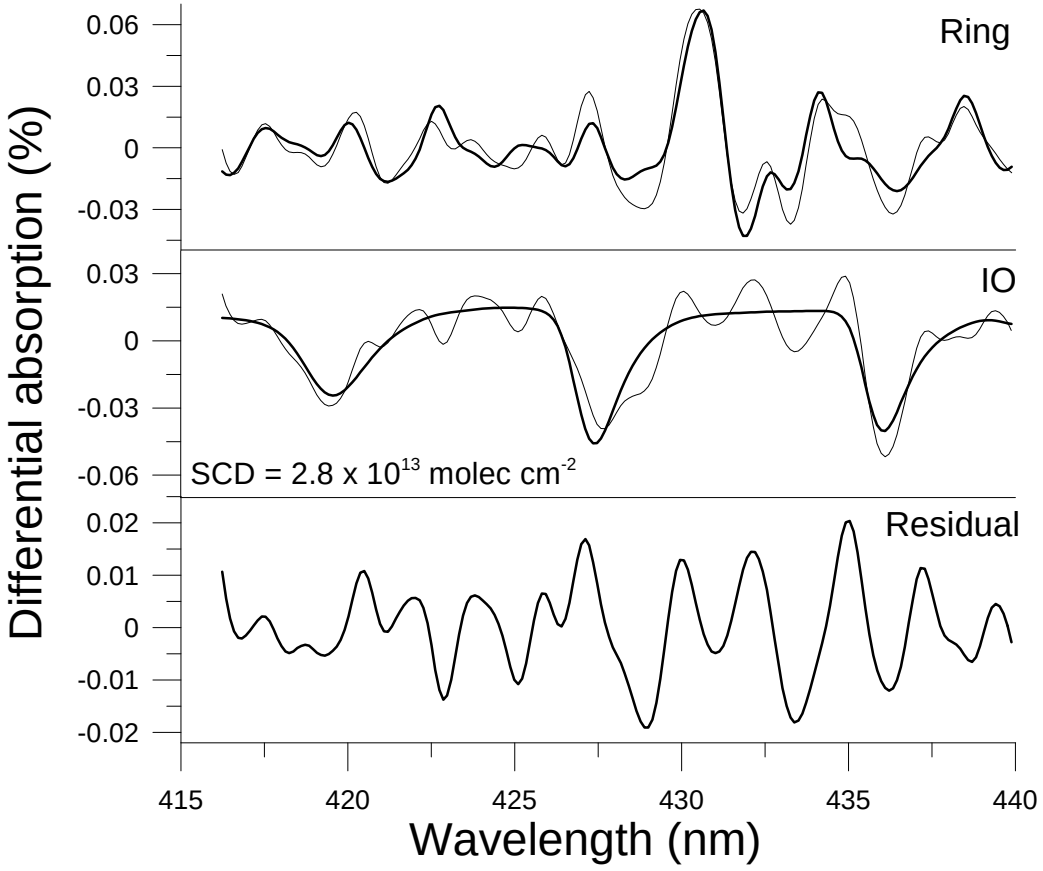

Figure 3.15: A spectral retrieval of IO for the 0° elevation angle at 85° SZA on 12st November, 2006, with a fitting window of 416.2–439.9 nm. The reference spectrum, measured in the zenith, was recorded during the preceding three minute interval. NO_2, O_3 and OClO were also used in the spectral fit, but since the stratospheric component was removed in this ratio these species were not observed in the fit. O_4 was also fitted but it has a weak absorption band in this wavelength range so there was no fit to the measured spectrum.

The cross sections are therefore convolved with the instrumental slit function to match the resolution of the measurements. The I_0 effect is corrected as described in Frieß (2001); Aliwell et al. (2002). The solar I_0 effect arises because the measured spectra, containing the finely structured Fraunhofer spectra, and the absorption cross sections are usually measured at different resolutions and with different light sources (Frieß, 2001; Aliwell et al., 2002).

The cross–sections used in this work are summarised in Table 3.1.

Species	Resolution	Temperatures [K]	Reference
NO_2	$0.1\,cm^{-1}$	220	Vandaele et al. (2002)
O_3	$5\,cm^{-1}$	203, 293	Voigt et al. (2001)
O_4	$2\,cm^{-1}$	296	Van Roozendael (2003, Pers. comm.)
BrO	$10\,cm^{-1}$	228, 298	Wilmouth et al. (1999)
IO	0.07 nm	298	Spietz et al. (2005)
OClO		204	Wahner et al. (1987)

Table 3.1: Trace gas cross sections used in the spectral fitting of NO_2, BrO and IO.

3.4.2 The Ring effect

The Fraunhofer lines in spectra from scattered sunlight observations are weaker and broader than those from direct sunlight observations. This in–filling of the Fraunhofer lines is termed the Ring effect, after Grainger and Ring (1962). It is now widely accepted that the Ring effect is due to Rotational Raman scattering (RRS), primarily by the diatomic N_2 and O_2 molecules (Brinkman, 1968; Kattawar et al., 1981; Fish and Jones, 1995; Vountas et al., 1998; Sioris and Evans, 1999). In RRS, the interaction between a rotating anisotropic molecule and the oscillating electric field of the electromagnetic radiation results in an induced dipole and the scattering is inelastic. If the molecule absorbs energy from the photon, the transmitted photon has a lower frequency and thus its wavelength is longer than the incident wavelength (Stokes scattering). Conversely, if the molecule is initially in an excited state, it may transfer energy to the photon, so the wavelength of the scattered photon is Raman shifted to a shorter wavelength (Anti–Stokes scattering).

Although the in–filling of the Fraunhofer lines is only a few percent or less, it is often much greater than the absorption by trace gases, and thus it can be a major source of error in the DOAS retrievals (Vountas et al., 1998; Langford et al., 2007). Therefore, a Ring spectrum is fitted in the spectral retrieval as a pseudo–cross–section. The proportion of Raman scattered photons to Rayleigh scattered photons increases with the amount of multiple scattering, and is also dependent on the geometry of the measurement (Brinkman, 1968; Fish and Jones, 1995). The magnitude of the Ring effect thus changes with SZA, and this must

be accounted for by including a Ring spectrum when taking the ratio of the observation spectrum with the reference spectrum, otherwise residual solar spectral features will remain in the observation spectrum.

As the degree of polarization of Raman scattered light is very small compared to the polarization of Rayleigh scattered light (Aben et al., 2001; Stam et al., 2002), the Ring spectrum can be determined by measuring scattered light in directions parallel and perpendicular to the Sun using a polarized spectrometer (Solomon et al., 1987). However, the Ring effect on the fine Fraunhofer structure also depends on aerosol scattering, which is weakly wavelength dependent. Additionally, the dependence of the light path on the polarisation direction possibly leads to trace gas absorption structures in the measured Ring spectrum (Fish and Jones, 1995; Hönninger et al., 2004b; Langford et al., 2007). Modelled Ring spectra (Chance and Spurr, 1997; Vountas et al., 1998; Aben et al., 2001; Stam et al., 2002; Wagner et al., 2009) bypass these limitations and show very good agreement with observed Ring spectra, so they are widely used in the spectral fitting and they have also been used in this work. However, modelled Ring spectra may also provide inadequate corrections to the Ring effect when wavelength–dependent aerosol scattering is not taken into account (Langford et al., 2007).

In addition to the effect of RRS on the Fraunhofer structures, it also reduces the depths of finely–structured absorption lines (especially for features less than 6 nm in width) of atmospheric trace gases (Fish and Jones, 1995). This is because the typical amount of wavelength shift caused by RRS in the visible region is approximately 1 nm (Fish and Jones, 1995; Platt et al., 1997). Thus, RRS has little effect on the broad ozone absorptions of the Chappuis band, but it causes a significant reduction in the optical depths of fine trace gas absorption features, with a subsequent underestimation of SCDs. For the 450 nm NO_2 line, Fish and Jones (1995) calculated a reduction in the line strength and SCD of NO_2 of up to 8% at 90° SZA and 12% at 95° SZA. Since the Ring effect increases with the amount of multiple scattering, the reduction in SCDs calculated for BrO at 350 nm is expected to be even greater. Multiple scattering on cloud and aerosol particles in certain conditions leads to further reductions in optical depths and thus in the derived trace gas SCDs (Vountas et al., 1998; de Beek et al., 2001).

3.4.3 Instrumental resolution function

When a spectrograph is used to measure the absorption spectrum, the entrance slit of the spectrometer grating, combined with the focussing and dispersing optics alter the shape of the spectrum. The instrumental resolution function or slit function describes the instrument properties and the way in which the finite resolution of the instrument affects the incoming light. The spectral resolution of the instrument is defined as the full width half maximum (FWHM) of the instrument function. The instrumental resolution function is the response of the spectrometer to a monochromatic input, and it is typically measured using the fine emission atomic emission lines of known wavelength from a mercury

lamp. It is essential that the instrumental resolution function remains stable and constant during measurements of solar spectra. A precise wavelength calibration of the measured spectra and the fitted absorption cross–sections is important, as misalignment is one of the most significant sources of error in the DOAS retrieval (Frieß, 2001; Aliwell et al., 2002).

Once the instrumental resolution function is determined, all measured spectra are corrected for instrumental effects by performing a mathematical convolution with the instrument resolution function (Stutz and Platt, 1996). In addition, all the cross–sections used in the spectral fitting, which are usually at a higher resolution than the instrument resolution, must be convolved with the instrumental resolution function so that they have the same resolution as the measured spectra.

3.4.4 Offset

Sources of offset include inelastic scattering, for example from the Ring effect, which can be approximated by an offset, or instrumental offsets such as the effect of stray light or of improperly removing the dark current noise (Aliwell et al., 2002). Noise in the detector can sometimes produce small negative signals, and these cannot be converted by the 16–bit analogue to digital converter. Therefore, to avoid negative signals, an electronic offset spectrum is applied to the measurements, and this must be subtracted from the measured spectra before the DOAS spectral fitting.

3.4.5 Dark current

In the absence of light there is a small current generated by the detector, called the dark current. As thermally excited electrons are the main cause of this current, cooling the detector to very low temperatures considerably reduces the dark current noise. As dark current is very sensitive to temperature fluctuations it is essential to maintain a constant detector temperature to ensure that the background dark current doesn't change during the measurement. Dark current generally only becomes important when the intensity of the observed light, and thus the signal–to–noise ratio is low. Low light intensity also requires long integration times, resulting in increased dark current noise. Therefore, dark current is more of an issue for zenith sky measurements when twilight spectra are ratioed with a midday reference spectrum. For MAX–DOAS measurements the time and SZA of the reference spectra are close to the observation spectra, so differences between the dark currents of the observation and reference are likely to be small. In this work, cooling of the detector to -20° resulted in an acceptable low level of dark current. The measurement of dark current spectra over long averaging times (e.g. 10–20 minutes) is preferred in order to reduce the random component of the dark current noise and thus obtain an accurate correction of the dark current in the observation spectra. While non–linear effects can require special techniques to correctly remove the dark spectrum in many detectors (Stutz and

Platt, 1996; Kreher, 1996; Frieß, 2001), the operation of the photo sensitive pixels well below saturation almost completely avoids such problems. Tests using a range of integration times from 20 seconds to 0.625 seconds show no significant change of dark spectrum shape (Johnston, 2010b, personal communication).

3.4.6 Aliasing due to spectral resolution

Aliasing is a common problem in electronic signal processing, which arises when the spectral resolution is too high for a given number of detector pixels. The spectral fitting of trace gases with low optical depth is very sensitive to changes in the instrument wavelength calibration. A wavelength shift of only a fraction of a pixel can cause strong artificial features in the spectra, which can be compensated by shifting and squeezing the spectrum. To minimize aliasing errors due to spectral under–sampling there must be a sufficient number of signal samples (detector pixels) across one interval of spectral resolution. If too few pixels are used a slight wavelength shift will cause a major change in the shape of the sampled spectra (Platt et al., 1997). Roscoe et al. (1996) calculated that 5–10 samples per resolution interval is enough to reduce the sampling error to an acceptable level.

3.4.7 Stray light

Most spectroscopic systems have some sources of stray light such as light scattered off optical elements, reflection off unused diffraction orders, or from the detector surface. Stray light can reduce the measured optical depth, enhancing the Fraunhofer residuals. It may also be wavelength dependent, which makes its correction more complicated (Platt et al., 1997).

Chapter 4

Monte Carlo Radiative Transfer Model

Solving problems associated with the propagation of light through a spherical, refracting atmosphere, where scattering and absorption may vary with location, is best achieved by applying a Monte Carlo radiative transfer model (RTM). Such models simulate the paths of an ensemble of photons through the atmosphere and estimate the resultant radiation field from the ensemble photon statistics.

An important application for Monte Carlo RTMs is the calculation of air–mass factors (AMFs) for the interpretation of UV–visible Differential Optical Absorption Spectroscopy (DOAS) observations (Perliski and Solomon, 1993; Hönninger et al., 2004b). AMFs represent the ratio of the effective optical path through the atmosphere to the vertical path (Noxon et al., 1979; Solomon et al., 1987). Integrated concentrations of absorbing gases along all light paths contributing to the measured spectra, known as slant column densities (SCDs), are the direct product of the DOAS analysis. SCDs can be converted into vertical column densities (VCDs) through division by AMFs. VCDs are independent of the measurement geometry and light paths, and are therefore more suitable than SCDs for universal interpretation and comparison with other independent measurements. The box–AMF for a prescribed layer in the atmosphere describes the sensitivity of a SCD measurement, with some prescribed measurement geometry, to the amount of the target trace gas in that layer. Monte Carlo radiative transfer models are well suited to air–mass factor calculations when the optical depth is relatively high, such as in clouds or at high solar zenith angles (SZA) and low telescope viewing elevation angles, because multiple scattering becomes important. Most analytical models do not treat multiple scattering well, especially for a three dimensional inhomogeneous atmosphere. Several important radical species undergo rapid conversion to and from their reservoir species, and their concentrations depend on photolysis rates and therefore on SZA. For these species, whose concentrations vary with SZA along the light path, Monte Carlo models can easily incorporate the effects of this photochemical enhancement. Other applications for Monte Carlo RTMs include analysis of the interaction of solar radiation with three dimensional clouds in the Earth's atmosphere (O'Hirok and Gautier, 1998a,b), calculation of polarization and radiance at various levels in the atmosphere and ocean (Kattawar et al., 1973; Emde et al., 2010) and simulation of solar radiation during a total eclipse (Emde and Mayer, 2007).

The NIWA Monte Carlo RTM (NIMO) was specifically developed for use in the retrieval of trace gas and aerosol profiles, and VCDs from SCDs measured by MAX–DOAS instruments. This chapter begins with a brief introduction to the radiative transfer equation (RTE) and the Monte Carlo (MC) technique in Sect. 4.1, followed by a detailed description of the direct backwards Monte Carlo ray tracing algorithm in Sect. 4.2. The calculation of radiances for any solar geometry using the simulation of adjoint photon trajectories in combination with the direct backwards MC trajectories is described in Sect. 4.3. The calculation of box–AMFs using these photon radiances and trajectories is then described in Sect. 4.4. The box–AMF and radiance results from a series of RTM comparison exercises (Wagner et al., 2007a) are presented in Sect. 4.5, along with some physical interpretation and discussion. NIMO results for these simulations show good agreement within the range of variability of the nine other RTMs that participated in the comparison exercises. These exercises provide an excellent and invaluable tool for testing a new RTM during its development. A test of the reciprocity principle for backwards or time–reversed radiative transfer is briefly presented in Sect. 4.6 and the influence of surface topography on the simulation of box–AMFs is presented in Sect. 4.7.

4.1 The Monte Carlo method for solution of the radiative transfer equation

The general integro–differential radiative transfer equation (RTE) for unpolarised monochromatic light describes the way the radiance, $I(\mathbf{A}, \omega)$, of a light beam changes due to scattering, absorption and emission of photons (Chandrasekhar, 1950; Marchuk et al., 1980; Thomas and Stammes, 1999; Liou, 2002; Marshak and Davis, 2005), where radiance (or monochromatic intensity) is the radiant power per area per solid angle per wavelength interval:

$$\omega \cdot \nabla I(\mathbf{A}, \omega) = -\beta(\lambda, \mathbf{A}) I(\mathbf{A}, \omega) + \frac{\beta_s(\lambda, \mathbf{A})}{4\pi} \int_{4\pi} I(\mathbf{A}, \omega') P(\mathbf{A}, \omega \cdot \omega') d\omega' + S(\mathbf{A}, \omega) \tag{4.1}$$

The gradient operator, ∇, indicates that the RTE is stated in terms of the rate of change in radiance along the beam in direction ω. The first term on the right–hand side describes the attenuation in radiance in the direction ω at location $\mathbf{A}$ due to extinction, $\beta = \beta_s + \beta_a$ (see Sects. 4.2.5 and 4.2.11). The second term describes the increase in radiance at $\mathbf{A}$ due to multiple scattering of photons into the direction ω from direction ω', where $P(\mathbf{A}, \omega \cdot \omega')$ is the scattering phase function (see Sect. 4.2.8), which is integrated over all directions ω' and normalised by the denominator 4π. The last term is the source function for photon thermal emission, which is negligible in the UV/vis/NIR wavelength region and can be omitted.

There are many RTMs available now, which are appropriate for different applications depending on the spectral region, the radiometric quantities to be

calculated, the spatial scale and the desired speed and accuracy. The RTE cannot be solved analytically, for anything but the simplest situations, and therefore various numerical methods are applied. RTMs fall into two main classes based on the numerical methods they use to solve the RTE. Firstly, there are deterministic or explicit numerical methods, such as the Discrete Ordinates method (Chandrasekhar, 1950; Liou, 2002; Gerstl and Zardecki, 1985; Spurr, 2006, 2008; Spurr et al., 2008; Sommersten et al., 2010) and the Spherical Harmonics Discrete Ordinates method (Evans, 1998), which discretise the whole radiation field and iteratively adjust elements of the field until the solution agrees with the RTE. The second class of RTMs are the Monte Carlo (or statistical) methods (Plass and Kattawar, 1968; Kattawar et al., 1973; Marchuk et al., 1980; Ishimoto and Masuda, 2002; Barker et al., 2003; Davis et al., 2005; Iwabuchi, 2006; Spada et al., 2006; Bates and Porter, 2008; Emde and Mayer, 2007; Nardino et al., 2008; Greiner et al., 2009), which estimate the desired radiative quantities statistically, with a confidence level dependent on the number of simulated photon trajectories. Monte Carlo methods have the advantage of being able to model specific atmospheric conditions more precisely than deterministic models, but they are usually slower.

Monte Carlo methods (Metropolis and Ulam, 1949) use repeated random sampling of a probabilistic model to simulate physical or mathematical processes and they tend to be used where deterministic algorithms are unfeasible or inaccurate. Light propagation in the atmosphere can be regarded as a Markov chain of photon collisions with the medium, in which the probability of each resultant absorption or scattering event is independent of previous or subsequent events. The Monte Carlo method uses random numbers, uniformly distributed between zero and unity, to simulate events with a probabilistic outcome, such as the scattering angle. The fate of each photon after each collision, whose outcome is prescribed by a probability density function (PDF), is simulated as a random process, much like the spin of a roulette wheel or the roll of dice. However, the outcome of such an event is not selected with uniform likelihood, but in such a way that accumulation of an ensemble of outcomes reproduces the original prescribed PDF.

First consider the elements of a discrete PDF, $f(x_i)$, i=1 to n, which prescribe the probability of a specific outcome for a certain event (x_i). The corresponding cumulative distribution function (CDF), $F(x)$, is then

$$F(x_i) = \sum_{j=0}^{i} f(x_j) \tag{4.2}$$

By selecting a uniformly distributed random number u in the interval [0,1], an outcome x_i is determined by

$$x_i = F^{-1}(u) \qquad 0 \leq u < 1 \tag{4.3}$$

This procedure is shown schematically in Fig. 4.1.

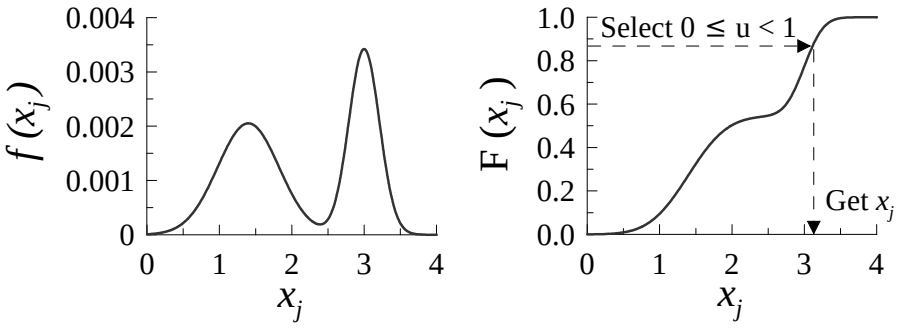

Figure 4.1: A PDF (left) is simulated with the Monte Carlo technique using its corresponding CDF (right).

4.2 The ray tracing algorithm

NIMO is written in object–oriented Delphi and the model physical environment is defined by a set of objects that represent the atmospheric constituents which absorb or scatter photons (e.g. Rayleigh scattering, aerosols, clouds, and absorbing trace gases such as O_3 and NO_2). The main function of these species objects is to return the scattering and absorption optical depths (τ_s and τ_a) for each photon path segment and the scattering angle for each scattering event. Additional objects define the ground radius and surface albedo as a function of latitude and longitude, and perform atmospheric refraction.

The paths of individual photons are tracked through a prescribed atmosphere in which absorption and scattering of the photons occur. As this model has been developed for UV–visible simulations and is not used in the infra–red region, photon thermal emission is not included. If a photon is absorbed in the real atmosphere this terminates its propagation and the photon ceases to exist. Rather than terminating the photon, each photon is given a statistical weighting ξ, set to unity at the start of its transect through the atmosphere. The weighting is reduced along each path segment in proportion to the probability of absorption of the photon by the various atmospheric constituents. In this sense each model photon can be thought of as carrying a likelihood or importance to the calculation, which can be attenuated even as the photon remains indivisible.

NIMO employs a three dimensional spherical coordinate system to track photons through the atmosphere. Any location ($\mathbf{A}$) within this coordinate system is specified using geographical latitude (Φ), longitude (Λ), and geocentric altitude (R), where R is defined as the radial distance from the center of the Earth.

$$\mathbf{A} = \begin{pmatrix} \Lambda \\ \Phi \\ R \end{pmatrix} \tag{4.4}$$

As the Earth's atmosphere is ellipsoidal, its radius of curvature varies with lati-

tude and direction of travel. However, it is assumed that treating the atmosphere as spherical is a very close approximation and the simulation of an ellipsoidal atmosphere would have a negligible effect on the radiative transfer calculations. The local Earth radius $R_e(\Phi)$ at a given latitude is calculated by

$$R_e(\Phi) = \sqrt{\frac{(R_q^2 \cos^2(\Phi))^2 + (R_p^2 \cos^2(\Phi))^2}{(R_q^2 \cos^2(\Phi)) + (R_p^2 \cos^2(\Phi))}} \tag{4.5}$$

where $R_q = 6378137\,\mathrm{m}$ is the Earth's equatorial radius, and $R_p = 6356752\,\mathrm{m}$ is the Earth's polar radius.

Although a photon propagates on a straight path, bent only slightly by refraction, the angles describing its direction in geographic coordinates change due to the sphericity of the Earth. NIMO uses a rectangular right–handed coordinate system with the origin at **A**, the x–Axis pointing towards North, the y–Axis pointing towards the West and the z–Axis in the direction of the zenith. A photon's local direction and distance of propagation within the geographical coordinate system is described by local spherical polar coordinates with the zenith angle (θ) between the local zenith and the direction of propagation, the azimuth angle West from North (ϕ), and the path segment length (l) over which the photon will travel.

$$\vec{\mathbf{P}} = \begin{pmatrix} \theta \\ \phi \\ l \end{pmatrix} \tag{4.6}$$

In the calculation of AMFs and radiances for MAX–DOAS measurements, photons are emitted from the detector entrance optics and their path is traced back to the top of the atmosphere (TOA). This backwards, or time–reversed RT, based on the principle of reciprocity (or optical mutuality) (Chandrasekhar, 1950; Marshak and Davis, 2005), is much more efficient for obtaining radiances at a point than the forward RT direction (see Sect. 4.6). For a zenith viewing telescope, a photon's initial direction of propagation is given by:

$$\theta = \arccos\left[u_1 + (1 - u_1)\cos\left(\mathrm{FOV}/2\right)\right], \quad \text{and} \tag{4.7}$$

$$\phi = 2\pi\, u_2 \tag{4.8}$$

where FOV is the angular field of view of the telescope and u_1 and u_2 are uniformly distributed random numbers in the interval [0,1]. The resultant distribution of photon starting directions is isotropic over the telescope FOV. For off–axis (non–zenith) viewing geometry the photon's initial propagation direction is then rotated into the telescope viewing direction using the rotation matrix derived in Sect. 4.2.8. Once the photon's wavelength, initial position and direction have been defined, the ray tracing algorithm, summarised in Fig. 4.2, is called iteratively until the photon's termination condition is reached. Each step in the algorithm is described in Sects. 4.2.1 to 4.2.11 below.

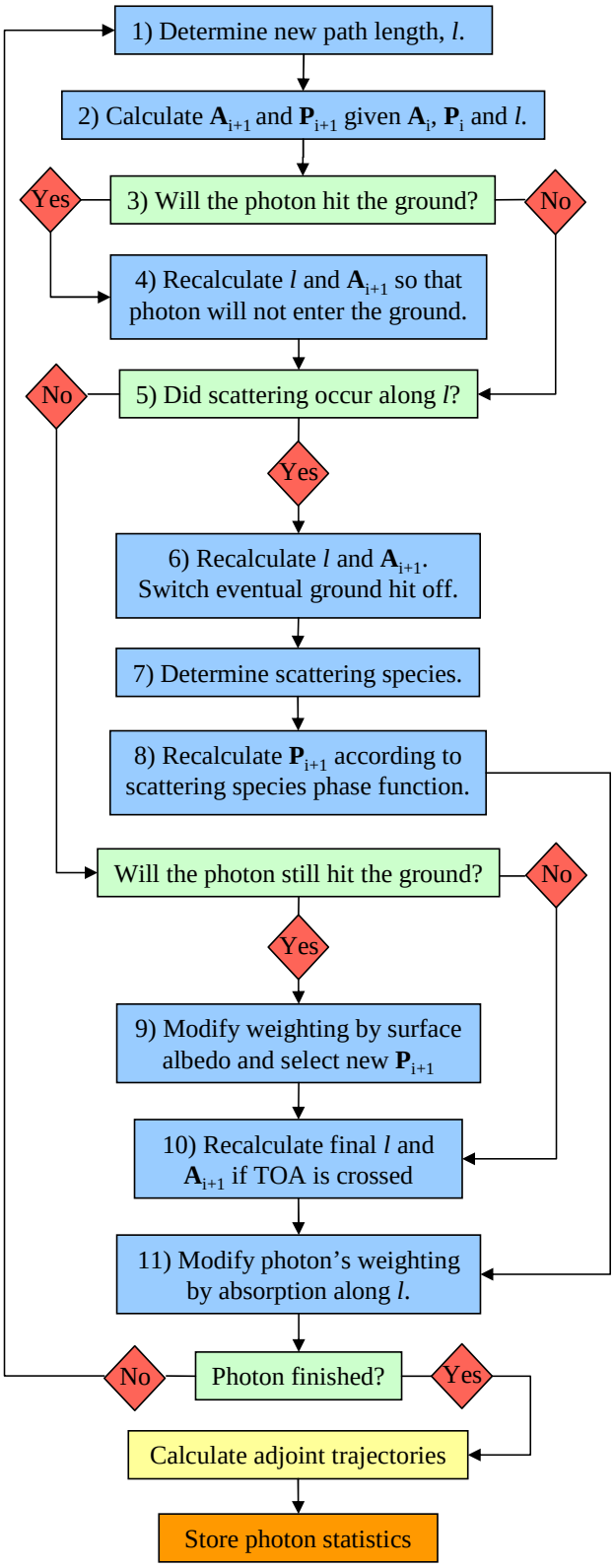

Figure 4.2: A schematic outline of the NIMO ray tracing algorithm. Each numbered box in the flow chart is explained in the corresponding section number from Sects. 4.2.1 to 4.2.11

4.2.1 Determine the photon path length

The total photon path length to the next scattering event is determined in two stages. The first path length step, based on the optical depth along the instrument's line of sight (LOS), transports the photon close to the scattering point. Subsequently, path steps of prescribed length with some random variability are taken until the scattering point is reached.

In order to sum the optical depth along any LOS, the path lengths and scattering coefficients in each discrete altitude layer are first determined. For model efficiency, the layer path lengths and scattering coefficients are calculated during model initialisation and stored in arrays. For a prescribed wavelength, the total scattering coefficient array, β_s, is created as described in Sect. 4.2.5. The total scattering optical depth along the LOS from the instrument to the TOA, τ_0, is then calculated for a given instrument viewing direction by tracing a single photon through the atmosphere in short fixed path length steps without scattering. The optical depth due to all scattering species is summed along this total refracted LOS path:

$$\tau_0 = \sum_{i=1}^{m} \sum_{j=1}^{n} \beta_s(i,j)\, l_i \tag{4.9}$$

for m layers and n species, where $\beta_s(i,j)$ is the scattering coefficient for species j in layer i, and l_i is the path length in the layer. The scattering coefficients are assumed to be constant within each layer. This calculation of τ_0 is appropriate for a FOV sufficiently narrow so that τ_0 does not vary significantly between different viewing directions within the FOV. For simplicity, the model Sun is treated as a point source. This approximation could introduce small errors at high SZAs where the optical thickness traversed by light from the upper and lower limbs of the Sun's disk can differ slightly.

In a plane–parallel atmosphere, the layer path lengths l_i for any given zenith angle are equal for all altitude layers. However, in a spherical atmosphere the zenith angle changes as the photon transects the atmosphere, and thus the layer path lengths also change. The unrefracted path, l_i, through a layer i of thickness dz at geocentric altitude R is calculated using the cosine rule:

$$l_i = \sqrt{R^2 \cos^2\,\theta_i + 2R\,dz + dz^2} - R\cos\theta_i \tag{4.10}$$

where θ_i is the zenith angle for upward–travelling photons or the nadir angle for downward–travelling photons. A two–dimensional array is created with the index of the zenith angle at the Earth's surface, θ_e from 0° to 90°, as one dimension and the index of layer altitude, in steps of $dz = 10\,\mathrm{m}$, as the second dimension. Coarse steps of 1° are made between consecutive θ_e at small zenith angles where differences in the layer paths are not very sensitive to changes in zenith angle. Progressively smaller steps are taken at higher θ_e, with steps of 0.005° close to 90° where the layer path lengths are very sensitive to changes in θ. For each value of θ_e the path length in each altitude layer is calculated using Eq. 4.10 with θ_i

determined using the sine rule:

$$\theta_i = \arcsin\left(\frac{R_i}{R_e}\,\sin\theta_e\right) \tag{4.11}$$

Refraction is not applied at this stage since the unrefracted path is used to calculate the new photon position and altitude as described in Sect. 4.2.2. Then, only once the new position is determined, is refraction applied to recalculate the path length and local zenith angle, and to shift the photon position by increasing the path angle γ subtended at the center of the Earth.

Optical depths are calculated during ray tracing using the mean scattering or absorption coefficient over all the traversed layers multiplied by the path length. This is faster than summing the optical depths for all layers individually, but since path lengths often differ between layers a layer–weighted mean must be used. For this purpose, an integrated relative path length array is created with the same dimensions as the path length array by dividing the path length in each layer by the path length in the lowest layer and summing these relative paths from the lowest layer up to the current layer:

$$\kappa_i = \sum_{0}^{i} l_i/l_0 \tag{4.12}$$

where κ_i is the cumulative relative path for layer i and l_0 is the path length in the lowest layer, so that κ_0 is always unity. The application of this relative path array for the calculation of layer–weighted means is explained where it is used in Sects. 4.2.5, 4.2.11 and 4.4.2.

Finally, an array of τ_s integrated from the surface to the TOA, is also created during model initialisation. This has the same dimensions as the path array and is simply calculated by multiplying the total scattering coefficients by the path lengths l_i in each layer and summing from the lowest layer up to the current layer:

$$\Sigma\tau_s(i) = \sum_{0}^{i} \beta_s(i)\, l_i \tag{4.13}$$

When deriving photon path lengths between scattering points, the Monte Carlo method is applied to statistically simulate the distribution of scattering optical depths, τ_s, between scattering points. Scattering attenuation can be treated in the same way as absorption attenuation using the Beer–Lambert–Bouguer law because, for the relatively low optical depths of atmospheric media, once a photon is scattered out of a path the probability of being scattered back into the same path is negligible. Following Beer–Lambert–Bouguer's law, the probability that a photon will travel an optical depth of τ before a collision is given by the transmittance:

$$T = I/I_0 = e^{-\tau} \tag{4.14}$$

where I_0 is the intensity (or the radiance at a point and in a particular direction) before traversing an optical depth τ and I is the intensity at the end of the

trajectory. The Equivalence Theorem (van de Hulst, 1980; Spada et al., 2006), states that scattering and absorption can be treated separately, so the optical thickness can be separated into scattering τ_s and absorption τ_a components. Thus, the probability of traversing an optical depth τ_s without scattering can be simulated by the random number u, and setting $\Delta T_s = e^{-\tau_s} = u$, we have

$$\tau_s = -\ln \Delta T_s \tag{4.15}$$

When the optical depth along the LOS is low, at long wavelengths in clear air for example, many photons traverse the atmosphere without scattering. Therefore, for model efficiency, photons are forced to scatter by biasing the probability distribution on the first path step so that

$$\Delta\tau_s = -\ln \left[1 - u(1 - e^{-\tau_0}) \right] \tag{4.16}$$

To compensate for this scattering bias, the photon weighting, ξ, must be multiplied by $1 - e^{-\tau_0}$, which represents the fraction of photons that would have scattered if no bias were applied (Marchuk et al., 1980; Oikarinen et al., 1999; Spada et al., 2006).

Depending on the wavelength, β_s profile and viewing direction, the path lengths between scattering events may be several kilometers or tens of kilometers. The scattering species and scattering coefficients may completely change along the path, especially for high viewing elevation angles. Therefore, in order to accurately simulate the scattering species and location, the initial scattering optical distance is set to a fraction, C, of $\Delta\tau_s$. For most values of θ, C is set to 0.8, so one long path step is taken followed by one or more short steps. Taking long path steps can introduce errors when photons are travelling horizontally or passing through a tangent point so shorter steps are selected by setting $C = 0.2$ when θ_i is $90^\circ \pm 2.5^\circ$.

Having simulated $\Delta\tau_s$ to the next photon position, the corresponding path length is determined using the array of $\Sigma\tau_s$. First, θ_e is calculated from θ_i by exchanging their positions in Eq. 4.11, and the θ_e index of the $\Sigma\tau_s$ array can then be derived. τ_s for the current altitude layer is multiplied by the maximum fraction of the layer width that could potentially be traversed in the direction of travel, since a photon is more likely to scatter somewhere in the middle of a layer rather than precisely at a layer boundary. A bisection algorithm is then used to converge on the altitude index of $\Sigma\tau_s$ where the difference in $\Sigma\tau_s$ between the start and end altitudes is equal to or greater than the simulated optical depth $\Delta\tau_s$.

For tangential photons, whose trajectories do not reach the Earth, τ_s is summed layer by layer using β_s and the layer path array for $\theta_e = 90^\circ$. The altitude index of the tangent layer is then simply subtracted from all the layer indices so that the tangential layer path length for any altitude is taken from the first layer in the array for $\theta_e = 90^\circ$, where the photon is tangential at the Earth's surface. As the atmosphere is thin relative to the radius of the Earth, the layer path lengths for a photon that is tangential at the Earth's surface are almost equal to the layer paths for a photon that passes through a tangent higher in the atmosphere.

Having obtained the altitude index for the scattering layer, the unrefracted path length is determined by subtracting the integrated path length for the lowest altitude index from the integrated path length for the highest altitude index. The vertical fraction of the starting layer traversed by the photon is also taken into account. Since τ_s is summed to layer boundaries, in most cases when scattering occurs it is greater than the simulated $\Delta\tau_s$. Thus, the path length is reduced back to the scattering point by an amount Δl, obtained by dividing the difference in τ_s by the scattering coefficient in the scattering layer i:

$$\Delta l = \frac{\tau_s - \Delta\tau_s}{\beta_s(i)} \tag{4.17}$$

When $\Delta\tau_s$ is not reached, downward–travelling photons are tested for ground penetration (see Sect. 4.2.3), and if true, the path length is reduced so that the photon just hits the ground. Upward–travelling photons that reach the TOA are flagged to be finished at this point so that the model proceeds directly to the adjoint calculation.

After this initial path step that approaches close to the statistical scattering point, subsequent path lengths are selected as a fraction of the photon's start altitude and contain a random component. Shorter path lengths are used when the photon is close to the surface and, for speed, longer path lengths are selected when the photon is travelling through the middle and upper atmosphere where composition changes more slowly with altitude and where the extinction coefficients and the rate of change in refractive index are small. As a default, the path length is set to 200 ± 100 m below 2000 m altitude and to one eighth of the altitude $\pm\, 25\%$ above 2000 m. The scattering point is reached when $e^{-\tau} \geq T$ for the refracted path (Sect. 4.2.5). For each path step after the first scattering event the transmittance, with respect to scattering, is selected using $T = u$ without the $1 - e^{-\tau_0}$ free path length bias. Once a scattering event occurs a new T is selected and an initial path step is selected by simulating $\Delta\,\tau_s$ to transport the photon close to the scattering point.

For twilight simulations from an instrument position located in the Earth's shadow (SZA$> 90°$) a different free–path length sampling scheme is used for the initial path step to the scattering point (Marchuk et al., 1980; Oikarinen et al., 1999). The path length is sampled using

$$l = u\,L \tag{4.18}$$

where L is the maximum path length along the LOS to the TOA. To compensate for the sampling bias, the photon weighting is then multiplied by $L\,e^{-\tau_s}\,\beta_s(z)$ where τ_s is the scattering optical depth along l and $\beta_s(z)$ is the scattering coefficient at the altitude, z, of the scattering point at the end of the path. At high SZAs this method is faster since a greater proportion of simulated photons have their last scatter point (in the backwards simulation direction) beyond the Earth's shadow region. Any photons having their last scatter point inside the shadow region before exiting the TOA are deemed to be physically impossible photons and they are not included in the radiance and AMF calculations.

Once a scattering event occurs, the length of the final path segment is adjusted using the method described in Sect. 4.2.6.

4.2.2 Calculate the new photon position

Given the initial position $\mathbf{A}_i$, propagation direction $\vec{\mathbf{P}}_i$ and path length l, a photon's new position $\mathbf{A}_{i+1}$ and direction $\vec{\mathbf{P}}_{i+1}$ at the end of the path segment can be calculated (see Fig. 4.3).

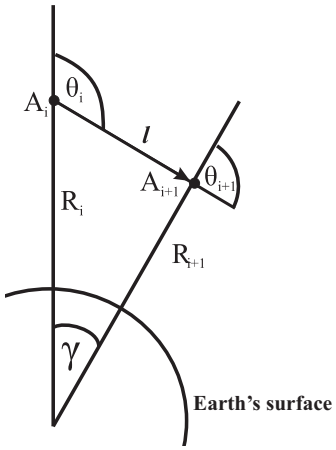

Figure 4.3: The geometry for the calculation of $\mathbf{A}_{i+1}$ from $\mathbf{A}_i$ and $\vec{\mathbf{P}}_i$.

R_{i+1} is calculated using the cosine rule:

$$R_{i+1} = \sqrt{l^2 + R_i^2 + 2lR_i \cos\theta_i} \tag{4.19}$$

The angle, γ, subtended at the center of the Earth by the path segment, without taking refraction into account, is simply calculated using the sine rule:

$$\gamma = \arcsin\left(\frac{l \sin\theta_i}{R_{i+1}}\right) \tag{4.20}$$

The calculation of γ with refraction included is outlined below.

Inclusion of refraction in the model redefines the photon's path through the atmosphere in such a way that R_{i+1} is unchanged, but γ and l are revised. The new latitude (Φ) and longitude (Λ) are then calculated using:

$$\Phi_{i+1} = \arcsin(\cos\gamma \, \sin\Phi_i + \sin\gamma \, \cos\Phi_i \cos\phi) \tag{4.21}$$

$$\Lambda_{i+1} = \Lambda_i + \arctan(-\sin\gamma \, \sin\phi, \, \cos\gamma \, \cos\Phi_i - \sin\gamma \, \sin\Phi_i \, \cos\phi) \tag{4.22}$$

Corrections are made to the latitude and longitude if the photon passes over the poles or across the 180° E/W meridian.

Due to the sphericity of the atmosphere, a photon travelling in a straight line experiences a change in propagation direction $\vec{\mathbf{P}}$ as expressed in local geographic coordinates. The new local zenith and azimuth angles of the direction vector $\vec{\mathbf{P}}_{i+1}$ at the new position $\mathbf{A}_{i+1}$ are therefore corrected for the new latitude and longitude:

$$\theta_{i+1} = \theta_i - \gamma, \quad \text{and} \tag{4.23}$$

$$\phi_{i+1} = \arctan(-\cos\Phi_i \, \sin\gamma \, \sin\phi_i, \sin\Phi_{i+1} \, \cos\gamma - \sin\Phi_i) \tag{4.24}$$

Refraction

The effect of refraction on zenith sky measurements was previously found to be significant only at large SZA, especially for tangential light paths at SZA $> 90°$, and for tropospheric absorbers (Perliski and Solomon, 1993). For MAX–DOAS measurements the effect is relatively small even for long lines of sight associated with low elevation angles and wavelengths in the visible region. The effect of sphericity is much more important than refraction for MAX–DOAS geometry (Wagner et al., 2007a).

The consideration of refraction in NIMO changes the position and propagation direction at the end of a path segment. To calculate these changes the position $\mathbf{A}_{i+1}$ is first calculated without the influence of refraction. The geocentric altitude R_{i+1} is not changed afterwards, but is used to recalculate the position $\mathbf{A}_{i+1}$ (by recalculating γ and l) and the new propagation direction $\vec{\mathbf{P}}_{i+1}$ (see Fig. 4.4).

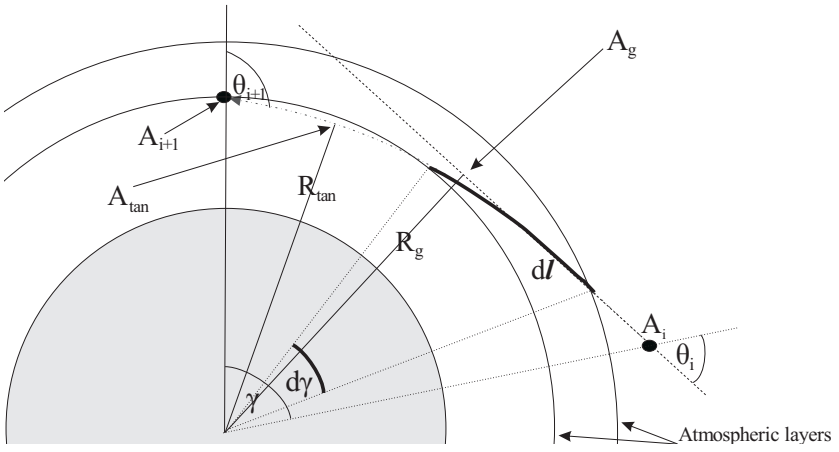

Figure 4.4: A refracted path. A_g is the tangent point for the unrefracted path at radius R_g and A_{tan} is the tangent point for the refracted path at radius R_{tan}.

First, the wavelength–dependent refractive index under standard temperature and pressure is determined using the empirical formula for dry air given in Ciddor (1996)

$$10^8 \, (n_s - 1) = \frac{5792105}{238.0185 - (1/\lambda)^2} + \frac{167917}{57.362 - (1/\lambda)^2} \tag{4.25}$$

for wavelengths $\lambda > 0.23\mu m$. This is similar to the formula given by Peck and Reeder (1972) and Bucholtz (1995), but amended for small changes in CO_2 concentration and temperature scale. The refractive index for a given altitude z is adjusted for temperature T(z) and pressure P(z) using

$$(n_{t,p} - 1) = (n_s - 1)\frac{T(S)}{T(z)}\frac{P(z)}{P(S)} \tag{4.26}$$

Snell's law in spherical geometry leads to the following formula (Rodgers, 2000)

$$R_g = n(R)\, R\, \sin\theta \tag{4.27}$$

where R_g is the geometric tangent radius, which remains constant along the path. R_g can be obtained at point $\mathbf{A}_i$ where $R = R_i$, $\theta = \theta_i$ and the refractive index $n(R_i)$ are known.

Since the model currently only includes refraction for a vertical refractive–index–gradient and not horizontally, the new propagation direction $\vec{\mathbf{P}}_{i+1}$ at point $\mathbf{A}_{i+1}$ is given by the corrected θ (the azimuth changes only due to sphericity). The angle θ_{i+1} at the point $\mathbf{A}_{i+1}$ can be calculated by rearranging Eq. 4.27 to obtain:

$$\theta_{i+1} = \arcsin\frac{R_g}{n_{i+1}R_{i+1}} = \arcsin\frac{n_i R_i \sin\theta_i}{n_{i+1}R_{i+1}} \tag{4.28}$$

which also takes the sphericity of the planet into account.

To obtain the change in the path length l and in the angle γ the integrals given in Rodgers (2000) are applied. These integrals are given in an orthogonal coordinate system. Since there is a singularity problem with the trigonometric functions when the photon's direction is tangential to a layer interface, the variable of integration used is:

$$x = R\cos\theta = n^{-1}(n^2R^2 - R_g^2)^{\frac{1}{2}} \tag{4.29}$$

The integrals are then:

$$\int dl = \int \frac{n^2R^2\, dx}{n^2R^2 - \zeta(R)R_g^2} \tag{4.30}$$

$$\int d\gamma = \int \frac{nR_g\, dx}{n^2R^2 - \zeta(R)R_g^2} \tag{4.31}$$

where

$$\zeta(R) = -\left(\frac{R}{n}\right)\frac{dn}{dR} \tag{4.32}$$

The composite Simpson's rule approximation is used to perform the numerical integrations for l and γ. The integration from points $\mathbf{A}_i$ to $\mathbf{A}_{i+1}$ is divided into m subintervals depending on the path length, and the intermediate altitudes, R, are approximated by taking equal altitude steps from the lowest altitude to the

highest altitude of the path. The corresponding refractive indices, n, at each altitude are then obtained from the precalculated n array.

$$\begin{aligned} l &= \left(2\sum_{j=1}^{m/2}\frac{n_{i+2j}^2R_{i+2j}^2}{n_{i+2j}^2R_{i+2j}^2-\zeta_{i+2j}(R)R_g^2}+4\sum_{j=1}^{m/2-1}\frac{n_{i+2j-1}^2R_{i+2j-1}^2}{n_{i+2j-1}^2R_{i+2j-1}^2-\zeta_{i+2j-1}(R)R_g^2}\right. \\ &+ \left.\frac{n_i^2R_i^2}{n_i^2R_i^2-\zeta_i(R)R_g^2}+\frac{n_{i+m}^2R_{i+m}^2}{n_{i+m}^2R_{i+m}^2-\zeta_{i+m}(R)R_g^2}\right)\times\frac{(x_{i+m}-x_i)}{3} \end{aligned} \tag{4.33}$$

$$\begin{aligned} \gamma &= \left(2\sum_{j=1}^{m/2}\frac{n_{i+2j}R_g}{n_{i+2j}^2R_{i+2j}^2-\zeta_{i+2j}(R)R_g^2}+4\sum_{j=1}^{m/2-1}\frac{n_{i+2j-1}R_g}{n_{i+2j-1}^2R_{i+2j-1}^2-\zeta_{i+2j-1}(R)R_g^2}\right. \\ &+ \left.\frac{n_iR_g}{n_i^2R_i^2-\zeta_i(R)R_g^2}+\frac{n_{i+m}R_g}{n_{i+m}^2R_{i+m}^2-\zeta_{i+m}(R)R_g^2}\right)\times\frac{(x_{i+m}-x_i)}{3} \end{aligned} \tag{4.34}$$

A special case occurs if the photon is going through the tangent point. The photon comes down, passes through a tangent point perpendicular to the local zenith vector and gains altitude again. Given the photon's initial geocentric altitude, R_i, and the direction θ_i, the distance to the tangent point is $R_i\cos(\pi-\theta_i)$. Therefore, the following conditions are checked to determine whether the photon passes through a tangent point:

$$\theta_i > \frac{\pi}{2} \tag{4.35}$$

$$l > -R_i\cos\ \theta_i \tag{4.36}$$

If the condition is true the pathlength and γ are integrated in two steps, first from $\mathbf{A}_i$ to $\mathbf{A}_{tang}$ and then from $\mathbf{A}_{tang}$ to $\mathbf{A}_{i+1}$. The geocentric altitude for a tangent point is given by

$$R_{tang} = \frac{R_g - n_kR_k}{n_{k+1}R_{k+1}-n_kR_k}(R_{k+1}-R_k)+R_k \tag{4.37}$$

where n_k and R_k are the refractive index and the geocentric altitude of the layer of the atmospheric grid just below R_g and n_{k+1} and R_{k+1} are for the layer just above R_g.

4.2.3 Test for ground penetration

At this stage it needs to be determined whether or not the photon penetrates the ground along the path to $\mathbf{A}_{i+1}$. An actual ground hit event is not yet performed (see Sect. 4.2.9) since there is still a chance that the photon will scatter on its path from $\mathbf{A}_i$ to $\mathbf{A}_{i+1}$ before it actually reaches the ground. The photon is flagged to have penetrated the ground if

$$R_{i+1} < R_E \tag{4.38}$$

where R_E is the Earth radius plus the local ground height at Φ_{i+1} and Λ_{i+1}, obtained from a digital elevation model. Since R_E may be a function of latitude and longitude, the model accounts for the effects of a varying surface topography. When very long path lengths are taken, occasionally photons slice through the ground and finish above the surface. Therefore, Eqs. 4.35 and 4.36 are used to test if the photon passes through a tangent point. Then the tangent altitude (without considering refraction) is checked and a ground hit is registered when

$$R \sin\theta < R_E \tag{4.39}$$

4.2.4 Modify the path length on ground penetration

If ground penetration occurs, the path length must be modified so that the photon hits the surface but does not continue below the surface. The model makes provision for a non–smooth surface where the geocentric radius of the ground at the end point may be different to where the photon actually penetrated the surface. First, a revised path length is calculated after setting R_{i+1} to the ground radius plus a small positive offset, which starts at zero and is incremented on every pass through the algorithm, and recalculating γ (see Fig. 4.3). The photon is then returned to $\mathbf{A}_i$ and a new value for $\mathbf{A}_{i+1}$ is calculated as outlined in Sect. 4.2.2. The photon may still be below the surface, for example if there was a hill between $\mathbf{A}_i$ and $\mathbf{A}_{i+1}$, in which case further iterations are performed until the end point of the photon path is at the surface. When a photon enters a hill while travelling horizontally or upwards, the bisection method is used to find the point along the path where the photon entered the hill. On the first step the path length is halved, and the new position, $\mathbf{A}_{i+1}$, is calculated. If the photon is above the ground at that point the new path length is set to three quarters of the original path length and if it is below the ground the new path length is set to one quarter of the original. This is repeated until the endpoint of the path is at the surface.

4.2.5 Test for scattering along the path segment

At this stage, having moved the photon to the end of the path, calculated the effect of refraction, and adjusted the photon position if ground penetration has occurred, the optical depth for each scattering species along l is determined. A wavelength–dependent integrated scattering coefficient array, β_s, with discrete altitude steps from the surface to the TOA, is created for each scattering species during model initialisation. The value of β_s at a given θ_e index i and altitude layer index z, weighted by the relative layer path length κ is

$$\beta_s(i,z) = \sum_{j=1}^{z} \beta_s(j)\left[\kappa(i,j) - \kappa(i,j-1)\right] \tag{4.40}$$

The amount of Rayleigh scattering per unit volume of air, given by the total

Rayleigh volume scattering coefficient β_{Ray}, is calculated for standard temperature and pressure ($T(S) = 288.15\,K$, $P(S) = 1013.25\,hPa$) using the analytic formulae from Bucholtz (1995). For $0.2\mu m < \lambda \leq 0.5\mu m$:

$$\beta_{Ray}(S) = 7.68246 \times 10^{-4}\,\lambda^{-(3.55212+1.35579\lambda+0.11563/\lambda)} \tag{4.41}$$

and for $\lambda > 0.5\mu m$:

$$\beta_{Ray}(S) = 10.21675 \times 10^{-4}\,\lambda^{-(3.99668+1.10298\times10^{-3}\lambda+2.71393\times10^{-2}/\lambda)} \tag{4.42}$$

Since β_{Ray} is directly proportional to the molecular number density n, β_{Ray} at altitude z is scaled from $\beta_{Ray}(S)$ using the relation:

$$\beta_{Ray}(z) = \beta_{Ray}(S)\frac{n(z)}{n(S)} = \beta_{Ray}(S)\frac{P(z)\,T(S)}{P(S)\,T(z)} \tag{4.43}$$

The scattering coefficient array β_s for Henyey–Greenstein particle scattering (Henyey and Greenstein, 1941; Toublanc, 1996) is created by linear interpolation from a prescribed aerosol extinction profile to the discrete altitude layers and τ_s is subsequently calculated using Eq. 4.44.

The scattering optical depth τ_s along each path segment, l, from altitude index z_1 to z_2 is calculated using the weighted mean scattering coefficient between the start and end altitudes:

$$\tau_s = l\varpi\,\frac{\beta_s(i,z_2) - \beta_s(i,z_1)}{\kappa(i,z_2) - \kappa(i,z_1-1)} \tag{4.44}$$

where ϖ is the single scattering albedo, which is unity for Rayleigh scattering and $0 < \varpi \leq 1$ for aerosol scattering:

$$\varpi = \frac{\sigma_s}{\sigma_s + \sigma_a} \tag{4.45}$$

where σ_s and σ_a are the scattering and absorption cross–sections. A high vertical resolution of 10 m is chosen to minimize potential interpolation errors that may arise due to the strong temperature and pressure gradients in the lowermost troposphere.

With two scattering species, Rayleigh and Henyey–Greenstein, the total scattering optical depth along the path is $\tau_s = \tau_{Ray} + \tau_{HG}$. The transmittance, $T_s = e^{-\tau_s}$, is calculated for each path step and the scattering criteria is met when the total transmittance, with respect to scattering, drops below the transmittance, ΔT_s, simulated at the beginning of the path (Sect. 4.2.1). Thus, by definition scattering occurs on path step N when

$$\prod_{i=1}^{N} e^{-\tau_{s_i}} \leq \Delta T_s \tag{4.46}$$

4.2.6 Recalculate the path length and position on scattering

If scattering occurs, the location of the scattering event along the path segment l must be calculated, since scattering is not assumed to always occur at $\mathbf{A}_{i+1}$. If, for example, there is an optically thick aerosol layer along l, the scattering probability is higher for the section of l within the aerosol layer than for the remainder of l and this must be accounted for. To accurately simulate the scattering location, the final path step l is divided into N increments (set to 1 m) and τ_{s_i} is calculated for each increment. The excess optical depth traversed to the end point of the path segment $\delta\tau_s$ is

$$\delta\tau_s = \tau_s - \Delta\tau_s = \ln \Delta T_s - \ln T_s \tag{4.47}$$

Starting from increment N and stepping backwards along l, τ_s is summed until

$$\sum_{i=N}^{i} \tau_{s_i} \geq \delta\tau_s \tag{4.48}$$

and the new path length is then i times the increment step–size. Given the new path length, l, the new photon position $\mathbf{A}_{i+1}$ is calculated from the previous position $\mathbf{A}_i$ and the direction vector $\vec{\mathbf{P}}_i$ (see Sect. 4.2.2).

4.2.7 Determine the scattering species

Assuming that scattering by individual species is independent, the probability of traversing an optical depth τ_s without scattering by any of N scattering species is

$$p(\neg s) = \prod_{i=1}^{N} e^{-\tau_{s_i}} = \prod_{i=1}^{N} p(\neg s_i) \tag{4.49}$$

where $\neg$ signifies logical negation.

The probability of scattering by any of the species is therefore

$$p(s) = p(s_1 \vee s_2 \vee ... \vee s_N) = 1 - p(\neg s) = 1 - e^{-\tau_s} \tag{4.50}$$

and similarly, the probability of scattering by any particular species i is

$$p(s_i) = 1 - e^{-\tau_{s_i}} \tag{4.51}$$

A consequence of the independence of scattering events is that two or more species could scatter in the same interval, or indeed one species could scatter more than once. As the probability of multiple scattering is equal to the product of the probabilities of the individual scattering events, the final path segment in which scattering occurs must be short enough so that $\tau_s \ll 1$ and the probability of multiple scattering is then negligible. Then it can be assumed that the scatter probabilities $p(s_i)$ for all species are mutually exclusive and thus additive. This is another reason why the first path step is not taken right to the scattering point (Sect. 4.2.1), since for long paths having high optical depth, the probability of multiple scattering becomes significant.

The conditional probability of scattering by species i, given that scattering has occurred, is given by Bayes' Theorem:

$$p\left(s_i|s\right) = \frac{1 - e^{-\tau_{s_i}}}{1 - e^{-\tau_s}} \tag{4.52}$$

Thus, using the uniform random number, u, and setting $p\left(s_0\right) = 0$, the scattering species i is selected where:

$$p\left(s_i\right) \leq u < p\left(s_{i+1}\right) \tag{4.53}$$

4.2.8 Calculate the new photon direction after scattering

Given the scattering species, the new photon propagation direction $\vec{\mathbf{P}}_{i+1}$ is determined using the scattering phase function $P(\mu)$, where $\mu = \cos\Theta$ and Θ is the scattering angle relative to the incident direction. The phase function is normalised to unity so that integrating over a sphere

$$\int\limits_{4\pi} \frac{P(\mu)}{4\pi}\, d\omega = \int\limits_0^{2\pi}\int\limits_0^{\pi} \frac{P(\cos\Theta)}{4\pi}\, \sin\Theta\, d\Theta\, d\psi = 1 \tag{4.54}$$

where $d\omega$ is an element of solid angle and ψ is the scattering azimuth angle, which determines the scattering plane of Θ around the axis of the incoming photon vector $\vec{\mathbf{P}}_i$. The scattering angle Θ is selected by setting $f(x) = P(\Theta)\sin\Theta$. The $\sin\Theta$ weighting of the scattering phase function arises from the use of polar rather than rectangular coordinates. This can be understood by considering a ring of area ds at a distance $r\,\sin\Theta$ from an axis of a sphere of radius r. The element of solid angle $\mathrm{d}\omega$ lying between Θ and $\mathrm{d}\Theta$ is

$$d\omega = ds/r^2 = 2\pi\, \sin\theta\, d\theta, \quad \text{and} \quad \int\limits_0^{\pi} d\omega = 4\pi \tag{4.55}$$

To illustrate, if the scattering was purely isotropic ($P(\mu) = 1$) and scattering angles were selected randomly without the $\sin\Theta$ weighting, a sphere centered on the scattering point would not be uniformly illuminated from within but would be illuminated with increasing intensity towards the zenith.

For a given wavelength, the CDF for the phase function of each scattering species is evaluated from 0 to π at discrete values of Θ_i. Then with

$$F(\Theta_i) = \sum_{j=1}^{i} P(\Theta_j)\, \sin\Theta_j \tag{4.56}$$

the scattering angle to the nearest degree is chosen so that

$$F(\Theta_i) \leq u < F(\Theta_{i+1}) \tag{4.57}$$

and interpolation is used to select the exact angle between Θ_i and Θ_{i+1}.

The scattering azimuth angle, ψ, is assumed to be isotropic for all scattering species and is given in radians by

$$\psi = 2\pi u \tag{4.58}$$

Given Θ and ψ, the photon's new propagation vector after scattering is derived from

$$\vec{\mathbf{P}}' = \begin{pmatrix} \cos\theta_i \cos\phi_i \sin\Theta \cos\psi - \sin\Theta \sin\phi_i \sin\psi + \cos\Theta \sin\theta_i \cos\phi_i \\ \cos\theta_i \sin\phi_i \sin\Theta \cos\psi + \sin\Theta \cos\phi_i \sin\psi + \cos\Theta \sin\theta_i \sin\phi_i \\ -\sin\theta_i \sin\Theta \cos\psi + \cos\theta_i \cos\Theta \end{pmatrix} \tag{4.59}$$

where θ_i and ϕ_i are the photon zenith and azimuth angles before scattering. θ_{i+1} and ϕ_{i+1} are then calculated from $\vec{\mathbf{P}}'$ using Eqs. 4.23 and 4.24.

The transformation equations for calculating the new direction after a scattering event are derived as follows. Given the rotation matrices around the y–axis in a rectangular, right–handed coordinate system:

$$R_y = \begin{pmatrix} \cos\theta & 0 & -\sin\theta \\ 0 & 1 & 0 \\ \sin\theta & 0 & \cos\theta \end{pmatrix} \tag{4.60}$$

and around the z-axis

$$R_z = \begin{pmatrix} \cos\phi & \sin\phi & 0 \\ -\sin\phi & \cos\phi & 0 \\ 0 & 0 & 1 \end{pmatrix} \tag{4.61}$$

the product of the two rotations is then

$$R_{yz} = R_y R_z = \begin{pmatrix} \cos\theta\cos\phi & \cos\theta\sin\phi & -\sin\theta \\ -\sin\phi & \cos\phi & 0 \\ \sin\theta\cos\phi & \sin\theta\sin\phi & \cos\theta \end{pmatrix} \tag{4.62}$$

R_{yz} is inverted to give

$$R_{yz}^{-1} = \begin{pmatrix} \cos\theta\cos\phi & -\sin\phi & \sin\theta\cos\phi \\ \cos\theta\sin\phi & \cos\phi & \sin\theta\sin\phi \\ -\sin\theta & 0 & \cos\theta \end{pmatrix} \tag{4.63}$$

The characteristic angles for a scattering event, θ_s (derived form the scatterer's phase function) and ϕ_s (randomly chosen within $[0, 2\pi]$) are given relative to the photon direction before the scattering event, $\vec{\mathbf{P}}_i$. With the rotation matrix R_{yz}^{-1} applied to a system tilted to $\vec{\mathbf{P}}_i$, the new direction is given by:

$$\begin{aligned} \vec{\mathbf{P}}' &= R_{yz}^{-1}\, \vec{\mathbf{P}}_i \times \vec{\mathbf{P}}_s \\ &= \begin{pmatrix} \cos\theta\cos\phi & -\sin\phi & \sin\theta\cos\phi \\ \cos\theta\sin\phi & \cos\phi & \sin\theta\sin\phi \\ -\sin\theta & 0 & \cos\theta \end{pmatrix} \begin{pmatrix} \sin\theta_s\cos\phi_s \\ \sin\theta_s\sin\phi_s \\ \cos\theta_s \end{pmatrix} \end{aligned} \tag{4.64}$$

leading to Eq. 4.59.

Rayleigh scattering phase function

The Rayleigh phase function describing the angular distribution of scattered energy by air molecules and very small particles (radii $\ll \lambda$) is given by (Chandrasekhar, 1950; Bucholtz, 1995):

$$P_{Ray}(\mu, \lambda) = \frac{3}{4(1+2\gamma)} \left[(1+3\gamma) + (1-\gamma)\mu^2)\right] \tag{4.65}$$

where γ is a correction factor for molecular anisotropy, defined by

$$\gamma = \frac{\rho_n}{2-\rho_n} \tag{4.66}$$

and ρ_n is the wavelength–dependent depolarization factor, interpolated from tabulated values given in Bucholtz (1995) and Bates (1984).

Henyey–Greenstein scattering phase function

When the particle size is comparable to or greater than λ for optical wavelengths, such as for most aerosols or cloud droplets, scattering has a much smaller wavelength–dependence than scattering on molecules and a more complex, forward–peaked phase function. Mie scattering theory (Mie, 1908; Wiscombe, 1980; Lee, 1998; Du, 2004; Gouesbet, 2009) can be used to model the angular distribution of scattered light intensity for spherical particles such as fog and cloud droplets, but other numerical approximations are needed for more complex shaped particles (see Mishchenko, 2009, for a review). A fast first–order approximation of the scattering phase function for aerosols and droplets, commonly used in RTMs, is the Henyey–Greenstein function (Toublanc, 1996):

$$P_{HG}(\mu) = \frac{1-g^2}{(1+g^2-2g\mu)^{\frac{3}{2}}} \tag{4.67}$$

where g is the asymmetry parameter

$$g = \frac{1}{2}\int_{-1}^{1} \mu P(\mu) d\mu \tag{4.68}$$

For isotropic scattering g is zero as for Rayleigh scattering, and g increases as the zeroth diffraction peak of the phase function becomes sharper. The asymmetry parameter quantifies the relative strength of the forward scattering peak for aerosol particles and may be negative if the phase function has a strong backwards scattering peak, with $g = 1$ for complete forward scattering and $g = -1$ for complete backscattering. The Henyey–Greenstein phase function is an adequate approximation for scattering patterns that are not too strongly peaked in the forward direction. In the comparison exercises a g value of 0.68 was used for urban aerosols and for smaller sea salt aerosols with a stronger forward scattering peak, g was set to 0.75 (Wagner et al., 2007a).

4.2.9 Modify the photon weighting and direction after a ground hit

If the photon does not scatter before hitting the ground, the photon's weighting ξ is multiplied by the fractional surface albedo, α. The new propagation direction, $\vec{\mathbf{P}}_{i+1}$, after reflection is selected according to the isotropic scattering properties of a Lambertian surface. Therefore, Θ is randomly sampled independently of the incident angle:

$$\Theta = \arccos\sqrt{u} \tag{4.69}$$

The new azimuth angle after reflection is also selected randomly using Eq. 4.58. For a Lambertian surface, a large number of simulated photons evenly illuminate a hemisphere over the point of ground reflection.

4.2.10 Test for photon termination

The photon is now tested to see if it meets the termination criteria. This will depend on the application of the model and in backwards mode it is generally when the photon exits the TOA, or if the model is being run in the forward direction, when the photon enters the entrance optics of the instrument.

For the direct backward model, as opposed to the adjoint simulation model, this test must be performed before the new ξ is calculated because if the photon overshoots the TOA, l is shortened so that the photon finishes exactly at the TOA. In contrast, for the adjoint simulation (see Sect. 4.3) the direct path from the last scatter event to the TOA is replaced by the final adjoint path. In the direct simulation, when the photon exits the atmosphere its θ and ϕ values are relative to the local coordinate system at the exit latitude and longitude. To calculate the equivalent solar zenith angle at the observation position, the photon propagation vector is parallel translated back to the latitude and longitude of the observer using Eqs. 4.83 and 4.84. In a parallel translation, the origin of the local coordinate system of the propagation vector is simply shifted to the new location.

A photon is also terminated if its ξ value falls below a threshold of 10^{-10}.

4.2.11 Modify the photon weighting by absorption

Since each photon tracked by the model is monochromatic with wavelength λ, attenuation by absorption along a photon path segment can be calculated using the Beer–Lambert–Bouguer law. The monochromatic intensity or radiance (I_λ) after travelling a distance l through an absorber is given by

$$I_\lambda = I_{\lambda_0}\, e^{-\beta_a\, l} \tag{4.70}$$

where I_{λ_0} is the intensity at wavelength λ at the beginning of the path segment and β_a is the mean absorption coefficient along the path. For trace gases

$$\beta_a = \sigma(\lambda, T)\ \rho(\Lambda, \Phi, R) \tag{4.71}$$

where σ is the absorption cross–section, which may depend on wavelength and temperature T, and ρ is the molecular number density of the absorber, which can vary with longitude, latitude and altitude. For non–conservatively scattering aerosols, the absorption coefficient is determined from the extinction coefficient, $\beta = \beta_s + \beta_a$, and the single scattering albedo ϖ:

$$\beta_a = (1 - \varpi)\,\beta \tag{4.72}$$

A wavelength–specific integrated absorption coefficient array, β_a, with discrete altitude steps from the surface to the TOA, is created for each absorber at the beginning of a model run (analogous to $\beta_\mathbf{s}$ in Sect. 4.2.5). The value of β_a for a given index i of the zenith angle at the Earth's surface θ_e and altitude layer index z is given by

$$\beta_a(i, z) = \sum_{j=1}^{z} \beta_a(j)\,[\kappa(i, j) - \kappa(i, j-1)] \tag{4.73}$$

where $\kappa(i, j)$ is the sum of relative path lengths from the ground to layer j (see Sect. 4.2.1). The absorption optical depth τ_a along each path segment l from altitude index z_1 to z_2 is calculated in the same manner as the scattering optical depth (see Eq. 4.44) using the weighted mean absorption coefficient between the start and end altitudes:

$$\tau_a = l(1 - \varpi)\frac{\beta_a(i, z_2) - \beta_a(i, z_1)}{\kappa(i, z_2) - \kappa(i, z_1 - 1)} \tag{4.74}$$

Since a model photon's probability weighting ξ is equivalent to its normalised radiance, its new weighting after travelling a distance l is

$$\xi_{i+1} = \xi_i \ \exp\left(-\sum_{j=1}^{m} \tau_a(j)\right) \tag{4.75}$$

where τ_a is summed over m absorbing species.

The ray tracing steps summarised in Fig. 4.2 and detailed in Sects. 4.2.1 to 4.2.11 are repeated until the photon termination condition (Sect. 4.2.10) is met. At this point the adjoint weightings are calculated as described in the following section.

4.3 Calculation of adjoint weightings

In the backward, or time–reversed direct simulation, the instrument SZA is determined by parallel–translating the local SZA at the photon's TOA exit location back to a point directly above the instrument and the solar azimuth angle (SAA) is defined as the bearing East of North from the instrument location to the photon's exit location. In general, AMFs and radiances are desired for specific SZAs including high SZAs and it can take a long time to obtain a statistically

sufficient number of photons to calculate box–AMFs with acceptably low variance using the direct MC simulation method. Therefore, NIMO employs the variance reduction technique of adjoint simulation (Marchuk et al., 1980; Marshak and Davis, 2005; Rozanov and Rozanov, 2007).

In the backward MC adjoint simulation, trajectories are simulated starting from the detector in a given direction, as outlined in Sect. 4.2, and at each collision a contribution function, Ψ, is calculated for the given SZA and SAA. This is effectively the probability that the photon would travel directly from the Sun to the collision point without being scattered out of the path or absorbed, which is, in the backwards direction, equal to the product of the probability of scattering from the incident direction into the direction of the Sun multiplied by the transmittance along the adjoint path from the collision point to the TOA.

$$\Psi(x, \Omega) = \frac{P(\Omega \cdot \Omega_S)}{4\pi} \exp\left[-\tau(x, x_S)\right] \tag{4.76}$$

where x and x_S are the collision and TOA exit locations respectively, Ω is the incident direction and Ω_S is the unit direction vector from the collision point to the Sun. The contribution functions modify the directly–simulated photon weighting ξ appropriately for the prescribed SZA and SAA.

The direct Monte Carlo simulated paths depend on the composition of the model atmosphere, the wavelength and the instrument viewing direction, but are independent of the SZA and SAA. Therefore, when one set of temperature, pressure, trace gas and aerosol profiles is used, it is possible to simulate a whole day of MAX–DOAS measurements for each elevation angle by simply recalculating the contribution functions for all the solar geometries after each direct photon trajectory has been generated. This allows fast MAX–DOAS retrievals in clear atmospheric conditions, but for changing aerosol conditions or when aerosol profiles are being retrieved, the direct simulated paths must be recalculated for every simulated MAX–DOAS measurement.

4.3.1 Creation of adjoint photon trajectories

Each contribution function is calculated by creating an adjoint photon trajectory in a single path step from each scattering point, including ground reflections, to the TOA in the direction of the Sun. The local SZA (θ_{S_i}) and SAA (ϕ_{S_i}), described by the vector $\mathbf{\Omega_{S_i}}$ at the scattering location $\mathbf{A}_i$, is calculated for the prescribed instrument SZA and SAA by a lateral translation of the Sun direction vector $\mathbf{\Omega_{S_0}}$ at the instrument location $\mathbf{A}_0$ to the location scattering point $\mathbf{A}_i$ using spherical 3D geometry. With the difference in longitude $\Delta\Lambda = \Lambda_0 - \Lambda_i$, the following transformations are made:

$$\mathbf{\Omega_{S_i}} = \begin{pmatrix} \cos\Phi_{S_i} & 0 & -\sin\Phi_{S_i} \\ 0 & 1 & 0 \\ \sin\Phi_{S_i} & 0 & \cos\Phi_{S_i} \end{pmatrix} \begin{pmatrix} 1 & 0 & 0 \\ 0 & \cos\Delta\Lambda & -\sin\Delta\Lambda \\ 0 & \sin\Delta\Lambda & \cos\Delta\Lambda \end{pmatrix}$$

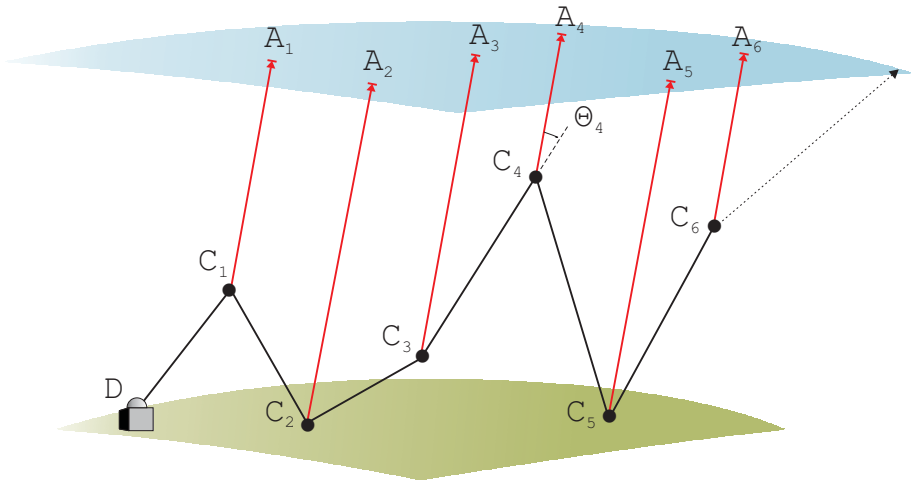

Figure 4.5: The determination of radiance by MC simulations of backwards and adjoint trajectories. Absorption attenuation is calculated along the direct photon paths between the detector and the collision points, C_1 to C_6. The probability of scattering into the direction of the Sun is determined at each collision point using the phase function of the scattering angle Θ. Extinction is calculated along the adjoint trajectories A_1 to A_6 for the prescribed SZA and SAA. The final direct MC path (dotted line) to the TOA is omitted from the calculation and replaced by the final adjoint trajectory A_6.

$$\begin{pmatrix} \cos\Phi_{S_0} & 0 & \sin\Phi_{S_0} \\ 0 & 1 & 0 \\ -\sin\Phi_{S_0} & 0 & \cos\Phi_{S_0} \end{pmatrix} \begin{pmatrix} \sin\theta_{S_0}\cos\phi_{S_0} \\ \sin\theta_{S_0}\sin\phi_{S_0} \\ \cos\theta_{S_0} \end{pmatrix} \tag{4.77}$$

$$= \begin{pmatrix} \sin\theta_{S_i}\cos\phi_{S_i} \\ \sin\theta_{S_i}\sin\phi_{S_i} \\ \cos\theta_{S_i} \end{pmatrix} \tag{4.78}$$

using the substitutions

$$S = \cos\Phi_0 \sin\theta_{S_0}\cos\phi_{S_0} + \sin\Phi_0\cos\theta_{S_0} \tag{4.79}$$

$$T = \sin\Delta\Lambda\sin\theta_{S_0}\sin\phi_{S_0} \tag{4.80}$$

$$U = \sin\Phi_0\sin\theta_{S_0}\cos\phi_{S_0} - \cos\Phi_0\cos\theta_{S_0} \tag{4.81}$$

leading to the new Sun direction vector in terms of the change in latitude and longitude:

$$\mathbf{\Omega_{S_i}} = \begin{pmatrix} \cos\Phi_i \times S - \sin\Phi_i(T - \cos\Delta\Lambda \times U) \\ \cos\Delta\Lambda\sin\theta_{S_i}\sin\phi_{S_i} + \sin\Delta\Lambda \times U \\ \sin\Phi_i \times S + \cos\Phi_i(T - \cos\Delta\Lambda \times U) \end{pmatrix} \tag{4.82}$$

The local SZA and SAA at the scattering location, $\mathbf{A}_i$, are then given by:

$$\theta_{S_i} = \arccos \mathbf{\Omega_{S_i}}_z \tag{4.83}$$

$$\phi_{S_i} = \begin{cases} \arcsin(\mathbf{\Omega_{S_i}}_y / \sin\theta_{S_i}) & \text{if } \mathbf{\Omega_{S_i}}_x \geq 0 \\ \pi - \arcsin(\mathbf{\Omega_{S_i}}_y / \sin\theta_{S_i}) & \text{if } \mathbf{\Omega_{S_i}}_x < 0 \end{cases} \tag{4.84}$$

An altitude and SZA–dependent correction factor is subtracted from the local SZA to account for the difference between the local SZA and the instrument SZA due to refraction. This ensures that the photon exits the TOA at the correct local SZA corresponding to the instrument SZA. The refraction correction factor is read from a lookup table, which is previously created by initializing photons at each combination of altitude and SZA in turn and taking the difference between the exit and start SZAs.

The unrefracted path length from the scattering point to the TOA is calculated using the cosine rule:

$$l = \sqrt{R_{TOA}^2 - R^2 + R^2 \cos^2\theta - R\cos\theta} \tag{4.85}$$

The refracted path length is then determined using the method described in Sect. 4.2.2.

The adjoint path weighting calculation accounts for total extinction, in other words scattering attenuation as well as absorption attenuation. The reduction in the model photon's weighting along the adjoint path is calculated using Eq. 4.75 using the total optical depth τ.

4.3.2 Determination of the probability of scattering towards the Sun

The probability S of scattering into the direction of the Sun after a collision, is given by the integral of the phase function of the scattering species oriented to the photon incident direction, across the solid angle subtended by the Sun's disk in the sky. However, the size of the Sun's disk is small enough that the integral can be ignored and the probability S can be taken directly from the phase function $P(\mu)$. The cosine of the scattering angle, μ, between the photon's incident direction Ω (θ_I, ϕ_I) and the Sun's direction Ω_S, (θ_S, ϕ_S), is given by

$$\mu = \cos\theta_I \cos\theta_S + \sin\theta_I \sin\theta_S \cos(\phi_I - \phi_S) \tag{4.86}$$

The relative probability of scattering from the incident direction towards the Sun is then given by

$$S = P(\mu)/4\pi \tag{4.87}$$

When more than one type of scattering particle is included in the model, a mixed phase function must be used (Oikarinen et al., 1999; Spada et al., 2006). With two functions, Rayleigh and Henyey–Greenstein, the ratio between the Rayleigh scattering coefficient and the total volume scattering coefficient (see Sect. 4.2.5) is determined at the scattering location by

$$f_s(\mathbf{A}) = \frac{\beta_{Ray}(\mathbf{A})}{\beta_{Ray}(\mathbf{A}) + \beta_{HG}(\mathbf{A})} \tag{4.88}$$

where, for a horizontally–homogeneous atmosphere, only the altitude at location $\mathbf{A}$ affects the scattering coefficients. The probability of scattering towards the

Sun (Eq. 4.87) is then based on the mixed phase function

$$P(\mathbf{A},\mu) = P_{Ray}(\mu)\, f_s(\mathbf{A}) + P_{HG}(\mu)[1 - f_s(\mathbf{A})] \tag{4.89}$$

For Lambertian surface reflection, which is isotropic over a hemisphere and independent of the incident angle, the normalised phase function is given by:

$$P(\mu_r) = \frac{\int_0^{2\pi}\int_0^1 2\mu_r\, d\mu_r\, d\phi}{2\pi} = 1 \tag{4.90}$$

where μ_r is the cosine of the angle of reflection relative to the normal. The probability of scattering towards the Sun after a Lambertian ground reflection is therefore

$$S = \mu_r/\pi \tag{4.91}$$

The photon weighting was already multiplied by the surface albedo α during the primary ray tracing as described in Sect. 4.2.9, so α is not applied in the adjoint probability calculation.

4.3.3 Calculation of the contribution functions and radiance

Finally, the total photon weighting, or normalised radiance, is given by the summation of weightings for all complete paths (direct plus adjoint paths) from the instrument to the Sun (see Fig. 4.5). The mean intensity for m backward photon trajectories i, each having n_i scattering events, is

$$\begin{aligned} I &= \frac{1}{m}\sum_{i=1}^{m}\sum_{j=1}^{n_i}\Psi(x_{ij},\Omega_{ij})\exp\left(-\int_{\mathbf{D}}^{S_{ij}}\beta_a(l)\,dl\right) \\ &= \frac{1}{m}\sum_{i=1}^{m}\sum_{j=1}^{n_i}\frac{P(\mathbf{S}_{ij},\theta_{ij})}{4\pi}\exp\left(-\int_{\mathbf{S}_{ij}}^{TOA_{ij}}\beta_s(l)\,dl - \int_{\mathbf{D}}^{TOA_{ij}}\beta_a(l)\,dl\right) \end{aligned} \tag{4.92}$$

where $\mathbf{D}$ refers to the detector location, $\mathbf{S}_{ij}$ is the scattering event location and TOA_{ij} is the point where the adjoint photon trajectory exits the atmosphere.

Thus, in terms of the discrete model path segments, the mean normalised radiance (or intensity) is

$$I = \frac{1}{m}\sum_{i=1}^{m}\sum_{j=1}^{n_i}\prod_{k=1}^{j}\xi_{ik}\prod_{k=1}^{j}\alpha_{ik}\,T_{ij}\,S_{ij} \tag{4.93}$$

where ξ_{ik} is the intensity weighting due to absorption attenuation along the trajectory between the scattering or surface reflection event $k-1$ (where $k=0$ is the detector, D) and k for photon i. α_{ik} is the surface albedo of scattering event k, which is always 1 for atmospheric scattering and $0 \le \alpha \le 1$ for ground reflection. T_{ij} is the transmittance along the adjoint path from the scattering event j of photon i to the Sun, and S_{ij} is the probability of this event scattering into the direction of the Sun.

4.4 Box–air–mass factor calculations

The principal application of NIMO is the calculation of AMFs and box–air–mass–factors (box–AMFs) to convert DOAS SCD measurements into VCDs and to calculate weighting functions, using box–AMFs, for the retrieval of trace gas profiles from MAX–DOAS measurements. A box–AMF represents the ratio of a partial SCD to a partial VCD in a prescribed atmospheric layer within which the trace gas concentration is assumed to be constant. This section gives a brief overview of the use of AMFs in the DOAS technique and then describes the intensity–weighted box–AMF calculation.

4.4.1 Application of AMFs in DOAS

Ground–based UV–visible DOAS is a remote sensing technique that can be used to make measurements of several important atmospheric trace gases. The DOAS retrieval technique applied to the measured spectra produces only SCDs, a weighted measure of the total number of molecules along the ensemble of paths traced by the photons through the atmosphere. To convert SCDs to VCDs it is necessary to divide the SCD by a factor which expresses the enhancement in the effective optical path through the atmosphere relative to the vertical path. These AMFs are calculated from a knowledge of the ensemble of paths of the measured radiation through the atmosphere and the typical vertical distribution of the species under consideration. The SCD, calculated using the so called exact method (Sarkissian et al., 1995), is given by

$$SCD = \frac{1}{\sigma}\left(-\ln\frac{\sum_{i=1}^{N}\xi_i}{\sum_{i=1}^{N}\xi_i^*}\right) \tag{4.94}$$

where σ is the absorption cross–section at the specified wavelength, ξ_i are the statistical weightings for N photons travelling through the model atmosphere, and ξ_i^* are the statistical weightings for the same ensemble of photon trajectories with absorption due to the species of interest excluded. This calculation is easily applied in the direct MC simulation as the photon trajectories represent the true physical trajectories. However, in the adjoint simulation the trajectories are independent of SZA and SAA, and thus they are not representative of the true physical trajectories for a given geometry. Therefore, in the adjoint simulation SCDs are calculated using box–AMFs as described in Sect. 4.4.2.

4.4.2 Box–AMFs

Appropriate box–AMF layers can be chosen based on a knowledge of typical expected trace gas profiles and the measurement technique or platform. For example, ground–based MAX–DOAS measurements are very sensitive to trace

gases in the boundary layer so it is useful to choose several thin layers (eg. 10–100 m) in the lowermost troposphere. Zenith sky DOAS is sensitive to the lower stratosphere at high SZAs so 1000 m layers from 10 km to 20 km altitude, for example, could be used to retrieve this profile information. Box–AMFs characterise the sensitivity of SCD measurements to trace gas perturbations as a function of altitude and for optically thin absorbers ($\tau \ll 1$), the box–AMFs serve as weighting functions (Rodgers, 2000). Box–AMFs (A_z) are calculated using the mean intensity–weighted geometrical path lengths with respect to layer thickness

$$A_z = \frac{\sum_{i=1}^{m} \xi_i l_{iz}}{\delta z \sum_{i=1}^{m} \xi_i} \tag{4.95}$$

for m photons where l_{iz} is the path length of photon i in layer z and δz is the vertical thickness of the layer. In the backward adjoint method the box–AMF calculation also includes the adjoint trajectories. For a single photon the layer path lengths are determined along each direct plus adjoint trajectory from the instrument to the TOA and weighted by ξ_{ij}, the weightings of the composite trajectories (see Fig. 4.5). The box–AMF calculation for the adjoint simulation is then

$$A_z = \frac{\sum_{i=1}^{m} \sum_{j=1}^{n_i} \xi_{ij} l_{ijz}}{\delta z \sum_{i=1}^{m} \xi_i} \tag{4.96}$$

for m photons, each with n_i collisions, where l_{ijz} is the path length in layer z for composite trajectory j of photon i. For long paths the layer path lengths at high zenith angles decrease as the photon travels towards higher altitudes, so the integrated relative path length, κ, described in Sect. 4.2.1 is used to determine the fraction of the total path that resides in layer z:

$$l_{ijz} = L_{ij} \times \left(\frac{\kappa_t - \kappa_{b-1}}{\kappa_T - \kappa_{B-1}} \right) \tag{4.97}$$

where L_{ij} is the total path segment length, t and b are the fine (10 m) layer indices for the top and bottom of the box layer and T and B are the indices for the top and bottom of the total path segment. A correction is also made when only part of a layer is traversed. The total SCD for a given trace gas profile is derived from the sum of the n box–AMFs weighted by the partial VCDs, V_z:

$$SCD = \sum_{z=1}^{n} A_z V_z \tag{4.98}$$

and the total AMF is

$$AMF = \frac{\sum_{z=1}^{n} A_z V_z}{\sum_{z=1}^{n} V_z} \tag{4.99}$$

4.5 Comparison with other radiative transfer models

NIMO was compared with nine other RTMs from eight international research groups using a series of exercises, presented in each section below, and described in detail by Wagner et al. (2007a). Temperature, pressure and ozone profiles from the 1976 US standard atmosphere (United States Committee on Extension to the Standard Atmosphere, 1976) and ozone cross sections measured by the SCIAMACHY instrument (Bogumil et al., 2003) were used. The exercises were performed at five wavelengths representing characteristic absorptions of important trace gases in the UV–visible region. The surface albedo was 3% in all of the exercises apart from one, in which the surface albedo was set to 80%. The telescope field of view was set to a single narrow beam ($< 0.1°$) for consistency between the models and the simulations were performed with 5×10^6 model photons. NIMO results were in good agreement with the other RTMs (Wagner et al., 2007a) within the range of variability around the multi–model median values. Several of the exercises were also performed using the direct backward MC simulation technique and the results (not shown here) were consistent with the adjoint simulation method. The fast ray tracing method, of selecting long path lengths based on the statistical mean free path length, was compared with a slower method using short path length steps for simulating both the direct and adjoint trajectories. The results using the two methods are almost identical.

4.5.1 Variation of wavelength

Rayleigh vertical optical depths and normalised radiances were calculated for the zenith telescope view at SZA 70° for the five prescribed wavelengths. NIMO results are in good agreement with the other models as shown in the inset plots of Fig. 4.6. Rayleigh vertical optical depth decreases with wavelength as $\tau_{Ray} \propto \lambda^{-4}$. Normalised radiance increases towards shorter wavelengths because multiple scattering increases the diffuse radiation, but strong ozone absorption reduces the radiance at 310 nm.

Figure 4.7 shows the box–AMFs at all wavelengths for a zenith viewing direction at SZA 70°. There is good agreement with the other models at all wavelengths as shown by the percentage deviation plots for 360 nm and 577 nm in Fig. 4.7. For atmospheric layers above the first scattering altitude the lengths of photon trajectories through the layers are determined by the direction of the direct solar rays, so the box–AMFs approach the geometrical approximation $1/\cos(SZA) \approx 2.9$. The geometrical light path lengths of the direct solar rays decreases higher in the atmosphere because the local zenith angle decreases below the SZA at the detector due to the sphericity of the atmosphere. At low altitudes most photons travel on a vertical path into the instrument so the box–AMFs approach close to unity, and the box–AMFs are greater for longer wavelengths since the mean scattering altitude is lower so more photons travel through the lower layers at the SZA before scattering down into the zenith viewing telescope. Multiple–

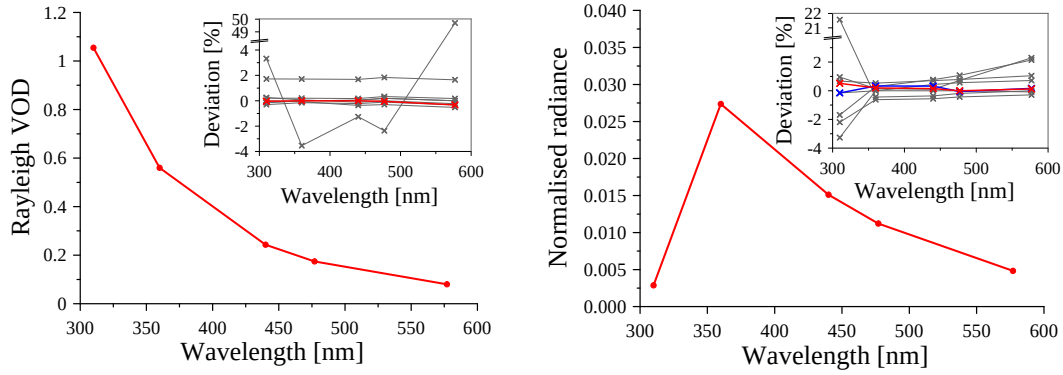

Figure 4.6: Vertical optical depth (VOD) with respect to Rayleigh scattering (left) and normalised radiance (right) for the zenith view at SZA 70° in a model atmosphere with pure Rayleigh scattering and ozone absorption. The inset plots show the percentage deviations of VOD and radiance as determined by the different RTMs from the median values of all the RTMs (excluding NIMO). NIMO is displayed in red, the NIMO short path segment test in blue, and the other models in grey.

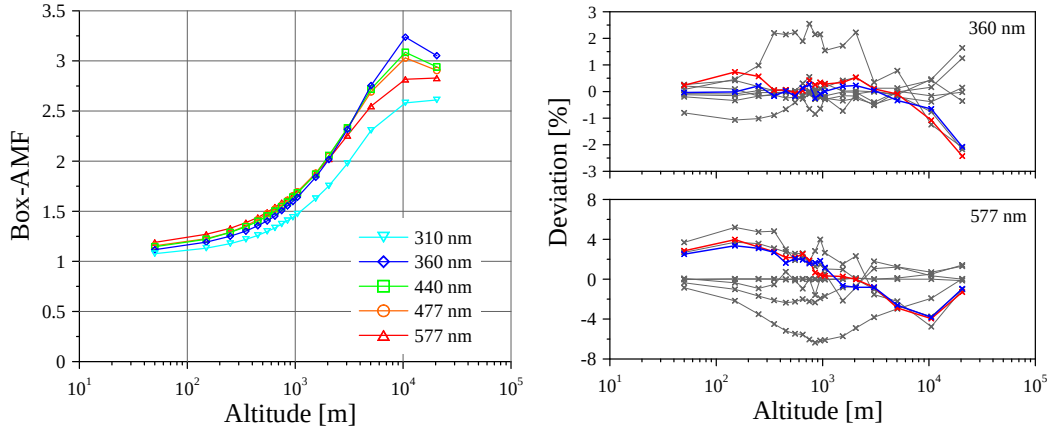

Figure 4.7: Box–AMFs as a function of altitude (on a logarithmic scale) at all wavelengths for the zenith view at SZA 70° in a model atmosphere with pure Rayleigh scattering and ozone absorption. The right–hand plots show the percentage deviations of box–AMFs at 360 nm and 577 nm from the median values of the other RTMs. NIMO is displayed in red, the NIMO short path segment test in blue (often obscured directly under the red line), and the other models in grey.

scattering, especially at shorter wavelengths, enhances the geometrical light path in all layers as seen in Fig. 4.8.

Light that passes through the ozone layer with long paths, or which undergoes multiple scattering in the layer, is heavily attenuated by ozone absorption at 310 nm, so that its contribution to the intensity at the detector is small. Therefore, the relative contribution from light that is scattered above the absorbing layer and travels through the layer with short vertical paths is much higher and

correspondingly the box–AMFs in and below the absorbing layer are reduced. The effect of ozone absorption on the box–AMFs for the different wavelengths was investigated by using the 440 nm ozone absorption cross–section for all wavelengths (Fig. 4.8, right panel). It is clearly seen, in the absence of strong attenuation by ozone, that the path enhancement due to multiple Rayleigh scattering increases at shorter wavelengths. There is another strong ozone absorption band at 577 nm, which reduces the box–AMFs compared to the 440 nm cross–section case, but the cross–sections at 360 nm and 477 nm are within an order of magnitude of the 440 nm cross–section so the effect of differences in absorption on the box–AMFs is very small. The right–hand plot of Fig. 4.8 illustrates the very high ozone optical depth at 310 nm, which is approximately 1500 times the optical depth at 360 nm, while the optical depth for a zenith angle of 70° is approximately three times the vertical optical depth, as expected from geometry ($1/\cos(SZA) \approx 2.9$).

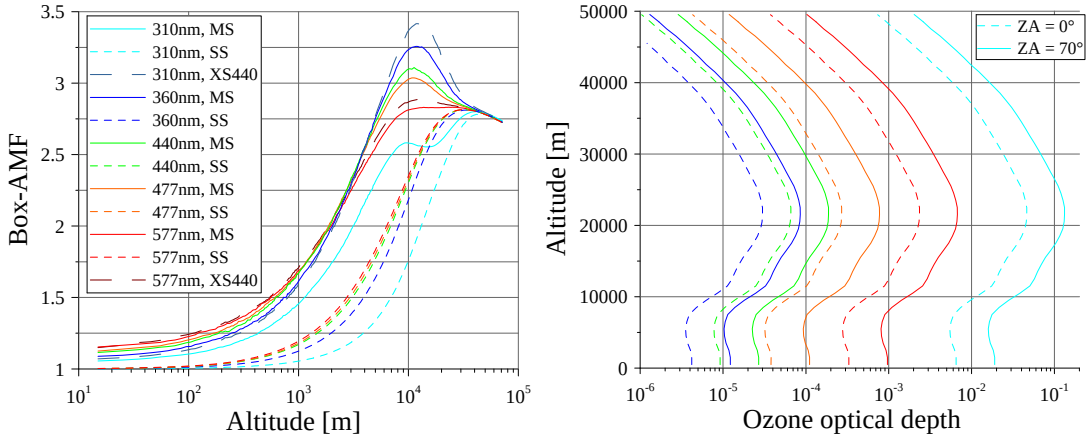

Figure 4.8: Box–AMFs for multiple scattering (solid lines) and single scattering (dashed lines) for the zenith view at SZA 70° with pure Rayleigh scattering and ozone absorption (left). Box–AMFs for 310 nm and 577 nm with the ozone absorption cross–section for 440 nm are displayed by the long–dashed lines (XS440). The right hand panel shows ozone optical depth per 1 km for layers up to 50 km. The solid lines represent photon paths with a zenith angle of 70° and the ozone vertical optical depth in each layer is shown by the dashed lines. Wavelength is indicated using the same colours as in the left–hand plot. Note the logarithmic x–axis scale.

4.5.2 Variation of elevation angle

Normalised radiances for 360 nm and 577 nm at SZA 20° are shown as a function of the telescope elevation angle in Fig. 4.9 and are consistent with the other models (Fig. 4.10). For scattered sunlight measurements, radiance depends on the optical depth along the line of sight and on the phase function at the relative angle between the telescope and the Sun. At 360 nm the optical depth remains high up to an elevation angle of 10° rather than increasing with decreasing elevation angle as would occur at smaller optical depths. Thus the increase in

radiance from 1° to 10° elevation is mainly due to the increase in the Rayleigh phase function with decreasing relative angle between the telescope and the Sun, but at higher elevation angles decreasing optical depth leads to an overall reduction in the radiance. At 577 nm, Rayleigh optical depth increases towards lower elevation angles, leading to increasing radiance from multiple scattering. However, the presence of an aerosol layer (A2, 0.5 km^{-1} from 0–2 km, Henyey–Greenstein asymmetry parameter of 0.68) produces the opposite effect due to the strong forward–scattering peak in the aerosol phase function. The radiance thus increases towards higher telescope elevation angles as they look closer to the direction of the overhead Sun at SZA 20°. The weaker wavelength–dependence of aerosol scattering compared to Rayleigh scattering explains the similar radiances for the two wavelengths when aerosol scattering is predominant.

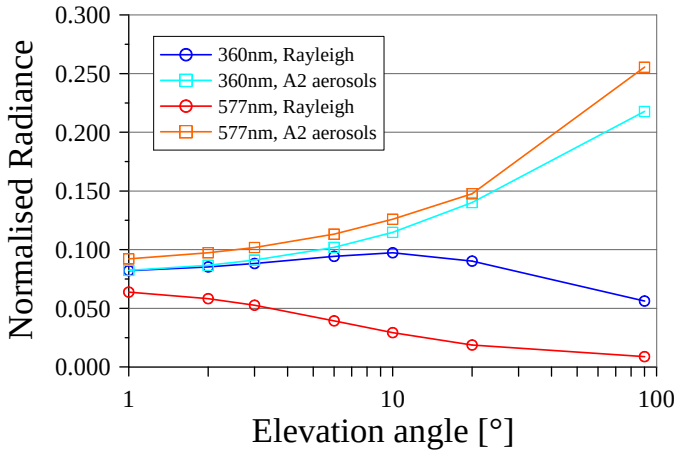

Figure 4.9: Normalized radiances as a function of elevation angle at SZA 20° for 360 nm and 577 nm with pure Rayleigh scattering and with an aerosol layer of 0.5 km^{-1} from the ground up to 2 km (A2). Note that the x–axis scale is logarithmic.

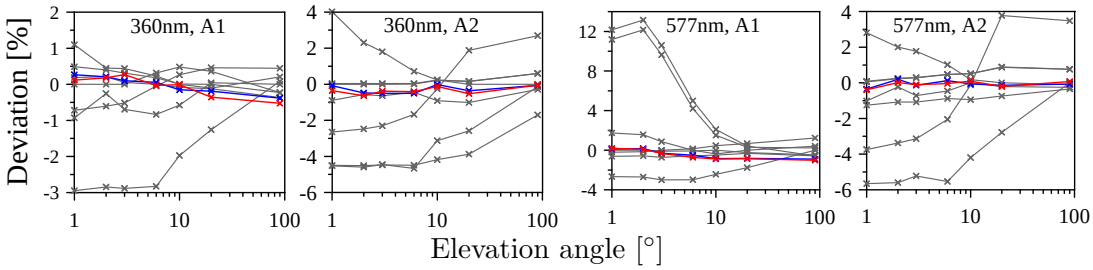

Figure 4.10: Percentage deviations in normalized radiances from the multi–model median as a function of elevation angle at SZA 20° for 360 nm and 577 nm with pure Rayleigh scattering (A1) and with an aerosol layer of 0.5 km^{-1} from the ground up to 2 km (A2). NIMO is displayed in red, the NIMO short path segment test in blue, and the other models in grey.

At low telescope elevation angles (α) the box–AMFs are high for the lowest altitude layers as most photons scatter above or within these layers and thus their box–AMFs are close to the geometrical approximation for a plane parallel atmosphere, $1/\sin\alpha$ (upper panels, Fig. 4.11). The mean free paths at 577 nm are much longer than at 360 nm due to the lower Rayleigh optical depth, hence the box–AMFs are greater. The implication of this is that, in the absence of strong overlapping spectral features of other species, MAX–DOAS measurements are more sensitive to trace gases with absorption structures at longer wavelengths. In addition, longer wavelengths can be used to resolve profile information to slightly higher altitudes since the low elevation angles receive radiance contributions from light scattered at higher altitudes due to the lower Rayleigh optical depth. Box–AMFs decrease for higher layers as the proportion of photons scattering below the layers increases and the photon paths through the layers thus approach $1/\cos SZA$, which is approximately 1.06 for SZA 20°.

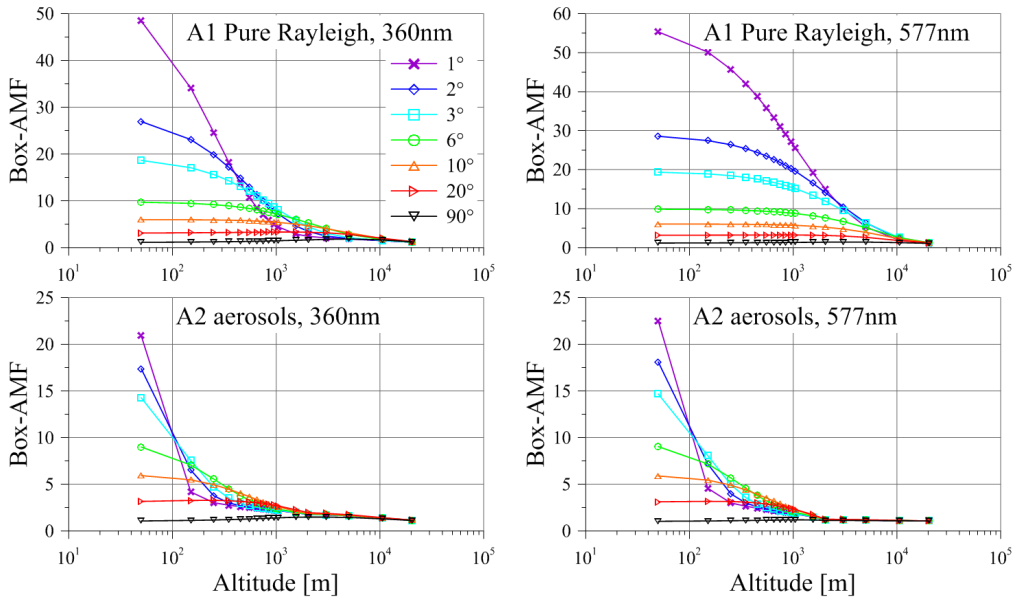

Figure 4.11: Box–AMFs for 360 nm and 577 nm at SZA 20° and 7 different elevation angles in a model atmosphere with pure Rayleigh scattering and ozone absorption (top panels) and with an aerosol layer of 0.5 km^{-1} from the ground up to 2 km (A2, bottom panels).

Multiple scattering by aerosols reduces the mean free path of photons in the aerosol layer, thus decreasing the average distance from the last scattering event into the telescope field of view. This effect is most pronounced for low viewing elevations where the paths would otherwise be much longer. Thus, box–AMFs are reduced by aerosol scattering relative to clear air, particularly for low viewing angles, and so the sensitivity of MAX–DOAS measurements at low SZA is decreased by strong aerosol scattering (lower panels, Fig. 4.11). Again, the box–AMFs are consistent with results from other RTMs (Fig. 4.12).

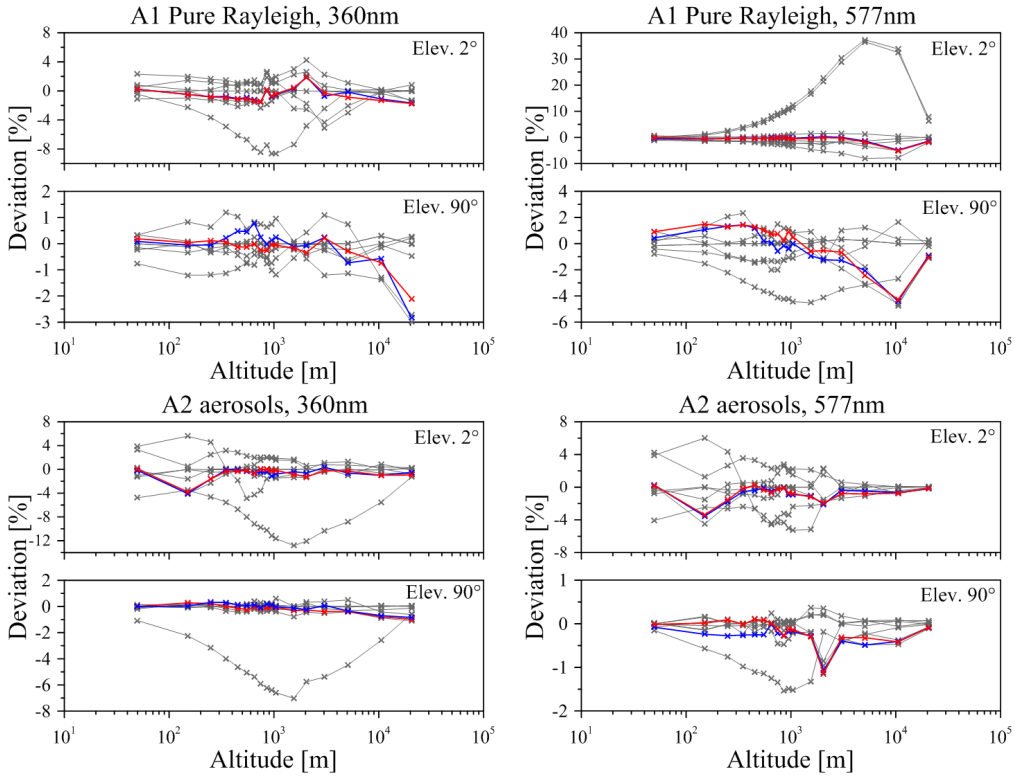

Figure 4.12: Percentage deviations in box–AMFs from multi–model means for 360 nm and 577 nm at SZA 20° in a model atmosphere with pure Rayleigh scattering and ozone absorption (top panels) and with an aerosol layer of 0.5 km^{-1} from the ground up to 2 km (A2, bottom panels). Only the 2° and 90° elevation angles are shown, but the deviations are similar for the other elevation angles. NIMO is displayed in red, the NIMO short path segment test in blue, and the other models in grey.

4.5.3 Variation of relative azimuth angle

Since the probability that a photon will scatter into the telescope is related to the phase function of the scattering species, the relative azimuth angle between the viewing direction and the Sun has a major influence on the observed radiance, but less influence on multiple–scattered photons than on single–scattered photons. The Rayleigh scattering phase function has maxima at 0° and 180° and a minimum at 90° (and 270°), which leads to the strong dependence of radiance on relative azimuth angle seen for 577 nm in Fig. 4.13). The minimum is more pronounced at 577 nm than at 360 nm because a greater proportion of the photons are single–scattered. Multiple–scattering tends to equalize the radiance from diffuse light in all directions and for this reason the azimuthal dependence of the normalised radiance along with absorption by O_4 can be used to retrieve information on the aerosol profile (Wagner et al., 2004; Wittrock et al., 2004; Frieß et al., 2006). The aerosol scattering phase function has a strong forward peak so the radiances at small azimuth angles relative to the Sun's azimuth are higher than radiances at large relative azimuth angles, while radiances in azimuthal

directions away from the Sun are lower than the pure Rayleigh radiances. At low to moderate aerosol optical depth (A3, 0.1 km^{-1} from 0 to 1 km, asymmetry parameter of 0.68) the pronounced aerosol forward scattering increases the probability of photons being scattered into the line of sight. This leads to higher radiances near the Sun's direction relative to pure Rayleigh scattering, but high aerosol optical depths (A2) severely attenuate the light in all viewing directions due to high multiple–scattering.

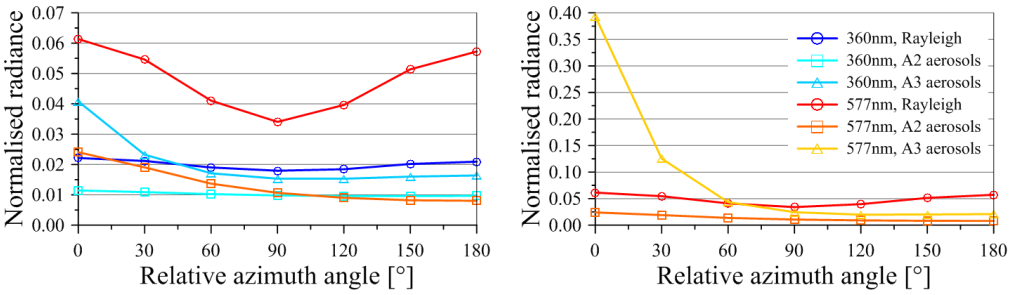

Figure 4.13: Normalised radiances as a function of relative azimuth angle at SZA 80°, a telescope elevation angle of 2°, and a surface albedo of 3% for 360 nm and 577 nm. The three aerosol scenarios are A1 (pure Rayleigh, no aerosols), A2 (high aerosol τ), and A3 (moderate aerosol τ), an aerosol layer of 0.1 km^{-1} from 0 to 1 km altitude. The 577 nm A3 aerosol case is shown separately in the right–hand plot since the radiances in the forward direction are much higher than for the other scenarios.

The results are within the range of variability of other models, though they are at the high end of the range (Fig. 4.14). The Monte Carlo simulation of the scattering species and the free path length is a critical factor in determining the radiances, especially when there is more than one scattering species, and it is important to deal with the probabilities correctly (see Sects. 4.2.1, 4.2.5, 4.2.6 and 4.2.7). However, to uncover the reasons for variations among models would take considerable effort as they can involve not only the way the physics is dealt with, but also errors in coding.

For all three aerosol scenarios at 360 nm and for the pure Rayleigh (A1) and high optical depth aerosol case (A2) at 577 nm, the relative azimuth angle does not significantly influence the box–AMFs (Fig. 4.15). The reason for this is that the Rayleigh optical depth at 360 nm and the aerosol optical depth for A2 are both high, so most photons are scattered close to the surface irrespective of relative azimuth angle. However, at 577 nm for the moderate aerosol case (A3, 0.1 km^{-1}, from 0 to 1 km) the box–AMFs are higher in the backward viewing direction than the forward direction. This is because the Rayleigh optical depth is low and in the forward direction most of the photons penetrate the aerosol layer at the SZA and then scatter off aerosols into the line of sight close to the ground, so the box–AMF is close to $1/\cos 80°$. In contrast, the probability of backscattering by aerosols is lower so in the backwards viewing direction a higher proportion of photons are scattered into the telescope from higher altitudes, further from the instrument, and thus traverse the lower layers at the viewing elevation angle.

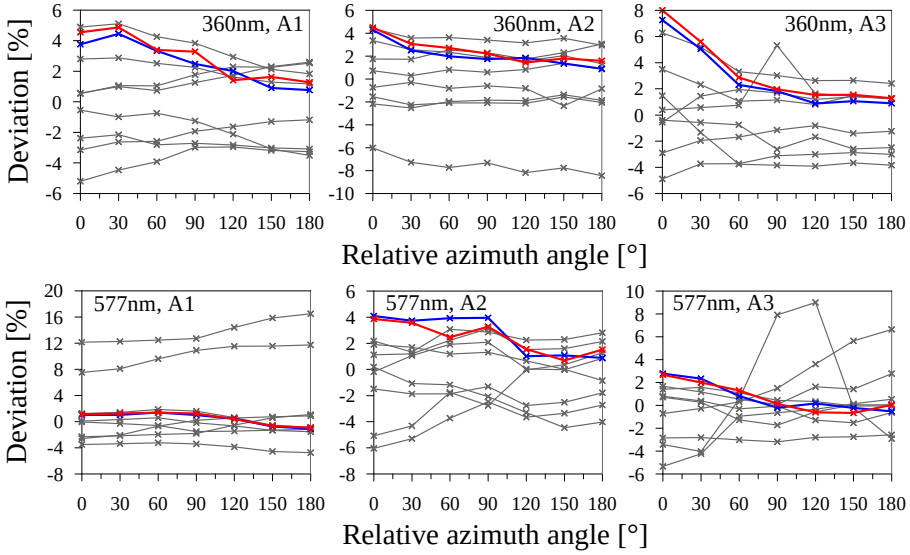

Figure 4.14: Percentage deviations of normalised radiances from the multi–model medians as a function of relative azimuth angle at SZA 80° and telescope elevation angle 2° for 360 nm (top) and 577 nm (bottom). The three aerosol scenarios are A1 (pure Rayleigh), A2 (high aerosol τ), and A3 (moderate aerosol τ). NIMO is displayed in red, the NIMO short path segment test in blue, and the other models in grey.

Again, NIMO shows good agreement with the other models with less than 3% deviation from the multi–model medians (Fig. 4.16).

4.5.4 The effect of high surface albedo

When a high proportion of the observed photons are scattered more than once, a high surface albedo can strongly enhance the radiance by reflecting photons rather than absorbing them. In contrast, for low optical depths when most of the observed photons are single–scattered the probability of photons being scattered into the line of sight after a ground reflection is very low. The exercise in Sect. 4.5.3 was repeated using a surface albedo of 80%, typical of fresh snow, instead of 3%. The radiances at 360 nm were nearly doubled by increasing the albedo from 3% to 80% with pure Rayleigh scattering, and nearly tripled when the optically thick aerosol layer (A2) was included (Fig. 4.17, left–hand plot). Multiple–scattering by moderate aerosols also enhances the effect of the higher surface albedo at most relative azimuth angles, but close to the azimuthal direction of the Sun the strong aerosol forward scattering peak reduces the probability of photons getting scattered into the telescope line of sight following a Lambertian reflection, relative to the more isotropic Rayleigh scattering. The enhancement in radiance by the increased surface albedo is much less at 577 nm since a higher proportion of photons are single–scattered (Fig. 4.17, right–hand plot).

The radiances are within the range of variability of the other models and, as for the 3% albedo case, they are close to the high end of the range (Fig. 4.18).

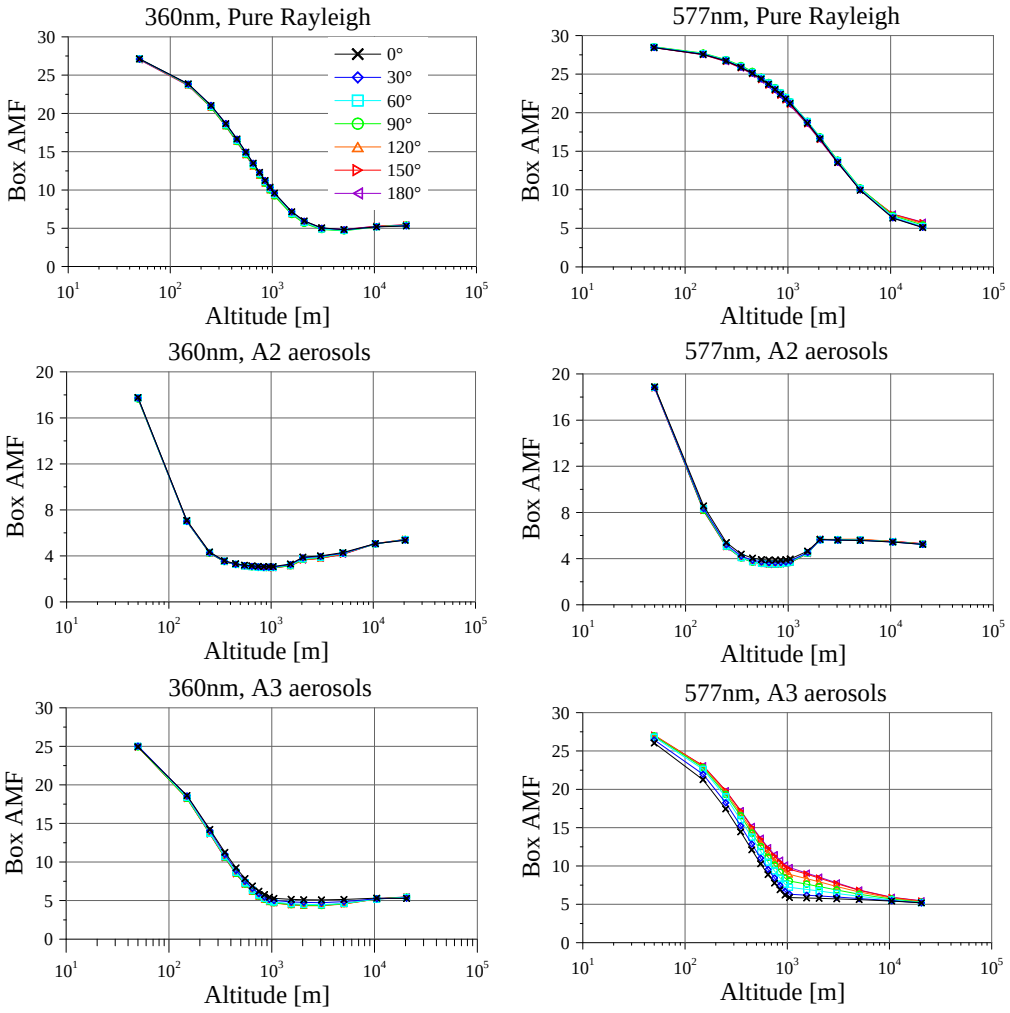

Figure 4.15: Box–AMFs for the two wavelengths (360 nm and 577 nm) and three aerosol cases (A1, A2 and A3) as a function of relative azimuth angle at SZA 80° with a telescope elevation angle of 2° and a surface albedo of 3%.

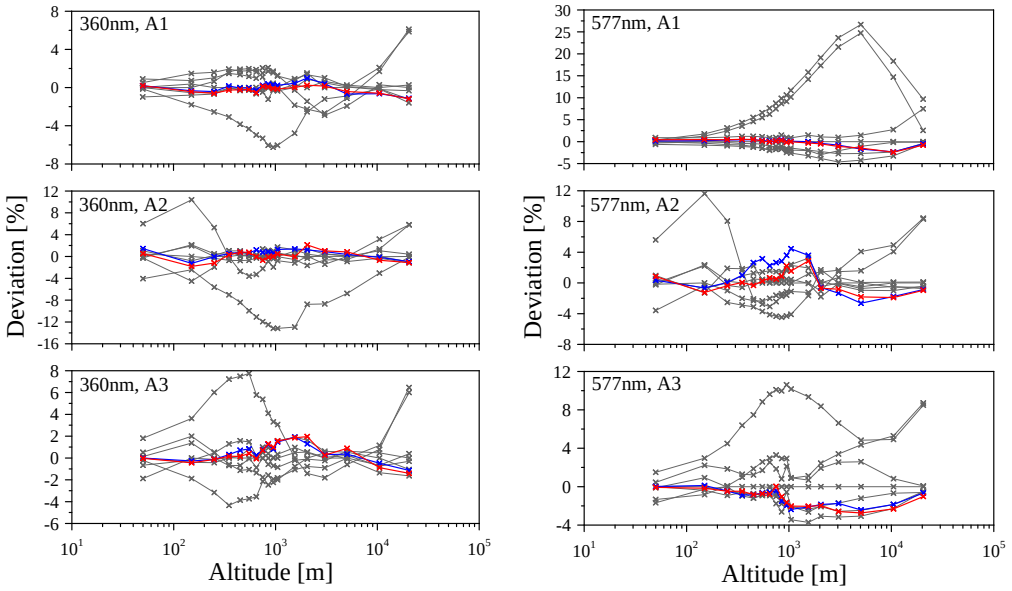

Figure 4.16: Percentage deviations in box–AMFs from the multi–model means for the two wavelengths (360 nm and 577 nm) and three aerosol cases (A1, A2 and A3) as a function of relative azimuth angle at SZA 80° and a telescope elevation angle of 2°. NIMO is displayed in red, the NIMO short path segment test in blue, and the other models in grey.

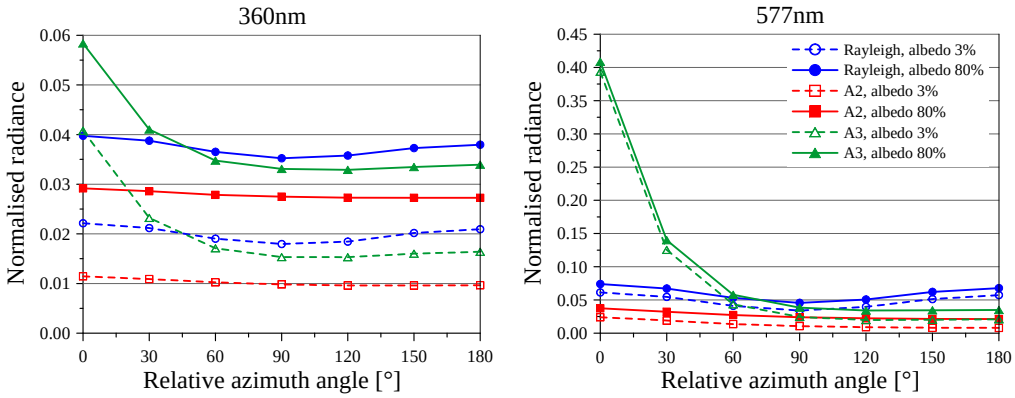

Figure 4.17: Comparison of radiances as a function of relative azimuth angle for surface albedos of 80% and 3%, SZA 80°, a viewing elevation of 2°, wavelengths of 360 nm and 577 nm, and the three aerosol scenarios, A1 (pure Rayleigh), A2 (high aerosol τ) and A3 (moderate aerosol τ).

The comparison with the short path segment simulation was not done for this exercise.

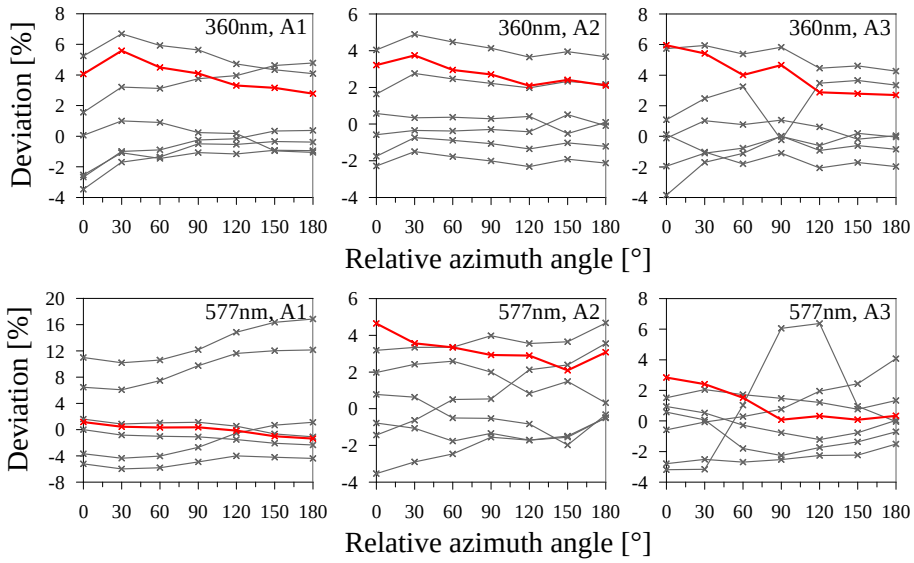

Figure 4.18: Percentage deviations in normalised radiances from multi–model medians as a function of relative azimuth angle for a surface albedo of 80%, SZA 80°, a viewing elevation of 2°, wavelengths of 360 nm and 577 nm, and the three aerosol scenarios, A1 (pure Rayleigh), A2 (high aerosol τ) and A3 (moderate aerosol τ). NIMO is displayed in red and the other models in grey. Note that the short path segment simulation was not done for this exercise.

Photon trajectories in layers near the ground can also be considerably lengthened by the increase in multiple scattering from surface reflection, significantly increasing the box–AMFs (Fig. 4.19). When aerosols are present, a large fraction of the observed radiance in the direction of the Sun comes from the strong forward scattering peak, especially at 577 nm where the Rayleigh optical depth is low, and so increasing the surface albedo has a relatively small influence on the box–AMFs. However, for azimuth angles away from the Sun the probability of Rayleigh scattering into the line of sight is higher than aerosol scattering so a greater fraction of the observed photons have undergone Lambertian reflection and box–AMFs are thus increased.

Fig. 4.20 shows the influence of the high surface albedo on the relative azimuth dependence of box–AMFs for 577 nm. In the pure Rayleigh atmosphere the effect is small, but in the moderate aerosol layer (A3), the increased albedo leads to greater relative azimuth dependence of the box–AMFs in the lowest layers (compare with Fig. 4.15).

The variability of the results from the different RTMs is similar to the albedo 3% case shown in Sect. 4.5.3, though not all the groups participated in this exercise (Fig. 4.21).

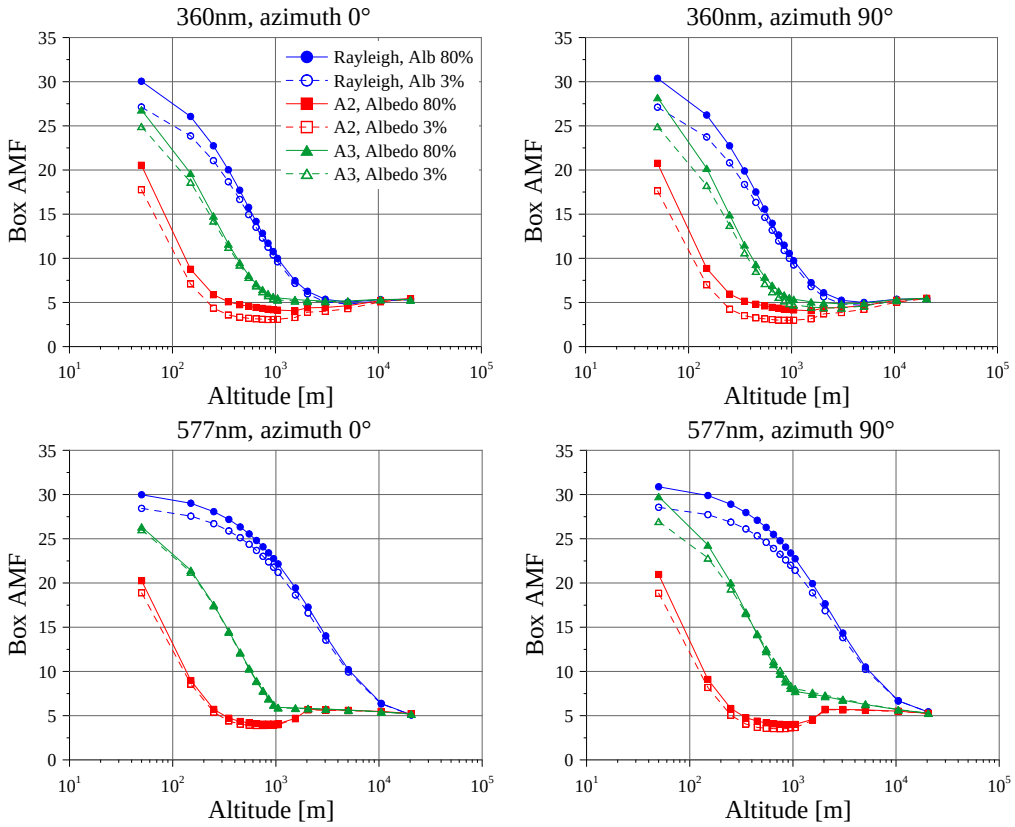

Figure 4.19: Comparison of box–AMFs for surface albedos of 80% and 3%, SZA 80°, a viewing elevation of 2°, wavelengths of 360 nm and 577 nm, and the three aerosol scenarios, A1 (pure Rayleigh), A2 (high aerosol τ) and A3 (moderate aerosol τ). The relative azimuth of 0° (left) is shown here as it differs slightly from the other angles, while the 90° case (right) is representative of the other angles.

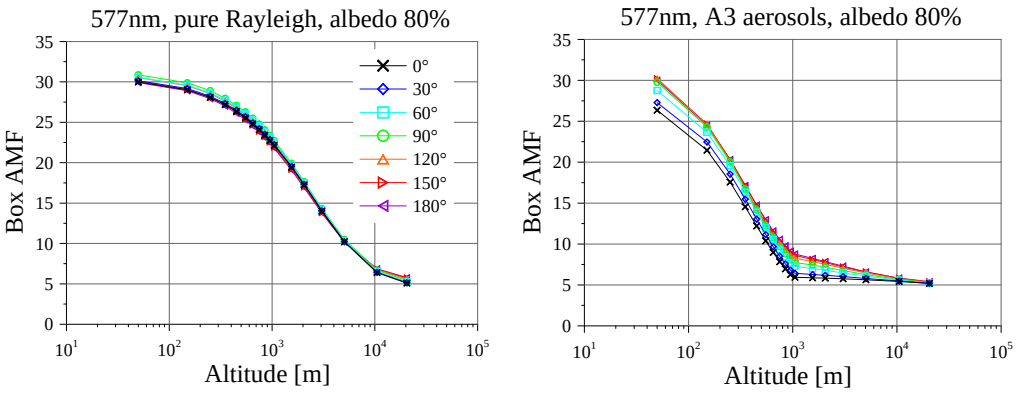

Figure 4.20: Comparison of box–AMFs at the different relative azimuth angles for surface albedos of 80% and 3%, SZA 80°, a viewing elevation of 2°, and a wavelength of 577 nm with pure Rayleigh scattering (left) and moderate aerosols (A3, right).

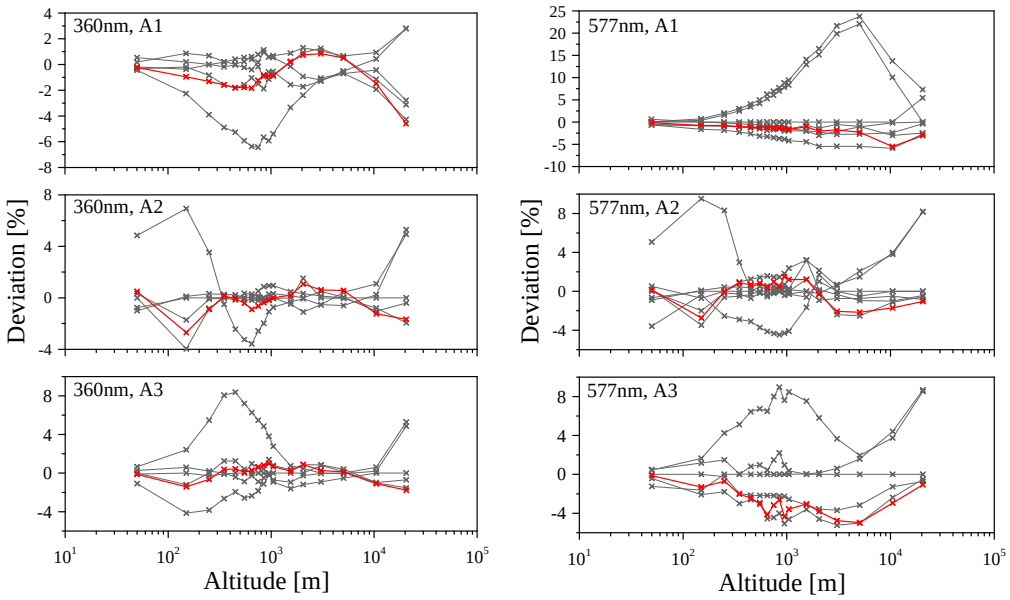

Figure 4.21: Percentage deviations of box–AMFs from the multi–model medians as a function of relative azimuth angle for surface albedos of 80% and 3%, SZA 80°, a viewing elevation of 2°, wavelengths of 360 nm and 577 nm, and the three aerosol scenarios, A1 (pure Rayleigh), A2 (high aerosol τ) and A3 (moderate aerosol τ). The deviation plots are only shown for the relative azimuth angle of 0°, but the deviations for the other angles are very similar. NIMO is displayed in red and the other models in grey. Note that the short path segment simulation was not done for this exercise.

4.5.5 The influence of the Henyey–Greenstein asymmetry parameter

The exercise in Sect. 4.5.3 was also repeated using a Henyey–Greenstein asymmetry factor of 0.75 instead of the 0.68 value previously used, giving a stronger aerosol forward scattering peak more typical of smaller particles. As expected, the normalised radiances in the 0° relative azimuth direction are enhanced, the effect is negligible for other relative azimuth angles (Fig. 4.22).

The inter–model variability is again similar to the case shown in Sect. 4.5.3, though not all the groups participated in this exercise (Fig. 4.23). The comparison with the short path segment simulation was not done for this exercise.

Fig. 4.24 compares the box–AMFs for the two different asymmetry parameters in the viewing direction towards the Sun. The stronger forward scattering peak results in a small increase in box–AMFs for the high optical depth aerosol layer (A2), but there is no effect for moderate aerosol optical depth (A3). The box–AMFs for all relative azimuth angles other than at 0° with an asymmetry parameter of 0.75 are almost identical to the results for an asymmetry parameter of 0.68, so the box–AMF plots and the percentage deviations are not shown.

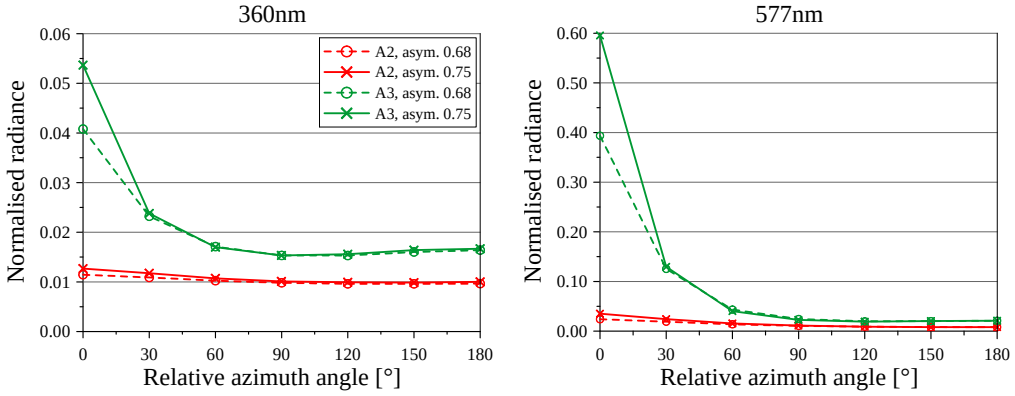

Figure 4.22: Comparison of radiances as a function of relative azimuth angle for Henyey–Greenstein asymmetry parameters of 0.68 and 0.75, SZA 80°, a viewing elevation of 2°, wavelengths of 360 nm and 577 nm, and the A2 (high aerosol τ) and A3 (moderate aerosol τ) aerosol scenarios.

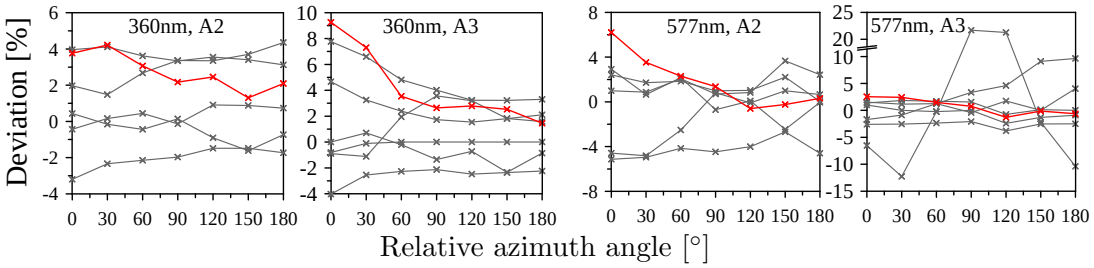

Figure 4.23: Percentage deviations of normalised radiances from the multi–model means as a function of relative azimuth angle for a Henyey–Greenstein asymmetry parameter of 0.75, SZA 80°, a viewing elevation of 2°, wavelengths of 360 nm and 577 nm, and the A2 (high aerosol τ) and A3 (moderate aerosol τ) aerosol scenarios. NIMO is displayed in red and the other models in grey. Note that the short path segment simulation was not done for this exercise.

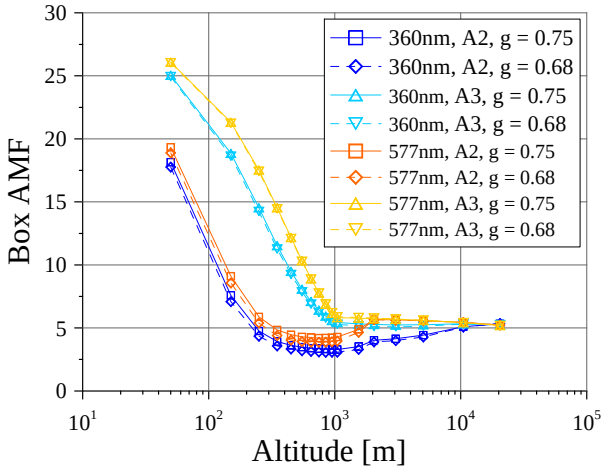

Figure 4.24: Comparison of box–AMFs with Henyey–Greenstein asymmetry parameters of 0.75 and 0.68 for the strong (A2) and moderate (A3) aerosol scenarios, at a relative azimuth angle of 0° and wavelengths of 360 nm and 577 nm.

4.6 Test of the reciprocity principle

The reciprocity principle states that every scattering and reflection event is reversible, so at a given location any change in the propagation direction $\Omega_1 \rightarrow \Omega_2$ will occur with equal probability in the opposite direction $\Omega_2 \rightarrow \Omega_1$, and the transmission functions are also unchanged when the directions are reversed. See Chandrasekhar (1950) and Marshak and Davis (2005) for detailed discussions on the formulation of the reciprocity principle. The backwards MC and adjoint simulations are based upon this assumption.

To test the reciprocity principle, a forward simulation of the Sun's parallel rays was performed by uniformly emitting photons perpendicularly downwards from a plane tangential to the TOA at the North Pole. For each photon that reached the surface, a detector was placed at that position and photons that entered the telescope field of view (FOV) were recorded. The SZA at the detector was then taken to be $90° - \Phi$, where Φ is the latitude of the ground at which the observation occurred. To increase the probability of photons scattering into the FOV, a short wavelength of 300 nm was chosen together with a wide FOV of 50° in the zenith direction, and in some simulations a FOV of 10° was used. Even with these conditions only $\sim$ 0.5% of photons entered the 50° FOV and only $\sim$ 0.02% entered the 10° FOV, so for an off–axis viewing direction with a narrow field of view, and thus a much smaller probability of catching photons, it would take several days of model runs to obtain enough photons for calculations of radiance and box–AMFs with sufficiently low variance. For the direct backward simulation, the probability of a photon exiting the atmosphere at the correct SZA is similarly low ($\sim$ 0.35% at SZA 20° and $\sim$ 0.15% at SZA 80°), though a narrow FOV does not significantly reduce the probability. In both the forward and backward directions the probabilities are increased slightly by the addition

of aerosols due to the increase in multiple scattering. The distribution of starting locations on the Sun plane for photons received by the telescope was compared to the distribution of photons hitting the plane after being fired out of the telescope and travelling in the time–reversed direction. For the backwards simulations the surface albedo was set to 0 for consistency with the forward MC model. The simulations were performed for several SZA with both pure Rayleigh scattering and with aerosol scenario A2 (see Sect. 4.5).

Fig. 4.25 summarises the results for SZAs of 20° and 80° with pure Rayleigh scattering. Similar results were obtained for other SZAs and with aerosols. The two histogram plots characterise the distribution of photons on the Sun plane, showing the number of photons (10000 in total) within each 1000 m radius concentric ring around the projection of the North Pole onto the plane, with the inner bin being the 1000 m circle enclosing the pole. The actual distribution of forwards photons emitted from the Sun plane that enter the telescope and backwards photons that start from the telescope and hit the Sun plane, is displayed on the circular plots, which has a radius of 80 km encompassing the majority of the simulated photons. The box–AMFs for the forward simulation, the direct backward simulation and the adjoint backward simulation were in agreement in all cases except for the 10° FOV case at SZA 80°, where box–AMFs calculated by the adjoint method were slightly higher between 30 km and 60 km than the other simulations. The reason for this is unknown and requires further investigation. The variance, seen as noise in the forward and direct backward simulations, is due to a sample size of only 10000 photons, which required several million starting photons. The forward and direct models would have to be run for several days to obtain enough photons for smooth results with low variance.

4.7 Surface topography

Local surface topography can have a major influence on the observed light paths and thus on the radiances and box–AMFs for MAX–DOAS measurement geometries. In general, to avoid complicating the radiative transfer, the instrument telescope is aimed in directions clear of nearby obstructions such as hills. The optical depth for the spectral region being measured should also be considered when choosing an appropriate viewing direction. However, in some cases, such as when making pollution measurements in a city or a valley, it is impossible to avoid nearby obstructions. In addition, local terrain such as mountains can affect the light paths even when the viewing direction itself is unobstructed. By including surface topography into a radiative transfer model, its effect on box–AMFs and radiances can be simulated, and this spatial information can be incorporated into trace gas and aerosol profile retrievals.

A digital elevation model (DEM) grid with a cell size of 1 km^2 was used in the simulation of coastal MAX–DOAS measurements at 350 nm, with a moderate aerosol profile, a SZA of 50°, and viewing elevation angles of $1°, 2°, 5°$ and 20°.

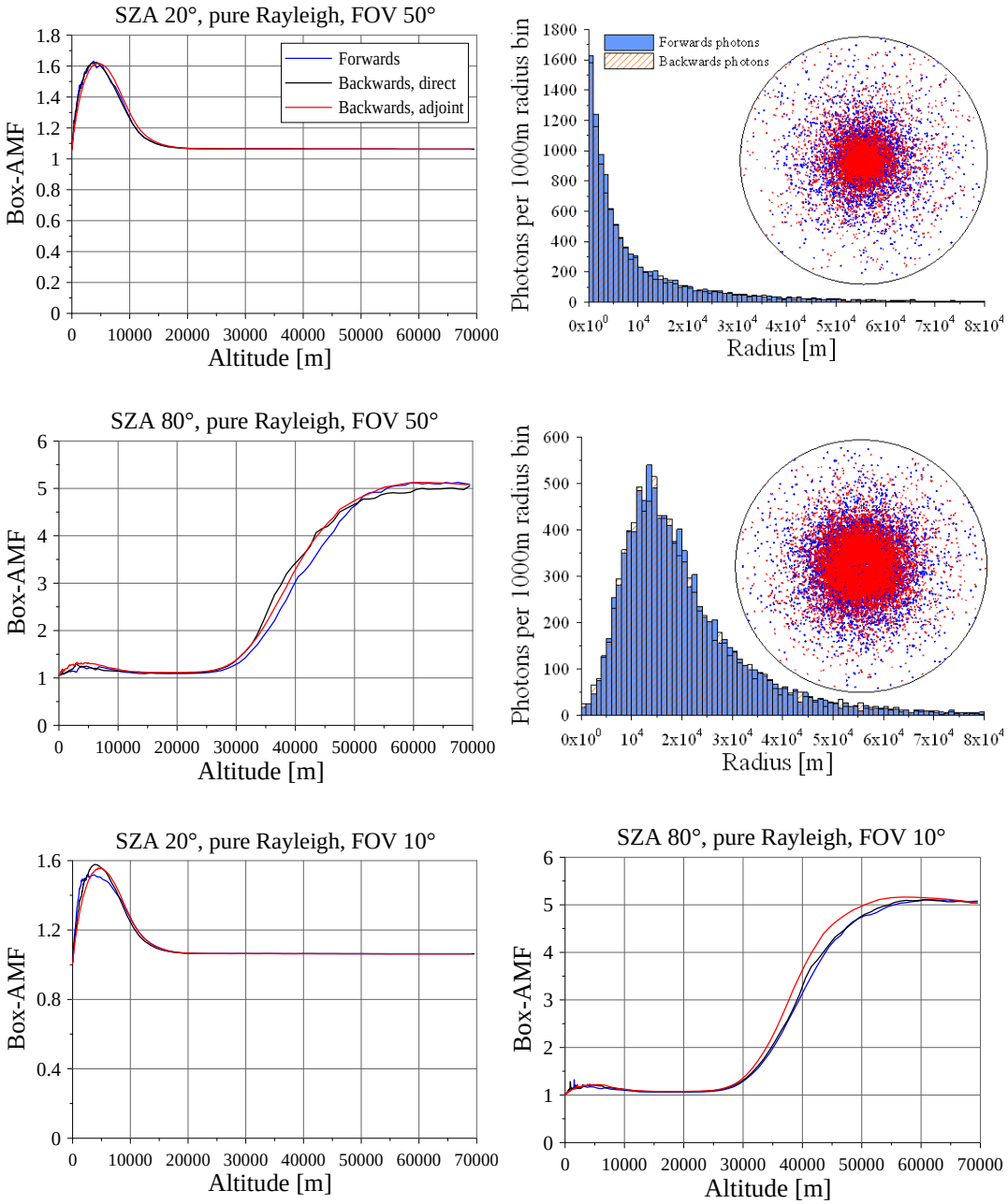

Figure 4.25: Comparison of box–AMFs calculated by the forward, the direct backwards, and the backwards adjoint simulations for a zenith viewing telescope with pure Rayleigh scattering and ozone absorption. The two top right–hand plots show the distribution of photons on the Sun plane, within a radius of 80 km from the centre, as a histogram, with the circular plots showing the actual distribution of photons leaving the plane that enter the detector (blue) and photons hitting the plane from the detector (red).

Fig. 4.26 shows the topography of the bay where the box–AMFs were simulated for two azimuthal viewing directions, one looking across the bay to a hill approximately 200 m high at about 1 km distance, and the second looking along the coast with an unobstructed horizon, both with the Sun directly behind the telescope. For the open sea the surface albedo was 7%, and for the land an albedo of 8% was used for the grass simulation and 80% to simulate fresh snow. Any photons hitting the ground at a location where the ground radius was equal to the local Earth radius at sea level were attenuated by the albedo of the sea, while photons hitting the ground at higher altitudes were assumed to be on land and their radiance weighting was attenuated accordingly by the land albedo.

Figure 4.26: Map showing the topography of the simulated measurement site (46.55° S, 169.62° E) and the two viewing azimuth directions.

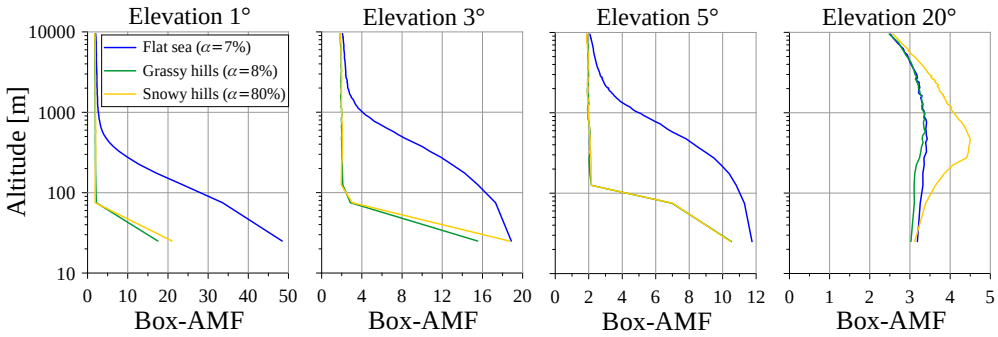

Figure 4.27: Box–AMFs at 50° SZA for four viewing elevations $(1°, 2°, 5°, 20°)$, two azimuth viewing directions (out to sea and towards a hill), and three surface albedo scenarios (sea: 7%; grassy hills: 8% for land and 7% for sea; and snow–covered hills: 80% for land and 7% for sea).

Box–AMFs for the three lowest elevation angles, which are obstructed by the nearby hill, were considerably reduced compared to the unobstructed sea view (Fig. 4.27). For the lowest altitude layer, from the surface to 50 m, the reduction in the box–AMF is small for the 3° and 5° elevation angles because even for the unobstructed view, photons travelling at those low angles only enter the lowest layer a kilometer or less away from the telescope. The higher albedo only slightly

enhances the box–AMFs for the low elevation angles since the majority of photons received in the narrow FOV of the detector after Lambertian reflection of the hill originate directly from the Sun or from scattering events higher in the atmosphere, so their trajectories through the lower layers are not enhanced. In contrast, the telescope line of sight at 20° looks above the hill so the box–AMFs are similar to the open sea view, only reduced slightly in the lowest layers because the presence of the elevated land reduces the possibility of multiple–scattered paths. With the increased surface albedo the box–AMFs for the 20° elevation over the land are significantly enhanced relative to the open sea box–AMFs since ground reflections facilitate more multiple–scattering in the layers.

4.8 Summary

A full spherical Monte Carlo RTM, NIMO, for simulating box–AMFs and radiances for MAX–DOAS measurement geometries, has been developed and is described in detail. The model uses the backwards MC adjoint simulation technique, initiating photon trajectories at the detector, simulating their trajectories to the TOA, and weighting their radiances by creating adjoint trajectories for the required SZAs and relative azimuth angles. NIMO was validated against nine other RTMs from eight international research groups using the comparison exercises presented in Wagner et al. (2007a). Box–AMFs and radiances for all tests were in agreement with the other models within the range of variability between models. The tests also demonstrate the sensitivity of MAX–DOAS measurements to the lowest atmospheric layers and to aerosols in these layers. A forward simulation of box–AMFs was compared with both the direct backwards MC and the adjoint simulations, and the results were in agreement as predicted by the reciprocity principle. Finally, surface topography was simulated in an example of the potential application of box–AMF calculations to coastal MAX–DOAS measurements.

The primary application of NIMO is the calculation of box–AMFs that are used in the calculation of weighting functions for the retrieval of trace–gas profiles from ground–based UV–visible MAX–DOAS measurements. Future development, proposed for NIMO, includes the addition of chemical enhancement for diurnally–varying species, polarization, rotational Raman scattering, Mie scattering, clouds, and a bidirectional reflectance distribution function. A useful advancement would be the modification of the adjoint calculation, as described in Marchuk et al. (1980, p. 86–95), to analytically determine weighting functions for non–linear aerosol profile retrievals. Typically, MC RTMs are too slow for the calculation of weighting functions by perturbing the aerosol extinction in each layer, thus the analytical evaluation is necessary if aerosol retrievals are to be performed within an acceptable time.

Chapter 5

Profile retrieval

Remote sensing is a cost effective way to make indirect measurements of temperature and composition of the atmosphere over large spatial scales from a single instrument located on the ground, or from a satellite or aircraft. The disadvantage of remote measurements is that the quantity being measured is often a complicated function of the quantity that is required. The inverse problem thus takes a known equation, the forward model, that expresses radiation as a function of the atmospheric state, and inverts it to obtain an expression of the atmospheric state in terms of radiation. In most cases this has no mathematically unique solution, so the most appropriate solution, consistent with the measurements, is chosen using an estimation technique. This chapter introduces the concepts of retrieval theory and optimal estimation theory that are described in detail by Rodgers (1976, 1990, 2000). An algorithm, developed in IDL (Interactive Data Language), for the retrieval of trace gas profiles from MAX–DOAS DSCD measurements is described, and the results from NO_2 profile retrievals for CINDI (Cabauw Intercomparison Campaign of Nitrogen Dioxide measuring Instruments) are presented as a validation for the retrieval algorithm.

5.1 The forward model

The inversion of DSCD measurements, to obtain information on the vertical distribution of the measured species, requires an accurate description of the physics of the measurement process. This "forward model" should include all the physics of the measurement to an accuracy that is better than the measurement. In practice, the complete physics of the measurement is not fully understood or it is so complicated that it must be approximated by the forward model $\mathbf{F}(\mathbf{x}, \mathbf{b})$, modified by the experimental error:

$$\mathbf{y} = \mathbf{F}(\mathbf{x}, \mathbf{b}) + \epsilon \tag{5.1}$$

where $\mathbf{y}$ is the vector of measurements (DSCDs) with error ϵ, $\mathbf{x}$ is the state vector containing the vertical distribution of the trace gas or aerosols being measured, and $\mathbf{b}$ are forward model parameters that influence the modelled DSCDs, but are not retrieved. Since the measurements are discrete quantities, while the vertical distribution to be retrieved, $\mathbf{x}$, is a continuous function, the problem is

formally ill–posed or underconstrained. Therefore, the state vector is discretised into a finite number of parameters depending on the resolution required and the information content of the measurement.

The forward model used for the retrieval algorithm in this work is the NIMO Monte Carlo radiative transfer model described in detail in Chap. 4. The input to the radiative transfer model includes the state profile $\mathbf{x}$, and the forward model parameters $\mathbf{b}$ such as temperature, pressure, ozone and aerosol profiles. The radiative transfer model then calculates the forward model DSCDs ($\hat{\mathbf{y}}$) and the weighting functions ($\mathbf{K}$).

5.2 The weighting function matrix

To examine the information content of a measurement, the forward model is linearised about some reference state $\mathbf{x_0}$, which can be any arbitrary, mean or retrieved state for optically thin trace gases measured by MAX–DOAS:

$$\mathbf{y} = \mathbf{F}(\mathbf{x_0}, \mathbf{b}) + \frac{\partial \mathbf{F}}{\partial \mathbf{x}}(\mathbf{x} - \mathbf{x_0}) + \frac{\partial \mathbf{F}}{\partial \mathbf{b}}(\mathbf{b} - \mathbf{b_0}) + \epsilon \tag{5.2}$$

The $m \times n$ weighting function matrix ($\mathbf{K}$) gives the sensitivity of the modelled DSCD (m) to changes in each discrete layer (n) of the state profile. The term weighting function arises historically in atmospheric remote sensing from nadir sounding of thermal emission of CO_2 (SIRS; Satellite Infrared Spectrometer), where the forward model was a weighted mean of the vertical profile of the Planck function (Wark and Fleming, 1966). It may also be called the Jacobian, since it is a matrix of derivatives, the kernel (hence $\mathbf{K}$), or the adjoint.

$$\mathbf{K} = \frac{\partial \mathbf{F}(\mathbf{x})}{\partial \mathbf{x}} \tag{5.3}$$

The matrix $\mathbf{K_b}$ is defined as the sensitivity $\partial \mathbf{F}/\partial \mathbf{b}$ of the forward model to the forward model parameters. The sensitivity of box–AMFs and consequently DSCDs to several forward model parameters, including SZA, relative azimuth angle (RAA), viewing elevation angle, aerosol extinction profile, Henyey–Greenstein asymmetry parameter and surface albedo are demonstrated in Chap. 4. A full sensitivity study of the effect of the temperature and pressure and ozone profiles on the modelled DSCDs is not presented here, but some comparisons were performed using a range of profiles for Antarctica inside and outside the ozone hole. Changes in these profiles had an effect on stratospheric box–AMFs, but the influence on MAX–DOAS DSCDs was negligible. Schofield et al. (2004) demonstrated that, for direct–sun zenith–sky retrievals using a single scattering radiative transfer model, the error contribution from uncertainties in temperature, pressure, ozone and aerosol profiles was small in comparison with the total retrieval error. For MAX–DOAS, where multiple scattering is important, uncertainty in aerosol extinction profiles can be a major source of uncertainty in the retrieved trace gas profiles (Wittrock et al., 2004; Sinreich et al., 2005).

When the derivatives cannot be determined algebraically, they are evaluated numerically by perturbing the state profile in the forward model. A method for the algebraic evaluation of derivatives in adjoint Monte Carlo radiative transfer is described in Chap. 4 of Marchuk et al. (1980), but the application is rather complicated. The algebraic method would be a useful addition to NIMO to allow the fast calculation of weighting functions necessary for non–linear optimal estimation retrievals of aerosol profiles. In the perturbation method, each element of $\mathbf{K}$ is given by

$$K_{ij} = \frac{\partial \mathbf{F_i}(\mathbf{x})}{\partial \mathbf{x_j}} = \frac{\hat{y}_{p_i} - \hat{y}_{0_i}}{\partial x_j} \tag{5.4}$$

where $\hat{y}_{0_i}$ is the unperturbed DSCD and $\hat{y}_{p_i}$ is the DSCD calculated after a perturbation ∂x_j is added to layer x_j. However, weighting functions for optically thin absorbers are linear with respect to the magnitude of the perturbations and thus can be calculated directly from the box–AMFs (see Chap. 4 for a description of the AMF and SCD calculations):

$$K_{ij} = \frac{(A_{ij} - A_{rj})\,\partial V_j}{\partial x_j} = (A_{ij} - A_{rj})\,\delta z_j \tag{5.5}$$

where A_{ij} is the box–AMF for SCD measurement i in altitude layer j, A_{rj} is the box–AMF for the reference SCD in the layer, ∂V_j is the partial VCD perturbation for the layer, and δz_j is the layer thickness. Thus, for linear retrievals of optically thin absorbers, the weighting function calculation in the radiative transfer model is very fast since perturbations are not applied. By far the most time–consuming part of the radiative transfer calculation is the determination of box–AMFs. Therefore, the weighting function matrices, calculated from the box–AMFs, are stored so that repeat retrievals can be performed at any future time using different *a priori* settings, in which case the modelled DSCDs are calculated directly for the *a priori* profile ($\mathbf{x_a}$) without reverting to the radiative transfer model:

$$\hat{\mathbf{y}}_a = \mathbf{K}\mathbf{x_a} \tag{5.6}$$

5.3 The maximum *a posteriori* solution

For a linear inversion, the sensitivity of the measurements to the state must be independent of the state and the forward model can then be described in terms of the constant $m \times n$ weighting function matrix, $\mathbf{K}$:

$$\hat{\mathbf{y}} = \mathbf{K}\mathbf{x} + \epsilon \tag{5.7}$$

Trace gases measured by MAX–DOAS are, by requirement of the technique, optically thin ($\tau \ll 1$) and so the linear maximum *a posteriori* (MAP) retrieval method can be safely applied. Optically thick absorbers and aerosols influence the radiance and hence the DSCDs in a non–linear way with respect to density, so an iterative numerical solution such as a Gauss–Newtonian method must be used (Rodgers, 2000).

Given a set of measurements $\mathbf{y}$ with their error covariance $\mathbf{S}_\epsilon$, the forward model $\mathbf{F}(\mathbf{x})$, and any available *a priori* information, the possible states $\mathbf{x}$ consistent with this information can be assigned a probability density function (PDF). The MAP optimal estimation method chooses the state that maximises the posterior conditional PDF $P(\mathbf{x}|\,\mathbf{y})$, meaning that $P(\mathbf{x}|\,\mathbf{y})d\mathbf{x}$ is the probability that $\mathbf{x}$ is in the interval $[\mathbf{x}, \mathbf{x} + d\mathbf{x}]$ for a given set of measurements $\mathbf{y}$. In contrast, the maximum likelihood (ML) solution maximises the conditional PDF $P(\mathbf{x}|\,\mathbf{y})$.

The linear maximum a posteriori solution can be written

$$\hat{\mathbf{x}} = \mathbf{x}_a + \left(\mathbf{K}^T\mathbf{S}_\epsilon^{-1}\mathbf{K} + \mathbf{S}_a^{-1}\right)^{-1}\mathbf{K}^T\mathbf{S}_\epsilon^{-1}\left(\mathbf{y} - \mathbf{K}\mathbf{x}_a\right) \quad (5.8)$$

$$= \mathbf{x}_a + \mathbf{S}_a\mathbf{K}^T\left(\mathbf{K}\mathbf{S}_a\mathbf{K}^T + \mathbf{S}_\epsilon\right)^{-1}\left(\mathbf{y} - \mathbf{K}\mathbf{x}_a\right) \quad (5.9)$$

where Eq. 5.8 is the n–form and Eq. 5.9 is the m–form, and the superscript T denotes the matrix transpose. In the n–form, the matrix to be inverted is of dimension $n \times n$ and this method is generally chosen when there are more state vector quantities to be retrieved than there are measurements. The m–form, with the inverted matrix of dimension $m \times m$, is generally chosen when there are more measurements than state vector quantities to be retrieved. For the retrievals in this work, the n–form MAP is used, since the number of state vector elements is greater than the number of measurements.

5.4 Characterisation and error analysis

Optimal estimation ideally chooses the best solution from all possible solutions that minimize the differences between the measured and modelled state vectors based on the measurements, their errors and the prior constraints. In order to understand and correctly interpret the retrieved state profile, it is important to understand how the solution is related to the true state and to understand the various sources of error that propagate into the retrieval.

5.4.1 The gain matrix

The gain matrix, or contribution function matrix, $\mathbf{G}_\mathbf{y}$, quantifies the contribution of each SCD measurement to the retrieved profile, or in other words the sensitivity of the retrieval to the measurement. It is calculated from the weighting function matrix and the measurement and *a priori* covariance matrices:

$$\mathbf{G}_y = \frac{\partial\hat{\mathbf{x}}}{\partial\mathbf{y}} = (\mathbf{K}^T\mathbf{S}_\epsilon^{-1}\mathbf{K} + \mathbf{S}_a^{-1})^{-1}\mathbf{K}^T\mathbf{S}_\epsilon^{-1} = \mathbf{S}_a\mathbf{K}^T(\mathbf{K}\mathbf{S}_a\mathbf{K}^T + \mathbf{S}_\epsilon)^{-1} \quad (5.10)$$

The second term on the right–hand side corresponds to the n–form MAP (Eq. 5.8) and the third term corresponds to the m–form (Eq. 5.9).

5.4.2 The averaging kernel matrix

The averaging kernel matrix, $\mathbf{A}$, describes the sensitivity of the retrieval to the true state and is the product of the gain and weighting function matrices:

$$\mathbf{A} = \frac{\partial \hat{\mathbf{x}}}{\partial \mathbf{x}} = \mathbf{G}_y \mathbf{K} \tag{5.11}$$

where $\hat{\mathbf{x}}$ is the retrieved state vector, in this case the vertical number density profile of the trace gas. The averaging kernel matrix has an important role in the characterization of the retrieval.

The transfer function relates the retrieval to the true state by describing the complete observing system, including the measuring instrument and the retrieval method. Linearising the forward model about an *a priori* $\mathbf{x}_a$ using the weighting function matrix, and linearising the retrieval with respect to $\mathbf{y}$ we have (Rodgers, 1990, 2000)

$$\hat{\mathbf{x}} - \mathbf{x}_a = \mathbf{R}\left[\mathbf{F}(\mathbf{x}_a, \hat{\mathbf{b}}), \hat{\mathbf{b}}, \mathbf{x}_a, \mathbf{c}\right] - \mathbf{x}_a + \mathbf{A}(\mathbf{x} - \mathbf{x}_a) + \mathbf{G}_y \epsilon_y \tag{5.12}$$

The first term on the right hand side represents the bias, which is the error that would result from a retrieval of error free measurements simulated with the forward model for the *a priori* state. The term $\hat{\mathbf{b}}$ is our best estimate of the forward model parameters and $\mathbf{c}$ is a vector of parameters, or *a priori* information used in the retrieval, that are unrelated to the measurements or forward model. The *a priori* state $\mathbf{x}_a$ represents the best knowledge we have about the atmospheric state before the measurement is made, so if the measurements are consistent with the state being exactly equal to $\mathbf{x}_a$ a well–behaved inverse method should retrieve the *a priori* giving a bias of zero.

The second term on the right hand side of Eq. 5.12 represents the smoothing of differences between the true state and the *a priori* state or linearisation point by the averaging kernel matrix. Rows of $\mathbf{A}$ are averaging kernels or smoothing functions and the retrieval $\hat{\mathbf{x}}$ at a given altitude is effectively an average of the total profile weighted by the corresponding row of $\mathbf{A}$. In an ideal retrieval, $\mathbf{A}$ would be a unit matrix, so that difference between the retrieved state and the *a priori* state at any given altitude would correspond directly to the departure of the true state from the *a priori* state. In practice, rows of $\mathbf{A}$ are generally functions with a single peak at the appropriate level, in cases where the measurements provide information to add to the *a priori* knowledge at that level, and with no significant peaks in levels where the measurements provide no reliable information.

The width of the averaging kernel peaks is a measure of the spatial resolution of the complete observing system including the measurements themselves, the forward model and the inverse method. For retrievals of ground–based MAX–DOAS DSCDs this is usually the vertical profile resolution, but it could also be applied to horizontal resolution when comparing measurements from different azimuthal viewing directions. There are various ways to define the resolution, including the full width at half maximum, which is misleading where the peaks

don't occur at the appropriate level, and the 'spread' (Backus and Gilbert, 1970; Rodgers, 2000), which tends to emphasize the negative peaks of the averaging kernels. A satisfactory measure, which is used here, is the reciprocal of the diagonal values of $\mathbf{A}$, which give the number of levels per degree of freedom for signal.

The area of an averaging kernel is a qualitative measure of the fraction of the retrieved state that comes from the measurements rather than the *a priori*. The area of an averaging kernel for a single level (or row of $\mathbf{A}$) is the sum of its elements, and is approximately unity at levels where most of the information comes from the measurements, or close to zero at levels where the retrieved state value comes from the *a priori* with no information added by the measurements. The vector of averaging kernel areas $\mathbf{Au}$, where $\mathbf{u}$ is a unit vector, can also be interpreted as the response of the retrieval to a unit perturbation in all levels of the state profile, so an ideal retrieval would have an area equal to the number of state elements.

The third term of Eq. 5.12 is called the retrieval error or retrieval noise and it is the error in the retrieval that comes from the measurement errors rather than from the inversion itself. It can be seen that, since the gain matrix $\mathbf{G}_y$ describes the contribution of each measurement to the retrieved value at each state level, the product of the gain matrix and the measurement error vector ϵ_y gives the contribution of the measurement errors to the error in the retrieval at each level.

5.4.3 Null space and row space

The state vector to be retrieved, $\mathbf{x}$, can be considered as a vector space of dimension n with each element representing a point in this state space. Similarly, $\mathbf{y}$ represents a vector space of dimension m, which can be referred to as the measurement space. The weighting function matrix $\mathbf{K}$ maps the state space onto the measurement space without including the measurement error ϵ, and the m weighting function vectors of $\mathbf{K}$ span some subspace of state space, known as the row space. The dimension of this subspace, known as the rank (p) of $\mathbf{K}$, depends on the number of linearly independent vectors and cannot be greater than m. If we construct a basis for state space with p orthogonal base vectors, there will be $n - p$ base vectors that are orthogonal to the row space and therefore do not contribute to the measurement vector. Thus, whenever $p < n$ there exists this so called null space, meaning that some elements of the state space cannot be obtained from the measurements. Singular vector decomposition can be used to find an orthogonal coordinate system or basis for $\mathbf{K}$ in order to identify the row space.

$$\mathbf{K} = \mathbf{U}\mathbf{\Lambda}\mathbf{V}^T \tag{5.13}$$

where $\mathbf{\Lambda}$ is a $p \times p$ diagonal matrix of non–zero singular values, $\mathbf{U}$ is the $m \times p$ matrix of left singular vectors describing the column space of $\mathbf{K}$, which is a subspace of measurement space, and $\mathbf{V}$ is the $n \times p$ matrix of right singular vectors that form a basis for row space. Structures in the state profile corresponding to structures

in the singular vectors can be interpreted as being retrieved independently, with a sensitivity given by the singular value.

The singular vectors of the weighting functions for a single set of simulated NO_2 measurements and their corresponding eigenvalues are shown in Figs. 5.8 and 5.9 for the 50 m and 200 m retrieval grids respectively. Further discussion on these is given in Sect. 5.6.

5.4.4 Degrees of freedom and information content

The degrees of freedom for signal (DFS) is a measure of information that describes the number of useful independent state quantities that are retrieved from a measurement. Consider the simple case of making a single direct measurement y of a scalar x with noise ϵ, where x has a prior variance of σ_a^2 and ϵ has a prior variance of σ_ϵ^2. The prior variance of y is then $\sigma_y^2 = \sigma_a^2 + \sigma_\epsilon^2$ and the best estimate of x is given by

$$\hat{x} = \frac{\sigma_\epsilon^{-2} x + \sigma_\epsilon^{-2} x_a}{\sigma_\epsilon^{-2} + \sigma_a^{-2}} = \frac{\sigma_a^2 x + \sigma_\epsilon^2 x_a}{\sigma_a^2 + \sigma_\epsilon^2} \tag{5.14}$$

Thus, if $\sigma_\epsilon^2 \ll \sigma_a^2$ then the measurement y provides one degree of freedom of information about the signal x and conversely, if $\sigma_\epsilon^2 \gg \sigma_a^2$ the measurement provides one degree of freedom information about the noise ϵ. Generalising to a vector of measurements $\mathbf{y}$ and a vector of state variables $\mathbf{x}$, the most probable state for a Gaussian distribution of state quantities is the least squares solution of

$$\chi^2 = (\mathbf{x} - \mathbf{x}_a)^T \mathbf{S}_a^{-1} (\mathbf{x} - \mathbf{x}_a) + \epsilon_y^T \mathbf{S}_{\epsilon_y}^{-1} \epsilon_y \tag{5.15}$$

with $\epsilon_y = \mathbf{y} - \mathbf{K}\mathbf{x}$. From Eq. 5.12 we have the minimum at

$$\hat{\mathbf{x}} - \mathbf{x}_a = \mathbf{G}_y(\mathbf{y} - \mathbf{K}\mathbf{x}_a) = \mathbf{G}_y\left[\mathbf{K}(\mathbf{x} - \mathbf{x}_a) + \epsilon_y\right] = \mathbf{A}(\mathbf{x} - \mathbf{x}_a) + \mathbf{G}_y \epsilon_y \tag{5.16}$$

The expected value of χ^2 at its minimum is equal to the number of measurements m, which can be separated into degrees of freedom for signal corresponding to the expected value of the first term in Eq. 5.15 with respect to the retrieved state $\hat{\mathbf{x}}$, and degrees of freedom for noise, given by the expected value of the second term. Substituting from Eqs. 5.16 and 5.10 it can be shown that the degrees of freedom for signal is given by the trace of the averaging kernel matrix $\mathbf{A}$, and thus each value on the diagonal of $\mathbf{A}$ corresponds to the degrees of freedom for signal at that retrieval point (see Rodgers (2000) for the full derivation).

Information content is defined as the factor by which the knowledge of a state quantity is increased as a result of making a measurement, and it is usually expressed as the logarithm to base two, with dimensionless units referred to as 'bits'. The Shannon information content (Shannon and Weaver, 1949), is defined in terms of the reduction in entropy of the knowledge of the state due to conducting the measurement. The information content of a measurement is thus the reduction in the logarithm of the number of possible states described by the

PDF. This is a generalization from the scalar concept of signal–to–noise ratio to a multivariate Gaussian distribution.

$$H = \frac{1}{2}\log_2|\hat{\mathbf{S}}^{-\mathbf{1}}\mathbf{S}_a| = -\frac{1}{2}\log_2|\mathbf{I}-\mathbf{A}| \tag{5.17}$$

where $\mathbf{I}$ is the identity matrix of dimension $n\times n$. The use of the determinant arises since it is equal to the product of the eigenvalues of a matrix, and the eigenvalues in turn are equivalent to the variances of independent Gaussian distributions that can be used to construct the PDF describing the knowledge of the state.

5.4.5 Error components

Measurement noise ϵ_y is usually random, unbiased, and uncorrelated between measurements, with an easily evaluated Gaussian error covariance matrix. The $m \times m$ covariance matrix $\mathbf{S}_\epsilon$ for MAX–DOAS measurement uncertainties is a diagonal matrix containing the variance in the DSCDs arising from the DOAS fitting of the measured radiances (see Chap. 3). The DOAS fitting errors are dominated by random noise and are thus assumed to be uncorrelated, so the extra–diagonal terms in $\mathbf{S}_\epsilon$ are all set to zero, although systematic fitting errors may lead to slightly correlated errors. DOAS fitting errors can overestimate the true variance in the measurements, particularly when a wide spectral fitting window is used, since the AMFs change across the fitting window and the errors need to be corrected for this slope (Johnston, 2010a, personal communication). A sensitivity test of the effect of varying the measurement errors on the retrieval is presented in Fig. 5.16 below.

The construction of the $n \times n$ *a priori* covariance matrix $\mathbf{S}_a$ is more complicated and acts, together with $\mathbf{x}_a$, as a critical tuning parameter in the retrieval (Schofield et al., 2004; Hendrick et al., 2004), as discussed in Sect. 5.4.6 below.

The total error covariance of the MAP retrieval $\hat{\mathbf{S}}$ is a combination of the *a priori* error covariance $\mathbf{S}_a$ and the measurement error covariance $\mathbf{S}_\epsilon$ weighted by the weighting function matrix $\mathbf{K}$:

$$\hat{\mathbf{S}} = (\mathbf{K}^T\mathbf{S}_\epsilon^{-1}\mathbf{K} + \mathbf{S}_a^{-1})^{-1} \tag{5.18}$$

$$= \mathbf{S}_a - \mathbf{S}_a\mathbf{K}^T(\mathbf{K}\mathbf{S}_a\mathbf{K}^T + \mathbf{S}_\epsilon)^{-1}\mathbf{K}\mathbf{S}_a \tag{5.19}$$

where Eq. 5.18 relates to the n–form MAP solution and Eq. 5.18 relates to the m–form. The total retrieval error covariance is the sum of the smoothing error covariance $\mathbf{S}_s$, the retrieval noise covariance $\mathbf{S}_m$ and the forward model parameter error covariance $\mathbf{S}_f$.

The covariance of smoothing error for an ensemble of states about a mean state is given by

$$(\mathbf{A}-\mathbf{I})\mathbf{S}_e(\mathbf{A}-\mathbf{I})^T \tag{5.20}$$

where $\mathbf{I}$ is a unit matrix and $\mathbf{S}_e$ is the covariance of the ensemble of states about the mean state. To estimate the smoothing error covariance contribution to the

total retrieval error, the *a priori* covariance must represent the covariance of a real ensemble of states, so $\mathbf{S}_a$ can be substituted for $\mathbf{S}_e$ in Eq. 5.20. Otherwise, it is better to regard the retrieval as an estimate of a state smoothed by the averaging kernel rather than an estimate of the true state with added smoothing error (Rodgers, 2000). Since any *a priori* error covariance matrix that we can construct is likely to poorly represent the error statistics of pollution events and bromine explosion events, an evaluation of smoothing errors is not necessarily very meaningful in these retrievals. Here, $\mathbf{S}_a$ is used as a tuning parameter, making the retrieval formally non–optimal, and it is likely to overestimate the true ensemble variance in the state profile.

The retrieval noise is $\mathbf{G}_y\epsilon$ with an error covariance matrix

$$\mathbf{S}_m = \mathbf{G}_y\mathbf{S}_\epsilon\mathbf{G}_y^T \tag{5.21}$$

Another source of error in the retrieval is the forward model parameter error $\mathbf{G}_y\mathbf{K}_b(\mathbf{b} - \hat{\mathbf{b}})$, which is the error that any bias in the estimated forward model parameters produces in the retrieval. The error covariance for this error source is

$$\mathbf{S}_f = \mathbf{G}_y\mathbf{K}_b\mathbf{S}_b\mathbf{K}_b^T\mathbf{G}_y^T \tag{5.22}$$

where $\mathbf{S}_b$ is the error covariance matrix of the forward model parameters $\mathbf{b}$.

5.4.6 Constructing an appropriate *a priori*

As the state profile being retrieved is a continuous function we need to provide some prior information about the state in order solve the problem. A prior constraint is required to choose the most appropriate retrieved profile from an ensemble of continuous profiles consistent with the measurement. This is done by restricting solutions that are in the null space or near–null space of the weighting function matrix, where the measurements provide no information. The function of prior constraints in stabilizing the retrieval is referred to as regularization. The regularization term in a MAP retrieval is the inverse of the *a priori* covariance matrix $\mathbf{S}_a^{-1}$, and setting the regularization term to zero would lead to the unconstrained least squares solution, known as the maximum likelihood (ML) solution. In the MAP method, the prior constraint is an *a priori* that ideally includes a mean state from an ensemble of likely states together with the ensemble covariance, or a prior PDF of the state. However, for many atmospheric species and regions of the atmosphere there exists little prior information, or there is no meaningful ensemble mean state and covariance, as in the case of pollution events or bromine explosion events. Even if an ensemble covariance is available for such episodic events, the statistics are non–Gaussian and the MAP solution will give different results from the Gaussian case. When the PDF is asymmetric, the covariance matrix does not provide sufficient prior information and higher order moments of the PDF are required.

The MAP inversion is a weighted mean of the true state $\mathbf{x}$ and the *a priori* state $\mathbf{x}_a$, with constant weights for linear problems and weights that depend

on the state for non–linear problems. Thus, the solution depends on both the measurement and *a priori* information, and the *a priori* contribution is a source of systematic error in the retrieval. The strong dependence of the DFS on the *a priori* error covariance $\mathbf{S}_a$ was already mentioned in Sect. 5.4.4. Another problem of regularization arises when comparing retrieved profiles that have different *a priori* information, where the uncertainty or the smoothing error of the difference in the profiles due their different *a priori* information must be estimated (Rodgers and Connor, 2003). As the information content of a retrieval depends on the *a priori* information, a retrieval may be non–optimal for a particular *a priori* covariance $\mathbf{S}_a$ and can even contain less information.

The state vector should be retrieved on a grid fine enough that the effects of discretisation are unimportant, and usually finer than the altitude resolution of the instrument (Rodgers, 2000; von Clarmann et al., 2003). Looking at the weighting functions and the structure of their leading singular vectors for a range of grid heights can be used to select an appropriate grid height. The finer the vertical grid, the greater the accuracy, but for speed and efficiency we want to use the least number of levels possible without a significant loss in accuracy or information. In the NO_2 retrievals presented below, two prescribed retrieval grid layer heights (50 m and 200 m) were used for comparison. Since the source of NO_2 pollution is at the surface and the highest NO_2 levels are usually found at or near the ground, $\mathbf{x}_a$ is assigned a maximum value at the surface, decreasing to a minimum at the maximum retrieval altitude.

Since no meaningful ensemble covariance is available, the retrieval is formally non–optimal and $\mathbf{S}_a$ is instead used as a tuning parameter. In this study, the variances on the diagonal of $\mathbf{S}_a$ are taken as the square of a percentage of the value in each level of $\mathbf{x}_a$. A lower threshold value, based on a percentage of the highest value in $\mathbf{x}_a$, is used to prevent very small or zero variances in the diagonal of $\mathbf{S}_a$. If the variances are too low then the retrieval will be biased towards $\mathbf{x}_a$ with less weight given to information from the measurements, while too loose a constraint will lead to over–interpretation of the measurements and the transposition of measurement noise into the retrieved state. Therefore, the percentage is chosen using the L–curve method described by Schofield (2003). Varying the percentage from very low to very high values and plotting the RMS of the retrieved $\hat{\mathbf{y}}$ fit to the measurements, the percentage is chosen where increasing the value further no longer leads to a major improvement in the fit. Fig. 5.14 below displays the L–curves for the retrieval of profiles from the simulated NO_2 DSCDs. As the variances depend on the values in $\mathbf{x}_a$, the appropriate percentage for the construction of $\mathbf{S}_a$ also depends on $\mathbf{x}_a$.

The diagonal elements of $\mathbf{S}_a$ are the variances of $\mathbf{x}_a$, but if the errors are correlated it is important to account for the covariances in the extra–diagonal elements of $\mathbf{S}_a$ as they add information, which can reduce the uncertainty in the knowledge of the state. Gaussian correlation functions are used to account for correlations between trace gas concentrations at different altitudes (Hendrick et al., 2004;

Barret et al., 2003).

$$\mathbf{S}_{a\,ij} = \sqrt{\mathbf{S}_{a\,ii}\mathbf{S}_{a\,jj}\exp\left(-\ln(2)((z_i - z_j)/\gamma)^2\right)} \tag{5.23}$$

where γ is the half width at half maximum of the Gaussian function, or half the correlation length, and z_i and z_j are the altitudes of grid levels i and j respectively. To keep the matrix well–conditioned, values of $\mathbf{S}_{a\,ij}$ smaller than 10^{-5} times the mean of $\mathbf{S}_{a\,ii}$ and $\mathbf{S}_{a\,jj}$ are set to zero. In the same way that the variances on the diagonal of $\mathbf{S}_a$ are optimized using the L–curve method, the correlation lengths can be chosen to optimize the information retrieved from the measurements (Hendrick et al., 2004). The effect of correlation length on the DFS of retrieved profiles and RMS fit of retrieved $\hat{\mathbf{y}}$ are displayed for the NO_2 simulation retrieval in Fig. 5.15 below.

5.5 The retrieval algorithm structure

The retrieval algorithm, summarised in Fig. 5.1, is written in IDL. It includes both forms of the linear MAP inversion as well as the non–linear Gauss–Newton iterative method, but in this work only the linear MAP inversion is used for trace gas profile retrievals. Measurement files containing SCDs or DSCDs in various formats can be read by the program. After creating the $\mathbf{S}_\epsilon$ and $\mathbf{S}_a$ arrays, $\mathbf{x}_a$, the geometries for $\mathbf{y}$, and any variable forward model parameters $\mathbf{b}$, are passed to the NIMO radiative transfer model (RTM). When the forward model parameters $\mathbf{b}$ are constant for a complete day or set of measurements, the RTM calculates $\hat{\mathbf{y}}$ and $\mathbf{K}$ for the entire period at once using multiple backward adjoint simulations for each Monte Carlo simulated photon path (see Chap. 4). However, when for example the aerosol extinction profiles change throughout the measurement period, NIMO must calculate $\hat{\mathbf{y}}$ and $\mathbf{K}$ for one retrieval interval at a time. The retrieval interval can be either a time interval, in which case all the measurements available within the interval are used in the retrieval, or it can be defined by a single scan or multiple scans of viewing elevation angles. The latter retrieval interval selection method is useful when instrumental inconsistencies result in incomplete scan sequences within a given time interval. The linear MAP inversion calculation (Eq. 5.8) is then performed and the results are saved to a file containing the profiles ($\hat{\mathbf{x}}$) with retrieval errors ($\hat{\mathbf{S}}$), plus files containing $\mathbf{A}$, $\mathbf{G}_y$, $\hat{\mathbf{y}}$, $\mathbf{H}$, and the fitting errors. Singular vector decomposition is used to perform matrix pseudo–inversions and to remove noise. For the retrievals in this work, the maximum permitted condition for the singular values was set to 5×10^4, and singular vectors with smaller singular values were set to zero. The final $\hat{\mathbf{y}}$ is calculated from $\mathbf{K}\hat{\mathbf{x}}$ in the linear retrieval, or by calculating $\hat{\mathbf{y}}$ for $\hat{\mathbf{x}}$ using the RTM for the non–linear retrieval. The retrieved profiles, errors and fit to the measurements are plotted at each retrieval interval.

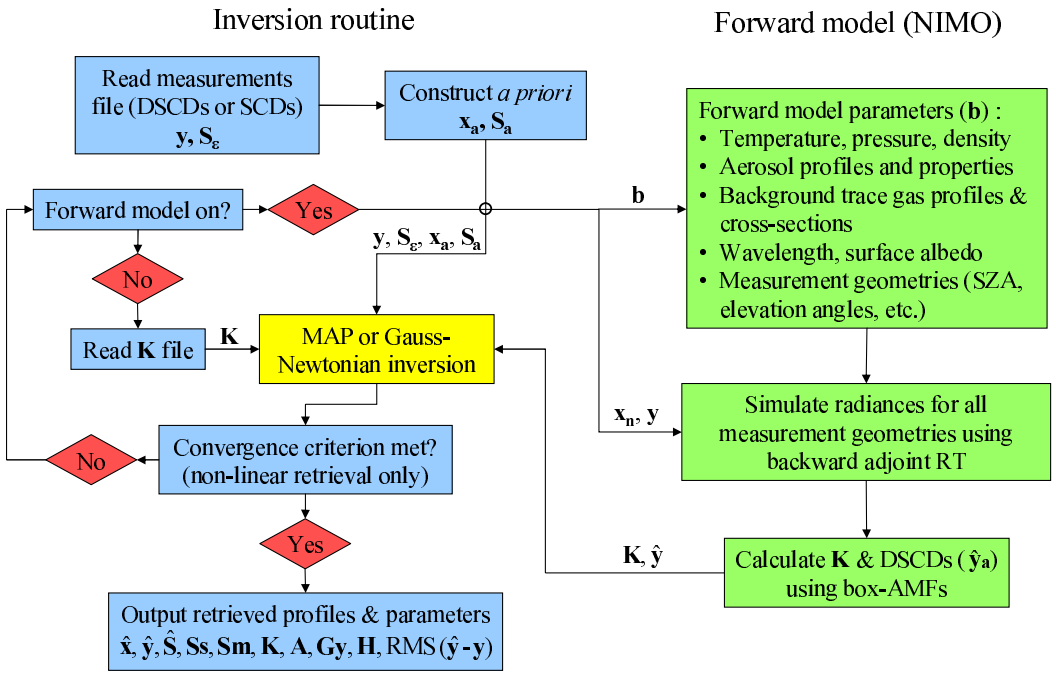

Figure 5.1: A schematic outline of the retrieval algorithm structure.

5.6 Retrieval of simulated NO_2 measurements

As part of the CINDI profiling intercomparison campaign, simulated NO_2 DSCDs for the 24th June 2009 were created by BIRA (Belgian Institute for Space Aeronomy) from eight prescribed NO_2 profiles using the LIDORT (Spurr, 2008) discrete ordinates RT model. Ten elevation angles were used; $1°, 2°, 4°, 5°, 6°, 8°, 10°, 15°$, and $30°$ with a reference angle of $89°$ (as the observation tower at Cabauw in the Netherlands obstructs the $90°$ view for some instruments). DSCD errors were based on DOAS fit errors from the BIRA UV/visible instrument with added Gaussian noise of 2×10^{14} molec cm^{-2}. Retrievals were performed in the visible (477 nm) and UV (360 nm) using a low and a high pollution aerosol profile for each wavelength, based on AERONET aerosol optical depth data (see Fig. 5.2). Temperature, pressure, and ozone profiles were based on the US Standard Atmosphere, the Lambertian surface albedo was 5% and the Henyey–Greenstein phase function was used for aerosol scattering with an asymmetry parameter of 0.67 and an aerosol single scattering albedo of 0.95. The *a priori* was constructed with a mixing ratio of 1 ppb at the surface, linearly decreasing to 0.01 ppb at 4 km. The *a priori* error for the diagonal elements of $\mathbf{S}_a$ was 100% of $\mathbf{x}_a$ at each level, with covariance in the extra–diagonal terms determined using Gaussian correlation functions. Two retrieval layer grids were used for each wavelength and aerosol case; a 200 m grid with a correlation length of 100 m and a 50 m grid with a correlation length of 25 m. The forward model SCD and weighting function calculations were performed using 50000 photons per SCD calculation for the 200 m grid retrievals and 100000 photons per SCD for the 50 m grid retrievals.

Profile retrievals were performed for every half hour interval throughout the day.

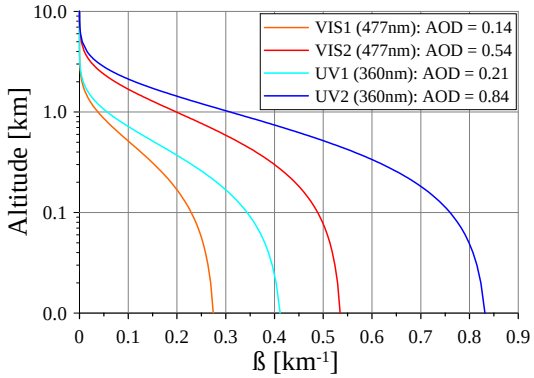

Figure 5.2: Aerosol extinction (β) profiles used in the creation of the simulated NO_2 DSCDs and in the profile retrievals.

The simulated DSCDs for prescribed profile number four with the low aerosol extinction profiles (VIS1 and UV1) at both wavelengths are shown in Fig. 5.3. Fig. 5.4 displays all the retrieved profiles for each of the eight sets of DSCDs at 477 nm for the low aerosol pollution (VIS1) case and the 50 m retrieval layer grid. The retrieved profile shape is constrained by the *a priori* profile, so the retrieved profiles show good agreement with true profiles one, two and six, as they are similar in shape to $\mathbf{x}_a$. The NO_2 in state profile five is all below 10 m, thus since the retrieval can only return one value for each 50 m layer, it underestimates the concentration, but the retrieved partial VCD up to 50 m agrees well with the true partial VCD (see Fig. 5.6). As the NO_2 layer thickness increases (profiles three and four), the retrieved profile shape is increasingly constrained both by the decreasing $\mathbf{S}_a$ variance and by the diminishing information contained in the measurements at higher altitudes. However, the partial VCDs for the NO_2 layers again show good agreement with the true values. For profile seven, these constraints of the *a priori* and information content also bias the NO_2 peak altitude of the retrieved profile below the true peak, and the shift is even greater for the higher raised NO_2 layer of profile eight. The retrieval errors (error bars) are relatively small in the lowest layers where most of the information comes from the measurements, but quickly approach the *a priori* errors at higher levels.

Differences between the retrieved profiles at different times of the day are mostly due to the varying DSCD errors from DOAS fitting. Since a midday reference was used, the DOAS fitting errors are higher in the morning than in the early afternoon (see Fig. 5.17). This results in the retrieval giving a greater weighting to the measurements with smaller errors, thus reducing the *a priori* constraint on the retrieved profiles in the afternoon relative to the morning. Another potential source of variation in the retrieved profiles are differences in scattering due to the relative positions of the sun and the viewing direction of the instrument, combined with the characteristics of the aerosol and Rayleigh scattering phase functions. Thus, the sensitivity of the measurements to different levels of the

profile, as described by **K**, can vary throughout a day of measurements. Using simulated measurements with constant state and aerosol profiles is an ideal way to perform sensitivity tests for the complete MAX–DOAS measurement system, thus assisting in the choice of elevation angles, azimuth viewing direction and even wavelength, although the choice of wavelength is limited by the availability of strong absorption features for the species of interest and the presence of overlapping spectra of other species (see Chap. 3).

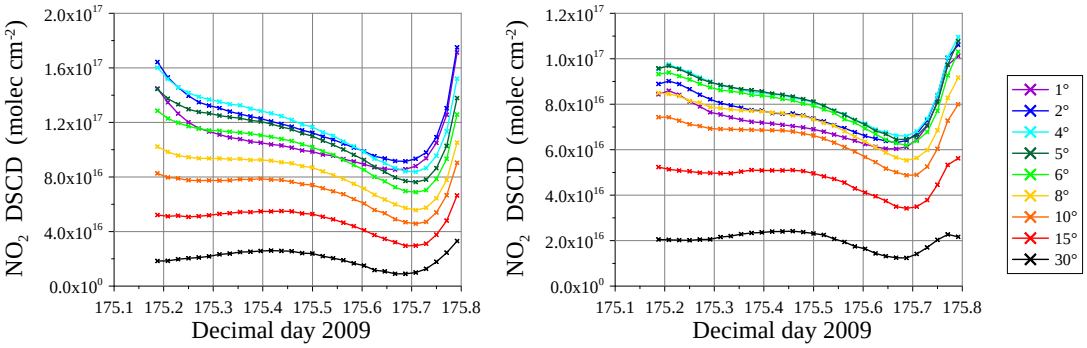

Figure 5.3: Simulated NO_2 DSCDs for profile four at 477 nm with VIS1 aerosols (left) and 360 nm with UV1 aerosols (right).

The mean retrieved profiles for each wavelength, aerosol profile and grid spacing are compared in Fig. 5.5. The greatest differences occur between the 200 m and 50 m grid retrievals, where the finer grid improves agreement for NO_2 profiles with a sharp peak near the surface, but the 200 m grid spacing performs slightly better for the thicker and raised NO_2 layers. The explanation for this is shown by the weighting functions in Fig. 5.7. The 1° and 2° elevation angle measurements provide high resolution information only for the lowest 100 m, but for higher layers the coarser grid has greater apparent sensitivity. No extra information is gained from the measurements, and in fact the DFS are slightly less for the coarser grid, as discussed in Sect. 5.4.6. However, the coarser grid in effect takes information from lower parts of each grid layer and spreads the partial VCDs from the combined finer layers over the coarser layers, which can result in an upward shift in the altitude of the retrieved profile. Also, the visual representation of the profile as a continuous line can be misleading when the profile consists of discrete values on a coarse layer grid. Other prior information about the likely profile structure, such as boundary layer heights from radiosonde measurements, could be used to select an appropriate grid spacing. Alternatively, a fine retrieval grid can be used and the partial VCDs for combined grid layers can be determined using **A** to select appropriate altitude ranges were the measurements provide sufficient information.

Profiles retrieved from the measurements in the visible region show better agreement with the true profiles than those retrieved from the UV measurements. This is because of increased multiple scattering at 360 nm, which reduces the mean free photon path lengths, resulting in reduced sensitivity of the measurements,

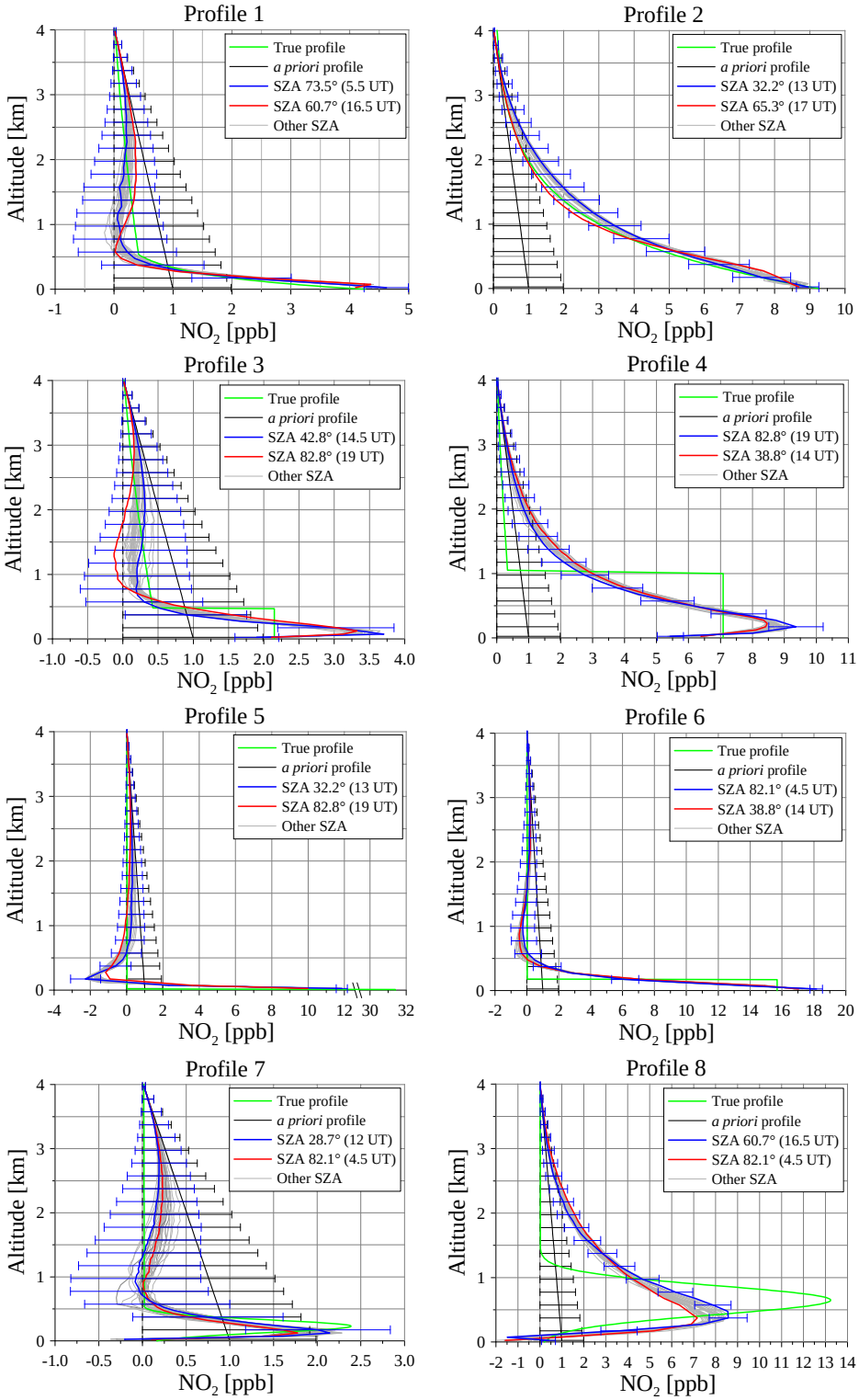

Figure 5.4: Profiles retrieved from the simulated DSCDs at 477 nm with low aerosol pollution (VIS1) and the 50 m grid. Profiles with the maximum retrieved NO_2 concentrations in the NO_2 layer are highlighted in blue and the minimum profiles are highlighted in red. Error bars are displayed for the *a priori* and maximum profiles.

especially for the low elevation angles, which look in the direction of the highest Rayleigh optical depth. The lower sensitivity at 360 nm is clearly illustrated by the weighting functions in Fig. 5.7. As a consequence, the signal–to–noise ratio is also lower at the shorter wavelength and the information contribution to the retrieval from the measurements is reduced. Increased multiple scattering can also explain the differences in the retrieved profiles for the higher aerosol extinction cases (VIS2 and UV2).

The retrieved partial VCDs, displayed in Fig. 5.6, show good agreement with the true partial VCDs in most cases, demonstrating that partial VCDs are a more reliable retrieval product than the profile shape. The partial VCDs in some layers of profiles five to eight are negative as a result of the inversion finding the solution with the best fit of the forward model DSCDs ($\hat{\mathbf{y}}$) to the measurements, limited by the row space of $\mathbf{K}$ and constrained only by the *a priori*. In Fig. 5.6, only the layers with positive VCDs are shown in order to directly compare the partial VCDs for those layers with the true VCDs. However, the retrieved total VCDs should also include the negative partial VCDs and not including them leads to a positive bias. The total VCDs that would result from the inclusion of the negative partial VCDs are indicated by the horizontal lines near the top of profiles five to eight (profiles one to four do not contain negative partial VCDs).

Weighting functions describe the sensitivity of the measurements to changes in the state. Fig. 5.7 shows weighting functions for early morning, midday and near sunset for the two wavelengths and low aerosol pollution. The advantage of MAX–DOAS measurements is that the box–AMFs, and therefore the weighting functions, for the troposphere generally show only a weak dependence on SZA and RAA (relative azimuth angle between the viewing direction and the sun). Thus, in contrast to zenith sky or direct sun DOAS, the sensitivity of MAX–DOAS changes very little throughout a day. In the case of the simulated NO_2 DSCDs, the weighting functions for the lowest viewing elevation angles increase with RAA due to the forward scattering peak of the aerosol phase function and they also increase towards high SZAs (see Chap. 4). In contrast, the weighting functions for high elevation angles decrease towards high SZA as a greater proportion of photons scatter above the retrieval altitude range. Also, for optically thin absorbers the weighting functions are linear, so they are independent of the absorber concentration.

The singular vectors, forming an orthogonal basis of the weighting functions for one scan sequence of nine elevation angles, are displayed in Fig. 5.8 for the 200 m retrieval grid and in Fig. 5.9 for the 50 m grid. In each case, there are nine right singular vectors corresponding to the number of measurements, but only the first four singular vectors have significant sensitivity, while the finer scale structures most likely come from noise in the radiative transfer calculations. For example, for the 200 m grid, structures described by the first basis vector are measured with a precision 3.6 times greater than the second vector, 14 times greater than the third and 840 times higher than the ninth singular vector. Nearly all the structure in the first four basis vectors is contained in the lowest one kilometer

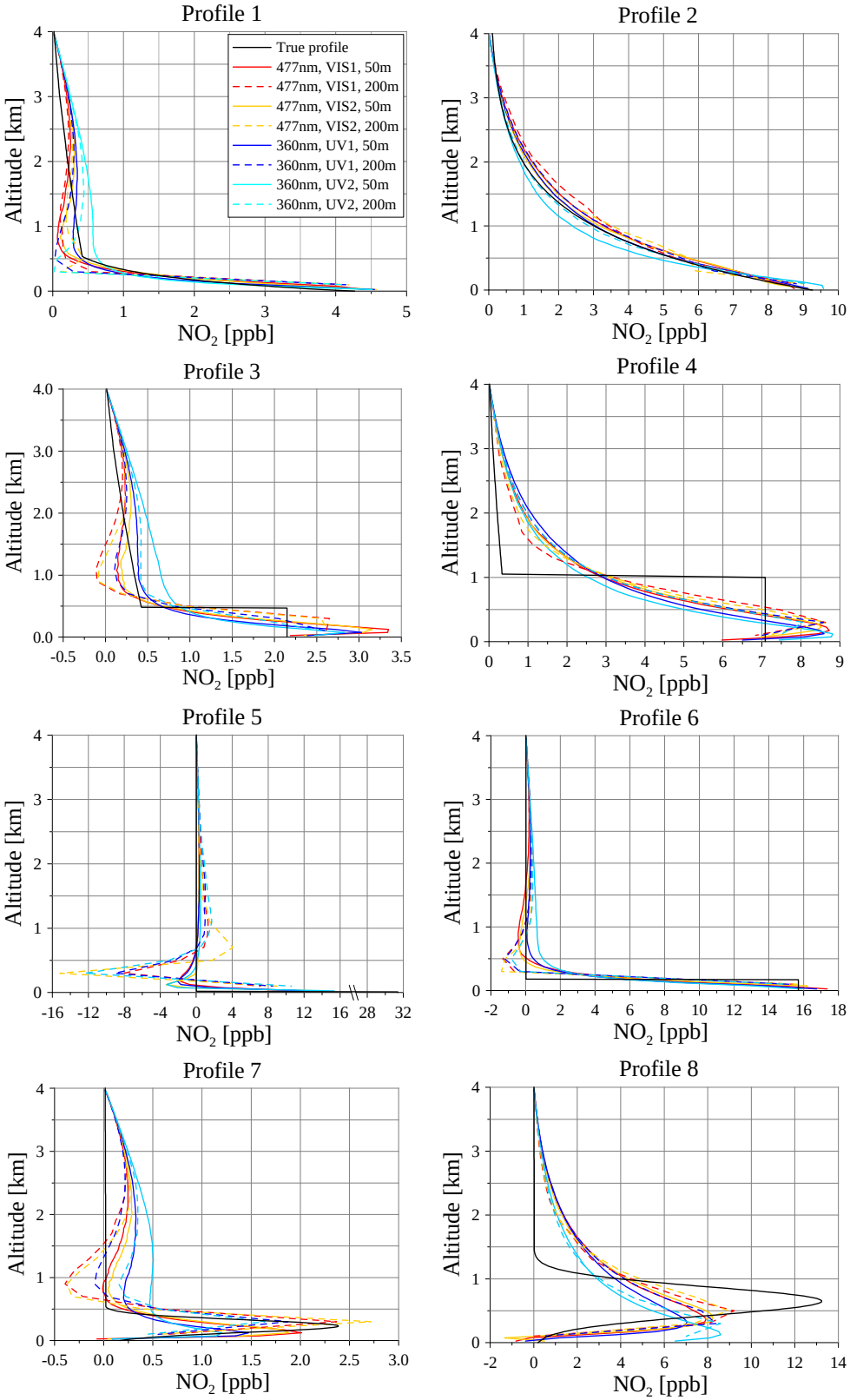

Figure 5.5: Comparison of the mean retrieved profiles from the eight retrieval situations (two wavelengths times two aerosol cases times two retrieval grid heights) for each of the eight true profiles.

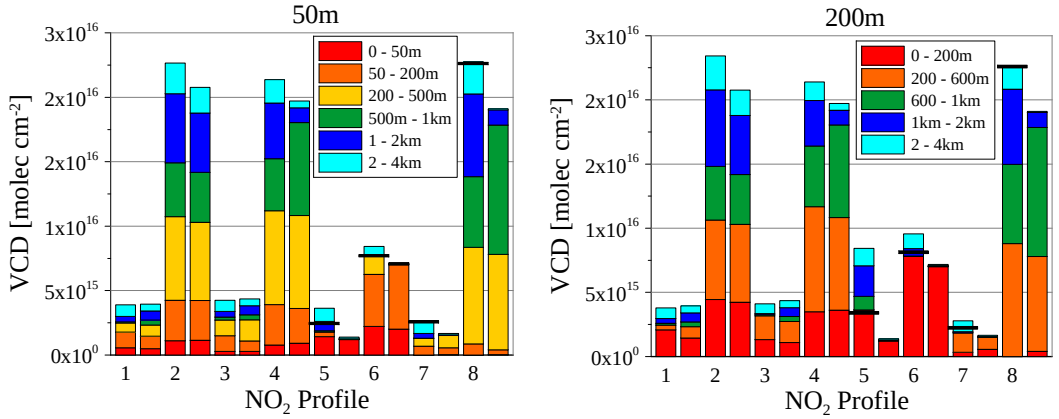

Figure 5.6: Partial VCDs for the eight prescribed profiles retrieved from the simulated DSCDs for 477 nm and VIS1 aerosols, with the 50 m grid (left) and the 200 m grid (right). For each profile the left–hand bar shows the retrieved VCDs and the right–hand bar shows the true VCDs. For ease of comparison, only layers with positive partial VCDs are shown. The horizontal lines on profiles five to eight indicate total VCDs with the negative partial VCDs included.

of the state profile. The singular vectors of $\mathbf{K}$ for an entire day (not shown) are almost identical to those for a single elevation scan sequence, since repeated scans add little extra information on the shape of the state profile, apart from the relatively minor influence of changing solar position or atmospheric conditions on the weighting functions. However, the singular values are in the range of 4 to 12 times higher than for a single elevation scan sequence, indicating increased sensitivity or precision, assuming that the state profile is unchanged throughout the measurement period as it is for these simulated measurements. For a full day, in this case 300 measurements, the maximum possible rank of $\mathbf{K}$ is equal to the number of retrieval layers n. However, only the first five singular vectors are measured with significant precision and the rest can be attributed to noise. This indicates that the row space contains only about four to five pieces of linearly independent information that can be obtained from the measurements. Even when the number of measurements are greater than or equal to the number of retrieved profile levels ($p = n$), aside from the issue of changes in the state profile over the measurement period, the sensitivity of the retrieval to the profile structure described by most of the basis vectors is very small and it can be said that these components lie in the null space of $\mathbf{K}$.

Each row of the Gain matrix $\mathbf{G}_y$ contains the contribution functions for the retrieval of one scan sequence of DSCDs, which describe the sensitivity of the retrieved profile at each level to each DSCD. The contribution functions corresponding to the same measurements as the weighting functions in Fig. 5.7 are presented in Fig. 5.10. Several observations can be made. Firstly, the contribution functions are always higher at midday than in the morning or evening. This is due to the smaller DOAS fitting errors in the middle of the day (see Fig. 5.17), so the retrieval gives more importance to these measurements and less weighting to

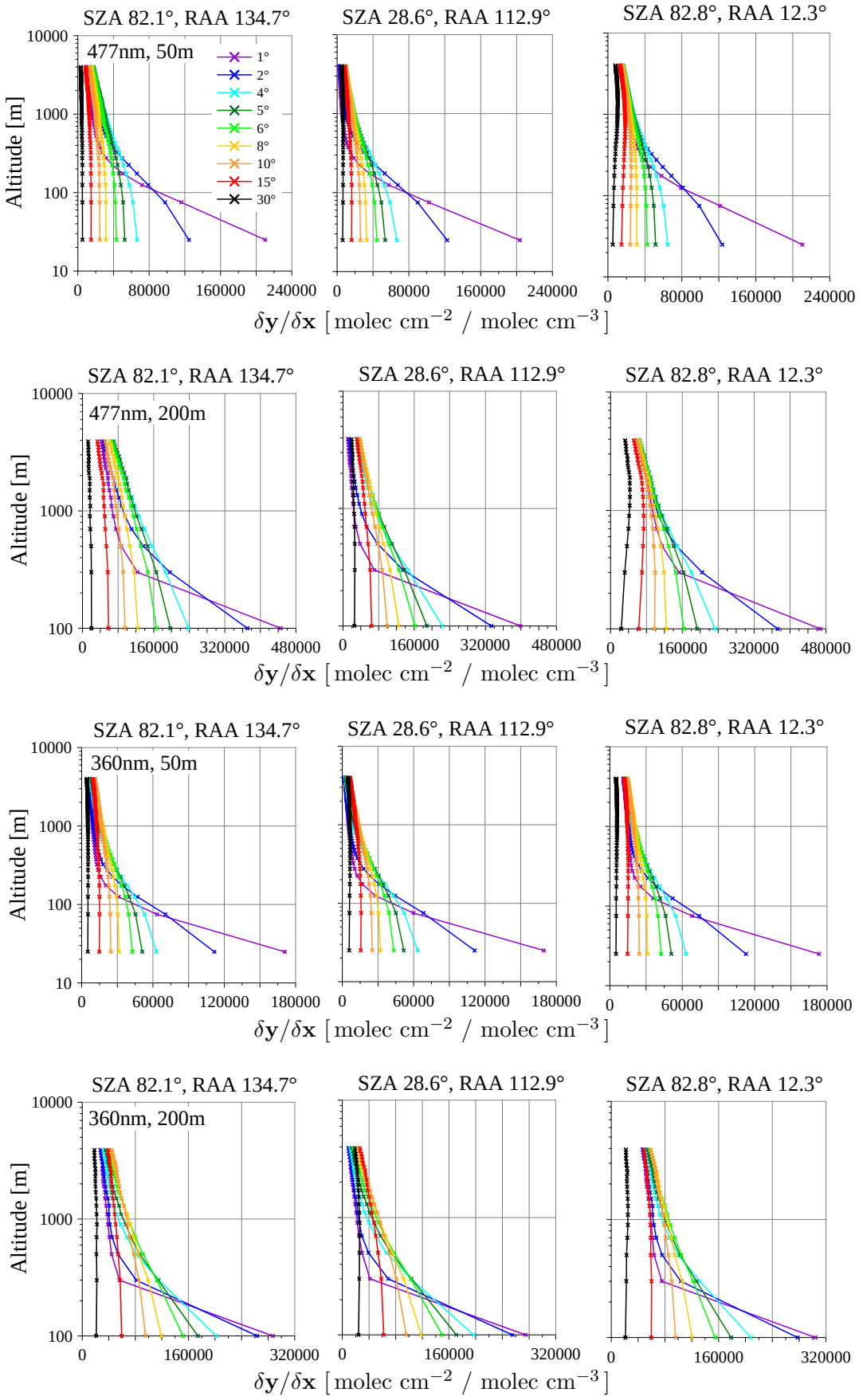

Figure 5.7: Weighting functions for three sun positions (early morning, midday and close to sunset) at 477 nm and 360 nm with the low optical depth aerosol profiles (VIS1 and UV1) and the 50 m and 200 m retrieval grids.

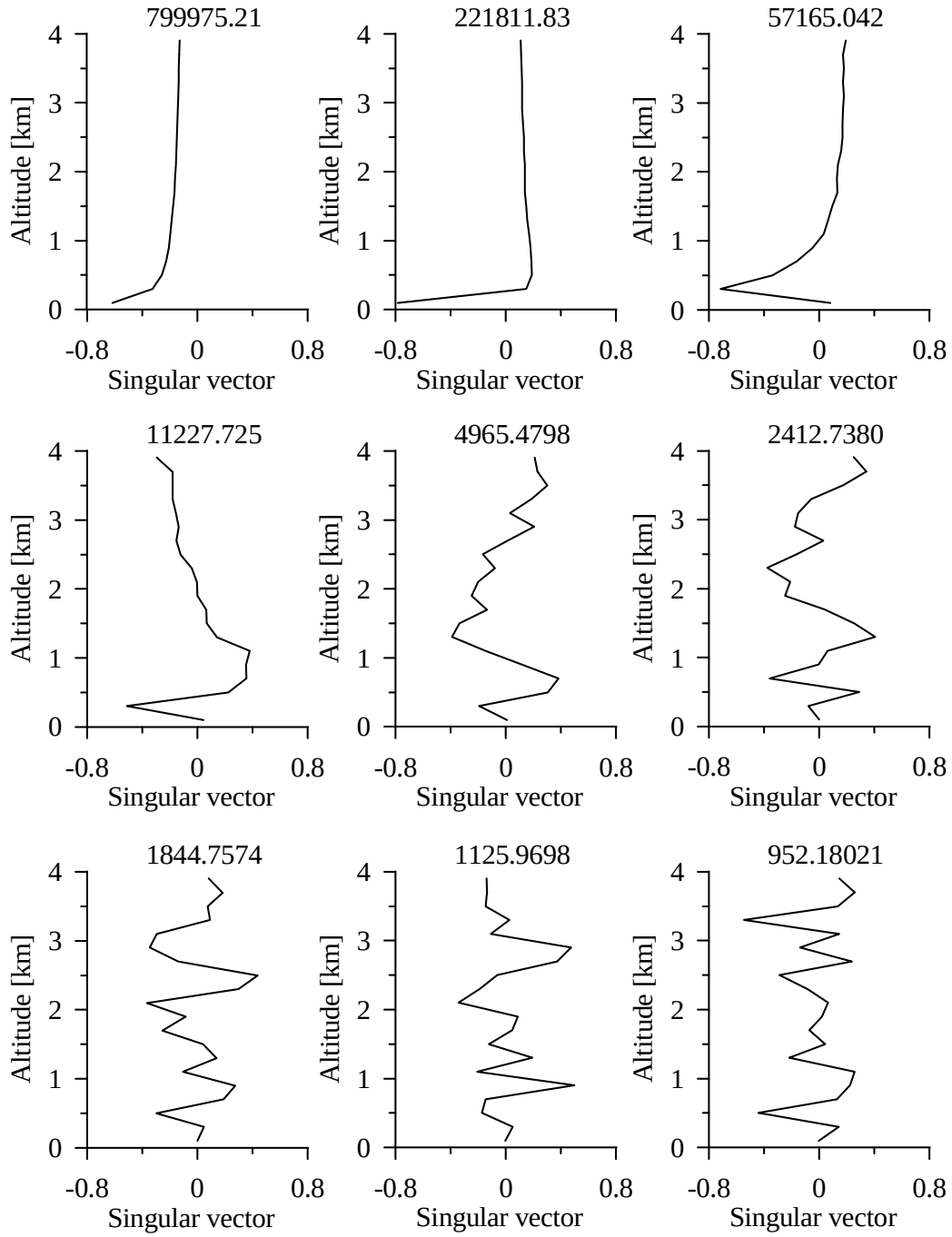

Figure 5.8: Singular vectors of the weighting functions of one set of viewing elevations at 477 nm with 200 m retrieval layers. The corresponding singular values are given above each plot.

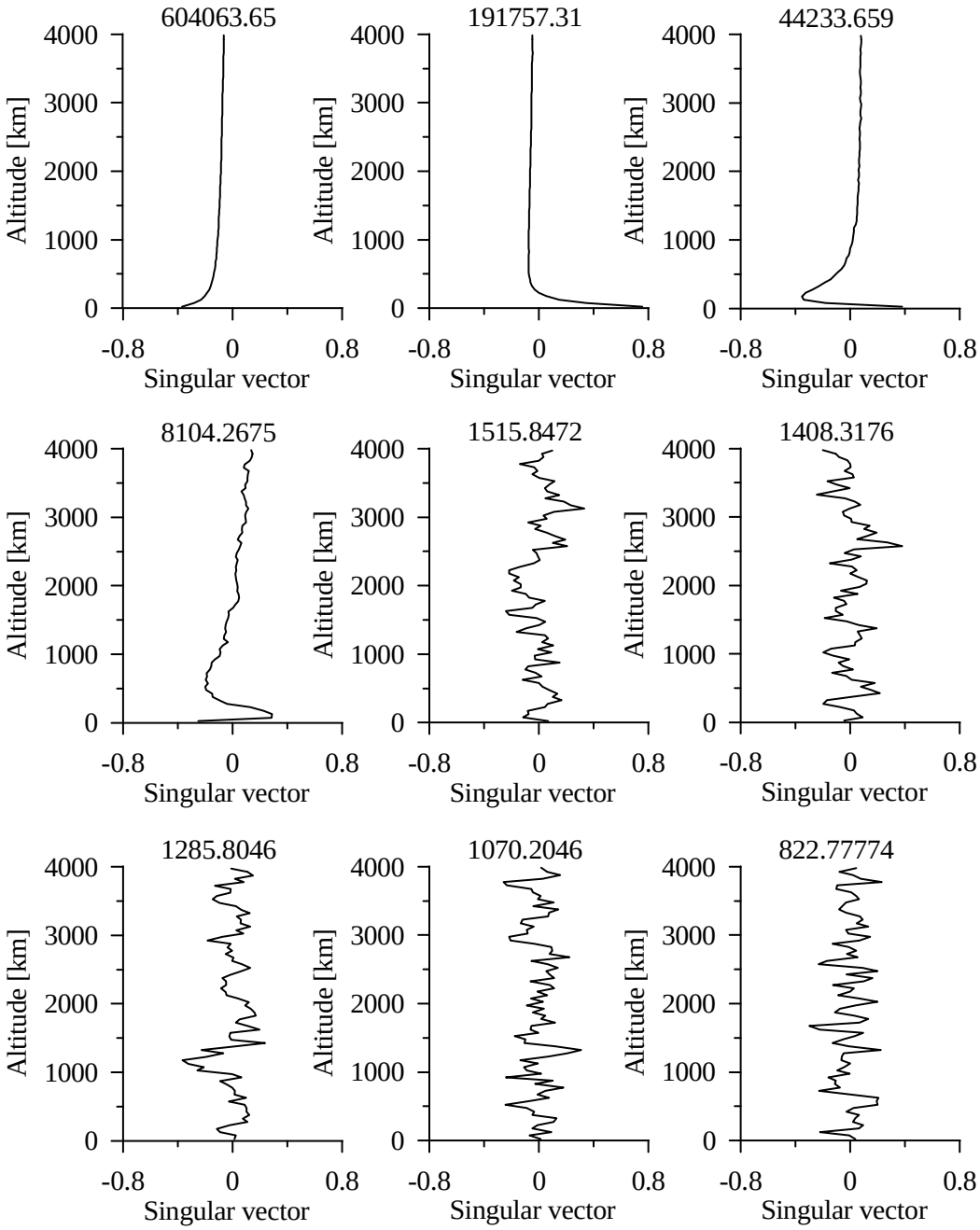

Figure 5.9: Singular vectors of the weighting functions of one set of viewing elevations at 477 nm with 50 m retrieval layers. The corresponding singular values are given above each plot.

the *a priori*. Secondly, the altitude of the main contribution peak increases with elevation angle, while the magnitude of the contributions decrease. The 1° DSCD always has the greatest contribution to the lowest layer, while the 15° and 30° DSCDs tend to contribute the most in layers between one and three kilometres. The contribution functions tend to be oscillatory, with a negative contribution in layers adjacent to strong positive peaks. In many cases, the peak contributions by different elevation measurements to the retrieval are very similar, so there is some redundancy in the information obtained from the different measurements due to the scattering characteristics for those geometries. This knowledge could be used to minimize the number of elevation angles in order to increase the temporal resolution of the measurements and thereby reduce systematic errors arising from changes in the state profile over the elevation scan time interval. The retrieval assumes that all the measurements within the retrieval time interval have sampled the same state profile, but transport or chemistry can lead to rapid changes in the measured state. In many cases, for the Cabauw NO_2 measurements, multiple DSCDs at the same elevation angle within the thirty minute retrieval interval have significantly different values, indicating either temporal changes or spatial inhomogeneities in the state profile or aerosols, or the presence of clouds. Systematic instrumental errors are another possible source of these discrepancies, and assuming that the atmospheric composition is stable over the retrieval interval, the mean residuals of the forward model fit to the measurements ($\mathbf{y} - \hat{\mathbf{y}}$) can indicate if systematic errors are present (see Fig. 5.17). Some improvement would be made by retrieving only a single scan, but a half hour retrieval interval was prescribed for CINDI in order to compare retrievals from different instruments. Thirdly, the contribution functions are obviously greater for the 200 m layers than for the 50 m layers, but more importantly, the relative contributions to layers above 100 m altitude are greater, as already explained in terms of weighting functions. Finally, the contributions of higher elevation measurements to the retrieved values at higher levels is greater for 477 nm than for 360 nm, consistent with the information obtained from the weighting functions.

Typical averaging kernels for a retrieved profile from one thirty minute interval of simulated DSCDs are shown in Fig. 5.11. In an ideal retrieval, each averaging kernel should sharply peak close to unity at the altitude of the layer it pertains to. In these retrievals, the averaging kernel for the lowest retrieval layer has a value close to unity in the lowest true state layer, indicating that nearly all the information in the retrieved value for that layer comes from the measurement of that layer with little or no smoothing from other levels of the true state. For the 50 m grid at 477 nm, the second and third level peaks occur at the appropriate altitude, but subsequent peaks fall progressively below the altitude of their retrieved state level indicating that much of the information about higher layers is influenced by true state values in lower layers. Successive averaging kernels for higher retrieval layers also become broader, so the retrieved values are smoothed over a wide vertical extent. The second level in the 200 m grid retrieval has a strong peak compared to the 50 m grid retrieval since it in effect combines the overlapping peaks for four 50 m layers, which all fall within the altitude range.

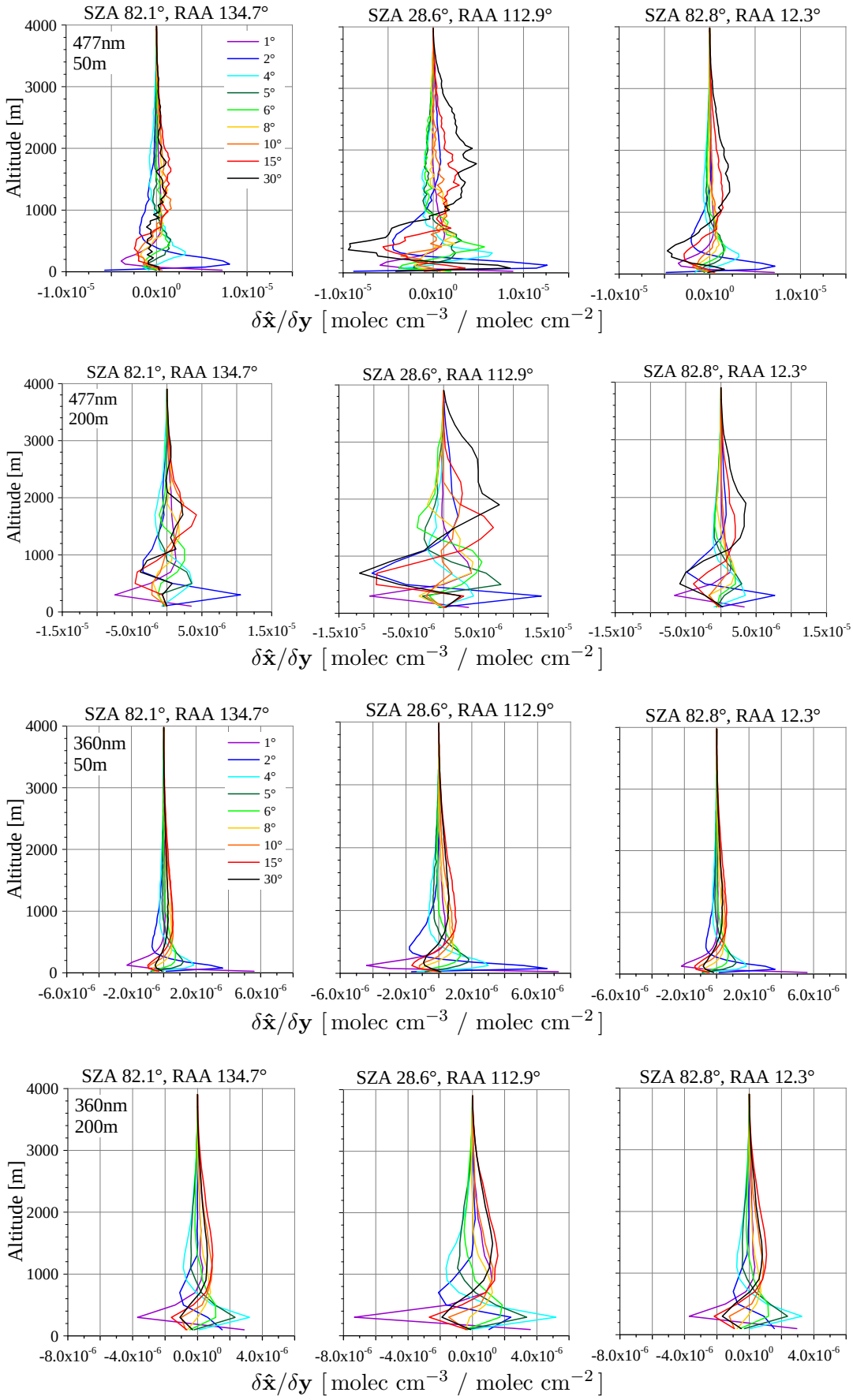

Figure 5.10: Contribution functions for three sun positions (early morning, midday and close to sunset) at 477 nm and 360 nm with the low optical depth aerosol profiles (VIS1 and UV1) and the 50 m and 200 m retrieval grids.

This result is also seen in the weighting functions and contribution functions. The averaging kernels at 360 nm are similar to 477 nm for the lowest retrieval layers, but the peaks for higher retrieval layers are smaller in magnitude and slightly lower. This is due to the shorter mean free paths in the UV region and thus reduced sensitivity of the measurements.

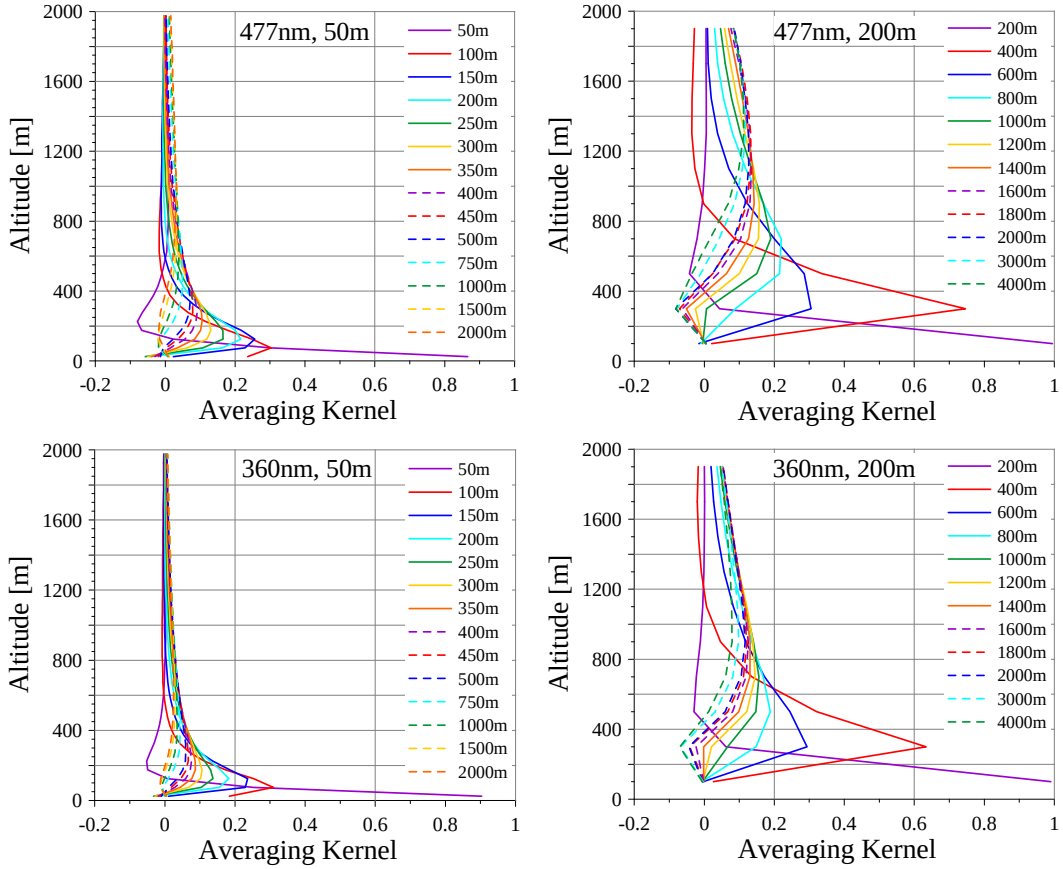

Figure 5.11: Averaging kernels up to 2 km for a single profile retrieved from thirty minutes of measurements at 477 nm (top) and 360 nm (bottom) with the 50 m retrieval layers (left) and 200 m layers (right). The different coloured lines represent retrieved values of $\hat{\mathbf{x}}$ at the different altitude levels given in the key.

The singular vectors of the averaging kernels, shown in Fig. 5.12, for a single retrieved profile have almost identical structure to the singular vectors of $\mathbf{K}$ as they describe the same information, but weighted by the relative covariances in the measurements and the *a priori*. The first three singular vectors have singular values close to unity, implying that the measurements contribute nearly all the information to these structures in the retrieved profile, with little or no influence from the prior constraints. The fourth singular vector has some information from the measurements but all subsequent singular vectors describe noise or structures that come from the *a priori* state. The sum of all the singular values is equal to the trace of $\mathbf{A}$ or the total degrees of freedom (DFS) for the measurements.

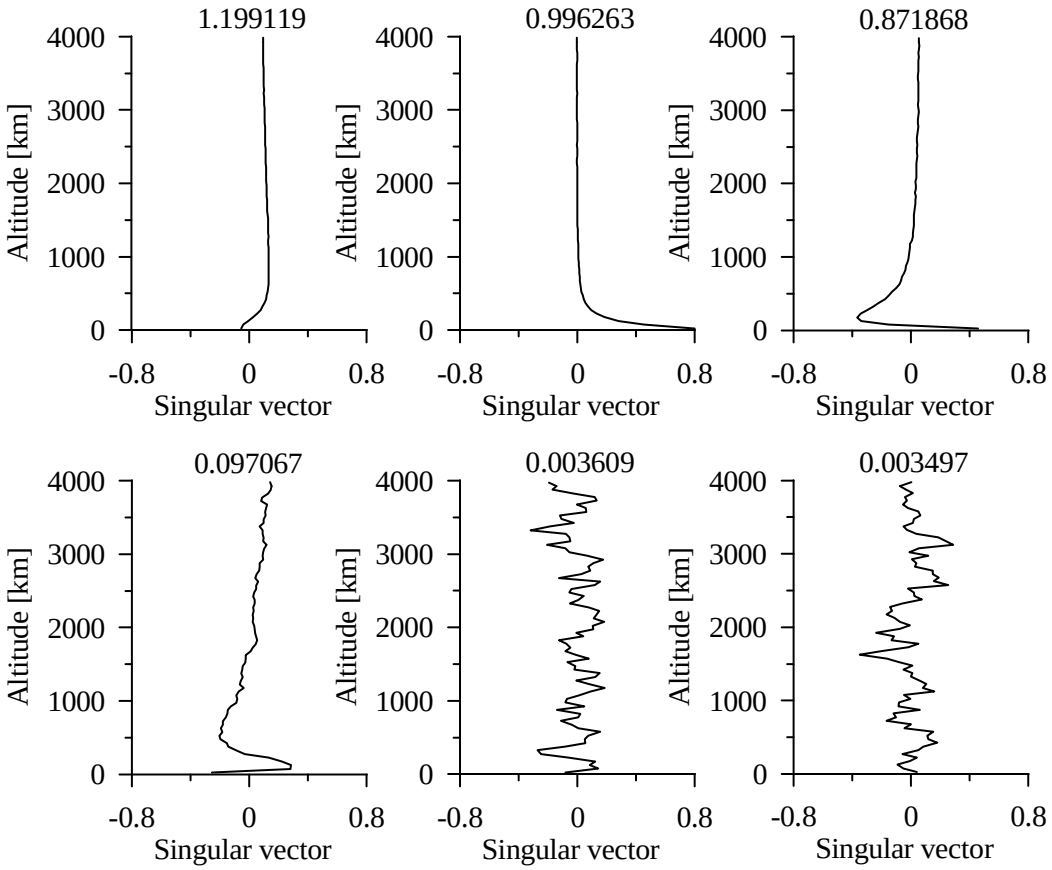

Figure 5.12: Leading singular vectors of the averaging kernels of one set of viewing elevations at 477 nm with 50 m retrieval layers. The corresponding singular values are given above each plot.

The diagonal values of **A** give the DFS for each retrieval level and thus are important, along with area and resolution, for the interpretation of the retrieved profiles. In Fig. 5.13, the cumulative sum of the diagonal of **A** is plotted from the ground to 4 km for each of the retrieved profiles throughout the day. The altitudes at which the diagonals of **A** sum to whole numbers can then be taken as range limits for partial VCDs that we can say are linearly independent retrieved values. The resolution of the averaging kernels can then be checked to ensure that the information contributing to these cumulative layers comes mostly from within the layer rather than being smoothed from other regions of the atmosphere. For example, in the 477 nm, 50 m grid case, one DFS is reached in the layer from the surface to 100 m, and a second DFS is obtained from 100 m to 350 m for measurements close to midday or 100 m to 600 m near sunrise and sunset. A third DFS is reached at around 2 km for measurements close to midday, but there are less than three DFS for measurements early and late in the day. The main reason for the higher DFS in the middle of the day is the lower DOAS fitting errors as seen in Fig. 5.17. Typically six to seven bits of information (**H**) are retrieved from the simulated DSCD measurements.

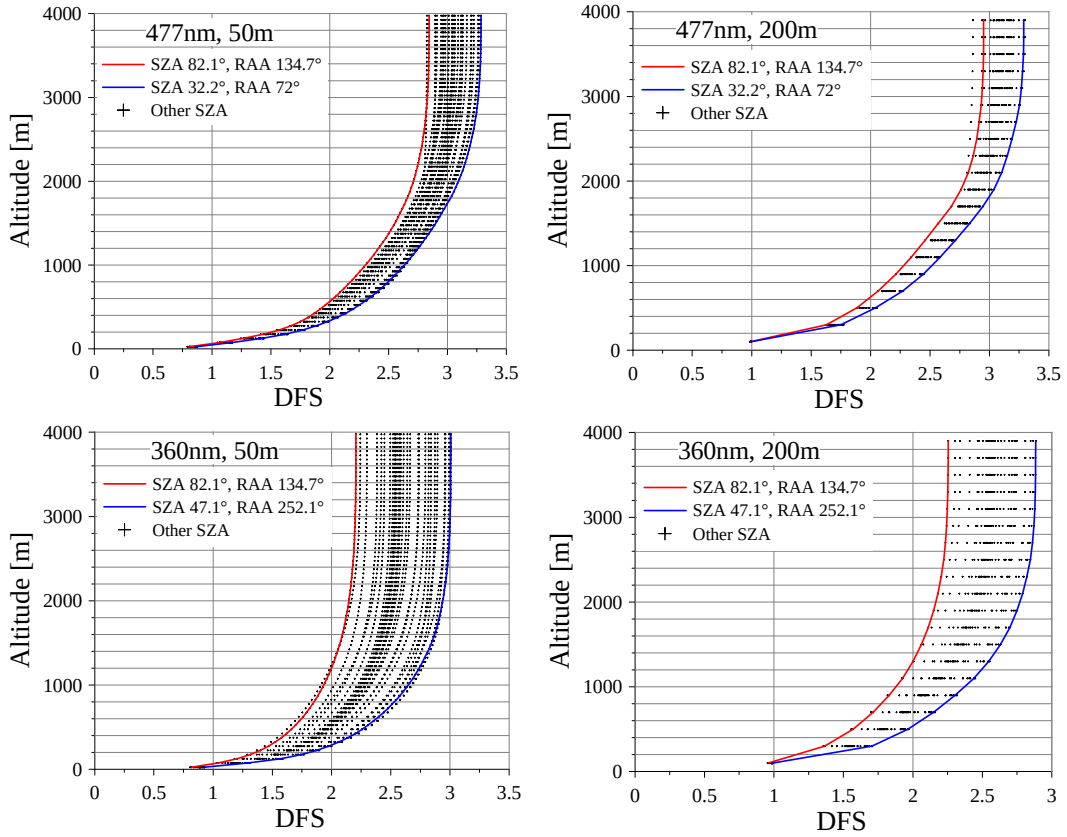

Figure 5.13: Cumulative DFS calculated from the trace of $\mathbf{A}$ for 477 nm (top) and 360 nm (bottom) with 50 m retrieval layers (left) and 200 m retrieval layers (right).

For the CINDI retrievals, $\mathbf{x}_a$ and the settings for $\mathbf{S}_a$ were prescribed for the campaign, but for the BrO and IO retrievals presented in Chap. 6 the L–curve method (Schofield, 2003) is used to optimize the percentage of $\mathbf{x}_a$ used for the variances in $\mathbf{S}_a$. From the L–curves shown in Fig. 5.14 for the two prescribed NO_2 *a priori* profiles, it can be seen that 60–80% would be appropriate for the 0.3 ppb *a priori* and 30–40% for the 1 ppb *a priori*. The curve of increasing DFS also starts to level off at those points. The right–hand plot of Fig. 5.14 illustrates that even for an $\mathbf{x}_a$ error of only 5% the retrieved profile is much closer to the true profile than it is to $\mathbf{x}_a$. With a 30% error in $\mathbf{x}_a$ the retrieved profile is already very close to the profile retrieved using the prescribed 100% of $\mathbf{x}_a$, but the retrieval errors in $\hat{\mathbf{S}}$ are much smaller due to the smaller $\mathbf{S}_a$ variances.

Hendrick et al. (2006) demonstrated a strong dependence of DFS (trace($\mathbf{A}$)) on the correlation length for zenith sky DOAS measurements of stratospheric NO_2, with the maximum DFS obtained using a correlation length of 8 km. The use of correlation length is more complicated in the MAX–DOAS retrievals because the information content of the measurements decreases rapidly with altitude and the structure of the true state can be unpredictable in comparison to stratospheric distributions. In addition, with decreasing variances on the diagonal of $\mathbf{S}_a$ towards higher altitudes, covariances between levels can become much larger than the

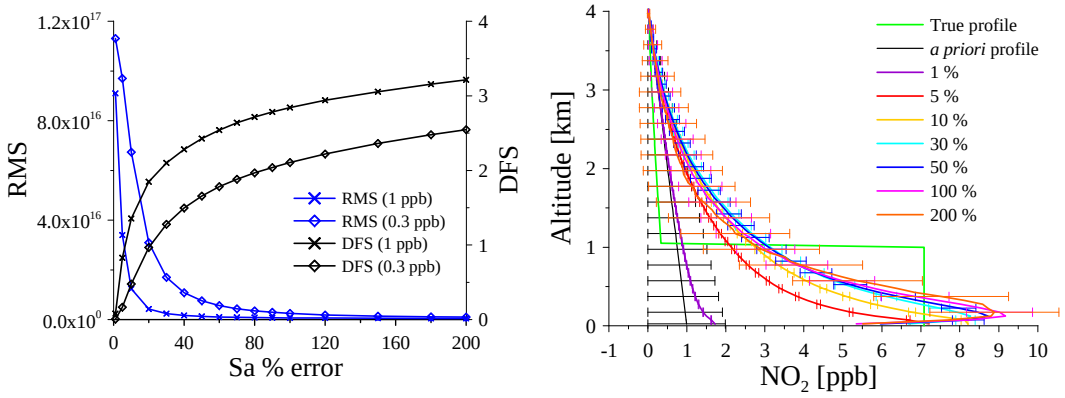

Figure 5.14: The left–hand plot displays the L–curves and DFS for the retrieval of simulated NO_2 profile four with the 1.0 ppb *a priori* used for the simulation retrievals and the 0.3 ppb *a priori* used for the measurement retrievals (see Sect. 5.7), and a correlation length of 25 m. The right–hand plot shows the effect of varying the percentage of the $\mathbf{x}_a$ used for the diagonal of Sa on the retrieved NO_2 profile at 4.5 UT.

variances. Fig. 5.15 shows a plot of the DFS and RMS fit of the modelled DSCDs to the measurements for increasing correlation lengths. Clearly, increasing the correlation length, while reducing the number of possible solutions, also gives more weight to the measurements and so the fit improves. The overall DFS also increase for the same reason, but the DFS for the lowest 100 m decrease because the measurements there are constrained by small covariance values carried from higher levels. One way around this problem is to construct $\mathbf{S}_a$ with fixed variances over selected levels, and correlation lengths appropriate to each set of levels, with no covariance allowed between sets of levels. The retrieval program developed in this work is set up to construct $\mathbf{S}_a$ in this manner, but this needs further testing.

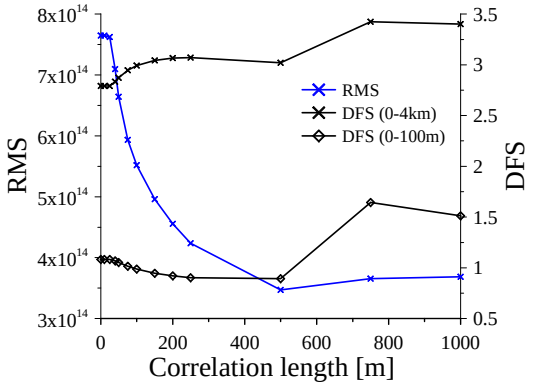

Figure 5.15: The effect of changing the correlation length on DFS and RMS for the retrieval of simulated NO_2 profile 4 at 4.5 UT. The 1 ppb *a priori* was used with 100% error for the diagonal elements of Sa and the 50 m retrieval grid.

The effect of measurement errors on the retrieval was investigated by scaling

the DSCD errors by factors ranging from 0.1 to 30 and looking at the RMS fit errors, DFS and the retrieved profiles (Fig. 5.16). As expected, the fit to the measurements improves as the measurement errors decrease, while the DFS increase since more weight is given to the measurements in the retrieval. The retrieved profile is still similar to the original, even when the errors are multiplied by a factor of 5 or 10 (right panel of Fig. 5.16). When the errors are reduced by a factor of 0.25 the retrieved profile is still smooth, but when reduced by a factor of 0.1 the retrieval starts to fit more noise from the measurements.

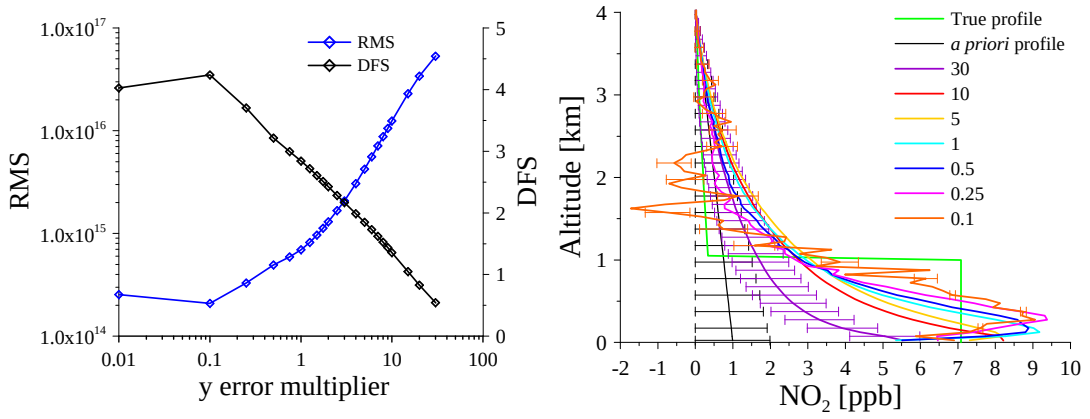

Figure 5.16: The effect of scaling the DSCD errors on DFS and RMS for the retrieval of NO_2 profile four (left) and the corresponding retrieved profiles (right). Note, both the RMS and multiplication factor axes are logarithmic, and error bars are shown for the profiles with error multiplication factors of 0.1 and 30.

The DSCD errors for the simulated measurements for NO_2 profile four are displayed in Fig. 5.17 along with the residuals and RMS for the forward model fit to the measurements. As expected, the RMS is proportional to the measurement errors since smaller measurement errors allow more weight to be given to the measurements in the retrieval. The mean residuals for $\mathbf{y} - \hat{\mathbf{y}}$ are always positive, indicating a systematic error in the measurements or in the forward model. Since these "measurements" were simulated using the LIDORT discrete ordinates RTM, the mean residuals indicate the DSCDs simulated by this model are on average higher than the DSCDs simulated by NIMO. The right–hand plot in Fig. 5.17 shows that for some elevation angles the DSCDs simulated by NIMO are less than the LIDORT DSCDs, for some angles they are greater, and they show good agreement for the 1° DSCDs. However, the differences are usually less than 1 or 2%, up to a maximum of 4% of the DSCD values, which is well within the range of variation between radiative transfer models demonstrated by Wagner et al. (2007a) (see Chap. 4).

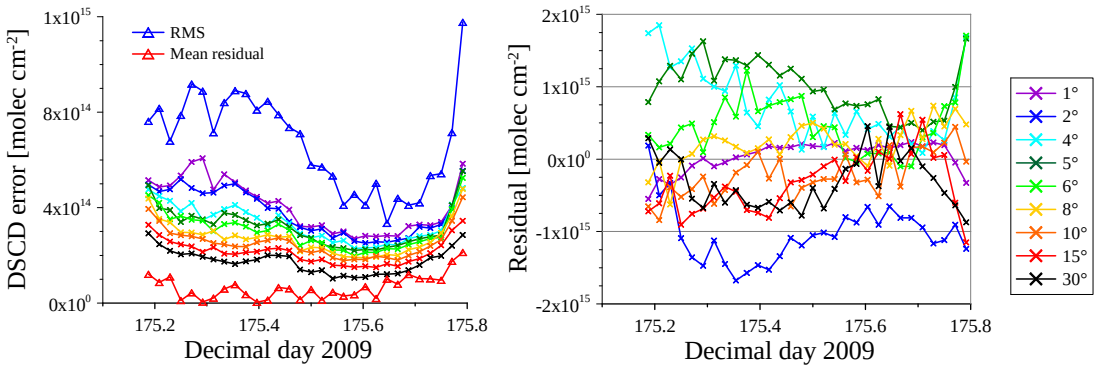

Figure 5.17: The left–hand plot displays DSCD errors, and the mean residuals and RMS of the fit to the measurements ($\hat{\mathbf{y}}$ to $\mathbf{y}$) for the retrieval of the 477 nm DSCDs simulated from profile four with VIS1 aerosols. The residuals for each elevation angle are shown in the right–hand plot.

5.7 Retrieval of Cabauw NO_2 measurements

Following the CINDI NO_2 measurement campaign in Cabauw, Netherlands in June and July 2009, five "golden" days with minimum cloudiness were selected for profile comparisons between participating groups. NO_2 measurements were made by the NIWA instrument on four of these "golden" days. To directly compare the profile retrievals, independent of instrumental influences, each group also retrieved profiles from the Bremen visible (477 nm) and UV (360 nm) instruments. The *a priori* was constructed with a mixing ratio of 0.03 ppb at the surface, linearly decreasing to 0.01 ppb at 4 km. The *a priori* error for the diagonal elements of $\mathbf{S}_a$ was 80% of $\mathbf{x}_a$ at each level, with covariance in the extra–diagonal terms determined using a correlation length of 100 m, and the retrieval layer grid height was 200 m. In addition to these "common" settings for all groups, the *a priori* settings for the simulation retrievals with a 50 m grid height (see Sect. 5.6) were also used. Profile retrievals were performed for every half hour interval throughout the "golden" days. Exponential aerosol extinction profiles with a scale height of 750 m from 0 to 4 km were provided for every thirty minutes on the five "golden" days by BIRA, based on AODs from AERONET (Aerosol Robotic Network) sun photometer measurements (Fig. 5.18). The aerosol extinction profiles from 4 km to 90 km were taken from climatology data with an AOD of 0.041. The forward model SCD and weighting function calculations were performed in NIMO using 25000 photons for the simulation of each SCD. All other forward model parameters were the same as for the simulation retrievals in Sect. 5.6.

A very wide spectral window (425–490 nm) was prescribed for the DOAS fitting, and the choice of forward model wavelength to represent this broad spectral range influences the retrieved NO_2 amounts since the box–AMFs change significantly over this wavelength range. A representative forward model wavelength should be chosen based on where the strongest absorption features occur and on the wavelength where the box–AMFs are close to the mean for the spectral range. A

wavelength of 445 nm would be ideal for these retrievals, but 477 nm was used as prescribed for the CINDI retrieval intercomparison. If the forward model wavelength is too long, the retrieved trace gas concentrations will be underestimated and if the wavelength is too short, the retrieval will overestimate the trace gas concentrations (see Chap. 4).

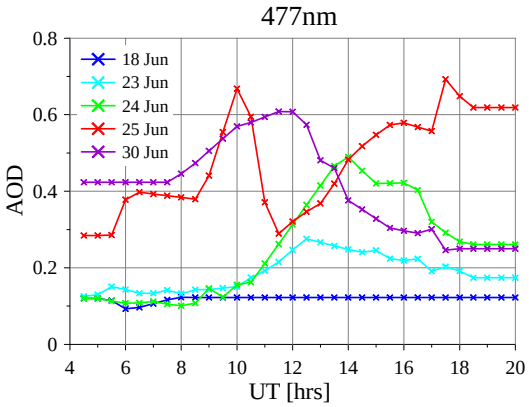

Figure 5.18: Aerosol optical depths at 477 nm from AERONET data for the 5 "golden days" at Cabauw.

For the retrieved state profile quantities to accurately represent the DSCDs derived from MAX–DOAS measurements the DSCDs calculated by the forward model ($\hat{\mathbf{y}} = \mathbf{K}\hat{\mathbf{x}}$ for the linear retrieval) must closely fit the measurements. Fig. 5.19 displays the DSCDs measured by the NIWA instrument on the 23$^{\text{rd}}$ of June together with the fitted forward model DSCDs and the RMS errors of the differences between the forward model and measured DSCDs. Frequently, there are inconsistencies between measurements within the retrieval interval, which may be due to temporal changes or spatial inhomogeneities in the state profile or in aerosols or clouds, or due to changes in the instrument, or systematic errors in the DOAS spectral fitting. The retrieval finds the best fit to the measurements within the limitations of the forward modelled weighting function matrix $\mathbf{K}$ and the prior constraints. For example, in Fig. 5.19, where there is a sharp dip in the DSCDs between 9:30am and 10:00am (decimal day $\sim$ 173.4), the model fit takes an average value. It is impossible to account for all the variations in the atmosphere or the instrument in the radiative transfer calculations, and the retrieval cannot account for unknown systematic errors in the measurement process. An advantage of retrieving on a finer grid, and therefore calculating $\mathbf{K}$ at higher resolution, is that the retrieved DSCDs are given greater freedom to fit the measurements more precisely. This is demonstrated by comparing the fits for the 50 m and 200 m retrieval grids in Fig. 5.19.

The DSCDs and the retrieved profiles for the four "golden" days measured by the NIWA instrument are displayed in Fig. 5.7. For each daily NO_2 contour plot, the profile with the highest surface NO_2 value is plotted in order to compare the 50 m and 200 m grid retrievals. As discussed in Sect. 5.6, the finer retrieval grid

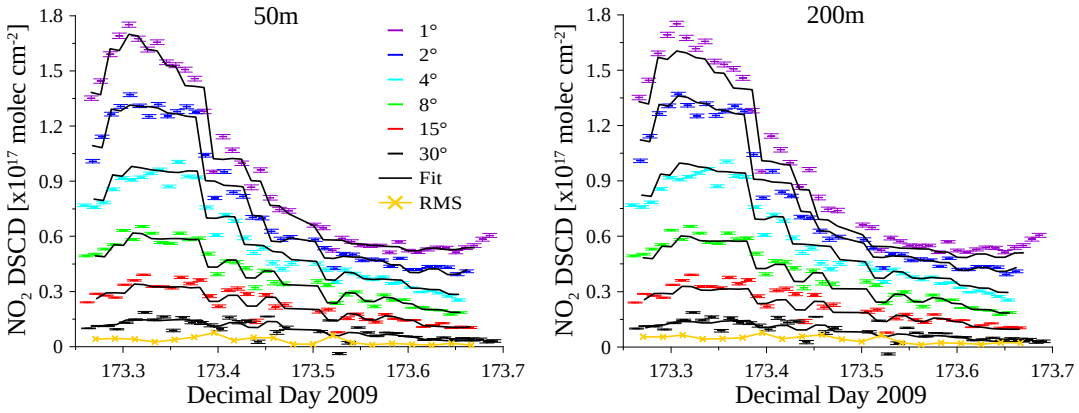

Figure 5.19: Measured and modelled DSCDs retrieved on the 50 m grid (left) and 200 m grid (right) together with their RMS fitting errors for the measurements made by the NIWA instrument at Cabauw on the 23rd of June 2009.

tends to concentrate the trace gas into the lowest layer, but the partial VCDs up to 200 m are similar for both grids. Fig. 5.21 shows the retrieved profiles from the Bremen visible (477 nm) instrument on all five "golden" days. When comparing the contour plots of retrievals from the two instruments, note that the Bremen measurements cover a longer period each day. The profiles retrieved from the two instruments are very similar, but retrievals from the Bremen instrument tend to have slightly higher NO_2 values. One reason for this is that the DSCD errors of the Bremen measurements are roughly half as much as the errors for the NIWA DSCDs (see Fig. 5.29), so more freedom is given to the retrieval to fit the measurements with less *a priori* constraint. The Bremen measurements also contain four extra elevation angles ($3°, 5°, 6°$ and $10°$), which increase the information content of the measurements.

The retrieved surface NO_2 concentrations for the two instruments and two retrieval grids are compared with EMPA (Swiss Federal Laboratory) in situ NO_2 measurements in Fig. 5.22. The retrieved surface NO_2 values are similar to the in situ measurements on the 18th of June, but do not show good agreement on the other days. The 50 m grid retrieval tends to overestimate the surface NO_2 concentration, suggesting that the height of the well–mixed NO_2 layer is generally much higher than 50 m. The means of the retrieved NO_2 values taken over the four lowest 50 m grid layers are very similar to the values for lowest layer of the 200 m grid retrieval, thus the partial VCDs for the two retrievals also agree.

The strong influence of the forward model aerosol extinction profiles on the retrieved surface NO_2 concentration is illustrated in Fig. 5.23. Using the VIS1 aerosol profile (see Fig. 5.2) for each entire day, the plots of retrieved surface NO_2 values follow the shape of the 1° DSCD plots, as is expected. The retrieved surface NO_2 also matches the changes in the in situ measurements very well, although the magnitude is too high, which indicates that the AOD of the VIS1 profile, in particular for the near surface layers, is greater than the true AODs. However, the

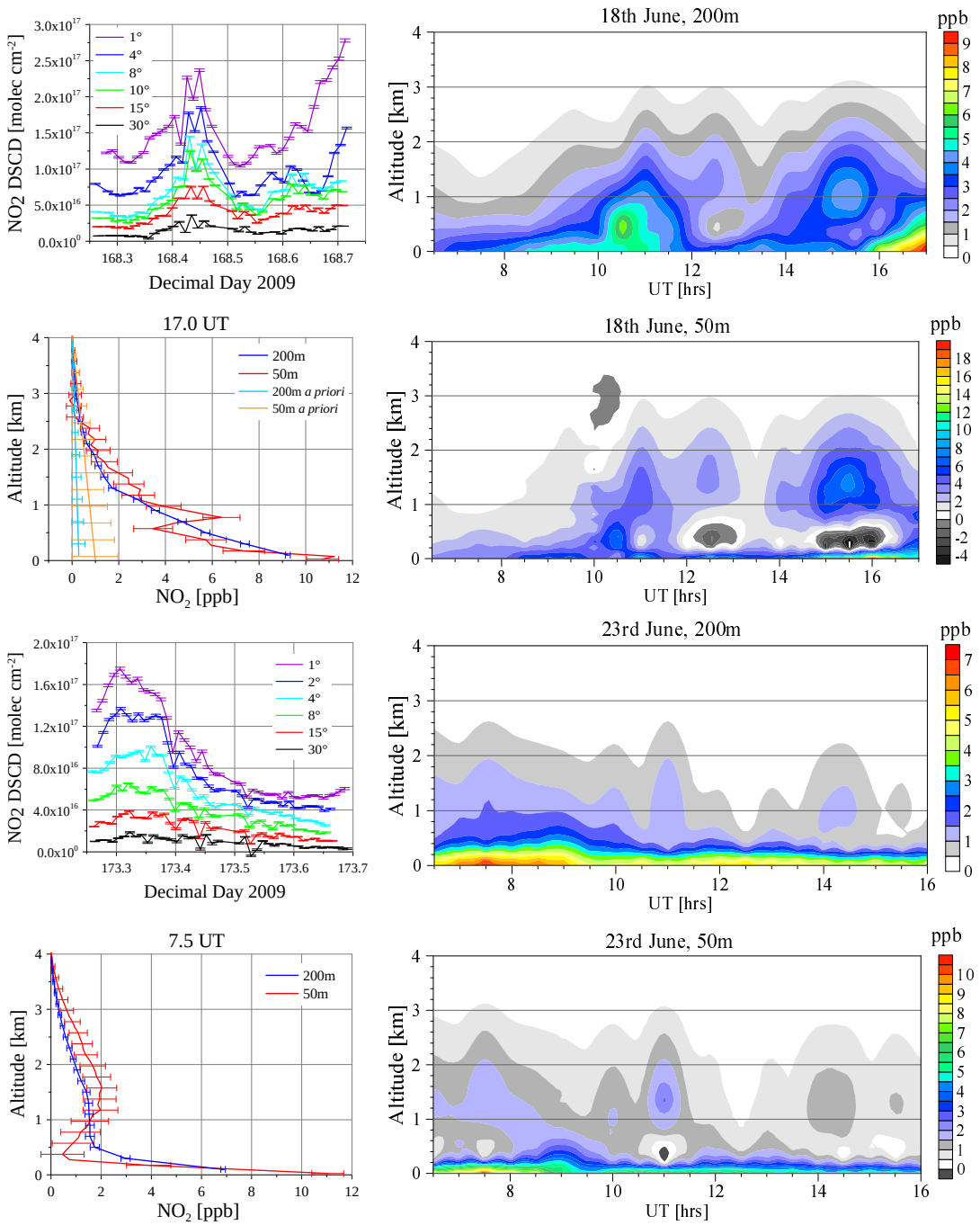

Figure 5.20: DSCDs measured by the NIWA instrument and the corresponding NO_2 profiles retrieved at thirty minute intervals for the four "golden days". The contour plots show the NO_2 mixing ratio profiles for the 200 m and 50 m retrievals. The maximum NO_2 profiles for each day are displayed as line plots to compare the 200 m and 50 m grid retrievals and their errors.

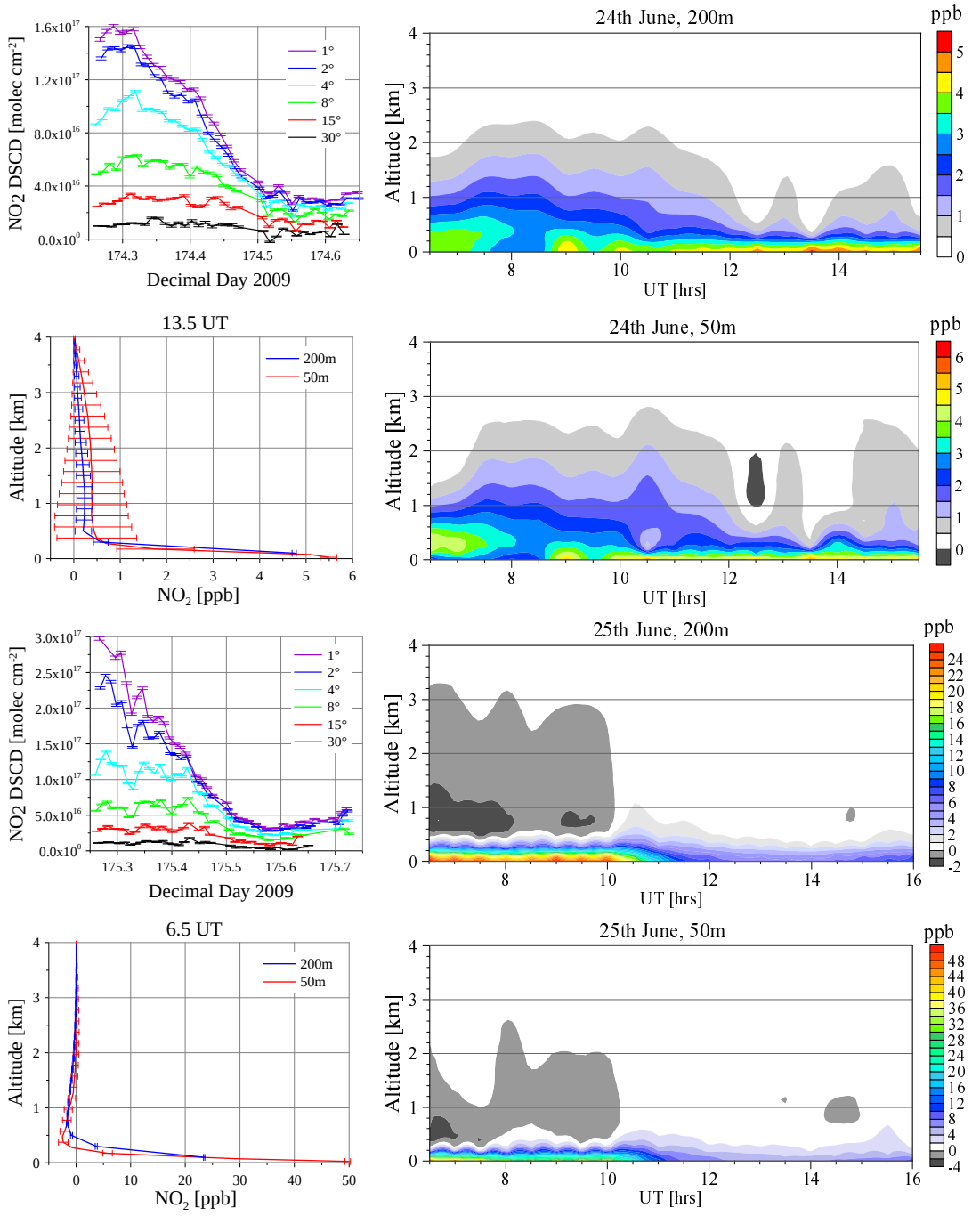

Fig. 5.7 (continued) DSCDs measured by the NIWA instrument and the corresponding NO_2 profiles retrieved at thirty minute intervals for the four "golden days". The contour plots show the NO_2 mixing ratio profiles for the 200 m and 50 m retrievals. The maximum NO_2 profiles for each day are displayed as line plots to compare the 200 m and 50 m grid retrievals and their errors. Compare the 200 m grid retrievals with the retrievals for the Bremen instrument in Fig. 5.21.

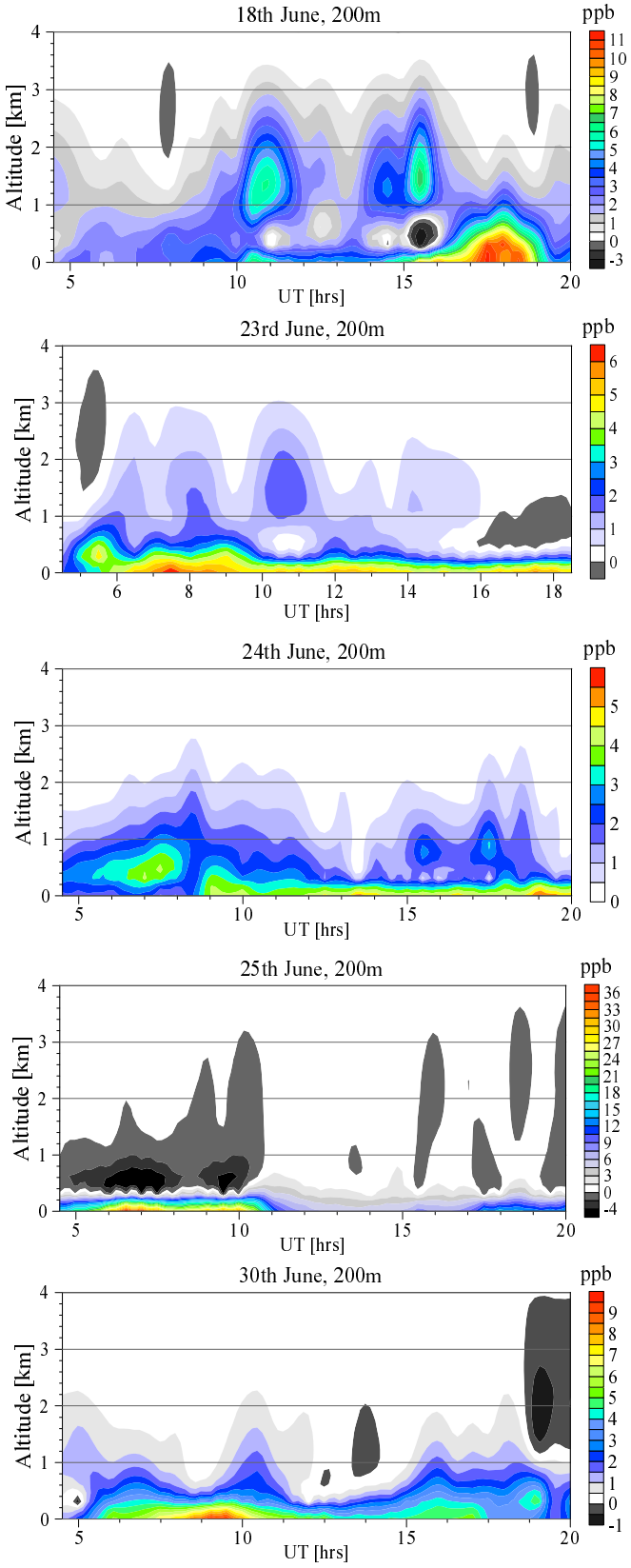

Figure 5.21: NO_2 profiles retrieved (using the algorithm developed in this work) from measurements made by the Bremen visible instrument for the five "golden" days, with the 200 m retrieval grid.

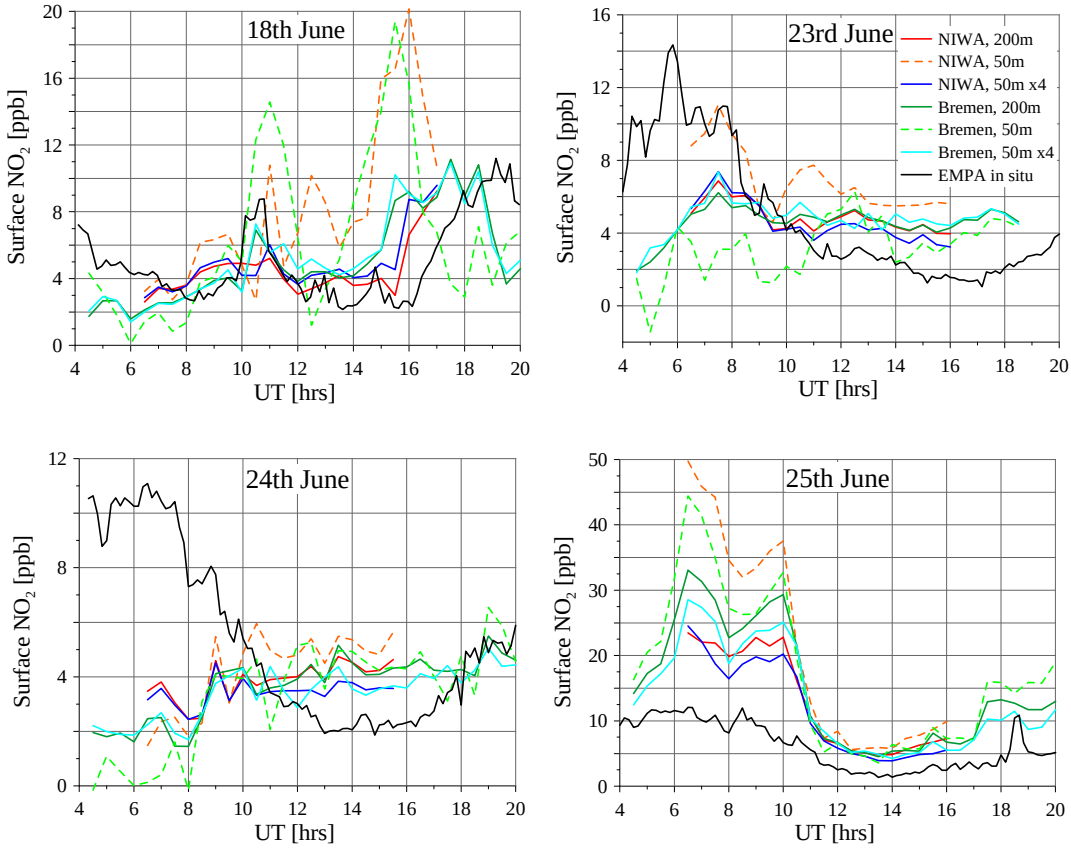

Figure 5.22: Retrieved surface NO_2 concentrations for the four "golden days" for both the NIWA instrument and the Bremen visible instrument using the 50 m and 200 m retrieval grids. The means of the four lowest 50 m retrieval levels are also shown.

surface NO_2 values retrieved using the aerosol profiles based on AERONET AOD measurements generally do not agree with the in situ measurements. For example, on the 24th June the DSCDs are high in the morning, but the AOD and surface extinction of the AERONET aerosol profile are less than the VIS1 profile, which leads to low retrieved surface NO_2 values. Conversely, the DSCDs measured in the afternoon are low, but high AOD and surface extinction result in retrieved surface NO_2 values that are higher than the in situ measurements. Multiple scattering on aerosols reduces the mean free photon path lengths, which in turn reduces the DSCDs, particularly for the low elevation angle measurements. Therefore, in the presence of strong aerosol extinction, the inversion has to put higher trace gas concentrations in the retrieved profiles in order to fit the modelled DSCDs to the measurements. While the AOD is important, the extinction or AOD near the surface is particularly critical for the forward modelled DSCDs. On the 18th June, for example, the AOD of the AERONET profile is up to six times more than the AOD of the "clear air" profile, but the retrieved surface NO_2 values are similar. The reason for this is the relatively low surface extinction, which although much higher than the "clear air" surface extinction, is only one third of the surface extinction in the VIS1 profile. This also points to another observation,

that below a certain extinction threshold aerosols only exert a weak influence on the retrieved trace gas profile.

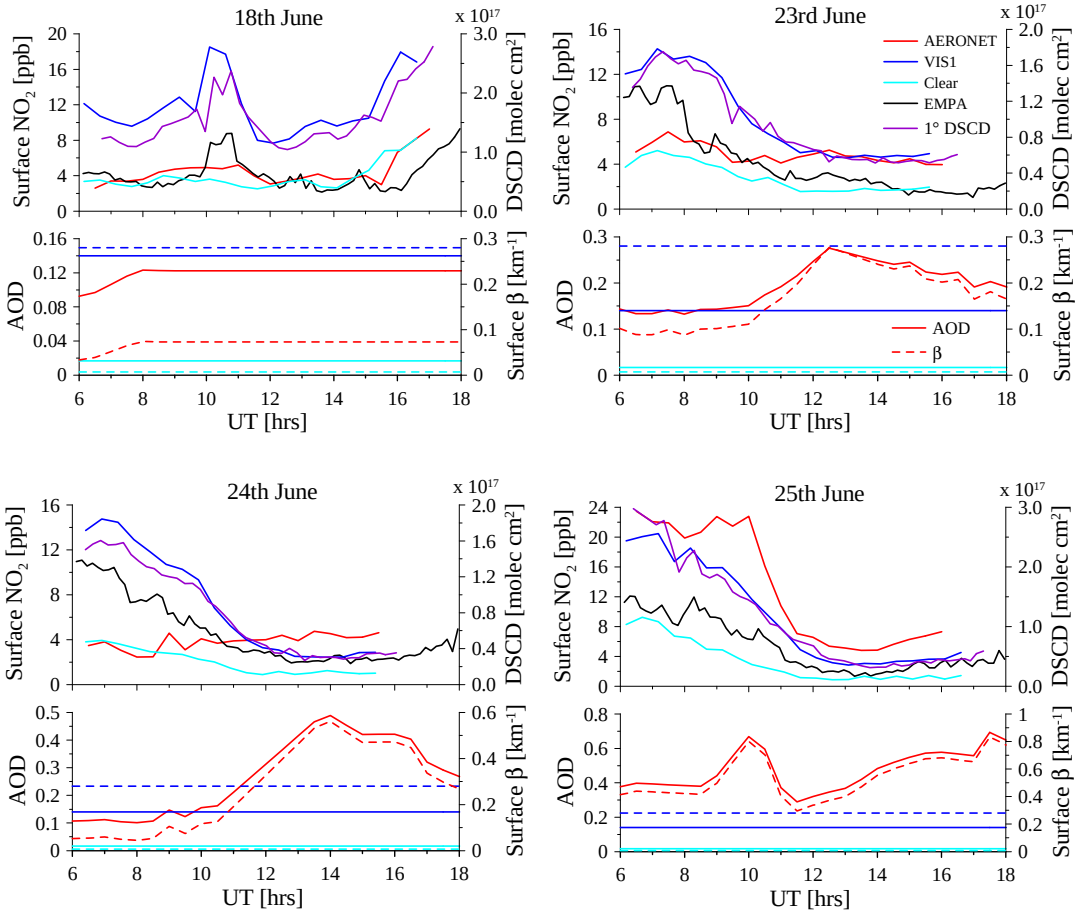

Figure 5.23: Surface NO_2 for the four "golden days" for the NIWA instrument retrieved using the 200 m grid and three different aerosol extinction profiles (AERONET, VIS1 and a low AOD clean air profile). DSCDs for the 1° viewing elevation angle are also shown for comparison with the retrieved surface NO_2 concentration. The AODs (solid lines) and surface aerosol extinction β (dashed lines) are shown on the lower panels of each plot.

The weighting functions for the Cabauw measurements are very similar to the weighting functions for the simulated DSCDs shown in Fig. 5.7, and the singular vectors are almost identical to those displayed for the simulated measurements in Figs. 5.8 and 5.9. Examples of typical contribution functions and averaging kernels for the NIWA and Bremen visible instruments are given in Fig. 5.24. The contribution functions and averaging kernels for the Bremen measurements are greater than for the NIWA measurements due to the lower DOAS fitting errors (see Fig. 5.29) and the added information content from the inclusion of extra elevation angles.

The averaging kernels, shown for the 200 m grid in Fig. 5.25, vary only slightly

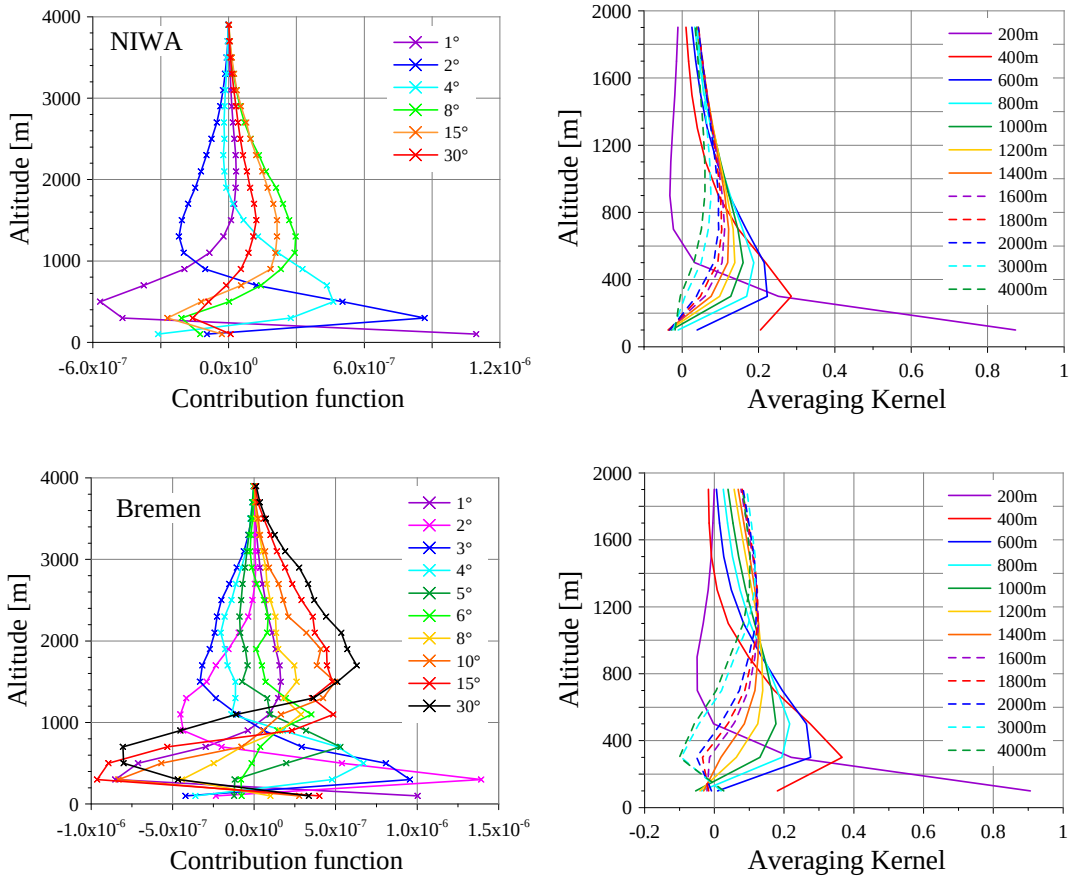

Figure 5.24: Contribution functions for a single set of elevation angles for the 200 m retrieval layers on the 23rd June (left) and the averaging kernels up to 2 km for one retrieved profile (right–hand plots) for the NIWA instrument (top) and the Bremen visible instrument (bottom).

throughout the day, mostly due to changes in the measurement errors rather than physical changes in the atmosphere. The retrieved value for the lowest layer comes mostly from the measurements and from the within the same altitude layer with negligible contribution from other layers. The retrieval for the second layer has a contribution roughly half from the measurements and half from the *a priori*, with some smoothing from state values in adjacent layers. The contribution of the measurements to the retrieved values in higher layers rapidly decreases and the retrieved values are smoothed from the true state over most of the retrieval altitude range. There is no significant information content in the measurements for state levels above 2 km.

The area of the averaging kernels gives a rough indication of the fraction of the retrieval that comes from the measurements, and should be close to unity for layers where the retrieval is accurate and close to zero where the retrieved value comes mainly from the *a priori*. The area is the sum of all the elements in a row of **A**, so a retrieved level can have high area but the information may have come from a very broad altitude region. Therefore, it is important to look at the

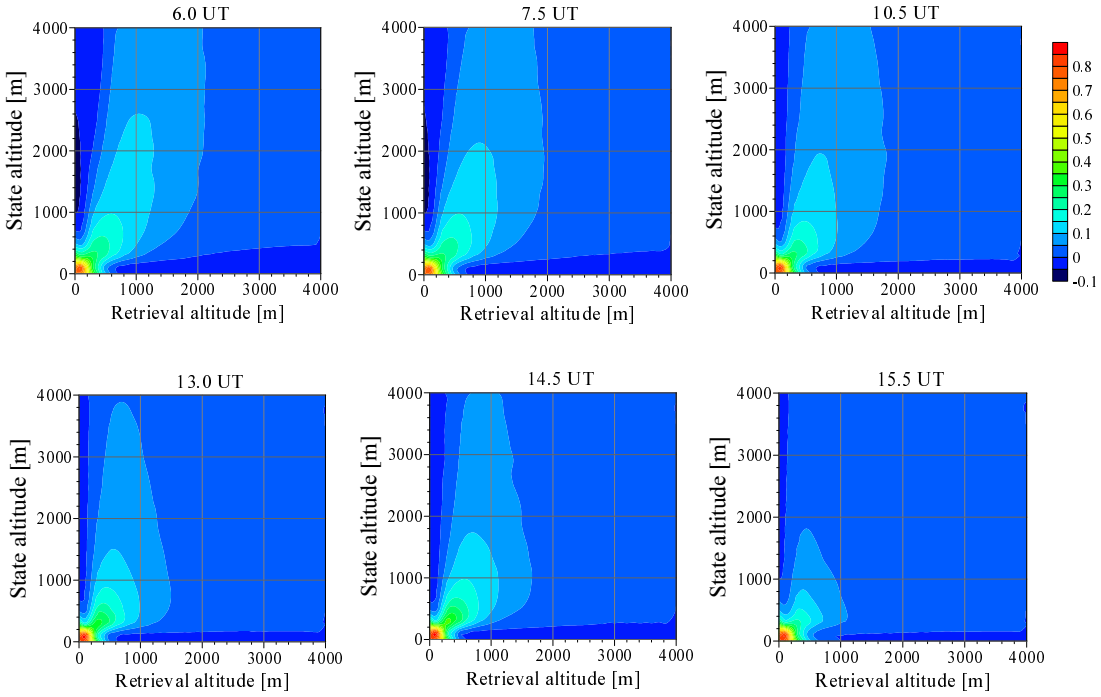

Figure 5.25: Averaging kernels at six time intervals throughout the day for profiles retrieved from NIWA measurements on the 23rd June with 200 m grid layers.

resolution of the averaging kernels. Fig. 5.26 displays the area and resolution of $\mathbf{A}$ for the retrieval of NIWA measurements from the 23rd June. For both grid heights the area is close to unity and the resolution is close to the layer width for the lowest layer. The second layer in the 200 m grid retrieval has an area greater than one because information is also incorporated from higher layers, as indicated by the vertical resolution of 600–800 m per degree of freedom. From approximately 150–250 m in the 50 m grid retrieval, the area is zero or negative due to the oscillatory near zero or negative lobes of the averaging kernels for the lowest layers and small negative values of the averaging kernels for much of the upper part of the retrieval region where the *a priori* provides all the information. In both grid retrievals there is a region where the area is around two, which comes from the broad shape averaging kernels with smoothing of information from all the higher layers. This may indicate that the $\mathbf{S}_a$ errors are set too high, as also supported by the L–curve optimization in Fig. 5.14, and so measurement noise is being interpreted as measurement signal.

The area, resolution and degrees of freedom together indicate that the most reliable retrieval product to report from these measurements are partial VCDs for three altitude regions. The plots in Fig. 5.27 give an indication of the altitude regions where the each DFS lies. For the 50 m retrieval from the NIWA measurements we have roughly one DFS from 0–100 m, one DFS from 100–800 m, and usually slightly less than one DFS remaining from 800–4000 m. The partial and total VCDs for these three altitude layers and their mixing ratios, assuming

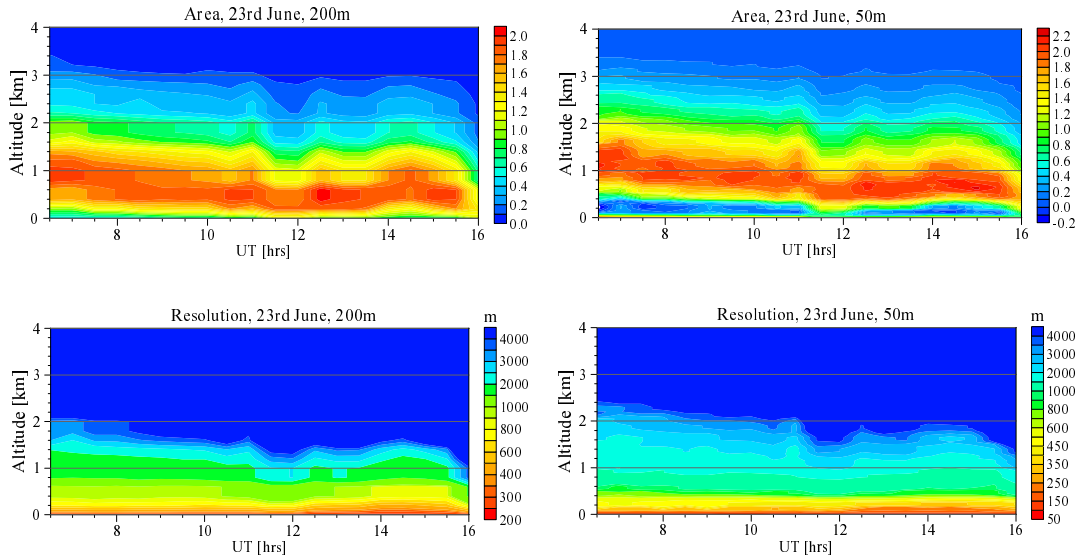

Figure 5.26: Area (top) and resolution (bottom) of the averaging kernels for the 200 m (left) and 50 m (right) grid for the retrieval of measurements made by the NIWA instrument on the 23rd June. Note, the dark blue region on the resolution plots includes resolutions of 4000 m or much greater, meaning that no information is contributed by the measurements for those layers.

homogenous mixing within each layer, are displayed for the four "golden" days in Fig. 5.28.

The variation in DFS throughout the day, seen in Fig. 5.27, is due to variation in measurement errors. The strong effect of the measurement errors on the DFS and the forward modelled DSCD fit to the measurements was shown in Fig. 5.17. Fig. 5.29 shows the lower errors and the correspondingly higher DFS for the Bremen measurements relative to the NIWA measurements. As a consequence of the lower errors, the residuals and RMS for the fit of $\mathbf{y} - \hat{\mathbf{y}}$ are also smaller for the Bremen measurements. The residuals also indicate a systematic error in the NIWA measurements in the middle of the day, probably due the instability in the detector temperature.

For zenith sky DOAS a single midday reference is used in the DOAS fitting, but for MAX–DOAS, using a single midday reference in the DOAS fitting and then subtracting the reference SCDs for each elevation sequence afterwards can introduce an unnecessary errors, as the instrument temperature, and therefore the instrument transmission function, changes slightly throughout the day. For example, high midday and afternoon ambient temperatures at Cabauw led to an increase in the detector temperature above -20° with a resultant change in the instrument function. In Fig. 5.30, the DSCD errors for the 1° elevation measurements are higher in the morning for the DOAS fitting with a single midday reference compared with the errors from DOAS fitting using the temporally nearest references. The DFS derived from the measurements decreases when the errors are high. The drop in DFS in the middle of the day is caused by incomplete

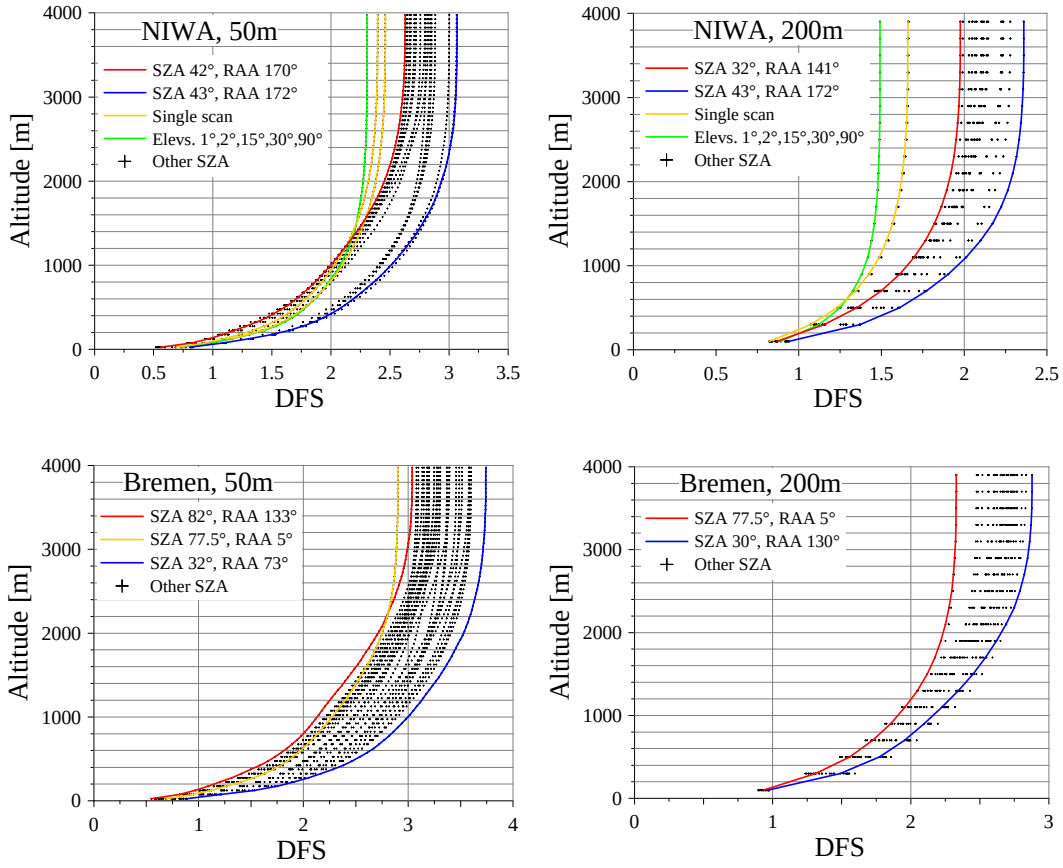

Figure 5.27: Cumulative degrees of freedom calculated from the sum of the diagonal elements of the averaging kernel matrix from the ground to 4 km for the NIWA instrument (top) and the Bremen 477 nm instrument (bottom). Note the reduced DFS for retrieval intervals containing incomplete scan sequences.

elevation scan sequences within the two half hour periods, since a series of zenith only measurements were made at midday. The Shannon information content (**H**) retrieved from the measurements is in the range of three to five bits for the NIWA measurements and five to six bits for the Bremen measurements.

5.8 Summary

A linear MAP retrieval algorithm was developed for the inversion of MAX–DOAS trace gas DSCDs to obtain vertical profile information. The accuracy of the retrieval algorithm was investigated by retrieving NO_2 profiles from artificial DSCDs that were simulated from known NO_2 profiles using a radiative transfer model. In most cases, the partial VCDs from the surface to 4 km were a good estimate of the true VCDs, in both the UV (360 nm) and visible (477 nm), and for both low and high aerosol pollution cases. The retrieved surface mixing ratios and profile shape showed good agreement for true profiles with a peak concentration

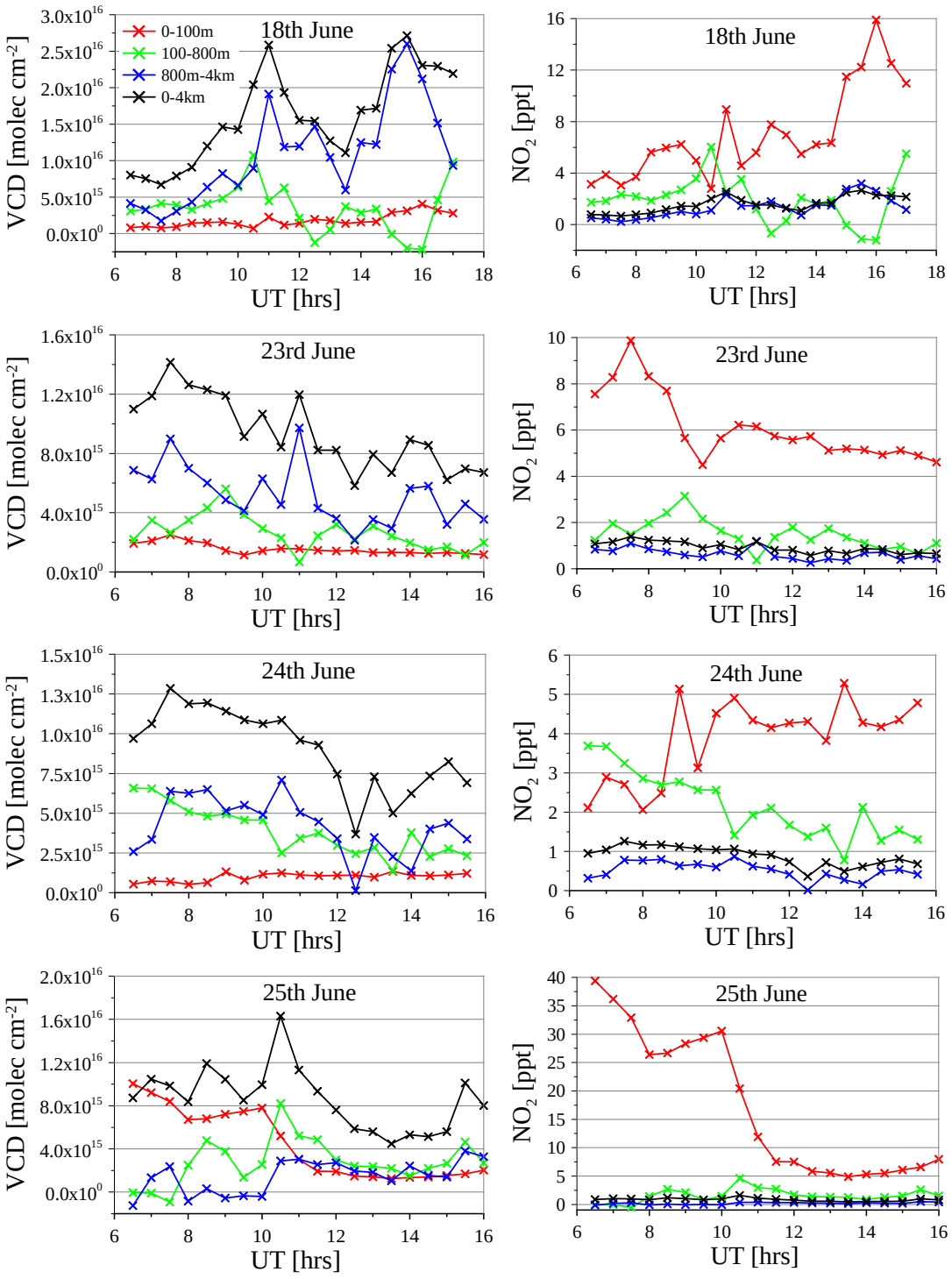

Figure 5.28: NO_2 partial VCDs and mixing ratios for the three selected altitude regions, retrieved from measurements made by the NIWA instrument on the four "golden" days.

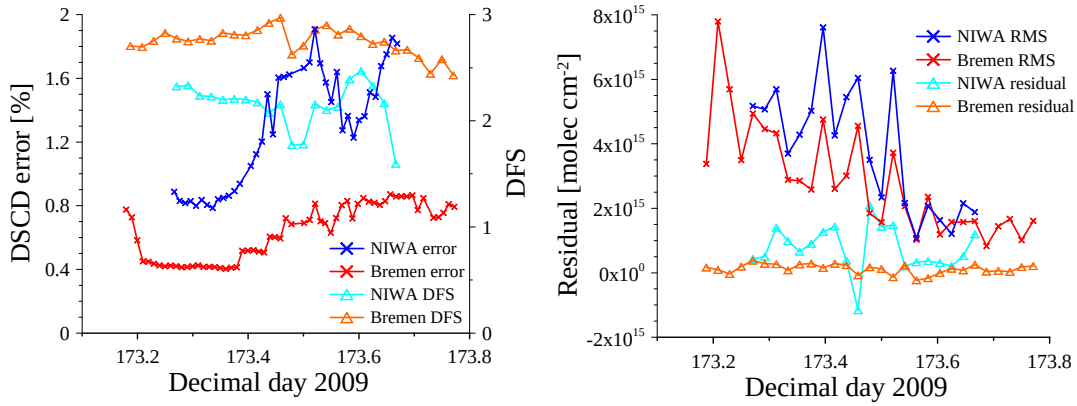

Figure 5.29: The left–hand plot shows the DOAS fitting errors in the 1° DSCDs for the NIWA and Bremen visible instruments on the 23rd June, and the DFS for the profiles retrieved with the 200 m grid. The residuals and RMS errors from the fit of the forward modelled DSCDs to the measurements from the two instruments are displayed in the right–hand plot.

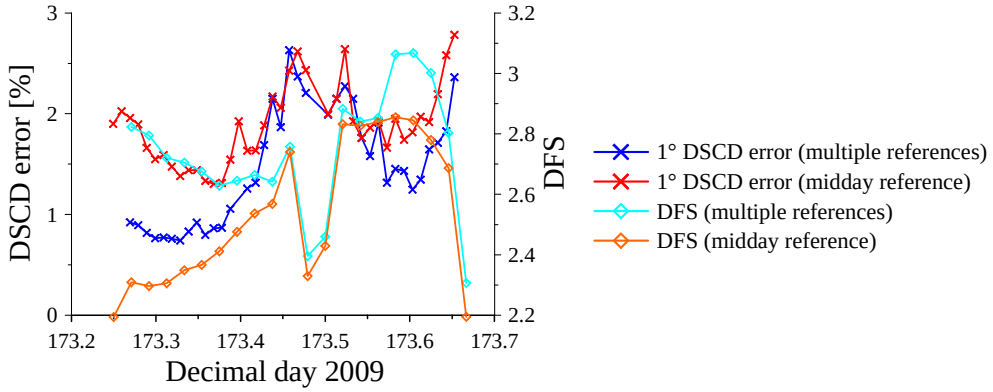

Figure 5.30: Comparison of DOAS fitting errors in the 1° elevation DSCD, and DFS for the retrieved profiles when using a single midday reference versus using the reference from each elevation sequence.

at or near the surface. The surface mixing ratios tended to be overestimated and the mixing ratios in higher layers underestimated for elevated trace gas layers or surface layers higher than about 200 m.

Two to three DFS were obtained from the measurements, depending on the measurement errors. The wavelength, SZA and relative azimuth angle also influenced the information content due to the different scattered light paths. The highest sensitivity was obtained in the visible, and typically at the smallest SZAs. The resolution of the retrieved profiles was similar to the retrieval grid size for the lowest retrieved layer and quickly decreased to around 1 km at 1 km altitude. The most reliable retrieval products to report are the VCDs and mixing ratios for the surface layers up to 50–200 m and the VCDs up to 4 km.

The importance of choosing an accurate aerosol extinction profile, when the aerosol optical depths in the near surface layers are higher than a certain threshold, was demonstrated for the retrieval of NO_2 measurements from Cabauw, Netherlands. Underestimating the aerosol extinction leads to an overestimation of the trace gas mixing ratios and vice versa. Therefore, the next step will be to implement aerosol profile retrievals using the O_4 DSCDs (Wagner et al., 2004; Frieß et al., 2006), and the retrieved aerosol profiles can then be used in the forward model calculations for the trace gas retrieval.

Choosing an appropriate *a priori* for retrievals of aerosols and trace gases presents a major difficulty, especially since these species often have highly variable profiles without any satisfactory estimates from a climatology, other measurements or models. Therefore, the addition of Kalman smoothing, using the previous retrieved state vector to estimate the *a priori* for the current measurement time, could potentially improve the accuracy of the retrieved profiles (Frieß et al., 2006).

Chapter 6

Antarctic results

In this chapter, the results from the two measurement campaigns conducted in McMurdo Sound, Antarctica during the spring of 2006 and 2007 are presented. The DSCDs from MAX–DOAS measurements of BrO and IO are presented in Sect. 6.1 together with the surface ozone and meteorology measurements. The observed bromine explosion and ozone depletion events are discussed in Sect. 6.2. Sect. 6.3.1 describes the profile retrieval settings, and the retrieved BrO and IO profiles and vertical columns are presented in Sects. 6.3.2 and 6.3.3. Surface meteorology, air mass back trajectory calculations and satellite measurements of BrO and sea ice are discussed in Sect. 6.4. The tethersonde measurements of ozone and potential temperature are presented in Sect. 6.5 and the results from mercury analysis of the snow samples are discussed in Sect. 6.6.

6.1 Halogens, surface ozone and meteorology

The complete time series of DSCDs and surface meteorology measurements made by the TARDIS at McMurdo, Cape Evans and Cape Bird in 2006 and 2007 are displayed in Figs. 6.1 to 6.4. The different coloured dots in the three upper panels represent the DSCDs for the different elevation angles. A clear separation between the column amounts for the different elevation angles, with higher slant column densities for lower elevation angles, indicates that there is a vertical gradient in the boundary layer trace gas concentration. Thus, the DSCDs show that detectable amounts of boundary layer BrO were present on many days in both 2006 and 2007. IO was detected on several days each year, mostly at Cape Bird.

Multiple scattering on blowing snow and ice particles, fog, cloud and sea salt aerosols alters the light paths through the atmosphere, and can lead to enhancement of the zenith or high viewing angle SCDs for trace gases in the stratosphere or in the altitude range of the clouds, but generally leads to a reduction in the SCDs for trace gases below the cloud layer, as the light tends to be diffused from most SZAs into a more vertical path (Van Roozendael et al., 1994; Erle et al., 1995; Wagner et al., 1998, 2002, 2004; Frieß et al., 2004). Multiple scattering reduces the SCDs for low elevation angles by reducing the path lengths from the last scattering event to the instrument, in other words the atmospheric visibility

is greatly reduced (Heckel et al., 2005; Frieß et al., 2006; Wagner et al., 2007a,b) (see Chap. 4). This results in DSCDs for the different elevation angles that are less clearly separated than in clear sky conditions, as the absorption paths for all viewing directions become very similar, thus reducing the sensitivity of the MAX–DOAS measurements. In addition, pure Rayleigh scattering, or the typical background aerosol profile used for the forward modelled DSCD and weighting function calculations, is no longer valid under these conditions.

The visibility in the boundary layer can be estimated by investigating the DSCDs of the O_2 collision complex O_4, which has several absorption bands in the UV–visible spectral region and an easily determined vertical profile (Wagner et al., 2002, 2004; Frieß et al., 2006). MAX–DOAS O_4 measurements can even be used to retrieve information on aerosol optical depth, extinction profiles and microphysical properties (Wagner et al., 2004; Frieß et al., 2006). The O_4 concentration is proportional to the square of the air density and therefore decreases exponentially with altitude, with a scale height of approximately 3.5 for polar conditions (Frieß et al., 2004). Thus in clear atmospheric conditions, the O_4 DSCDs are clearly separated with the greatest DSCDs for the lowest viewing elevation angles, whereas in poor visibility, such as in fog or blowing snow, the O_4 DSCDs are low and poorly separated or overlapping. The effect of clouds on the light paths, and thus on the DSCDs for the off–axis angles, depends on the cloud ceiling height. For clouds above about 1 km, the effect on the AMFs at 350 nm can be very small (Wagner et al., 2007b). Therefore, since most days during the campaigns were cloudy, the O_4 DSCDs were used to select suitable cloudy days for retrievals, in addition to the few cloudless days. The spectral retrieval of O_4, which has a strong absorption band at 361 nm, was performed using the same cross–sections and wavelength fitting window (337–362 nm) as BrO (see Chap. 3).

Data gaps in the DSCD measurements arise due to various reasons, including snow on the tracker window, making direct sun measurements, the tracker sticking at one elevation angle, and the spectrometer switching off due to low battery level.

The hourly average TEI–49C surface ozone measurements from Arrival Heights are displayed for both years, and the 2B–205 ozone measurements are shown for 2007 (the 2B–205 was not available in 2006). The 2B–205 measurements, taken at one minute intervals, are smoothed using a one hour running average. The Aeroqual measurements from 2006 (not shown) were very noisy and were therefore unusable. Therefore, as the variations in the 2007 sea ice ozone measurements generally follow the measurements at Arrival Heights, with a few small differences and a more or less constant offset, the Arrival Heights ozone measurements are taken as a reasonable approximation of variations in ozone concentration at the measurement sites in 2006. The 2B–205 was calibrated with the TEI–49C at Arrival Heights before and after the measurements at each site, and the 2B–205 data displayed here has been corrected for small offsets from the TEI. The consistently lower ozone mixing ratios on the sea ice relative to Arrival Heights could be attributed to background levels of BrO and IO in the boundary layer, while

Arrival Heights at 185 metres above the sea ice, is likely to be frequently above the boundary layer and thus be replenished with ozone from the free troposphere. Aeroqual data is shown for days 269 to 282 in 2007 only for comparison with the 2B–205. There is a general baseline agreement with the 2B–205 measurements but the Aeroqual measurements are noisy, and the effect of wind on the flow rate in the sensor can be seen, for example, on day 281.

Temperature, pressure, relative humidity and wind speed and direction, measured by the Vaisala WXT510 at approximately one metre above the ground, are displayed in the lower three panels of each figure (relative humidity is shown on the same panel as surface ozone). The Vaisala measurements, taken at 15 second intervals, are smoothed using a 10 minute running average. Only average wind speeds are displayed here, and maximum gust speeds were often considerably greater.

6.2 Ozone depletion and bromine explosion events

According to the criterion for an Antarctic tropospheric ozone depletion event (ODE) of a $\geq$10 ppb reduction in ozone for five hours or more, used by Wessel et al. (1998), one ODE occurred on 4$^{\text{th}}$ October 2006 (day 277) and one on the 14$^{\text{th}}$ to 15$^{\text{th}}$ October 2007 (day 287–288). In addition, three smaller surface ozone minima can be identified in 2007, which can be referred to as partial ozone depletion events. This episodic nature of ODEs is typical for coastal Antarctic sites (Kreher et al., 1997; Jones et al., 2006; Helmig et al., 2007) in contrast to first year sea ice zones in both the Arctic and Antarctic, where almost continuous low ozone and elevated BrO concentrations are observed (Hopper et al., 1998; Wagner et al., 2007b; Bottenheim et al., 2009; Pöhler et al., 2010).

During the 2006 ODE, observed on 4$^{\text{th}}$ October, surface ozone at Arrival Heights decreased from 30 ppb to 11 ppb within 19 hours, before returning to normal again within 7 hours. This coincided with a storm event, with visibility less than 100 m, blowing snow, and wind from the prevailing easterly direction with average speeds of 5–12 m s^{-1} and gusts of over 20 m s^{-1}. The onset of the ozone depletion event coincided with the arrival of the storm, as can been seen in Fig. 6.1, where the relative humidity rapidly increased from about 40% to 90% and the average wind speeds increased from below 5 m s^{-1} to over 15 m s^{-1}. The temperature increased from -30°C before the event to -11°C at the end. The increase in humidity to near saturation was most likely due to the sublimation of blowing snow particles, which are typically present at wind speeds above $\sim$8 m s^{-1} (Mann et al., 2000). Sublimation of blowing snow releases water vapour and removes heat from the surrounding air, both leading to increased relative humidity. The surface ozone concentration recovered to the level observed before the event approximately 11 hrs before the end of the storm. This may be explained by the break–up of the stratified boundary layer due to turbulence and thus mixing with free tropospheric air. The passing of fronts often leads to break–up of the capping

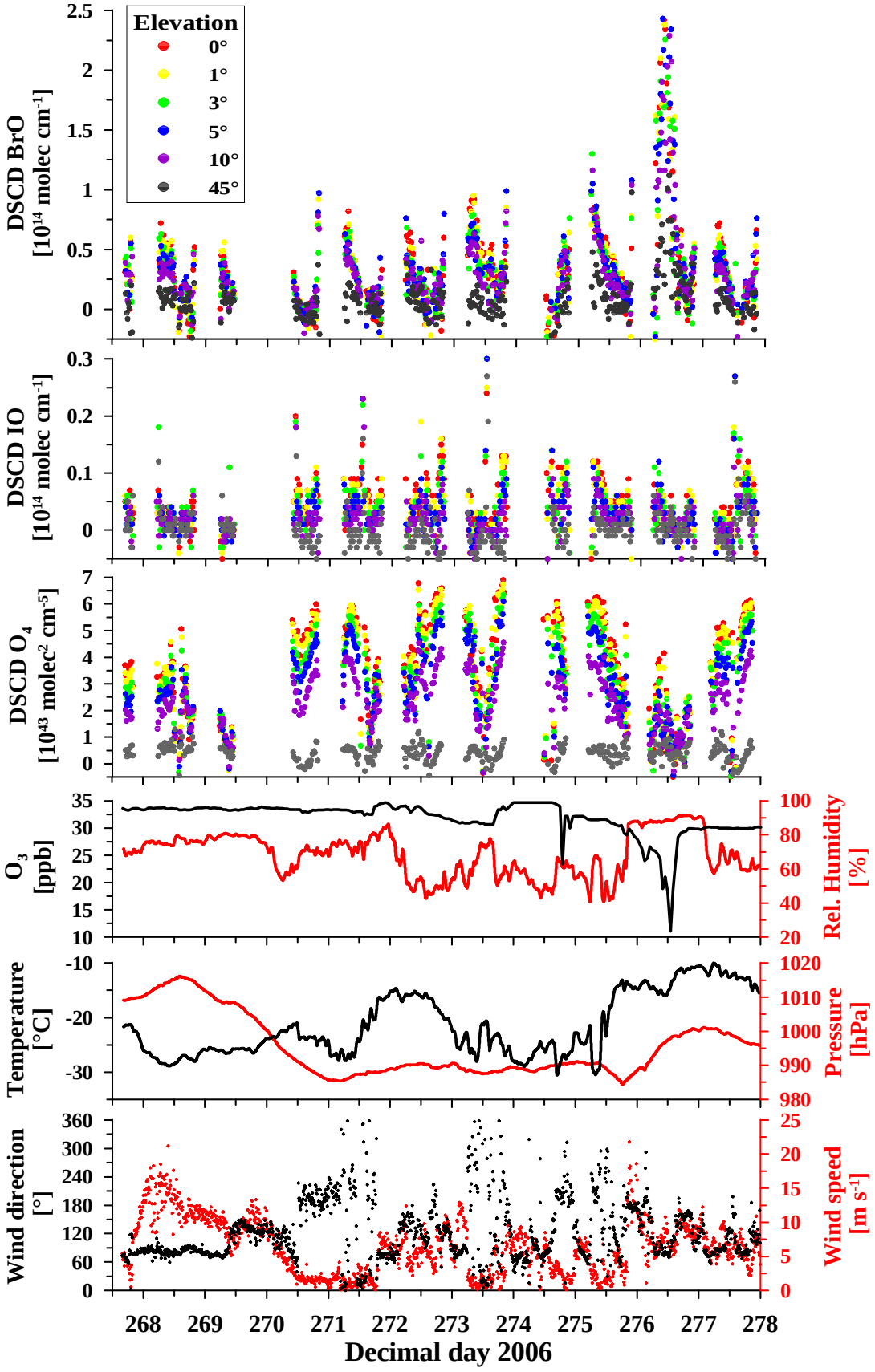

Figure 6.1: Part 1. BrO, IO and O_4 DSCDs, surface O_3 and surface meteorology at McMurdo, 25th September to 5th October 2006.

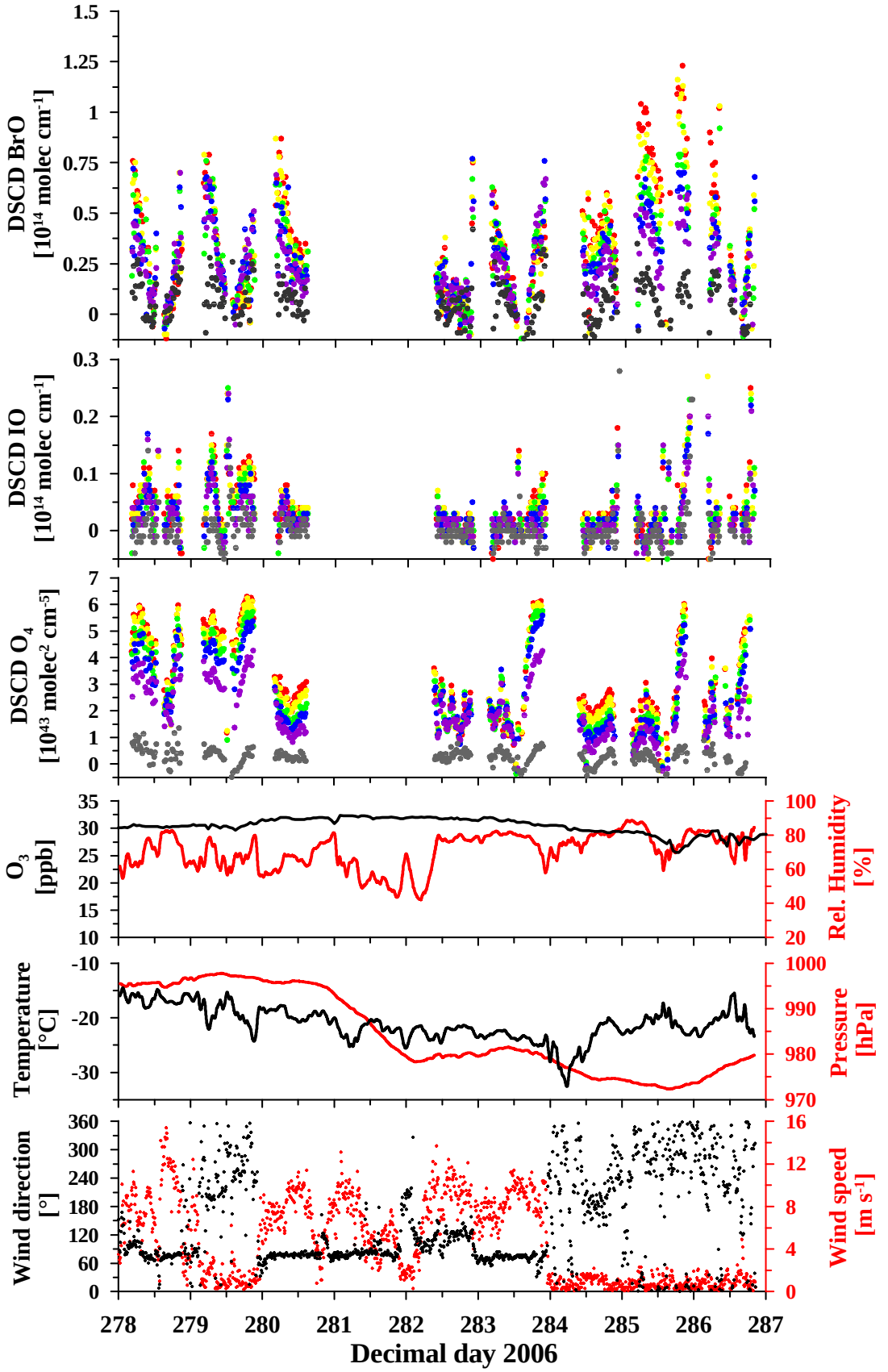

Figure 6.1 Part 2. BrO, IO and O_4 DSCDs, surface O_3 and surface meteorology at McMurdo, 6th to 14th October 2006.

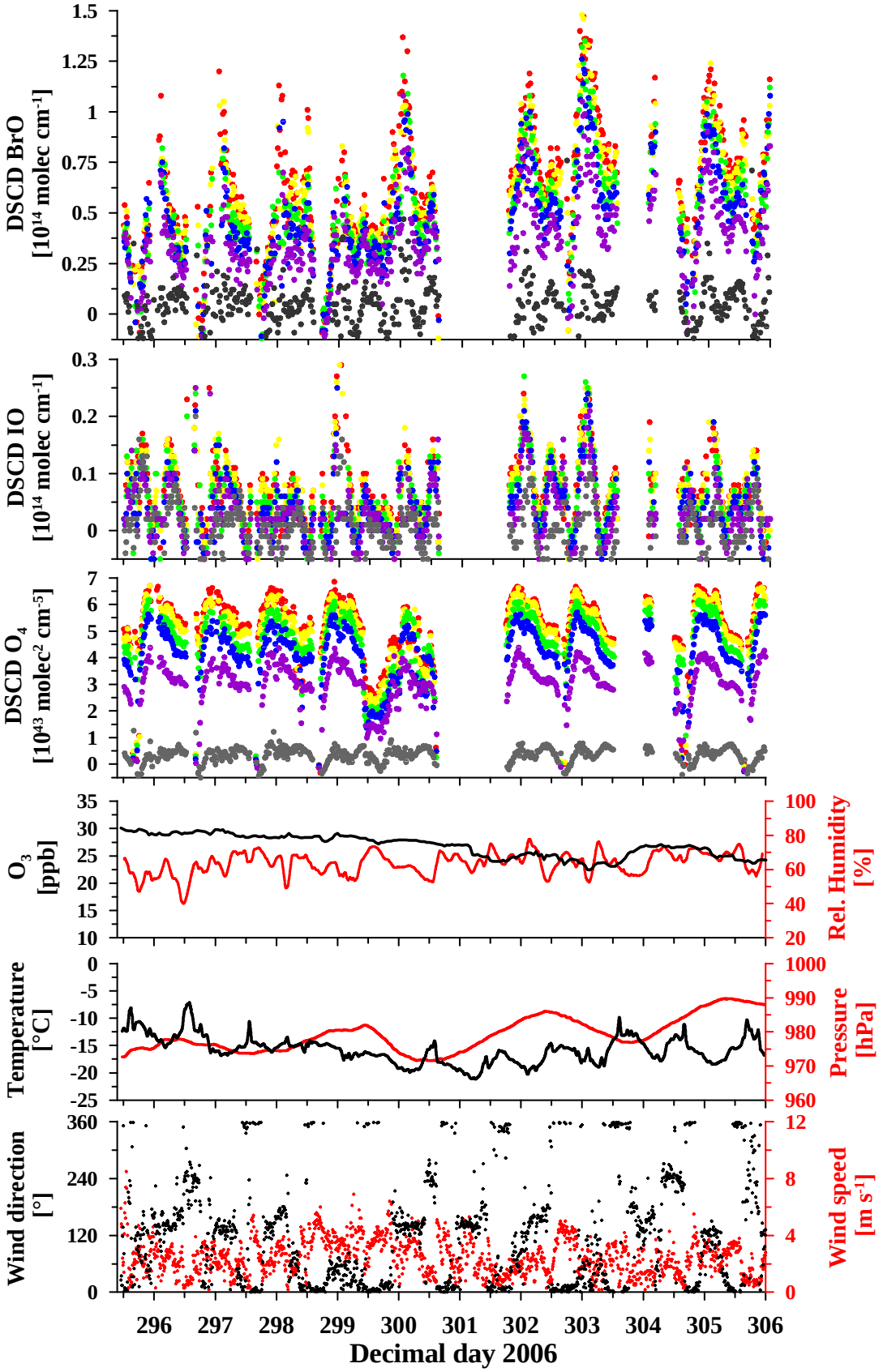

Figure 6.2: Part 1. BrO, IO and O_4 DSCDs, surface O_3 and surface meteorology at Cape Bird, 23rd October to 2nd November 2006.

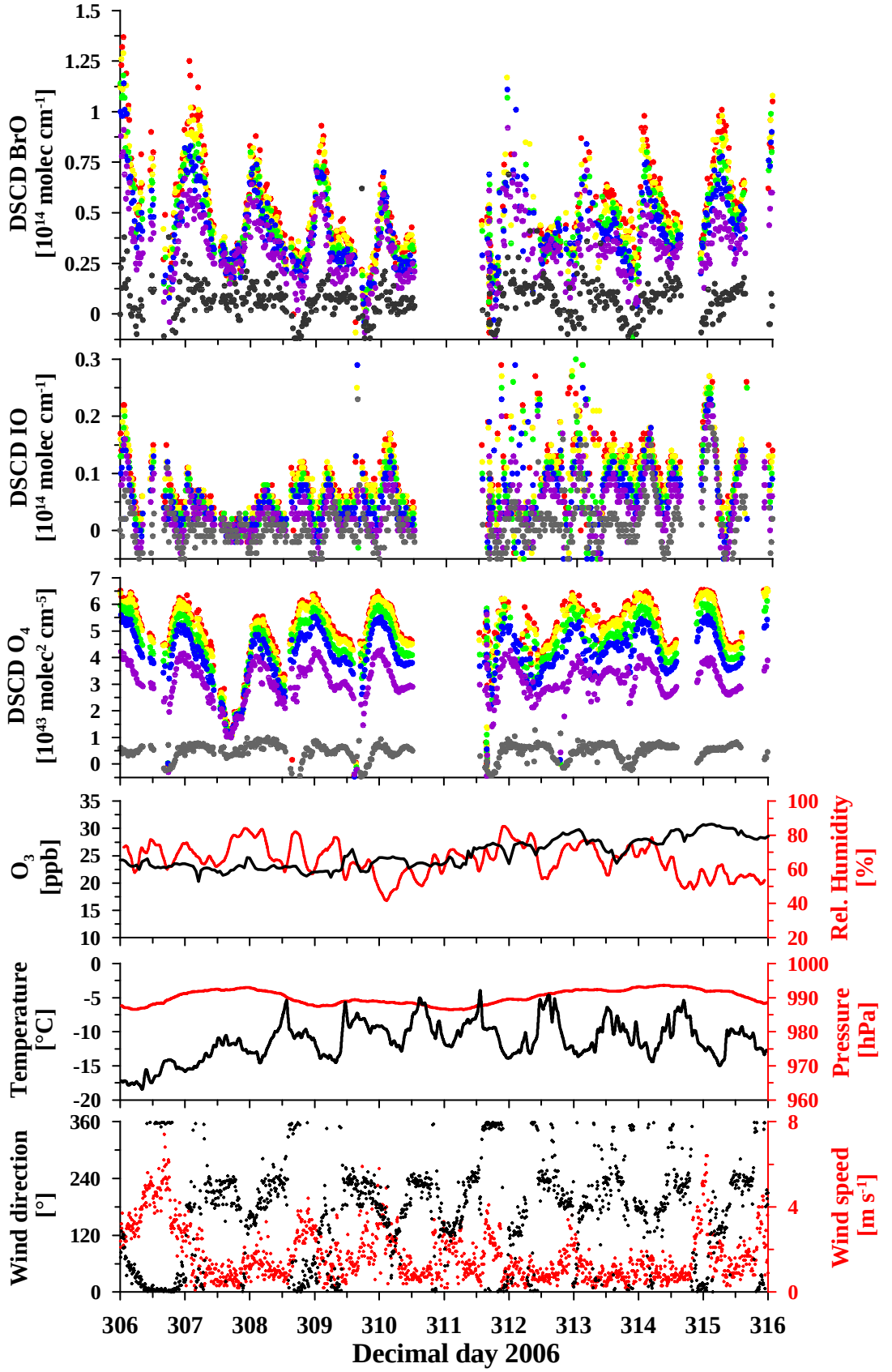

Figure 6.2 Part 2. BrO, IO and O_4 DSCDs, surface O_3 and surface meteorology at Cape Bird, 3rd to 12th November 2006.

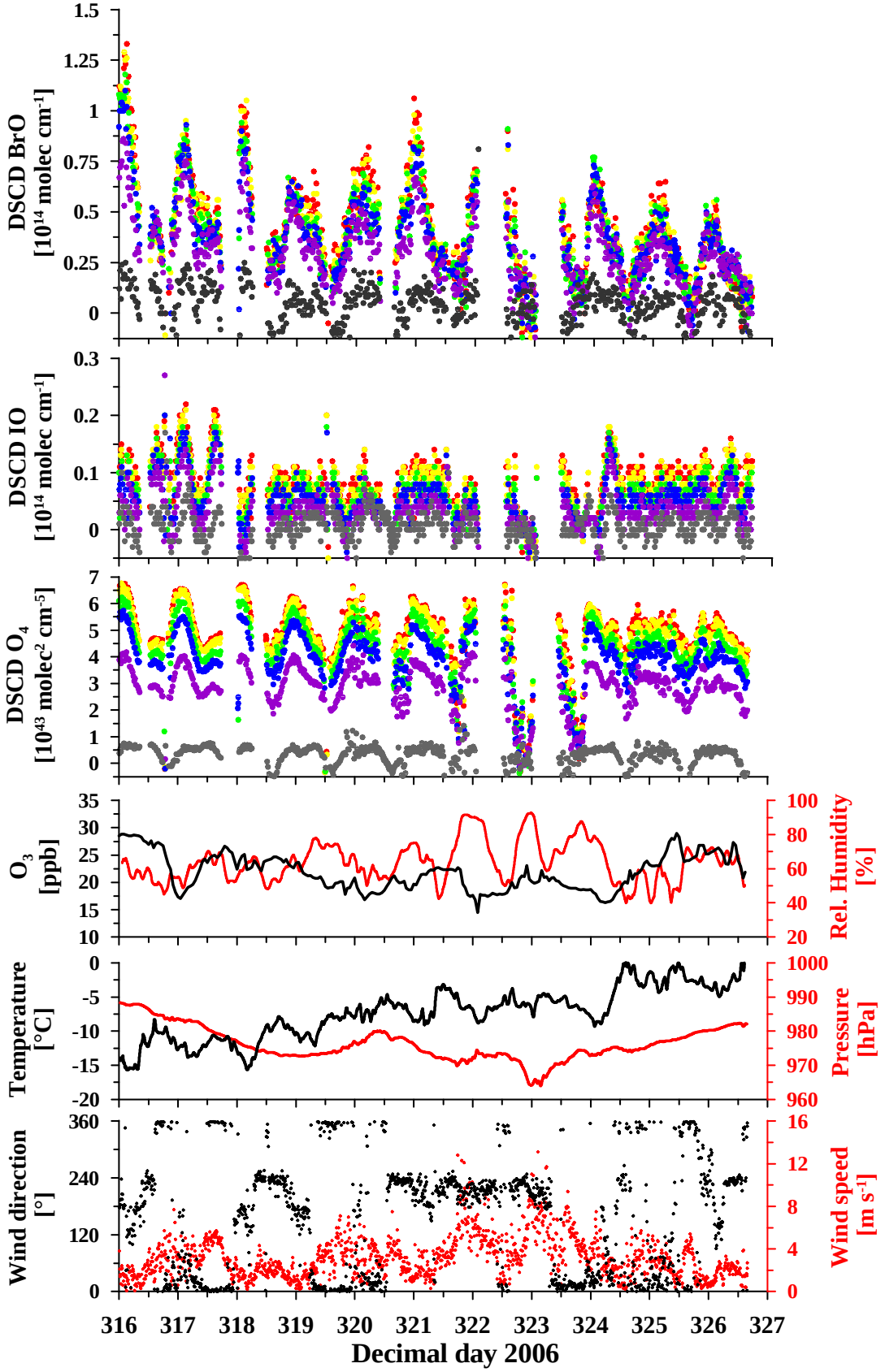

Figure 6.2 Part 3. BrO, IO and O_4 DSCDs, surface O_3 and surface meteorology at Cape Bird, 13th to 23rd November 2006.

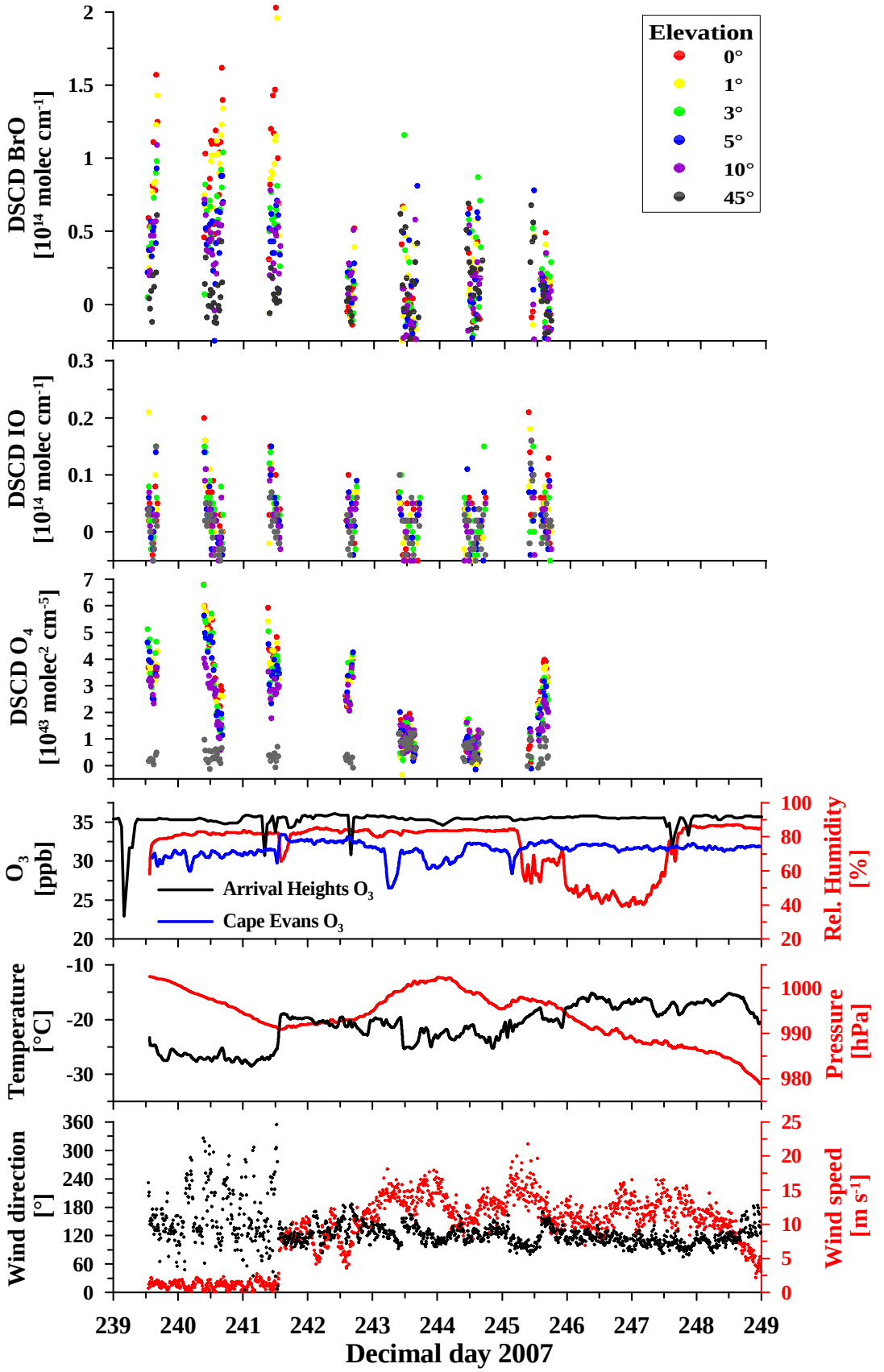

Figure 6.3: Part 1. BrO, IO and O_4 DSCDs, surface O_3 and surface meteorology at Cape Evans, 28th August to 6th September 2007.

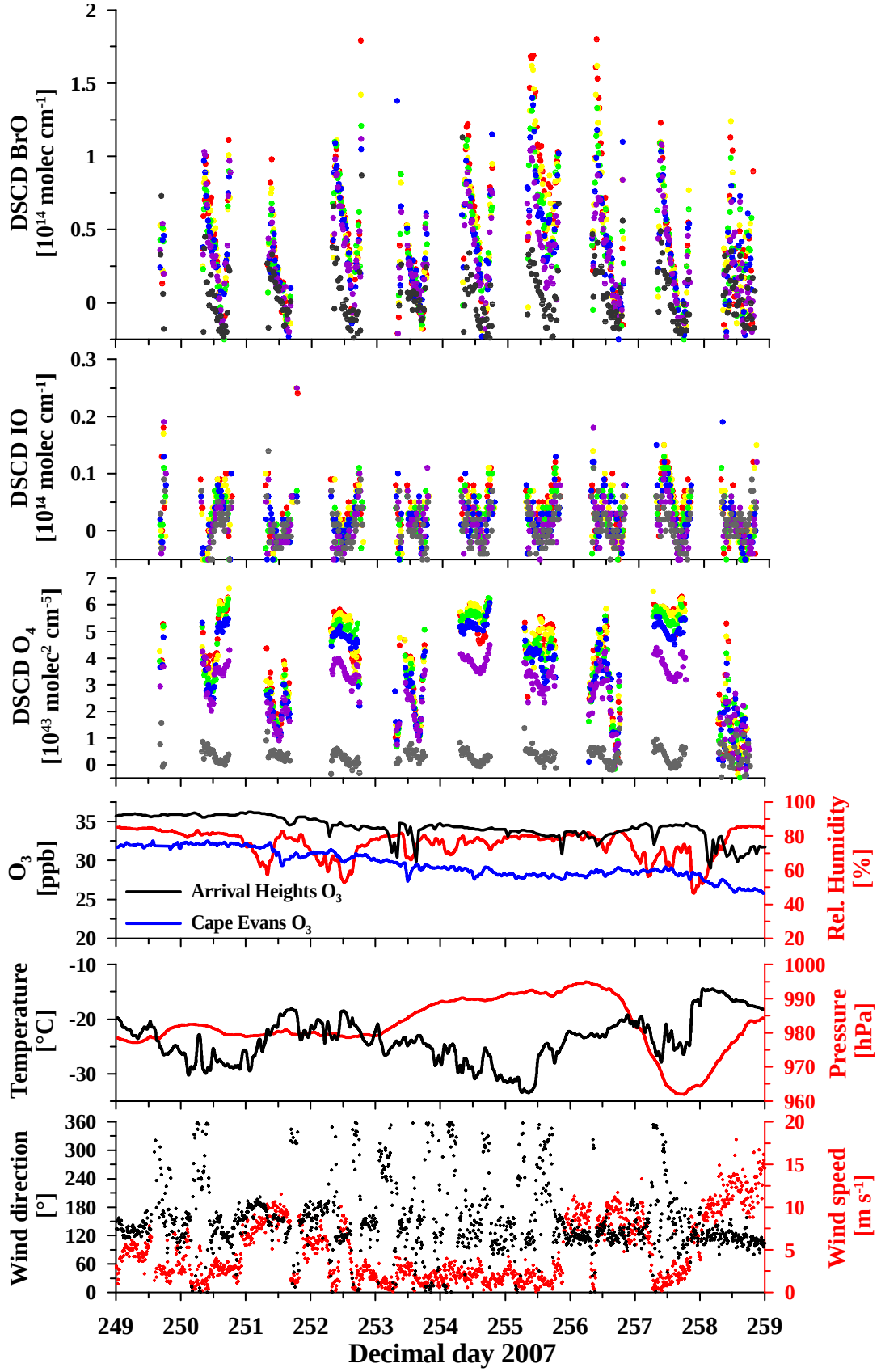

Figure 6.3 Part 2. BrO, IO and O_4 DSCDs, surface O_3 and surface meteorology at Cape Evans, 7th to 16th September 2007

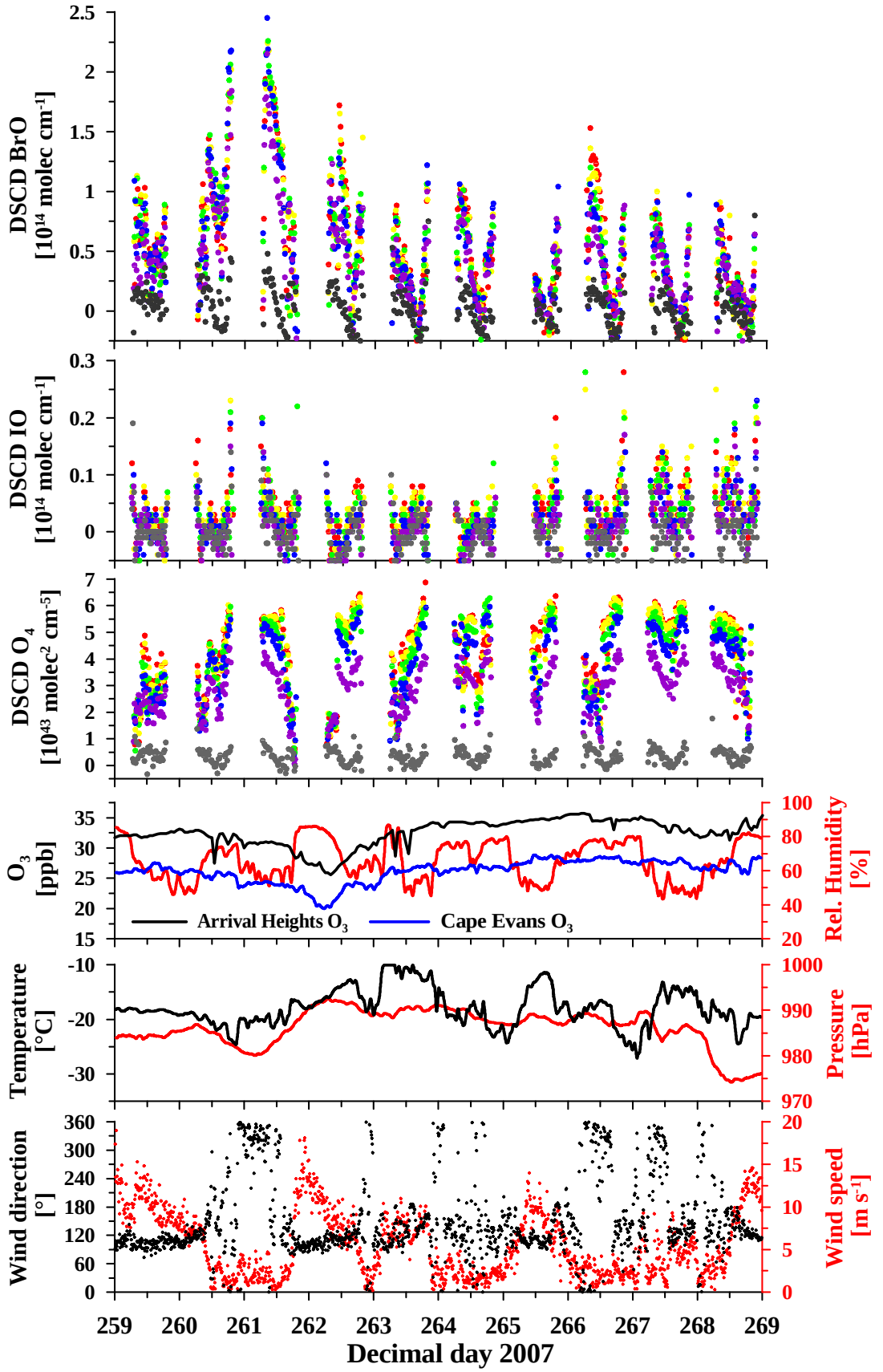

Figure 6.3 Part 3. BrO, IO and O_4 DSCDs, surface O_3 and surface meteorology at Cape Evans, 17th to 26th September 2007

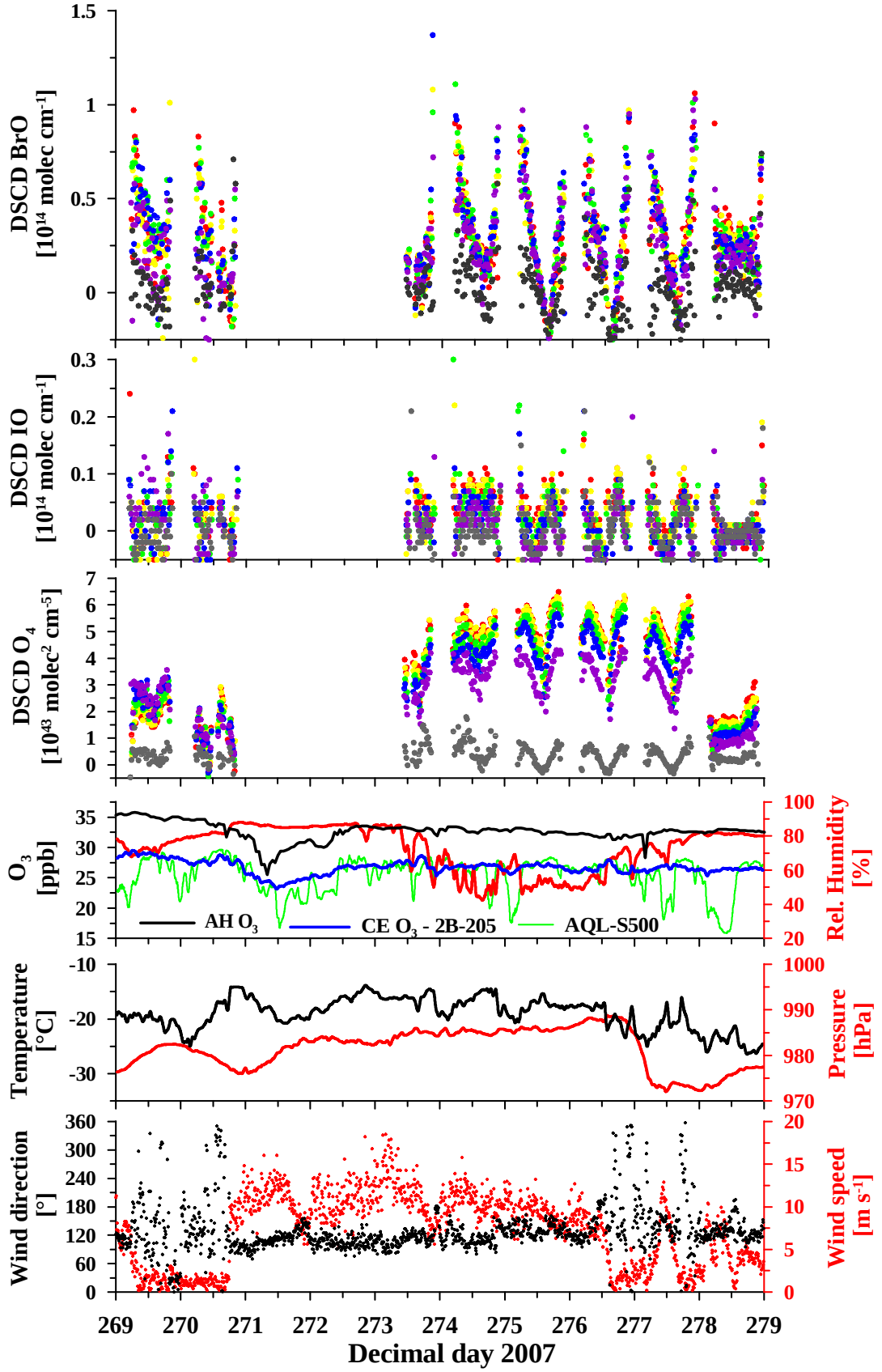

Figure 6.3 Part 4. BrO, IO and O_4 DSCDs, surface O_3 and surface meteorology at Cape Evans, 27th September to 6th October 2007

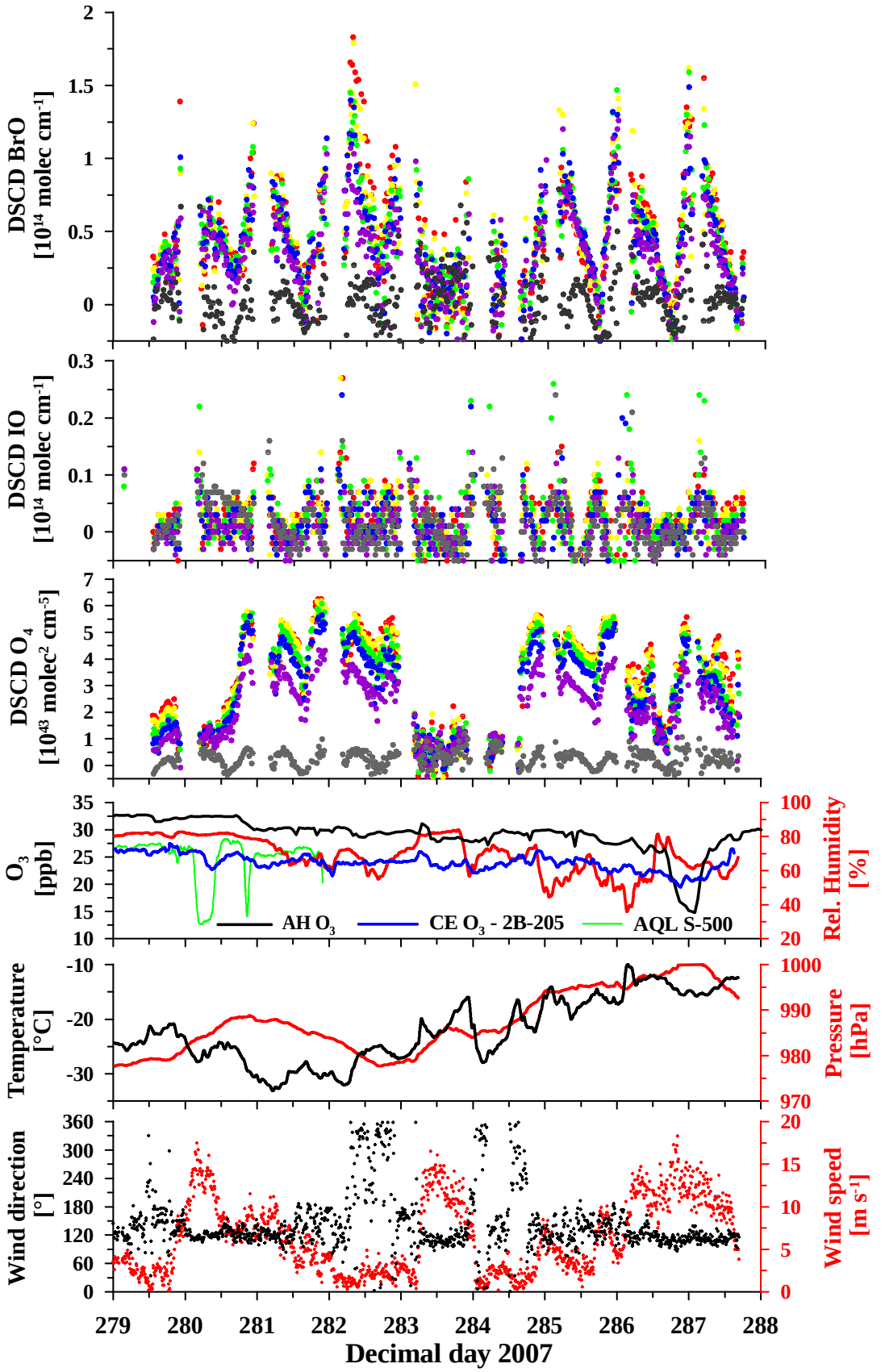

Figure 6.3 Part 5. BrO, IO and O_4 DSCDs, surface O_3 and surface meteorology at Cape Evans, 7th October to 15th October 2007

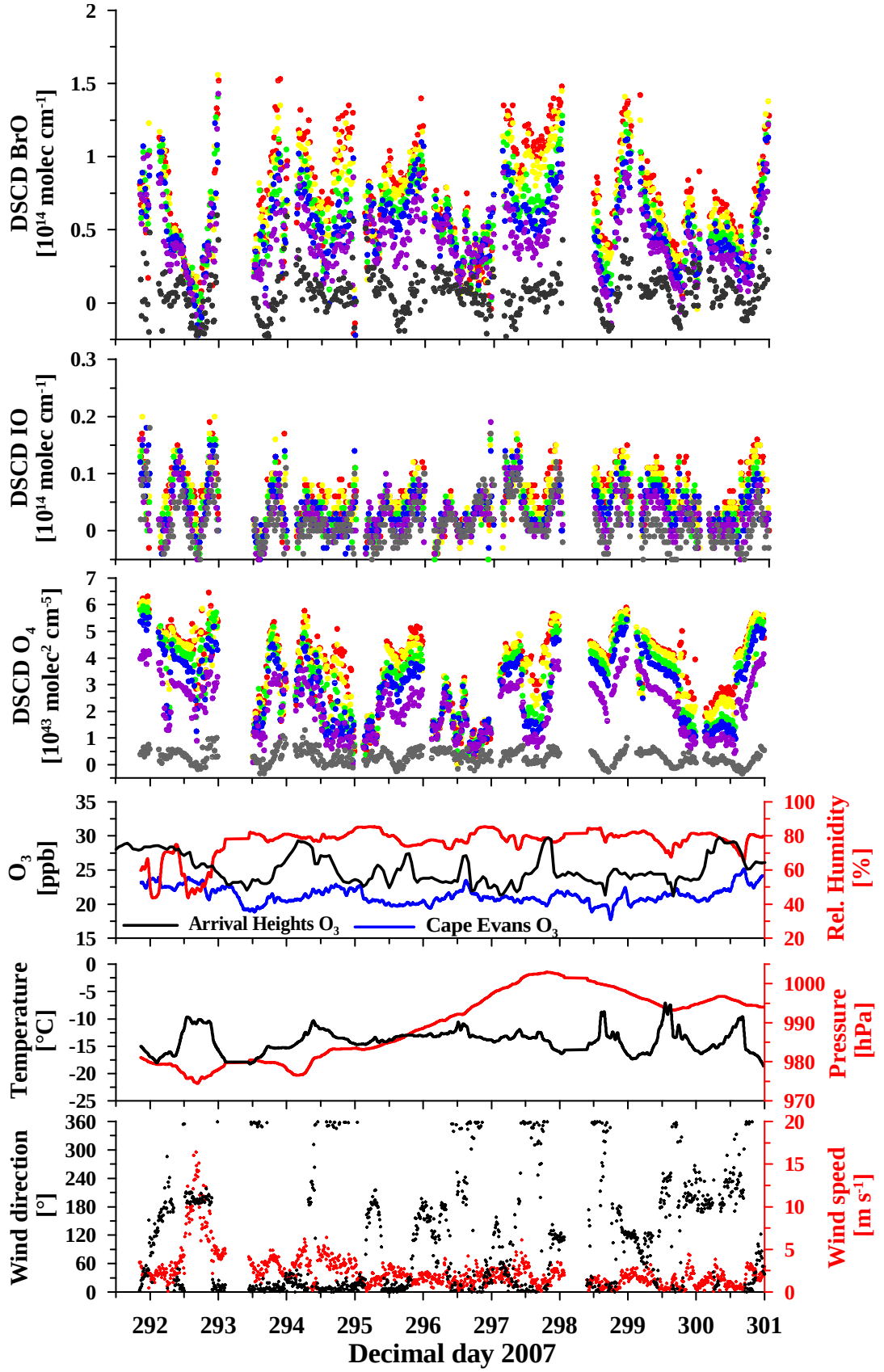

Figure 6.4: Part 1. BrO, IO and O_4 DSCDs, surface O_3 and surface meteorology at Cape Bird, 19rd to 28nd October 2007.

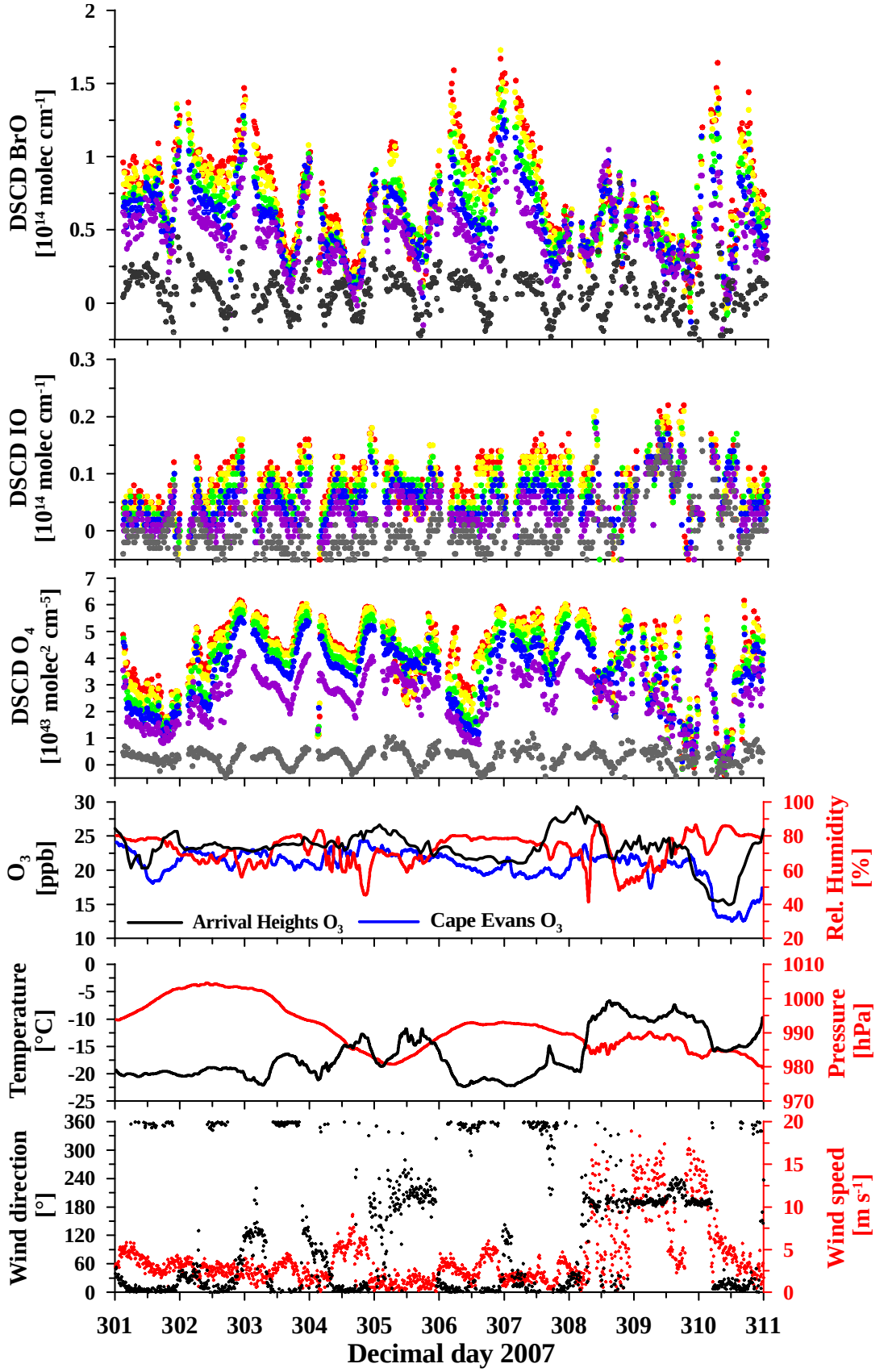

Figure 6.4 Part 2. BrO, IO and O_4 DSCDs, surface O_3 and surface meteorology at Cape Bird, 29th October to 7th November 2007.

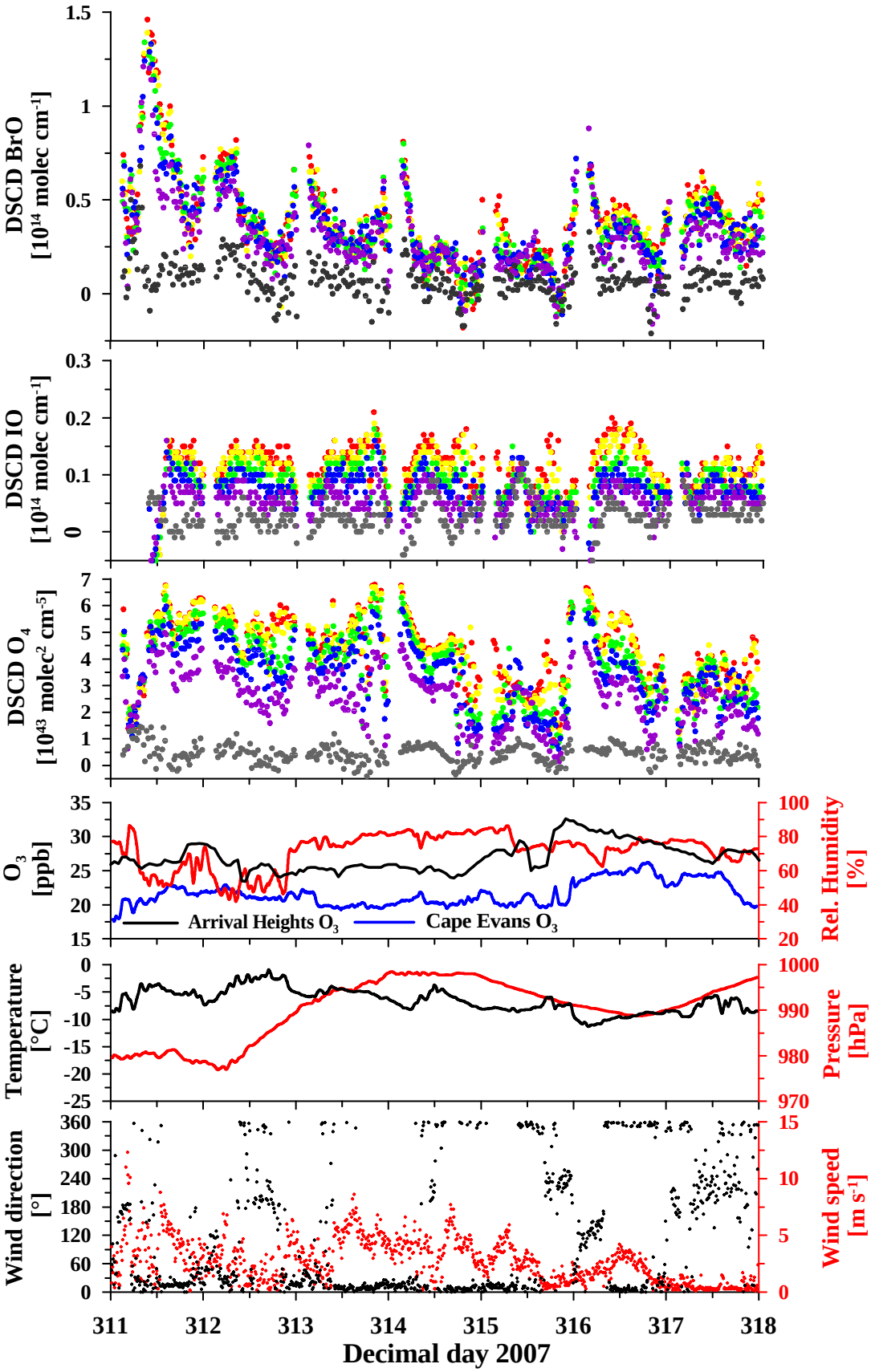

Figure 6.4 Part 3. BrO, IO and O_4 DSCDs, surface O_3 and surface meteorology at Cape Bird, 8th to 13th November 2007.

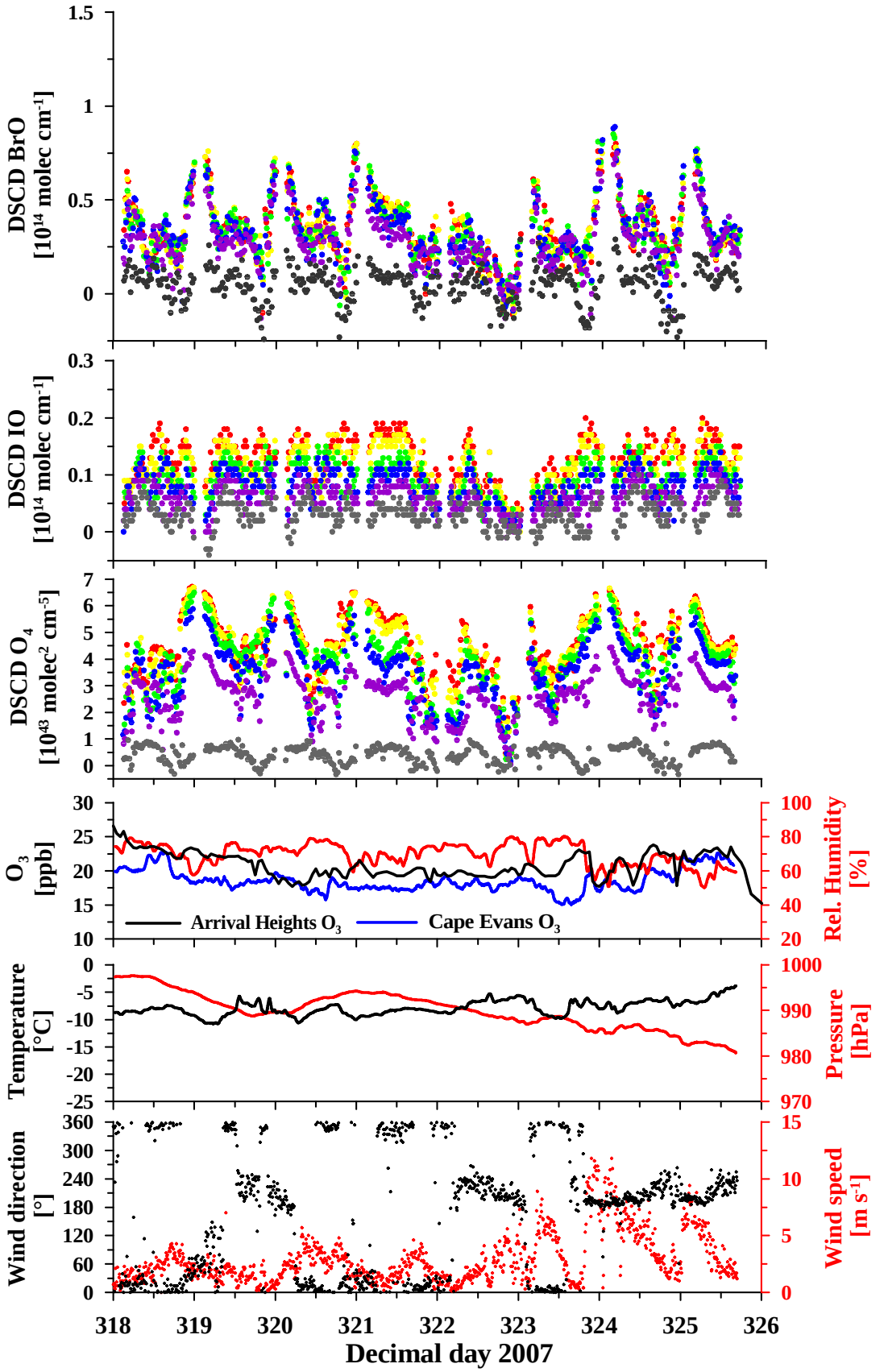

Figure 6.4 Part 4. BrO, IO and O_4 DSCDs, surface O_3 and surface meteorology at Cape Bird, 14th to 21st November 2007.

inversion and strong vertical mixing leading to the transport of bromine into the free troposphere and mixing of ozone into the boundary layer (Simpson et al., 2007b).

Elevated BrO DSCDs were observed during the event and rapidly dropped to background levels at about the same time that the ozone mixing ratio reached the minimum, but this may be coincidental with a decrease in visibility and thus a loss of measurement sensitivity. Multiple scattering in the fog and blowing snow results in similar light path lengths in all viewing directions, as clearly demonstrated by the overlapping O_4 DSCDs. It is nearly impossible to correctly model the paths using a radiative transfer model, and in addition, the measurements contain very little vertical information due to the similar light paths. In the morning, the BrO DSCDs were high for all viewing elevations (up to 2.5×10^{14} molec cm^{-2}) except for 45°, while the O_4 DSCDs were low in all directions, indicating that there was a high concentration of BrO near the surface. During blowing snow conditions in McMurdo Sound it was frequently observed that the layer of poor visibility extended only a few metres above the sea ice, consistent with observations by Mann et al. (2000). Thus, some part of the enhancement in the BrO DSCDs may have come from BrO present above the layer of fog and blowing snow, where the light paths would be longer. In the afternoon, both the BrO and O_4 DSCDs become very low, consistent with an observed decrease in visibility. It is possible that BrO was still present, but the equal AMFs in all viewing directions rendered the measurements totally insensitive.

The back trajectories for this day (see Sect. 6.4) indicate that the air–mass was most likely of continental origin rather than from sea ice zones to the north. This suggests that the event was locally produced rather than from transport. Previously, it has generally been assumed that the presence of a stable shallow inversion layer during calm conditions, which isolates the boundary layer air and thus concentrates the reactions, is crucial for a boundary layer ODE to occur (Lehrer et al., 2004; Simpson et al., 2007b; Anderson and Neff, 2008). ODEs that occur during storms have often been attributed to the transport of ozone–depleted air masses from first year sea–ice regions (Simpson et al., 2007b). One explanation may be that the heterogenous bromine explosion reactions are facilitated by large surface areas and increased ventilation on wind–blown saline ice and snow (Yang et al., 2008; Jones et al., 2009; Yang et al., 2010). Drifting and blowing snow has an effective surface area, in contact with the turbulent air, many orders of magnitude greater than stationary snow, and the ice particles are also well ventilated by continual sedimentation (Anderson and Neff, 2008).

Jones et al. (2009) modelled the effect of wind speed, linearly increasing the boundary layer height from 10 metres in calm conditions to over 100 metres at wind speeds of 20 m s^{-1}, and increasing the surface area and ventilation of snow and ice particles. Assuming sufficient Br^- ions and the correct pH are present in the ice, this trade–off leads to a maximum ODE potential in a calm stratified boundary layer and a second maximum at wind speeds of 15–20 m s^{-1}. Another possible trigger for the bromine explosion reactions during storm events could

be a decrease in pH, which can occur as the relative humidity increases (von Glasow and Sander, 2001; Simpson et al., 2007b). Yang et al. (2008) estimated sea salt aerosol production and bromine release during blowing snow events and suggested that the rate of aerosol production from blowing snow can be more than an order of magnitude greater per unit area than production rates on the open ocean under similar weather conditions.

Four partial ODEs were observed during the 2007 measurements. The first occurred from the 18$^{\text{th}}$ to 20$^{\text{th}}$ September (days 261–263), with a decrease of ozone by ∼7 ppb in 62 hours. Boundary layer BrO was observed during calm, relatively clear weather on days 261–262, with the peak retrieved boundary layer BrO for 2007 occurring on day 262, during which the surface ozone mixing ratio decreased from 27 ppb to 23 ppb within 48 hours. However, the most rapid decline in ozone, from 23 ppb to 20 ppb in 12 hours, occurred with the onset of high winds and blowing snow on the night of day 262–263. The wind direction changed from the north–westerly quarter to the prevailing east–southeasterly direction, the wind speed increased from $<5\,\mathrm{m\,s^{-1}}$ to $>12\,\mathrm{m\,s^{-1}}$, and the humidity increased from ∼55% to 85%. Similar to the pattern observed for the 2006 ODE, the ozone level started to increase as the humidity and wind speed decreased and it recovered to 24 ppb at the time when the humidity dropped to 60% and the wind speed reduced below $7\,\mathrm{m\,s^{-1}}$. The two bromine explosion events observed by Kreher et al. (1997) at Arrival Heights were also initiated during high surface winds, blowing snow and poor visibility, and recent studies give further evidence for bromine release during storms (Yang et al., 2008; Jones et al., 2009; Yang et al., 2010; Begoin et al., 2010).

The second partial ODE for 2007, occurred during a three day storm starting on the 29$^{\text{th}}$ September (day 272), for which the DSCDs are not usable as the tracker was covered by snow. Again, similar to the ODE in 2006, the start of the ozone decline coincided with the arrival of the storm, with an increase in mean wind speeds from $<2.5\,\mathrm{m\,s^{-1}}$ to $>7.5\,\mathrm{m\,s^{-1}}$, an increase in relative humidity from ∼80 to 90%, a temperature increase from -25°C to -15°C and an initial drop in pressure. The ozone mixing ratio decreased from approximately 28 ppb to 24 ppb in ∼20 hours and slowly recovered back to 28 ppb after a further 48 hours when the humidity and wind speed started to decline.

The third ODE in 2007 occurred during high winds of $10–15\,\mathrm{m\,s^{-1}}$ and increased humidity from the afternoon of 14$^{\text{th}}$ October (day 287) to midday on the 15$^{\text{th}}$ October (day 288). The surface ozone on the sea ice only decreased slightly, but the ozone mixing ratio at Arrival Heights declined from ∼28 ppb to 15 ppb, which was less than the ozone on the sea ice at Cape Evans (∼20 ppb). This may have been due to an elevated air–mass depleted in ozone, transported from first year sea ice zones, as discussed in Sect. 6.4.

It is less clear to identify specific ozone minima from mid–October onwards where the ozone levels measured at both Arrival Heights and Cape Bird are more variable than in the first half of the spring, and show a declining trend. The

gradual decline in surface ozone from August to November follows the annual cycle typical for polar regions, with a maximum during the dark winter months due to weak ozone sinks, and a minimum during the late spring and summer when the ozone sinks are greater than the sources from production and transport (Helmig et al., 2007). The increased variability and the decline in surface ozone during this period could also be attributed to the presence of open leads and the breaking up and refreezing of sea ice, increasing the availability of saline snow and ice surfaces, including frost flowers (Kaleschke et al., 2004), and increasing the relative humidity, which in turn may lead to a reduction in pH necessary for ozone depletion reactions (Mozurkewich, 1995; von Glasow and Sander, 2001; Simpson et al., 2007b). However,by the end of November, the warmer temperatures start to become unfavourable for the bromine explosion reactions (Piot and von Glasow, 2008).

A clear ozone minimum occurred at both Cape Bird and Arrival Heights on the 7$^{\text{th}}$ November (day 311) 2007. It was snowing and foggy at Cape Bird in the morning with strong winds from the south, often $>15\,\mathrm{m\,s^{-1}}$, and the surface ozone decreased from $\sim$23 to $\sim$13 ppb in 12 hours. The ozone started to recover soon after the wind direction changed to the prevailing northerly and the wind speed dropped below $5\,\mathrm{m\,s^{-1}}$. The weather cleared in the afternoon and the peak retrieved surface BrO of $\sim$8 ppb (see Sect. 6.3.2) was observed at the same time as the ozone started increasing.

6.3 Retrieval of boundary layer BrO and IO profiles

6.3.1 Retrieval settings

One temperature–pressure profile was used for all the retrievals, based on the mean of McMurdo Station radiosonde measurements for September and October 2007.

Climatological aerosol extinction profiles from 6–30 km were calculated from Light Detection and Ranging (LIDAR) backscatter ratios measured at McMurdo Station between 25$^{\text{th}}$ August and 30$^{\text{th}}$ 1990–1991 and 1994–2003. Measurements of Polar Stratospheric Clouds (PSCs) were excluded as well as measurements from 1991–1993 to avoid elevated aerosols from the Pinatubo eruption. LIDAR data was obtained from ftp.cpc.ncep.noaa.gov/ndacc/station/mcmurdo/ames/lidar/. The aerosol extinction coefficients were converted from the LIDAR wavelength of 532 nm to the DOAS wavelength using the relation

$$\beta(\lambda) = \beta(\lambda_0) \left(\frac{\lambda_0}{\lambda} \right)^{\alpha} \tag{6.1}$$

where $\beta(\lambda)$ and $\beta(\lambda_0)$ are the volume scattering coefficients for the DOAS wavelength λ and the LIDAR wavelength λ_0 respectively, and α is the Angstrom exponent, which is related to the size distribution of the aerosols. An Angstrom

exponent of 1.2 was used, based on sunphotometer measurements (Shaw, 1980). The lower tropospheric component of the aerosol profiles was based on typical wintertime aerosol optical depth (AOD) measurements for Lauder, New Zealand, since the aerosol optical depths there are comparable to Antarctica (Shaw, 1980; Liley and Forgan, 2009). The mean Angstrom component for Lauder, of ∼1.2 (Liley and Forgan, 2009), was used to scale the extinction values to the correct wavelength. The AOD at 350 nm was 0.012 from the surface to 3 km, 0.0149 for the troposphere and 0.002 for the stratosphere. The AOD at 427 nm was 0.0095 from the surface to 3 km, 0.012 for the troposphere and 0.0016 for the stratosphere.

A single scattering albedo of 0.99 was chosen as an approximate representative value for unpolluted sea salt aerosols (Anderson et al., 1999; Dubovik et al., 2002; Hu et al., 2007; Kudo et al., 2008). A Henyey–Greenstein asymmetry parameter of 0.7 was used for BrO at 350 nm based on (Kudo et al., 2008) and 0.65 for IO at 427 nm based on values for marine aerosols given by Fiebig and Ogren (2006).

A surface albedo of 0.8 was used, based on SUV–100 spectroradiometer measurements at Arrival Heights from September to November (Bernhard et al., 2006) and broadband measurements for first year sea ice measured by Brandt et al. (2005). The albedo is highest for fresh snow surfaces and decreases as the snow melts and becomes contaminated with aerosols or particulates (Grenfell and Perovich, 2004; Light et al., 1998; Perovich et al., 2002). The surface albedo also tends to be higher under cloudy conditions than clear sky conditions (Brandt et al., 2005). The surface albedo at Cape Bird is likely to be more variable than at McMurdo and Cape Evans because the sea ice was often broken, with wide leads of open water (albedo of about 0.07 in the visible region (Brandt et al., 2005)), and exposed rock on the beach and cliffs behind the instrument. In addition, surface albedo varies with wavelength (Grenfell and Perovich, 2004), and albedos for surfaces not covered in snow or ice tend to be much lower in the UV region than in the visible (McKenzie et al., 1996; Wuttke et al., 2006). However, in the absence of specific data, a surface albedo value of 0.8 was chosen for the retrievals of all measurements. Wittrock et al. (2004) demonstrated that using an inappropriate surface albedo only has a significant effect on the retrieved vertical columns in the viewing azimuth direction towards the Sun (see Chap. 4). This is a potential source of inaccuracy in the radiative transfer calculations for measurements taken during short periods of an hour or so in the afternoons when the Sun passed across the instrument viewing azimuth direction, which was towards the north–west.

Surface topography also influences the light paths, but the effect is expected to be relatively small since the viewing direction of the instrument was always unobstructed across the sea ice. Surface topography was not included in the radiative transfer calculations.

For BrO, a fixed *a priori* profile was created with a grid resolution of 50 metres and a mixing ratio of 1 ppt at the surface, linearly decreasing to 0.1 ppt at 3 km. The maximum altitude was chosen based on the information contained in the

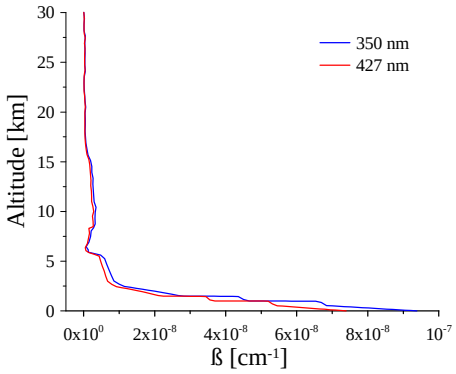

Figure 6.5: Aerosol profiles used in the BrO (350 nm) and IO (427 nm) retrievals, based on a typical Lauder profile for June from 0–5.5 km and on McMurdo LIDAR measurements for 1990–1991 and 1994–2003 for 6–30 km.

weighting functions at 350 nm, which rapidly decreases above 2 km (see Chap. 5). The error covariance matrix $\mathbf{S}_a$ was constructed with variances on the diagonal equal to $(1.2 \times x_a)^2$ at each altitude level, with the error percentage level selected using the L–curve shown in Fig. 6.6. The extra–diagonal covariance terms were determined using Gaussian correlation functions with a correlation length of 25 metres (see Chap. 5).

For IO, a fixed *a priori* profile was created with a grid resolution of 20 metres and a mixing ratio of 0.5 ppt at the surface, linearly decreasing to 0.05 ppt at 2 km. The error covariance matrix $\mathbf{S}_a$ was constructed with variances on the diagonal equal to $(1.0 \times x_a)^2$ at each altitude level, with the error percentage level selected using the L–curve shown in Fig. 6.6. The extra–diagonal covariance terms were determined using Gaussian correlation functions with a correlation length of 10 metres (see Chap. 5).

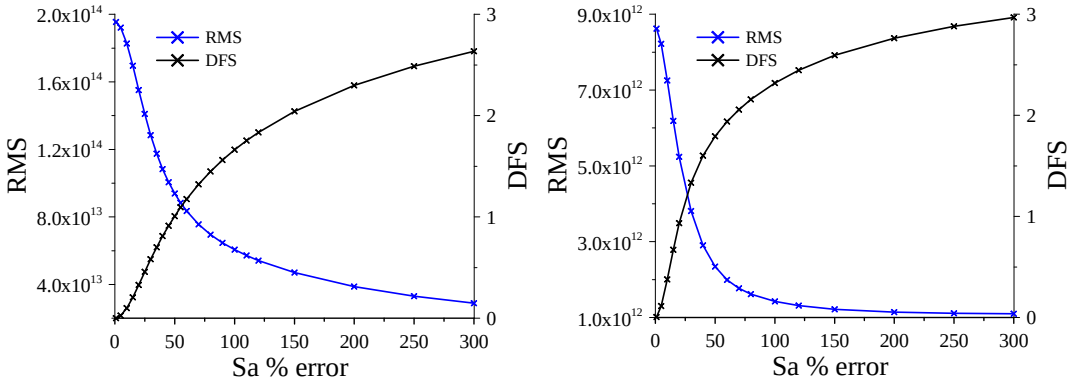

Figure 6.6: L–curves for the BrO profile retrieval (left) from the measurements on 19$^{\text{th}}$ of September, 2007 (Day 262) at Cape Evans, and for the IO profile retrieval (right) for 13$^{\text{th}}$ November 2007 (Day 317).

One profile was retrieved for each set of seven elevation angles (0°, 1°, 3°, 5°, 10°, 45°, 90°), taking approximately 21 minutes (three minutes accumulation time per elevation). An extra angle of 20° was added from the 3rd November 2007 onwards, making the total scan time 24 minutes. Thus, over 60 profiles were retrieved per day for measurements in the second part of the season with 24–hour daylight.

6.3.2 BrO profiles

The DSCDs shown in Sect. 6.1 indicate that boundary layer BrO was present on several days in both 2006 and 2007. However, the weather was frequently cloudy, or there was blowing or falling snow, making it very difficult to accurately model the scattering. Therefore, using cloud cover observations and webcam images of the sky taken at the instrument site, several "golden" days, with minimal or no cloud cover, were selected for profile retrievals. Retrieved diurnal BrO profiles from four "golden" days in each year are displayed in Figs. 6.7 and 6.8. The peak profile for each day is shown in the line plots with the retrieval errors indicated by error bars.

In general, the retrieved BrO was concentrated in the layer from the surface to 50 m, which is consistent with some studies of boundary layer height over the sea ice (Jones et al., 2009), but lower than other cases (Frieß et al., 2004). Simpson et al. (2007b) reviewed several studies and gave a typical height range for ODEs of 100–400 m. However, the retrieved profiles are also constrained by the information available from the measurements, which is greatest near the surface, and by the *a priori* profile shape, so lifted or thick trace gas layers are typically not well reproduced by the retrieval (see Chap. 5). The mean degrees of freedom for the 50 m surface layer for all retrieved days in 2006 and 2007 is 0.8±0.1, indicating that most of the information about the lowest layer has come from the measurements rather than from the *a priori*. The retrieved BrO profiles on the 19th September 2007 (Fig. 6.8) indicate that the boundary layer, containing BrO, was much higher than on most other days, despite the relatively low wind speeds in the morning. The surface BrO values retrieved on this day possibly overestimate the true surface BrO mixing ratios, and a better estimate may be obtained by assuming an evenly mixed layer up to 100 m, where one degree of freedom for signal (DFS) is retrieved from the measurements, giving a mixing ratio of ∼9.5 ppt instead of ∼11.3 ppt. The potential temperature profile from the radiosonde sounding at McMurdo Station on this day (not shown) has multiple inversion layers from the surface to ∼100 m, 100–250 m, 250–600 m and 600–1400 m (see Sect. 6.5).

As there were very few clear days, especially in 2007, retrievals were also performed on cloudy or partially cloudy days, which were chosen using the O_4 DSCDs as described in Sect. 6.1. Surface BrO mixing ratios as a function of SZA are displayed for all retrieved days in Figs. 6.9 and 6.10 for 2006 and 2007 respectively.

For most days, there is a clear pattern of diurnal variation with a peak in BrO

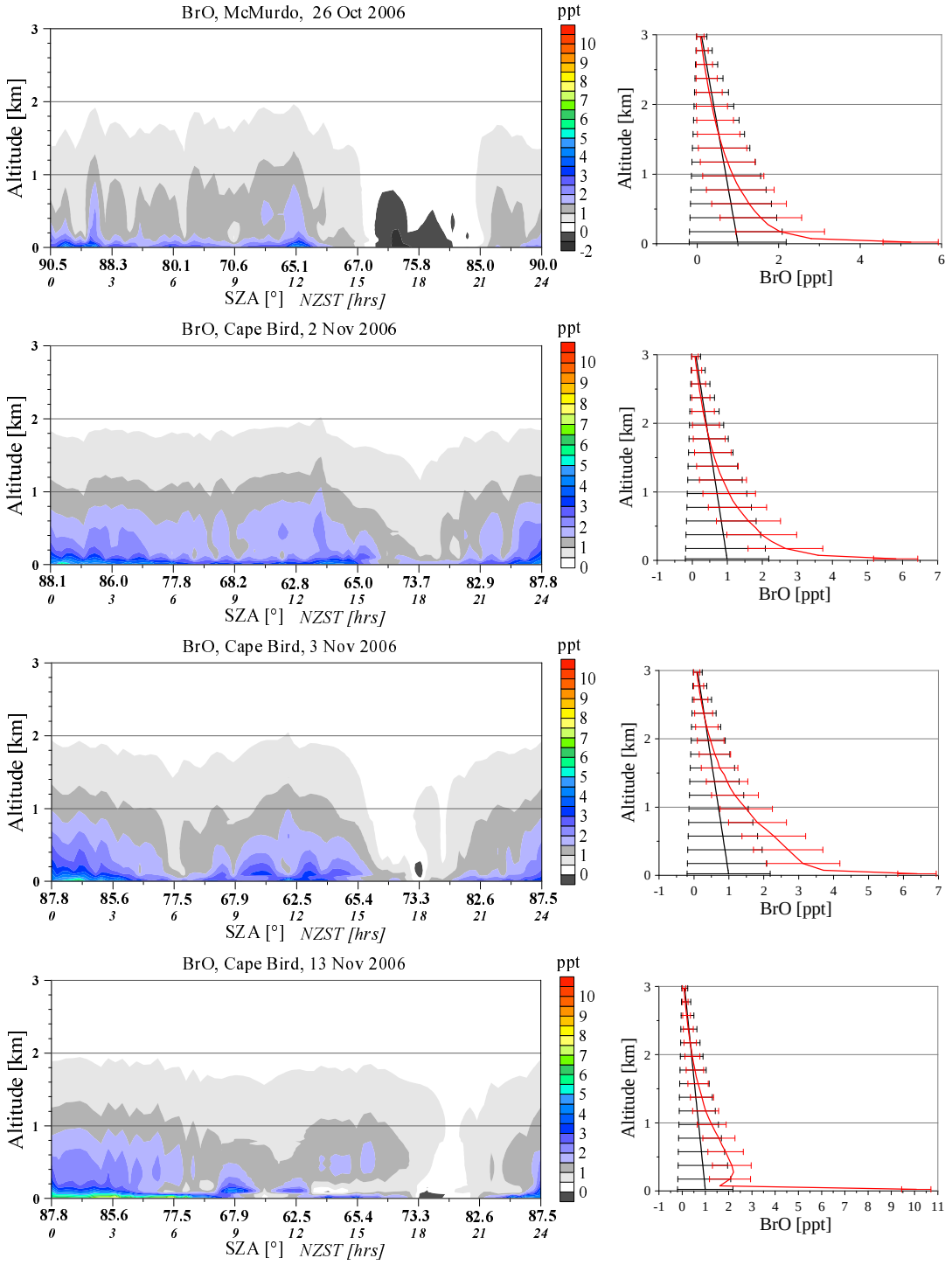

Figure 6.7: BrO mixing ratio profiles retrieved for four "golden days" of 2006. The *a priori* (black) and retrieved (red) profiles with errors for the highest surface mixing ratios for each day for are shown in the right–hand plots.

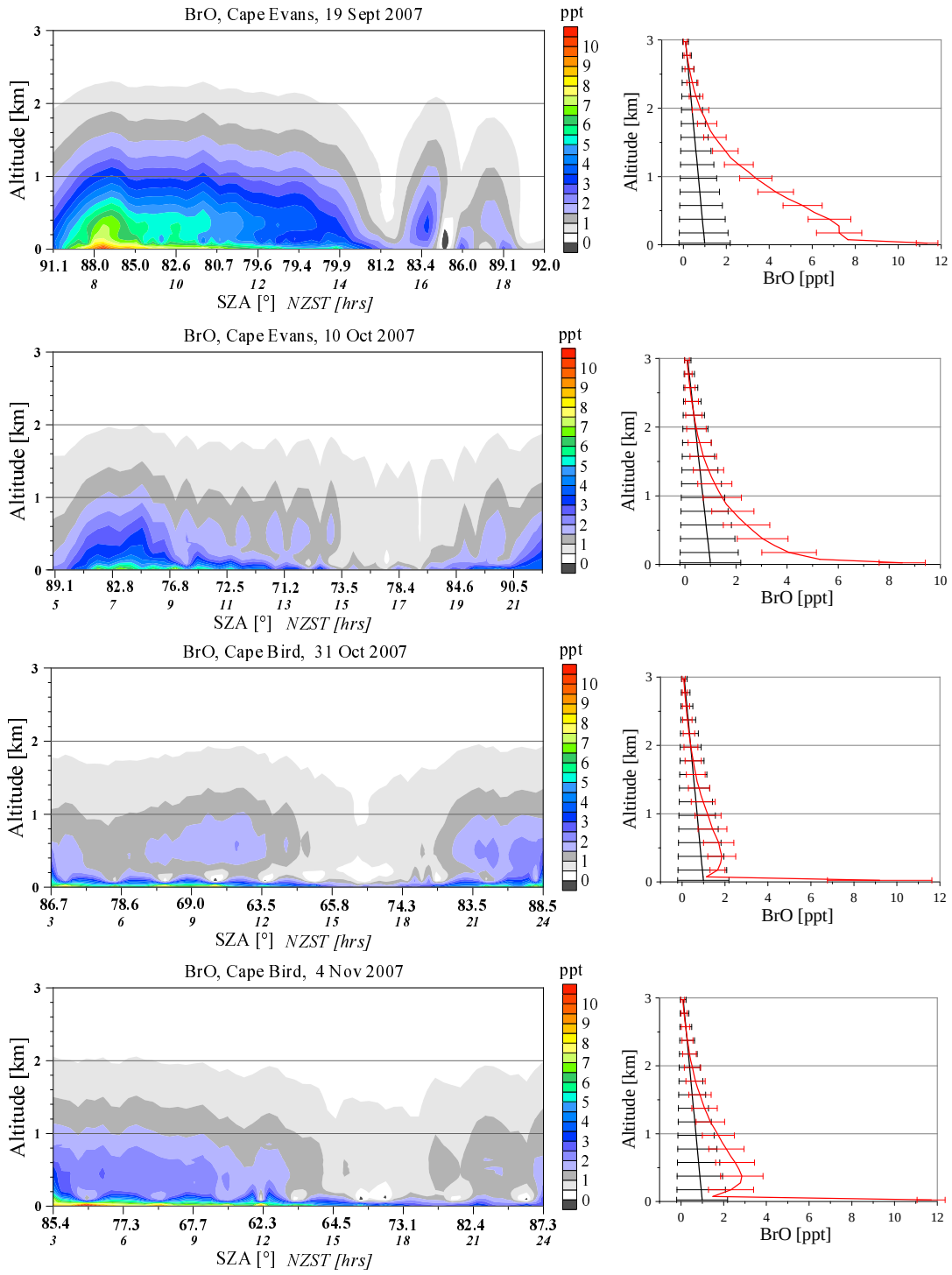

Figure 6.8: BrO mixing ratio profiles retrieved for four "golden days" of 2007. The *a priori* (black) and retrieved (red) profiles with errors for the highest surface mixing ratios for each day for are shown in the right–hand plots.

at or near the highest SZAs in the morning and evening. Note, the upper plot in Fig. 6.10 shows days in September 2007, whereas the first retrieved days for 2006 in Fig. 6.9 are from October. In September, the BrO concentrations are initially low before sunrise and rapidly increase to a peak at around 86°–88° SZA. During the long nights in September, the photolysis of Br_2 ceases and bromine is taken up into reservoir species or deposited into the snow pack (Simpson et al., 2007b). In the absence of photochemistry, the boundary layer lifetime of BrO is about two hours (Saiz-Lopez et al., 2007b).

The highest photolysis rates of Br_2 occur when Sun is at the smallest SZA, therefore it follows that the highest BrO concentrations should occur around midday. Additionally, the transfer of bromine from the aqueous phase to the gas phase is dependent on the formation of HOBr from HO_2, via the photolysis of O_3 (von Glasow et al., 2002), which also has a maximum at midday. The diurnal variation of both BrO and IO observed by Saiz-Lopez et al. (2007b) at Halley Station, for example, was correlated with the amount of solar radiation. However, at high SZA the multiple molecular scattering in the lower troposphere leads to strong attenuation of shorter wavelengths relative to longer wavelengths. The photolysis of Br_2 and BrCl is more efficient for wavelengths in the visible region than the photolysis of O_3, so the production of OH and HO_2 starts later and finishes earlier in the day than the production of Br, resulting in the morning and evening BrO peaks. At midday, the photolysis rate of O_3 has a sharper peak than the photolysis of Br_2, so the concentrations of HO_2 are sufficiently high to reduce the BrO mixing ratios (von Glasow et al., 2002; Pöhler et al., 2010).

Fig. 6.11 displays the daily maximum BrO partial VCDs for the two lowest retrieval layers from the surface to 100 m and for the layers from 100 m to 1 km and 1 km to 3 km. The retrieved mixing ratios and partial VCDs are generally lower in 2006 than in 2007. As demonstrated for NO_2 retrievals in Chap. 5, the partial VCDs are a more reliable retrieval product than the profile shape.

The combined DFS for the daily peak BrO VCDs in the two lowest layers is 0.95±0.09 for 2006 and 1.0±0.1 for 2007. The total degrees of freedom for the daily peak VCD is 1.7±0.2 with Shannon information content H=1.8±0.4 in 2006 and 1.8±0.3 with H=2.0±0.6 in 2007. Thus, about two independent pieces of information are obtained from the measurements. The daily peaks in the BrO VCDs tend to occur at high SZA, which is where the light intensity is the lowest and the signal–to–noise ratios in the measurements are therefore also relatively low. This generally results in slightly lower DFS for the times of the peak profiles relative to the retrieved profiles at lower SZA as shown for 19th September (day 262) 2007 in Fig. 6.12. Most of the information content, as well as the retrieved trace gas VCD above 100 m, is below 1 km.

The retrieved BrO mixing ratios for the surface layer up to 50 m and the two combined layers up to 100 m, together with the mercury concentrations in the snow samples (see Sect. 6.6), are summarized in the box and whisker plot in Fig. 6.13. Since the retrieved BrO mixing ratios do not follow a Gaussian distribution, a

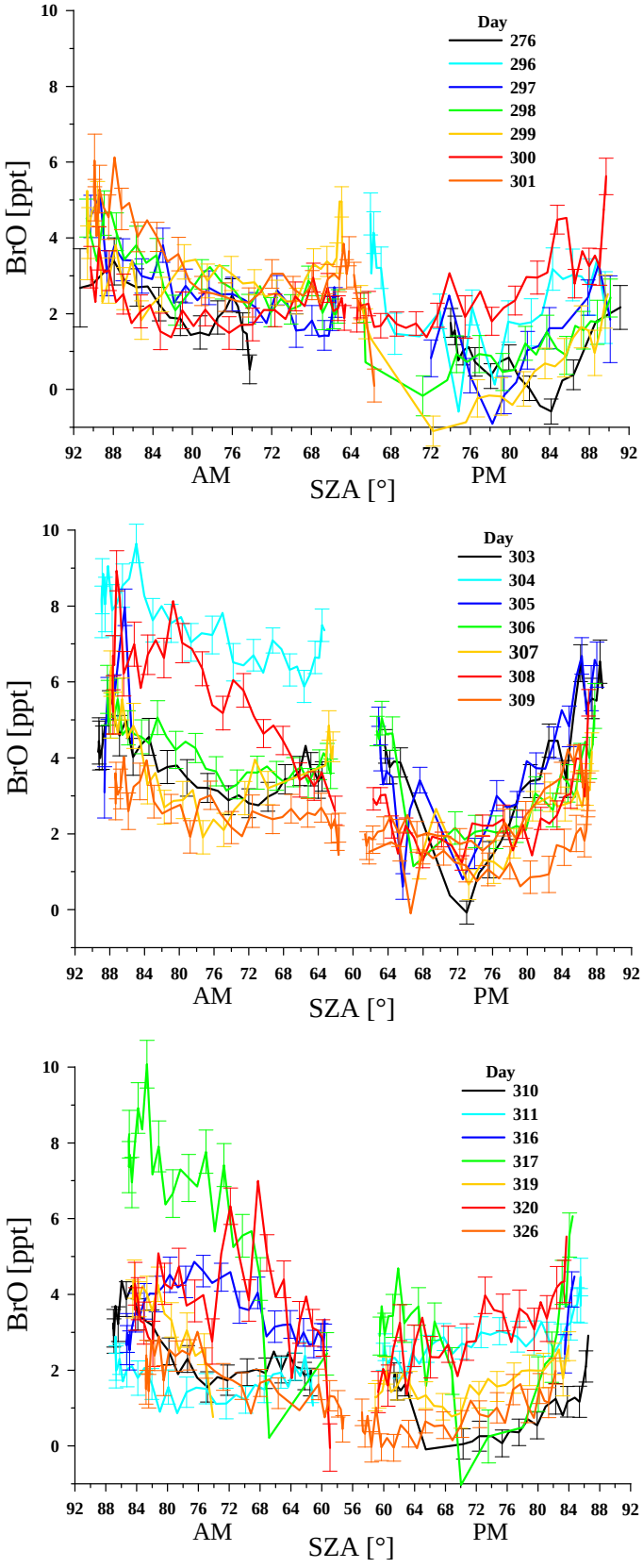

Figure 6.9: Retrieved BrO surface mixing ratios for early (top), mid (middle) and late (bottom) season 2006.

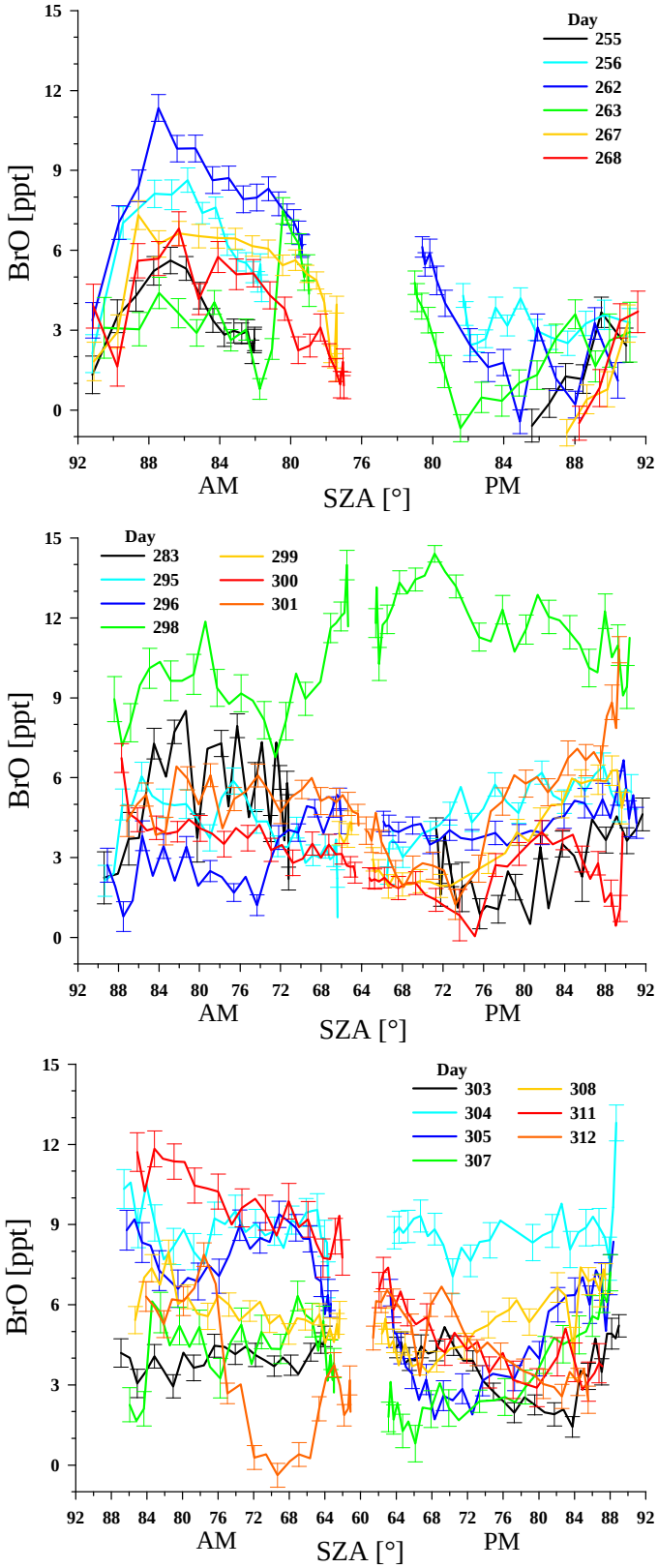

Figure 6.10: Retrieved BrO surface mixing ratios for early (top), mid (middle) and late (bottom) season 2007.

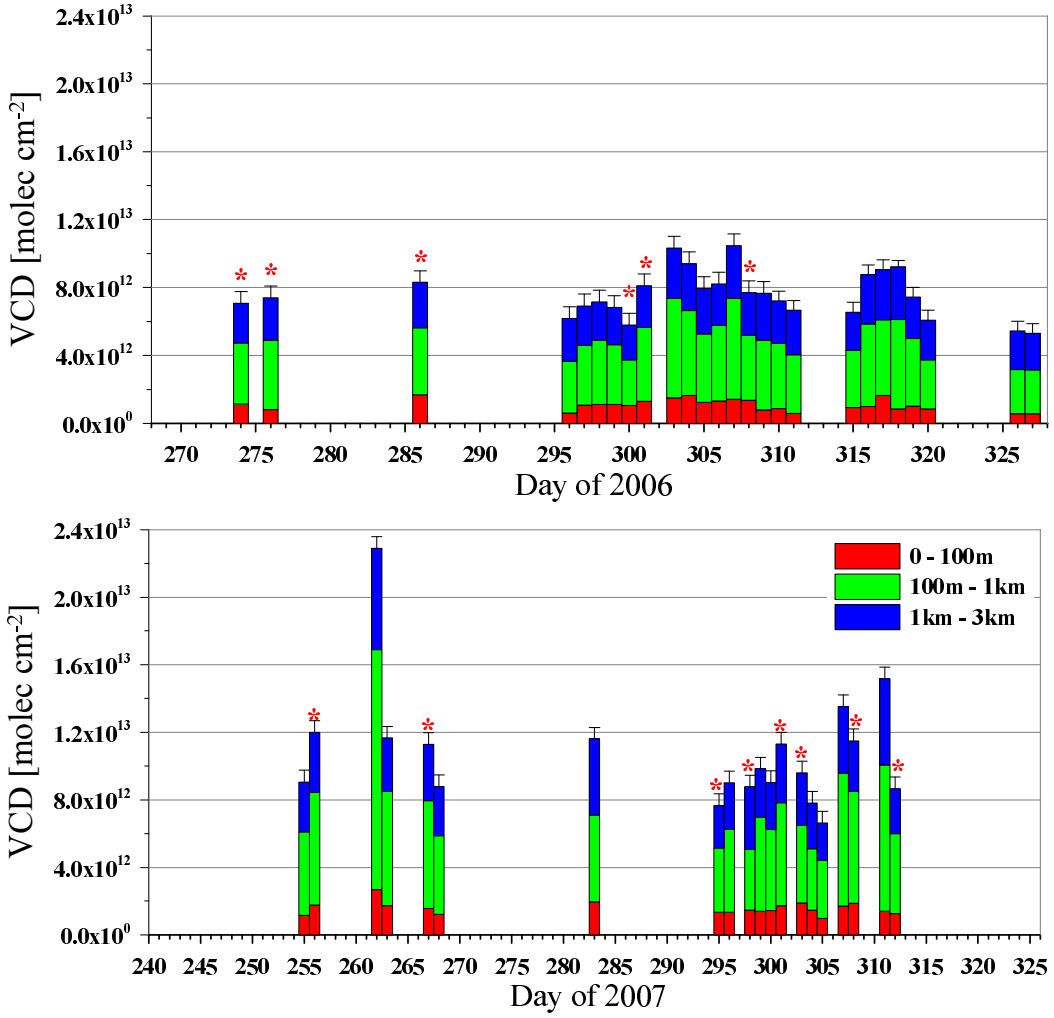

Figure 6.11: Retrieved BrO partial VCDs from the surface up to 100 m, 100 m to 1 km and 1 km to 3 km for 2006 (top) and 2007 (bottom). Cloudy days with a small disturbance in the O_4 DSCDs are indicated with an asterisk.

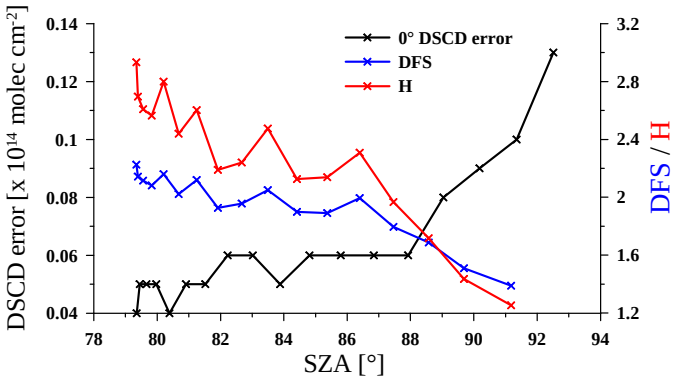

Figure 6.12: Error in the 0° DSCDs, degrees of freedom for signal (DFS) and Shannon information content (H) versus SZA for 19$^{\text{th}}$ September, 2007.

non–parametric Wilcoxon rank sum test was used to test the significance of the differences between years and between sites. The median and maximum retrieved BrO mixing ratios were significantly higher in 2007 than in 2006. The median surface BrO mixing ratio of 7.5±0.5 ppt in 2007 is significantly higher than the 2006 median of 5.2±0.5 ppt, with a Wilcoxon rank sum p–value of 0.0001, which is the probability that the difference arose by chance alone. The maximum retrieved surface BrO mixing ratio was 12.0±0.6 ppt in 2006 and 14.4±0.3 ppt in 2007. The median partial VCD from the ground to 3 km was $9.7\pm0.07 \times 10^{12}$ molec cm^{-2} in 2007, which is significantly higher than the median of $7.4\pm0.06 \times 10^{12}$ molec cm^{-2} for 2006 ($p = 4.3 \times 10^{-5}$). However, the true errors are higher than the retrieval errors, due to uncertainties about the boundary layer height, the profile shape, and forward model parameters including aerosols, and surface albedo as well as the effect of clouds on the light paths. Note that the days with highest VCDs do not necessarily correspond to the highest surface mixing ratios, as a shallow layer of concentrated trace gas will often have a lower VCD than a thicker layer of lower concentration. However, for thicker trace gas layers the retrieval tends to overestimate the trace gas concentration in the lowest layer and underestimate the concentration in the layers above (see Chap. 5).

The observed boundary layer BrO mixing ratios are consistent with, though slightly lower than typical springtime values seen at other coastal polar sites, such as 4–17 ppt at Alert (Hausmann and Platt, 1994; Morin et al., 2005) and a maximum of 20 ppt measured by Saiz-Lopez et al. (2007b) at Halley Station. Ship–based measurements over sea ice have found much higher BrO mixing ratios, for example several tens of ppt were observed by Wagner et al. (2007b) over Antarctic sea ice, and up to 41 ppt was reported in the Amundsen Gulf (∼71°N, 121°-123°W), Arctic (Pöhler et al., 2010).

It is interesting to note that both boundary layer BrO and the total mercury concentrations in the snow samples were higher in 2007 than in 2006. It is possible that the higher mercury concentrations were caused by oxidization of gaseous elemental mercury (Hg^0) by BrO, but it would require several years of observations

to test whether the mercury concentrations in the snow are correlated with BrO mixing ratios from year to year.

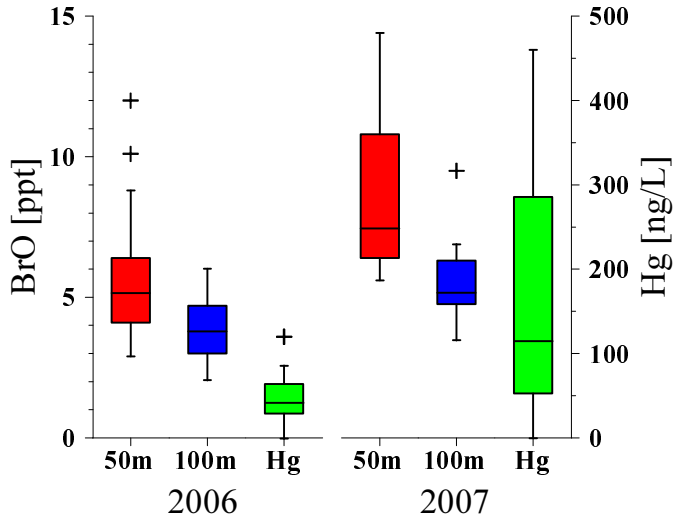

Figure 6.13: Box and whisker plot summarising retrieved BrO mixing ratios for the 50 m and 100 m surface layers, and Hg concentrations in snow samples for 2006 and 2007. Outlier values are indicated by the plus symbol.

The greater BrO mixing ratios in 2007 may have resulted from the more extensive areas of first year sea ice in McMurdo Sound relative to 2006, as the multi–year sea ice broke–out as far back as the Erebus Glacier Tongue in the previous summer. Fig. 6.14 shows sea ice extent and percentage ice concentration in McMurdo Sound in late February 2006 and 2007. The sea ice images from the Advanced Microwave Scanning Radiometer – Earth Observing System (AMSR–E) aboard the Aqua (EOS PM) satellite, were obtained via the IUP Bremen website (www.iup.uni–bremen.de:8084/amsredata/asi_daygrid_swath/l1a/). The grid resolution of the pixels is 3.125 km, but even at this scale it can be clearly seen that the minimum sea ice cover was less in 2007 than in 2006.

A major factor influencing the reduced sea ice break–out in 2006, both within McMurdo Sound and at Cape Bird, was the blocking effect of the C–16 iceberg illustrated in Fig. 6.15, taken from the NASA Moderate Resolution Imaging Spectroradiometer (MODIS) aboard the Terra (EOS AM) and Aqua (EOS PM) satellites.

Hollwedel et al. (2004) observed inter–annual variations in the magnitude of the BrO columns measured by GOME and suggested that melting of multi–year sea ice in the summer leads to more extensive first year ice area and therefore an increased source of tropospheric BrO. The higher boundary layer BrO mixing ratios observed in 2007 relative to 2006 are consistent with higher monthly mean VCDs observed by the nadir viewing Scanning Imaging Absorption Spectrometer for Atmospheric Chartography (SCIAMACHY) aboard the ENVISAT satellite from

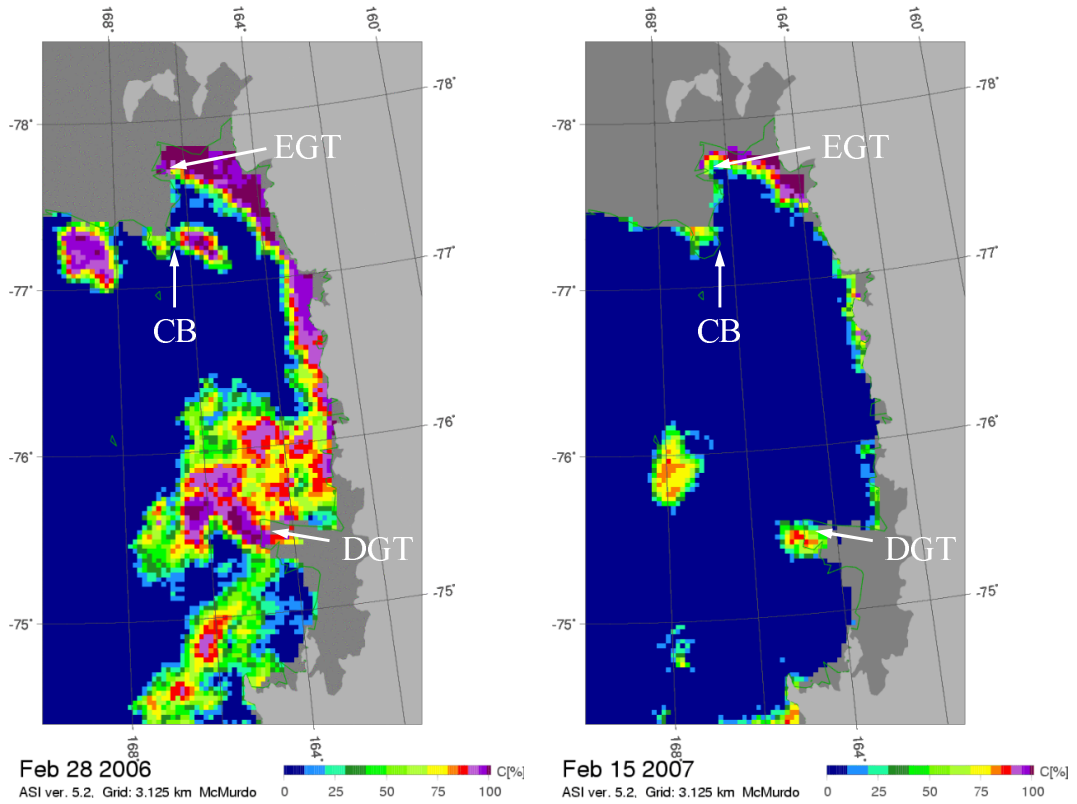

Figure 6.14: Sea ice annual minimum extent and percentage ice concentration in McMurdo Sound in late February 2006 (left) and 2007 (right). EGT=Erebus Glacier Tongue, CB=Cape Bird, DGT=Drygalski Glacier Tongue. (From www.iup.uni–bremen.de:8084/amsredata/asi_daygrid_swath/l1a/).

September through to November 2007 (Fig. 6.16). These images were obtained from the IUP Bremen SCIAMACHY data browser website (www.iup.physik.uni–bremen.de/doas/bro_from_scia.htm). Although, the events observed in McMurdo Sound were most likely locally produced, the cause of the higher BrO levels in McMurdo Sound may be related to the cause of the higher BrO VCDs for the sea ice regions to the north of the Ross Sea. However, the melting of multi–year sea ice further into McMurdo Sound in 2007 is on a relatively small spatial scale and it would not explain the higher VCDs seen in the vast sea ice zones north of McMurdo Sound. Jones et al. (2010) has recently proposed that the large–scale BrO clouds observed from satellites and high altitude ODEs are driven by atmospheric low pressure systems, and that bromine explosion events that occur at low wind speeds under shallow inversion layers have a limited impact on these large–scale BrO clouds. Begoin et al. (2010) used GOME–2 measurements together with a trajectory model to investigate a major arctic bromine explosion event associated with a cyclone. The authors suggested that high surface wind speeds could have lifted aerosols or blowing snow into a plume within which BrO recycling continued for several days. This is a likely possibility, but Salawitch (2010) has recently suggested that stratospheric intrusions of BrO can make

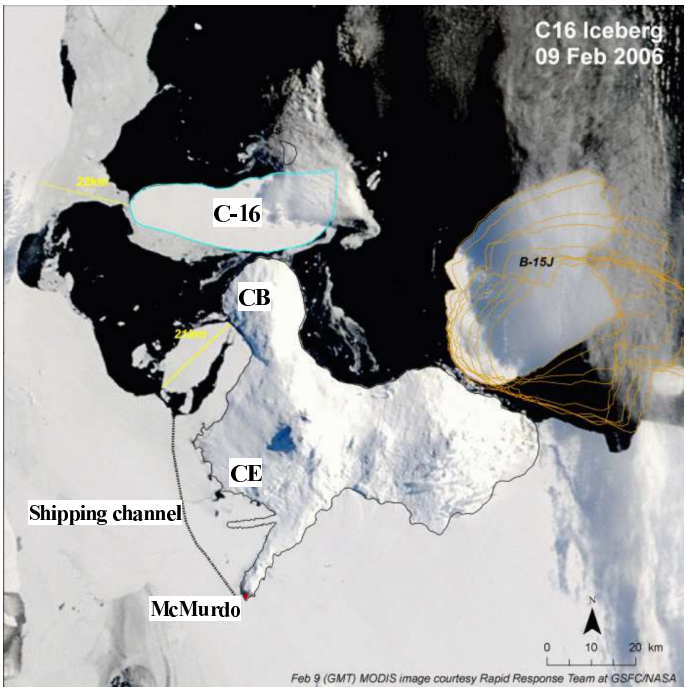

Figure 6.15: The C–16 iceberg blocking McMurdo Sound in February 2006. CB=Cape Bird, CE=Cape Evans. (MODIS image provided by Antarctica New Zealand).

substantial contributions to the tropospheric columns retrieved from satellite measurements, and that too much importance may have been given to surface BrO emissions.

Fig. 6.17 compares the February minimum and October maximum sea ice extents for Antarctica in 2006 and 2007. These AMSR–E images have a 6.25 km grid resolution. The summer minimum sea ice extent is slightly less in 2006 than 2007, but the maximum extent in October is greater in 2007, which may be a factor contributing to the higher VCDs observed by SCIAMACHY in 2007.

6.3.3 IO profiles

The DSCDs indicate that boundary layer IO was present on a number of days in both 2006 and 2007, but retrievals are only presented here for clear days and days with O_4 DSCDs that indicate good visibility and minimal cloud effects on the AMFs (see Sect. 6.1). Days with peak retrieved mixing ratios of ≤ 0.5 ppt were also excluded as being too close to the detection limit of the instrument. Typical retrieved IO mixing ratio profiles for one "golden" day from each year are shown in Fig. 6.18, along with the peak profile for the day. The retrieved profiles for all days indicated that the IO layer was always close to the surface. This is consistent with long–path DOAS observations by Saiz-Lopez et al. (2007b) at Halley Station. Frieß et al. (2010) has suggested that most of the IO is contained in the snowpack and that high multiple scattering within the snow enhances the

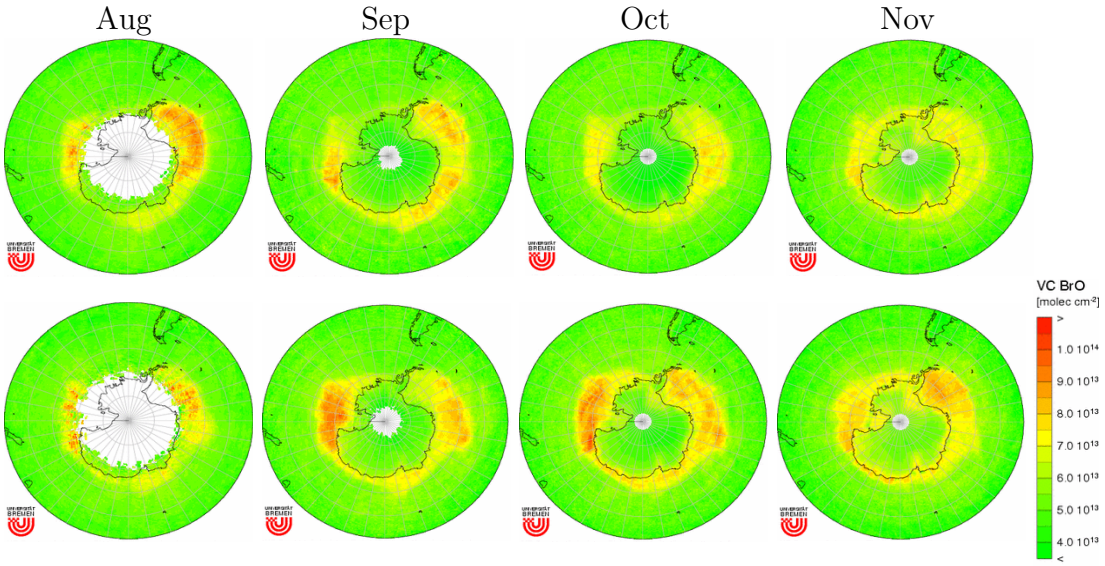

Figure 6.16: Monthly mean BrO VCDs measured by SCIAMACHY from August to November 2006 (top) and 2007 (bottom). Note, the Ross Sea is the large bight on the left–hand side of each Antarctic outline map and the white area in August is the polar night region that cannot be measured by the SCIAMACHY nadir viewing DOAS instrument. (From www.iup.physik.uni–bremen.de/doas/bro_from_scia.htm).

IO SCDs in all viewing directions.

Fig. 6.19 shows the retrieved IO surface mixing ratios up to 20 metres versus SZA for the clearest days in 2007. For days 258 and 268 in September, there is a morning and evening peak in the IO mixing ratio, which could be explained by photolysis rates and the reaction of IO with HO_2 as described for BrO in Sect. 6.3.2 (Vogt et al., 1999). The IO mixing ratio then declines rapidly at sunset and it is zero or below the detection limit at sunrise, since with no photolysis during nighttime, IO is quickly converted into its reservoir species (Vogt et al., 1999; Stutz et al., 1999; McFiggans et al., 2000). From late October onwards (lower plot in Fig. 6.19) the pattern of diurnal variation is opposite to the early season pattern, with IO mixing ratios peaking at midday when photolysis rates are the highest. This pattern, tracking the amount of solar radiation, was also observed by Saiz-Lopez et al. (2007b) at Halley Station. It is unclear why the pattern of diurnal variation is different during the period of 24–hour daylight compared to early spring, but it may be due to changes in HO_x chemistry (Bloss et al., 2010).

The peak daily retrieved IO mixing ratios from the surface to 20 metres are shown in Fig. 6.20. The mean DFS for this surface retrieval layer for all retrieved days in 2006 and 2007 was 0.83±0.09. The median IO mixing ratio was 1.6±0.2 ppt for 2006 and 1.4±0.2 ppt for 2007 with no significant difference between years, and the maximum retrieved IO mixing ratio was 2.6±0.1 ppt. However, the true errors are higher than this due to uncertainties about the boundary layer height and profile shape. These values are very low compared to other Antarctic measurements.

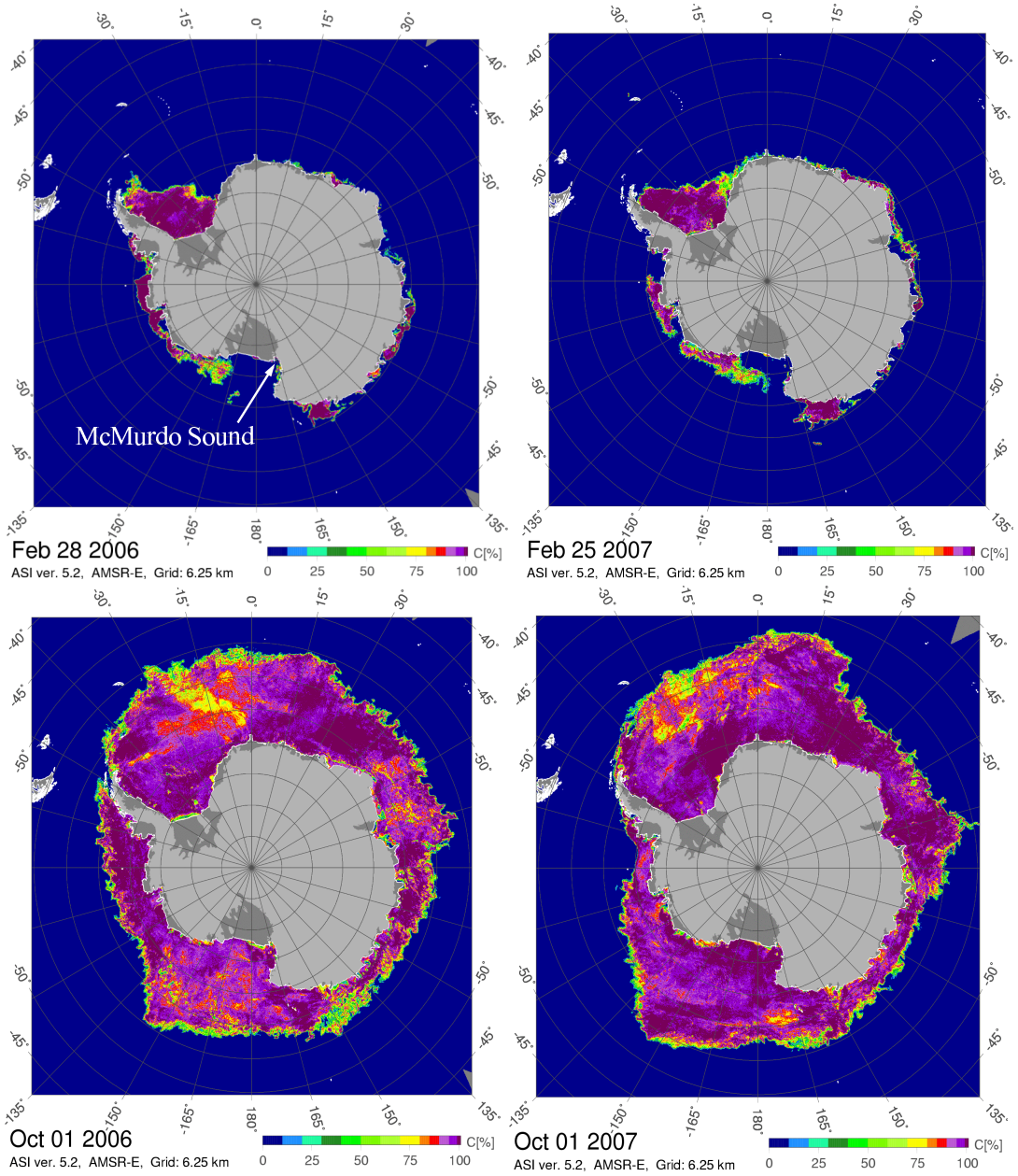

Figure 6.17: Antarctic sea ice annual minimum extent in February (top) and maximum in October (bottom) for 2006 (left) and 2007 (right). (From www.iup.uni–bremen.de:8084/amsredata/asi_daygrid_swath/l1a/).

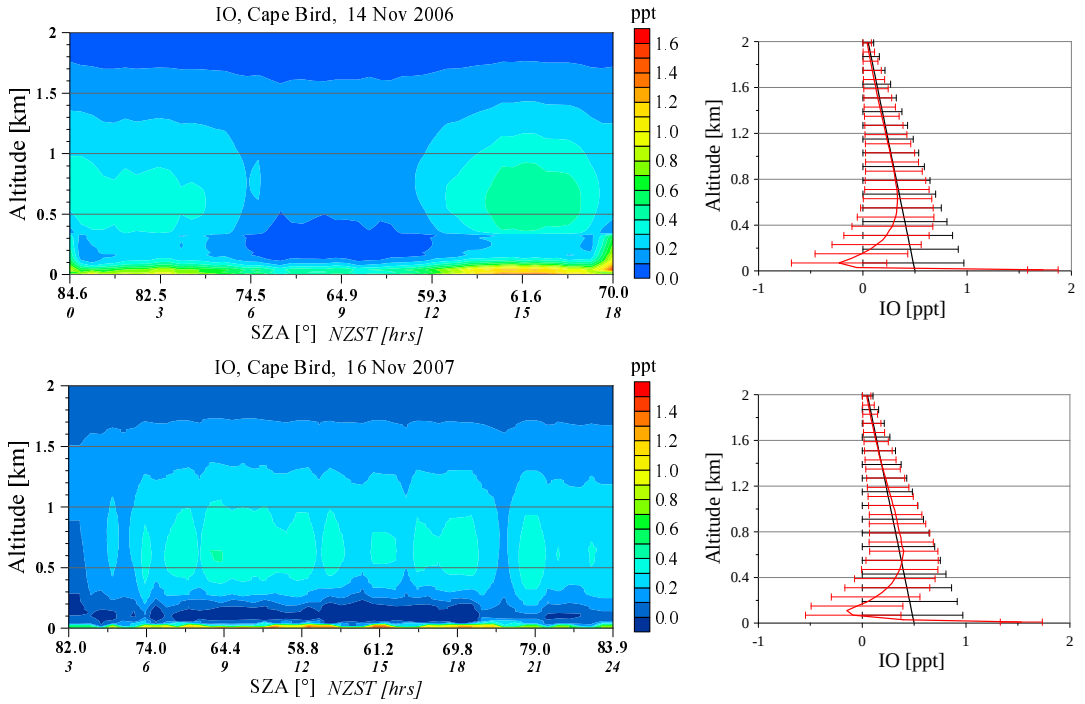

Figure 6.18: IO mixing ratio profiles retrieved for two "golden days" in 2006 (top) and 2007 (bottom), with the *a priori* (black) and retrieved (red) profiles with errors for the highest surface mixing ratios for each day displayed in the right–hand plots.

Saiz-Lopez et al. (2007b) measured up to 20 ppt of IO in the boundary layer using long–path DOAS and Frieß et al. (2010) estimated concentrations in the order of 50 ppb of IO in the interstitial spaces of the snowpack. Due to high multiple scattering within the snow, and the high snow albedo, most of the IO apparently observed by MAX–DOAS in the boundary layer might then be attributed to high concentrations of IO in the snowpack. SCIAMACHY observations in 2005–2006 show elevated IO columns around the Antarctic coastline, with the largest IO clouds seen in the Weddell Sea region and, to a lesser extent, in the Ross Sea (Schönhardt et al., 2008). Frieß et al. (2010) recently retrieved extremely high IO mixing ratios in the ppb range in snow. Therefore, the low IO mixing ratios could be explained if most of the IO was present in the interstitial air spaces in the snow rather than in the boundary layer air itself. In this case, the zenith measurements would also contain a strong signature of IO absorption relative to the low elevation angle measurements, because of the high snow albedo and multiple scattering. Since, the zenith measurement from each scan sequence was used as the reference in the DOAS analysis, the IO DSCDs could have been greatly reduced.

The IO mixing ratios observed here are also less than those reported for mid–latitude coastal sites, of about 4–6 ppt (Alicke et al., 1999; Allan et al., 2000) and up to ∼29 ppt at Mace Head, Ireland (Seitz et al., 2010). However, even small concentrations of IO could lead to a significant increase in the oxidizing

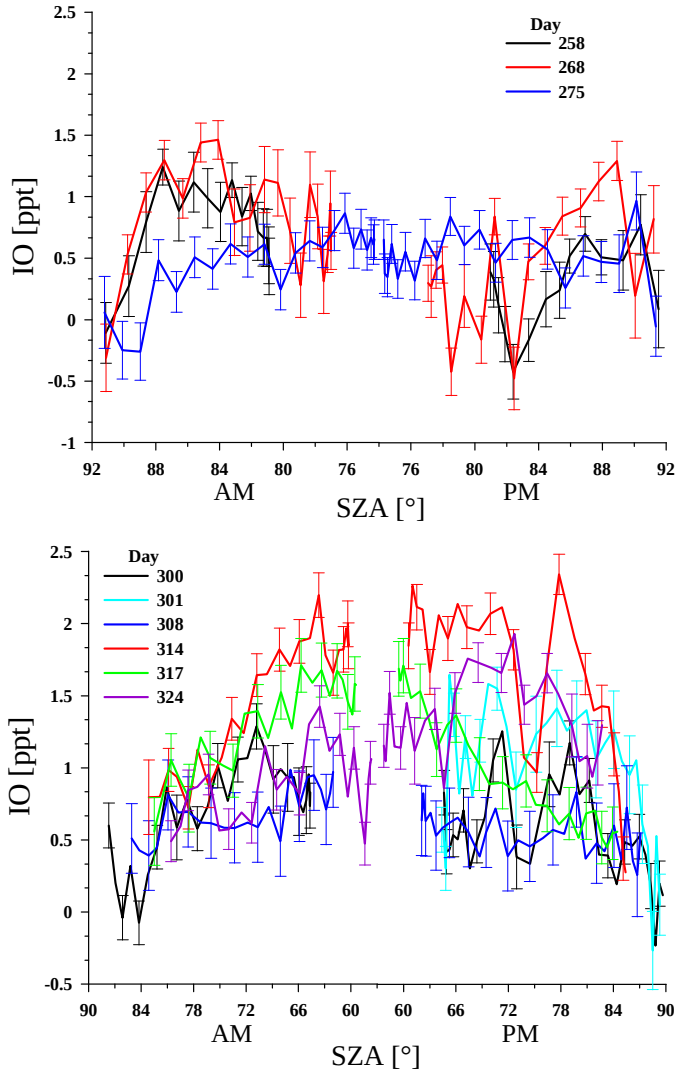

Figure 6.19: Retrieved IO surface mixing ratios versus SZA for Cape Evans (top) and Cape Bird (bottom) in 2007.

capacity of the boundary layer and in the rate of ozone depletion compared with bromine chemistry alone (Saiz-Lopez et al., 2008). So far, no reliable observations of boundary layer IO have been made in the Arctic, though measurements by Wittrock et al. (2000) indicated that low concentrations have been present.

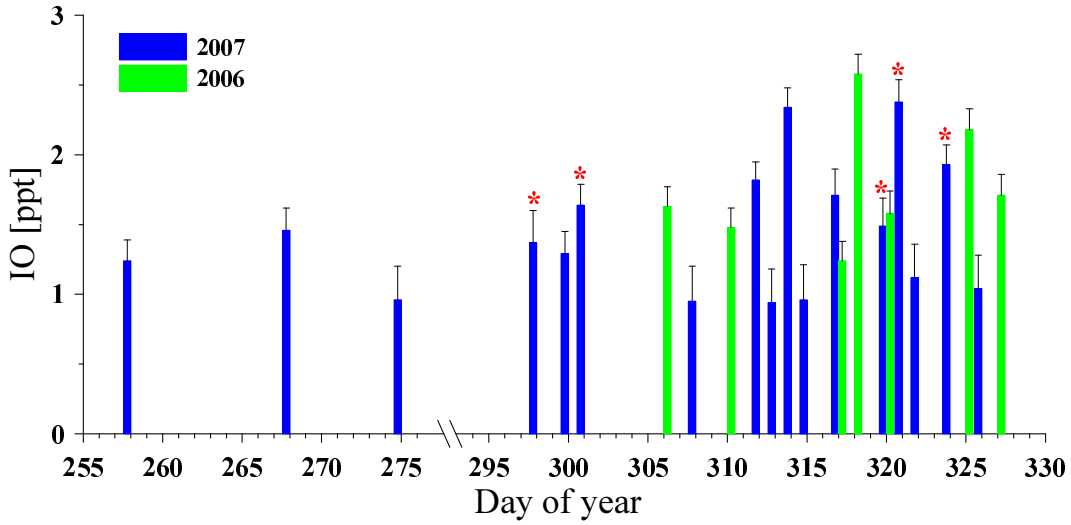

Figure 6.20: Maximum retrieved IO surface mixing ratios for 2006 and 2007. Cloudy days with some disturbance in the O_4 DSCDs are indicated with an asterisk.

6.4 Surface meteorology and air–mass origin

Surface meteorology is already discussed in relation to ODEs in Sect. 6.2, but in this section surface meteorology and air mass back trajectories are discussed in detail in relation to both the BrO observations and ozone minima.

6.4.1 Temperature

ODEs have been found to strongly anti–correlate with temperature and predominantly occur at temperatures below -20°C (Tarasick and Bottenheim, 2002; Pöhler et al., 2010), but Bottenheim et al. (2009) observed many ODEs at temperatures well above -20°C during a year long trans–Arctic ocean drift experiment. It is thought that the flux of bromine and sublimated humidity from the sea ice to the air is proportional to the temperature difference between the ice surface and the air (Piot and von Glasow, 2008; Pöhler et al., 2010). Thus, when the air is much colder than the sea ice surface, the flux from the ice surface to the air is greater.

With two types of bromine explosion events, one occurring in calm cold conditions, and a second type in windy, blowing snow conditions, which are often associated with warmer temperatures, the temperature effect is less well–defined. Nevertheless, the temperatures were frequently near or below -20°C when boundary layer BrO was observed during calm conditions, for example, on days 285–287

in 2006 (Fig. 6.1), and days 240–242, 255–256, 261–262, 283, (Fig. 6.3) 301–304, and 307–308 (Fig. 6.4) in 2007.

Frost flowers were frequently observed on the refrozen tide crack and leads at Cape Bird during these coldest periods when BrO was observed. Frost flowers have been extensively discussed as a potential source of bromine to the air, either directly (Kaleschke et al., 2004; Simpson et al., 2005; Piot and von Glasow, 2008) or as wind–blown frost flower aerosols (Rankin et al., 2000; Kalnajs and Avallone, 2006; Piot and von Glasow, 2008).

6.4.2 Wind speed and direction

Wind rose plots, summarising the prevailing wind directions and wind speeds at each measurement site, are displayed in Fig. 6.21. The predominant wind direction at each site is a result of katabatic winds from the Antarctic plateau modified by the orography of Ross Island and Mount Erebus. No overall correlation of enhanced BrO with wind direction was found, but in cases where BrO enhancement was associated with calm conditions, there was an associated change in wind direction away from the prevailing katabatic flow.

In several cases, boundary layer BrO was observed during calm conditions, suggesting that a shallow boundary layer formed, allowing the concentration of BrO near the surface. For example, on days 284–287 in 2006 (see Fig.6.1, Part 2), the BrO DSCDs indicated increased BrO near the surface compared to the previous days during windy conditions. The weather cleared in the afternoon of day 287, and the retrieved surface BrO mixing ratio was the highest observed for 2006. However, some care should be taken in the interpretation, since the visibility on the previous days was poor, as seen in the O_4 DSCDs, and the apparent increase in boundary layer BrO may have been at least partially due to the effect of improved visibility or a lifting of the cloud ceiling height on the light paths. Another example of an increase in boundary BrO that occurred during calm weather can be seen on day 283 in 2007. Elevated boundary layer BrO was also observed from days 294–308 in 2007 at Cape Bird during relatively calm conditions ($<5\,\mathrm{m\,s^{-1}}$), then disappeared on days 309–310 when the wind speed increased to over $10\,\mathrm{m\,s^{-1}}$ and reappeared again when the wind dropped on day 311. These qualitative observations provide evidence for the positive influence of a shallow inversion layer and cold temperatures on the release of RHS from the sea ice and snow. Regular concurrent measurements of boundary layer height using radiosonde soundings or Sonic detection and ranging (SODAR) on the sea ice, would be very useful for further interpretation.

Conversely, on days 307–308 in 2006, the wind speed decreased from $>4\,\mathrm{m\ s^{-1}}$ to $< 2\mathrm{m\ s^{-1}}$ while the direction changed from northerly to southerly, but there was little change in the BrO concentration. All of the observed partial ODEs, with the exception of day 311 in 2007, occurred during windy conditions, which is consistent with the hypothesis that the bromine explosion reaction is facilitated on saline blowing snow or frost–flower aerosols (Piot and von Glasow, 2008; Yang

et al., 2008; Jones et al., 2009; Yang et al., 2010).

The air–mass origin for all wind directions was nearly always from the Antarctic continent rather than from sea ice regions to the north (see Sect. 6.4.3). This is in contrast to observations at Halley Station (Saiz-Lopez et al., 2007b; Jones et al., 2009) where ODEs are often associated with changes in wind direction, since the wind direction there is well correlated with the long-distance air mass origin, while at Neumayer station, which is 7 km inland, the occurrence of ODEs is not significantly correlated with local wind direction, but is associated with long–distance air–mass sources from extensive sea ice zones (Frieß et al., 2004).

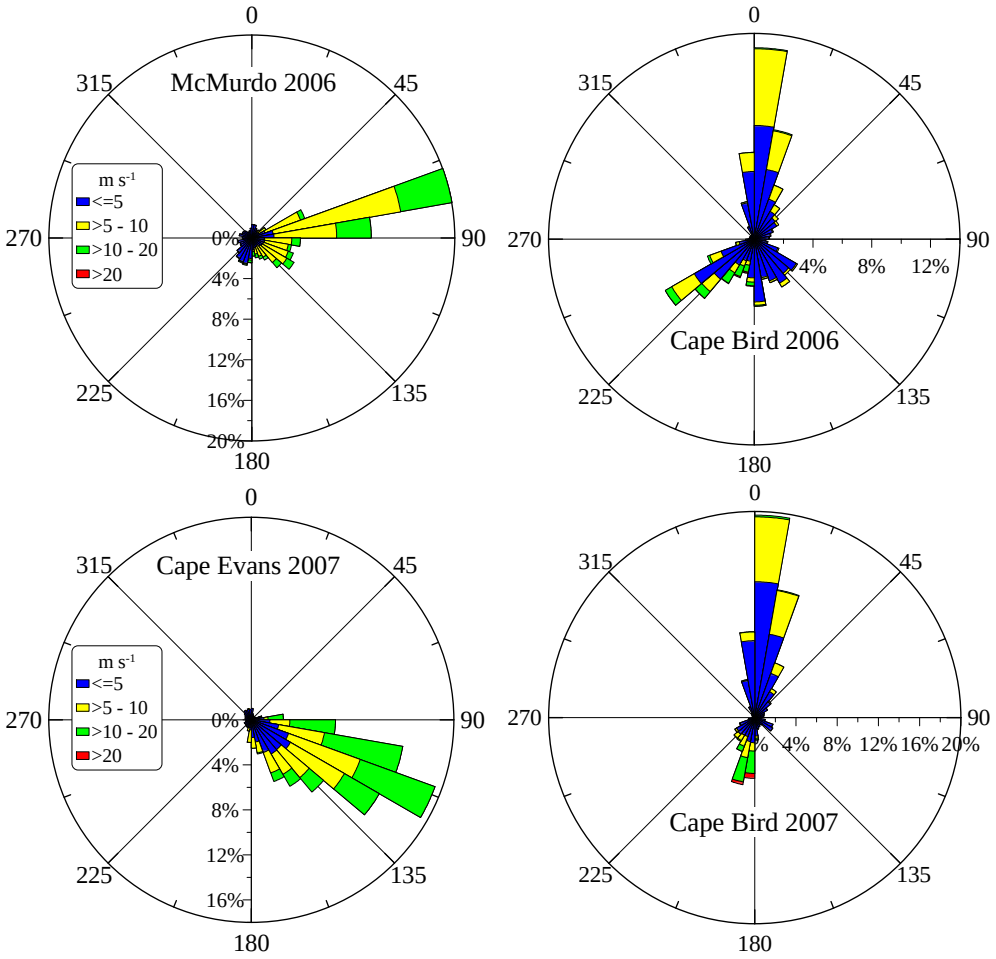

Figure 6.21: Wind speed and direction for the three sea ice measurement sites in 2006 and 2007. The radial axis scale represents the percentage of the time that the wind direction was coming from each 10° sector and the area of each coloured portion of the segment represents the proportion of the time the wind speed was in the range given in the colour scale.

6.4.3 Back trajectories

Back trajectories were calculated using the Hybrid Single–Particle Lagrangian Integrated Trajectory (HYSPLIT) model (Draxler and Hess, 1998) on the NASA Air Resources Laboratory (ARL) website (http://ready.arl.noaa.gov/HYSPLIT.php). The trajectory calculations were performed using the vertical velocity fields of the Global Data Assimilation System (GDAS1) meteorological archive data from the National Center of Environmental Prediction (NCEP). Eight 48–hour back trajectories were calculated for the air masses starting at 10 metres altitude, at 12 hour intervals covering each period when elevated boundary layer BrO was observed. In addition, 120–hour back trajectories were calculated for the air–masses at 10 metres, 500 metres and 1000 metres altitude for days when the highest BrO was observed or ozone depletion occurred.

The back trajectories for both 2006 and 2007 are displayed in Figs. 6.22 and 6.23 respectively. In 2006, the air mass origin was from inland in all cases of elevated boundary layer BrO and for the ODE that occurred during the storm on the 4$^{\text{th}}$ October (day 277). On most days in 2007, the back trajectories were of continental origin, with the exception of the two storm events on the 29$^{\text{th}}$ September (day 272) and the 14$^{\text{th}}$ October (day 287) during which ozone minima occurred. In both cases, the air masses at 500 metres had traversed sea ice regions 3–5 days previously. Contact with the sea ice was made for the back trajectories of day 287, while the back trajectories for day 272 passed about 500 metres above the ice. It is possible that BrO was present at that altitude above the sea ice, and it may even reach a maximum concentration at the top of the boundary layer in some situations (Wagner et al., 2007b). It is interesting to note that in both cases greater ozone depletion was observed at Arrival Heights than on the sea ice, which is consistent with transport of a lifted layer containing low ozone previously depleted in sea ice covered zones (Frieß et al., 2004). However, there are uncertainties in the back trajectory model, the meteorological fields used to generate the back trajectories and in the accuracy of the 2B–205 ozone analyser, so this can only remain as an interesting observation requiring long term ozone measurements on the sea ice to compare with Arrival Heights.

6.5 Ozonesonde profiles

Fourteen tethersonde profiles were measured in 2007 (six at Cape Evans, one at McMurdo, and seven at Cape Bird) using a helikite (see Chap. 3). The accuracy of the 2Z Electrochemical Concentration Cell (ECC) ozonesonde at surface pressures is about 6–10% (Barnes et al., 1985). For tethersonde flights, an additional source of error may arise from the Venturi effect of wind blowing across the sampling tube, thus affecting the flow rate. For example, the 9$^{\text{th}}$ October was windy and there is some scatter in the ozone values, whereas the 27$^{\text{th}}$ October was calm and there ozone values are steady. The Vaisala RS–80 has a stated accuracy of 0.4°C for temperature and 0.5 hPa for pressure.

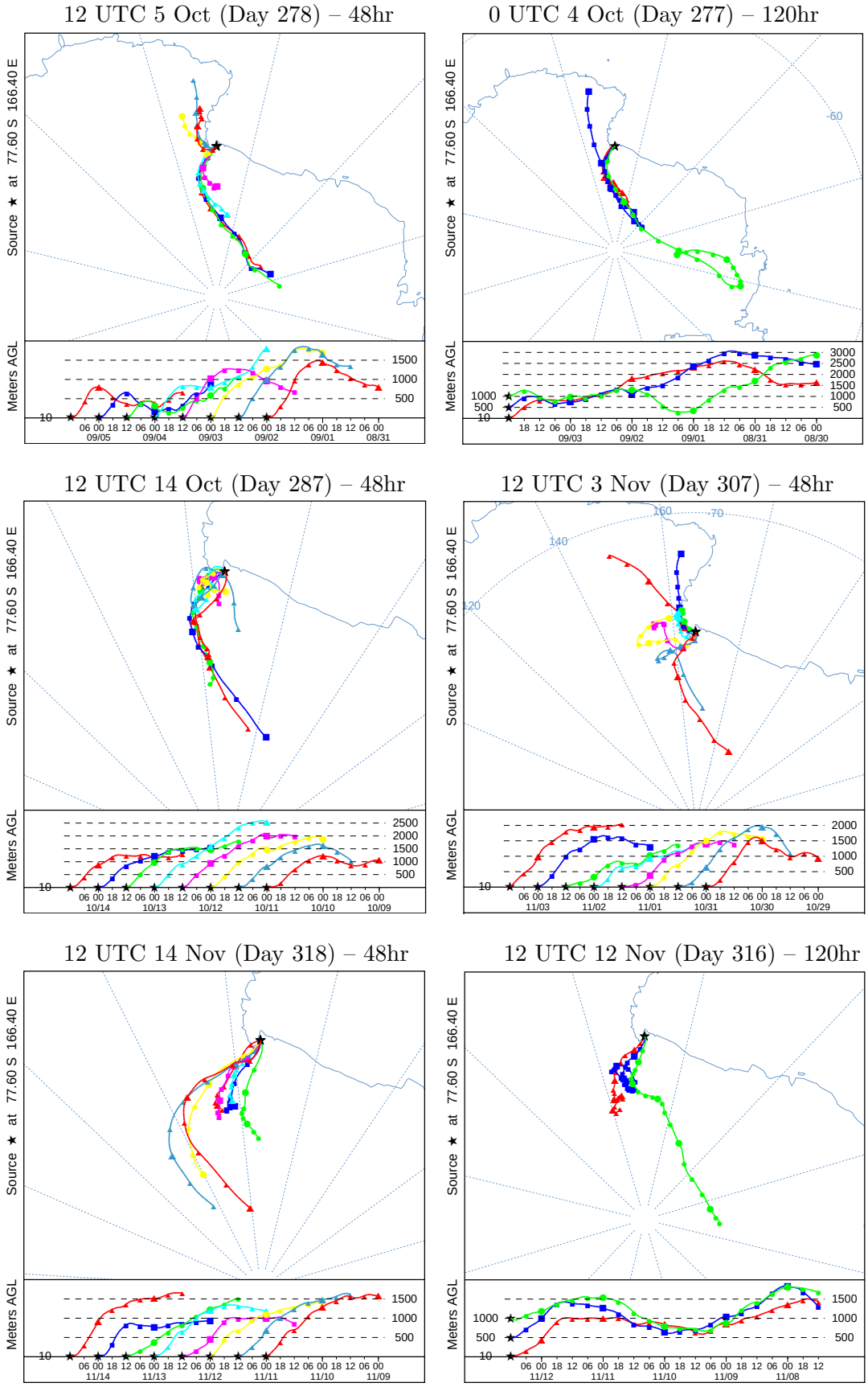

Figure 6.22: HYPLIT back trajectories for days with the highest retrieved surface BrO mixing ratios in 2006. The top panels show the Antarctic coastline, with the sea ice towards the top right of each map, and the bottom panels show the vertical profile versus time for each back trajectory. The back trajectory start time and length in hours is given in each title. Times are in UTC (NZST –12hrs) and day of year is for NZST.

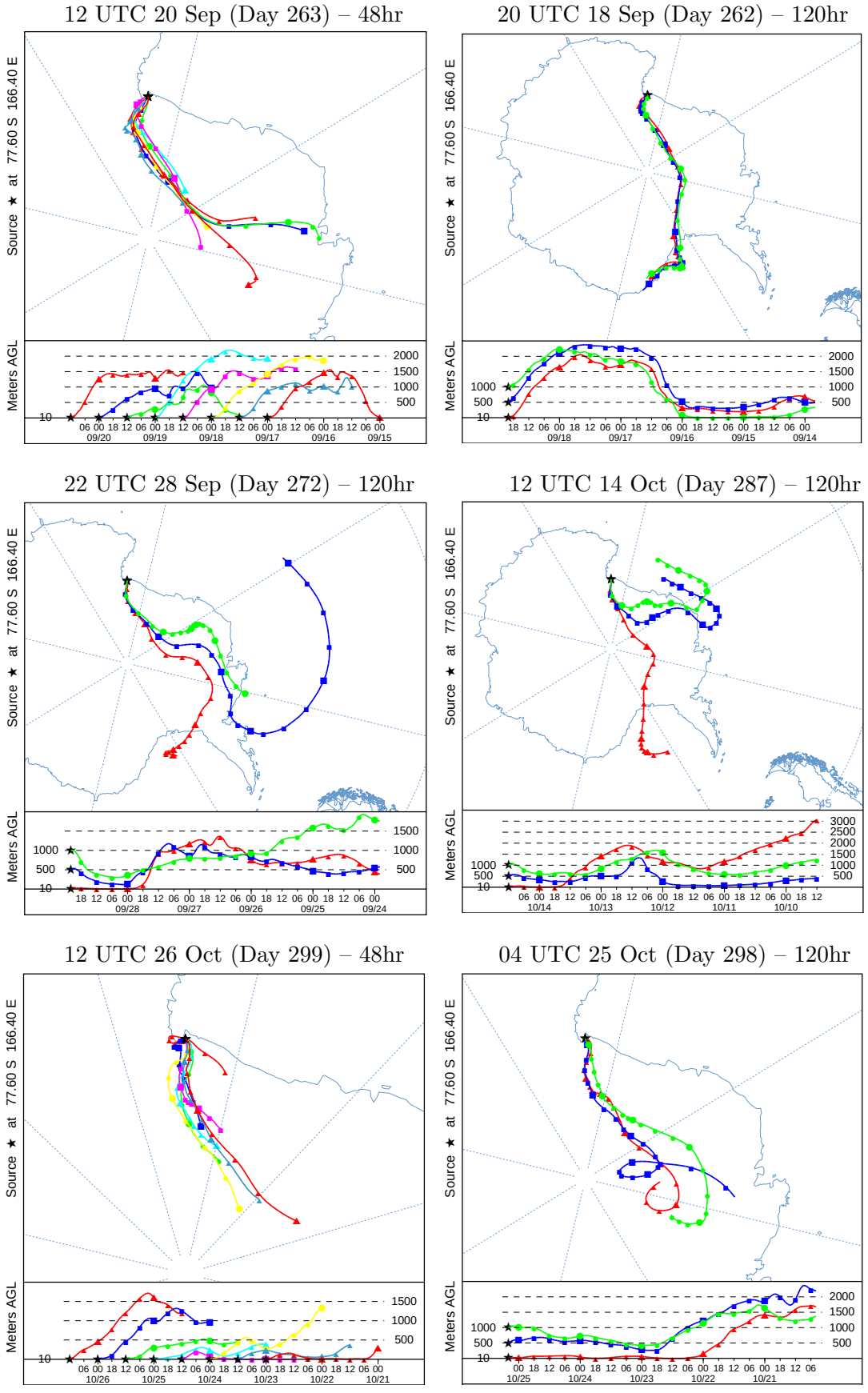

Figure 6.23: HYSPLIT back trajectories for days with the highest retrieved surface BrO mixing ratios in 2007. The top panels show the Antarctic coastline, with the sea ice towards the top right of each map, and the bottom panels show the vertical profile versus time for each back trajectory. The back trajectory start time and length in hours is given in each title. Times are in UTC (NZST –12hrs) and day of year is for NZST.

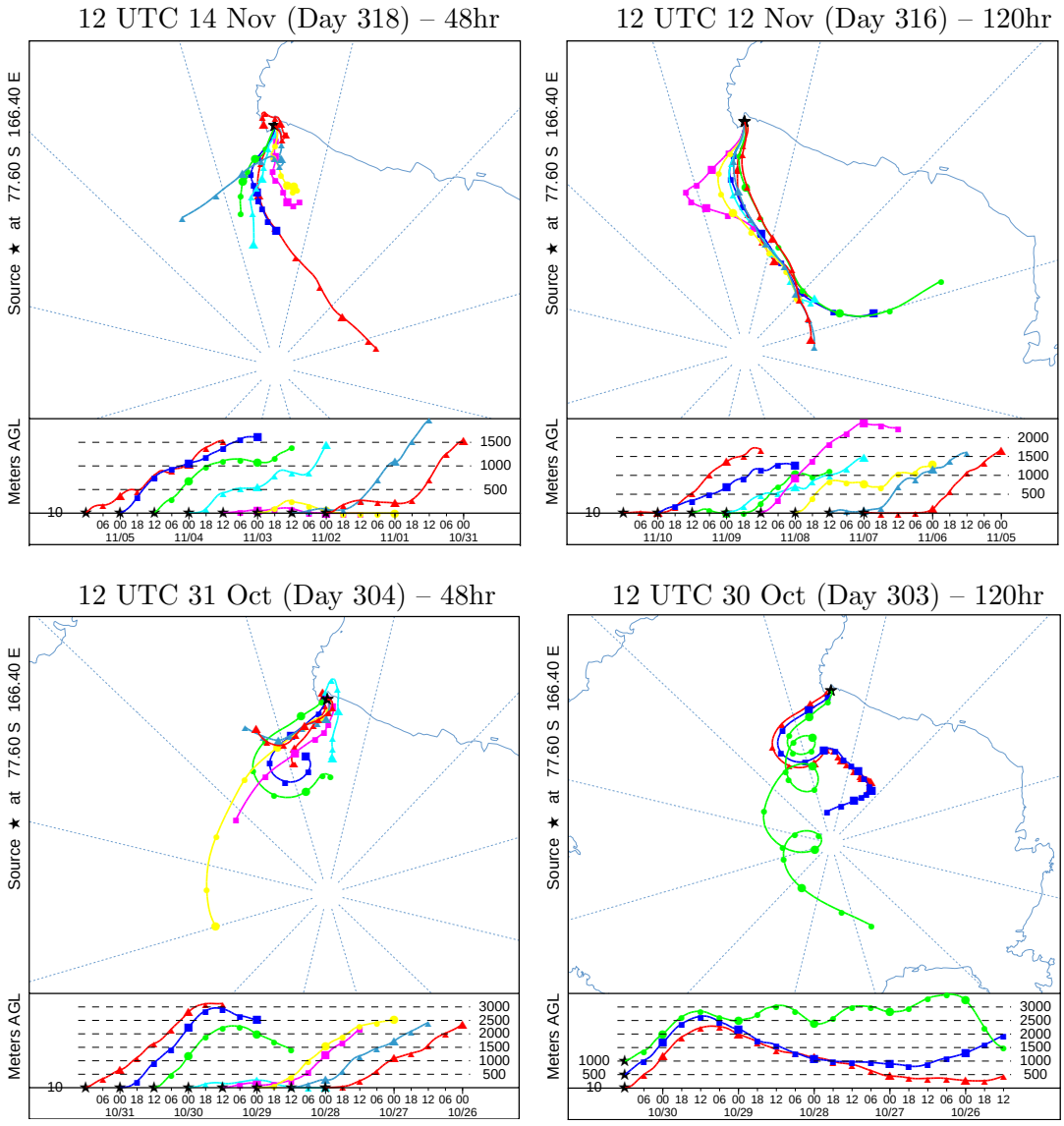

Fig. 6.23 continued. HYSPLIT back trajectories for days with the highest retrieved surface BrO mixing ratios in 2007. The top panels show the Antarctic coastline, with the sea ice towards the top right of each map, and the bottom panels show the vertical profile versus time for each back trajectory. The back trajectory start time and length in hours is given in each title. Times are in UTC (NZST -12hrs) and day of year is for NZST.

Fig. 6.24 shows six profiles representing the different situations observed for all the soundings. Significant surface ozone depletion was only observed for the profile on the 11th September (day 254), though it is uncertain whether the higher surface ozone concentrations on the descent, ∼30 minutes later was a real increase in ozone or a problem with the ECC sonde. The positive potential temperature gradient indicates a stable stratified inversion layer, and there was a strong capping inversion at 40 m, below which the ozone mixing ratio decreased towards the surface. The weather was calm and cold, but the visibility was not ideal for MAX–DOAS measurements and boundary layer BrO was not detected until the following day during similar, but clearer conditions.

Strong shallow inversion layers were observed up to ∼25 m on the 21st September, 50 m on the 4th October, and ∼6 m on the 1st November at Cape Bird. Note that the sonde apparently does not descend below about 10 m on the 1st November, but this was due to a problem with the radiosonde pressure sensor. On other days stable inversion layers with a positive potential temperature gradient were observed, such as on the 9th October, or well–mixed boundary layers, indicted by a neutral potential temperature gradient, such as on the 27th October.

Jones et al. (2010) observed multiple inversion layers from both tethersonde and ozonesonde soundings during ODEs over the ice shelf at Halley Station, and the lowest inversion height for all six tethersonde soundings was between 10 m and 40 m at wind speeds below 7 m s^{-1}. Additionally, ozone depletion above 1 km was always preceded by a low pressure system, and this was consistent with published ozonesonde soundings for Antarctica.

One or two radiosonde soundings daily are routinely made at McMurdo Station (77.85° S, 166.67° E), located on the southern tip of Ross Island near Arrival Heights. The potential temperature profiles were investigated for 155 radiosonde soundings from late August to November 2006 and 155 soundings from the same period in 2007 (from ftp.cpc.ncep.noaa.gov/ndacc/ndsc/mcmurdo/o3sonde/).
The profiles showed considerable structure, with two or more inversion layers, present at different altitudes on most days, with the highest layer frequently occurring between 1–3 km. These inversion layers were typically defined by inflections within the overall positive potential temperature gradient, rather than being single steps in potential temperature. The mean height of the inversion layers nearest the surface was 175±140 m in 2006 and 230±200 m in 2007, with a range from approximately 30 m to 1500 m. However, the orography of the site, surrounded steep hills, buildings and exposed rock is likely to influence the boundary layer structure. In addition, the launch site was ∼30 m above the sea ice, and the ascent rate of the sondes is ∼8.5 m s^{-1} in the first 100 m to ∼6 m s^{-1} at 5 km and one measurement is made every two seconds. Thus, the resolution of the near surface radiosonde measurements on the scale of shallow inversion layers finer than 50 m, is poor.

In contrast to the Arctic, where air–masses depleted in ozone are usually confined to a surface inversion layer (Anlauf et al., 1994; Solberg et al., 1996), ozone

depleted air–masses in the Antarctic can often be elevated layers bounded by inversion layers above and below. Elevated inversions can arise due to the influence of katabatic winds (Wessel et al., 1998) or from advection of warm air from the sea ice over a cold stable boundary layer on the ice shelf (Frieß et al., 2004; Anderson and Neff, 2008). McElroy et al. (1999) also reported enhanced BrO in the arctic troposphere, measured from high–altitude aircraft, and suggested that convective transport above ice leads lifts ice crystals and water droplets as well as BrO, well above the MBL. These ice crystals would then provide surfaces for heterogeneous reactions to recycle BrO in the free troposphere. A multiple inversion layer structure was observed in most of the McMurdo Station radiosonde soundings, but not in the sea ice tethersonde profiles. The maximum altitude of 120–350 m reached by the helikite was below the range of most elevated inversion layers seen at McMurdo Station, which were generally above 500 m.

6.6 Mercury

Surface snow samples were collected in glass sampling vials and analysed for total (elemental and oxidized) mercury content by Steve Brooks at the National Oceanic and Atmospheric Administration (NOAA). Note that total mercury analysis doesn't give specific information on the proportion of the mercury that is oxidized (Hg^{2+}) and therefore in a bioactive form that is easily taken into the biosphere (Lindberg et al., 2002). The results are displayed in Fig. 6.25 together with the surface ozone mixing ratios. No relationship was observed between the concentration of total mercury in the snow and changes in the surface ozone or surface BrO mixing ratios each year. However, the median and maximum mercury concentrations measured in 2007 were noticeably greater than in 2006, though with high variability in the measurements is it difficult to conclude whether this is a statistically significant difference.

Since the mercury measurements do not follow a Gaussian distribution, the Wilcoxon rank sum test was used to test the significance of the different concentrations between years, between sites, and between freshly–fallen and old snow samples. The median mercury concentration in the snow samples for 2006 was 41.5 ng/L, which is comparable to the lower range of total mercury levels measured by Brooks et al. (2008) in October to November 2003 and to levels measured in the Arctic snowpack (Lindberg et al., 2002). The maximum concentration was 120 ng/L in 2006 and 460 ng/L in 2007, which is slightly above the maximum recorded by Brooks et al. (2008), and the median mercury concentration was 111.2 ng/L in 2007, which is significantly higher than in 2006 ($p=2.9 \times 10^{-5}$). This is comparable to enhanced snowpack mercury levels observed at Barrow, Alaska (Brooks et al., 2006), while Douglas et al. (2005) reported concentrations as high as 820 ng/L in snow and frost flowers near sea ice leads in Barrow. As surface BrO mixing ratios were also higher in 2007 (see Sect. 6.3.2), this might explain the higher mercury concentrations in the snow pack (Fig. 6.13).

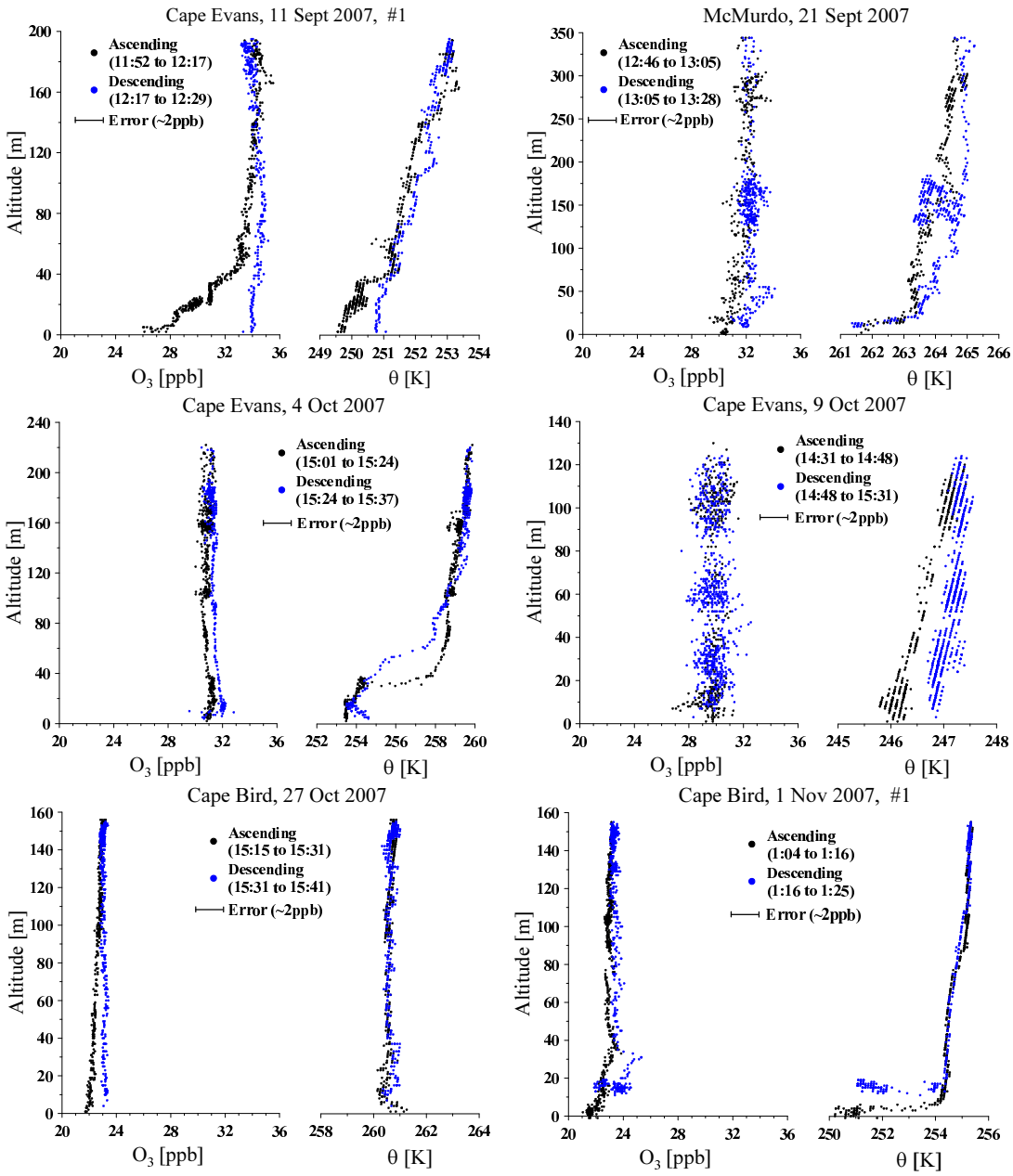

Figure 6.24: Tethersonde (helikite) ozone and potential temperature profiles.

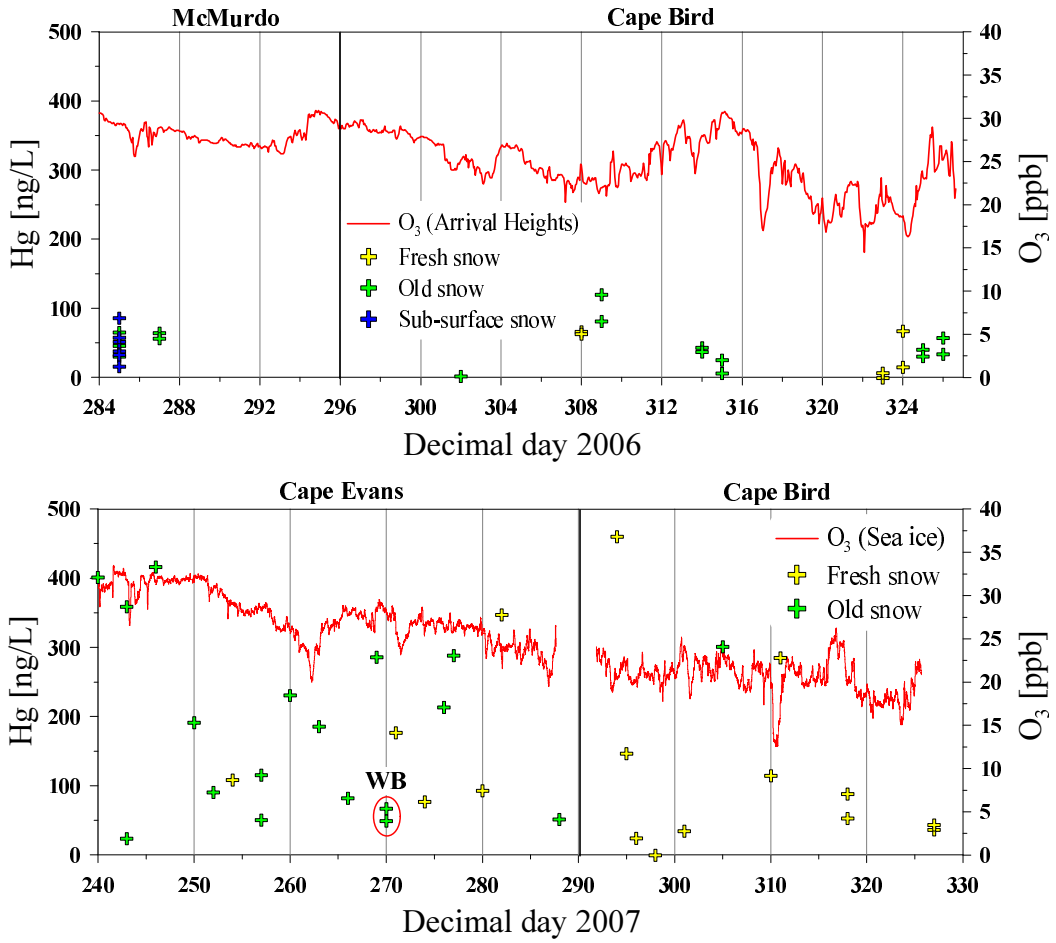

Figure 6.25: Mercury concentrations in snow samples, and surface ozone mixing ratios for 2006 (top) and 2007 (bottom). WB=Windless Bight.

There was no significant difference in mercury concentrations between sites in 2006 and a weakly significant difference between Cape Bird and Cape Evans in 2007, with a median mercury concentration of 176.3 ng/L in surface snow at Cape Evans and 70.3 ng/L at Cape Bird (p=0.13). This is contrary to the expectation of higher snowpack mercury levels closer to the sea ice edge (Brooks et al., 2008). However, since all except one of the samples from Cape Bird in 2007 were of freshly–fallen snow, it cannot be determined if the difference was mainly due to the site or to the snow age. Therefore, the comparison between fresh and old snow in 2007 was only made for the Cape Evans samples, to avoid the effect of site differences. There were no significant differences between the mercury concentrations in freshly–fallen and old snow in either 2006 or 2007.

Fig. 6.26 shows an increase in mercury concentration with depth for snow samples from various snow depths down to the sea ice surface on the 12th October 2006 (day 285). The maximum mercury concentration was found for the sea ice sample at the bottom of the snow pit. This may indicate that high BrO concentrations occurred during formation of the sea ice, and during earlier snow storms, which

oxidized gaseous mercury from the air leading to its deposition on the sea ice. However, there is considerable variation in measured mercury concentrations for samples taken on the same day or consecutive days, so the uncertainties in the measurements are high. Several snow pits and samples would be required to verify whether the deeper snow layers had higher mercury concentrations.

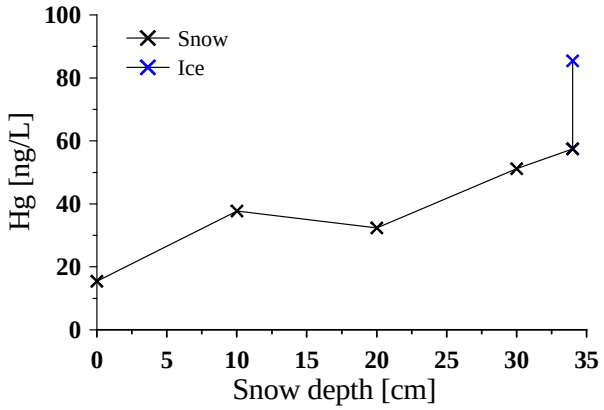

Figure 6.26: Mercury concentrations at different depths below the snow surface at the McMurdo site on the 12th October 2006.

6.7 Summary

Boundary layer BrO was observed on several days in both 2006 and 2007, both during calm, cold conditions and during windy conditions with blowing snow. This is consistent with the hypothesis that bromine explosion reactions can be initiated either under a low capping inversion layer that concentrates the reactants, or with blowing saline snow and ice that creates a large surface area for heterogenous reactions. Four out of the five observed partial ODEs occurred during conditions of high winds and blowing snow. Elevated boundary layer BrO was observed during these events, with the exception of one event when measurements were not possible due to snow covering the tracker.

Optimal estimation retrievals were performed for days when the O_4 DSCDs indicated good visibility, similar to clear cloudless conditions. Aerosol optical depths during clear weather are typically extremely low for Antarctica, and the retrievals are relatively insensitive to small changes in the aerosol extinction profile for low optical depths, giving results similar to those for a pure Rayleigh atmosphere (see Chap. 5). Box–AMFs are also relatively insensitive to small changes in the temperature–pressure profiles (see Chap. 4). However, in future it would be recommended to perform a series of sensitivity tests of the retrieved profiles to changes in various forward model parameters, in particular the aerosol extinction profile.

The median partial VCDs up to 3 km were $9.7 \pm 0.07 \times 10^{12}$ molec cm^{-2} in 2007, with a maximum of 2.3×10^{13} molec cm^{-2}, and $7.4 \pm 0.06 \times 10^{12}$ molec cm^{-2} in 2006, with a maximum of $1.05 \pm 0.07 \times 10^{13}$ molec cm^{-2}. The maximum surface BrO mixing ratio was ∼14.4 ppt and the median of the peak retrieved surface mixing ratios for each day was ∼5.2 ppt in 2006 and ∼7.5 ppt in 2007. These values are comparable with, though slightly lower than other coastal polar boundary layer BrO measurements, but much lower than BrO concentrations measured above sea ice zones in the open ocean. The greater BrO concentrations observed away from the coast could be due to higher sea salt concentrations, which are frequently replenished by the opening of fresh leads, higher photolysis rates, and the transport of air parcels having long sea ice contact times.

One reason for the higher BrO mixing ratios in 2007 could be the more extensive areas of first year sea ice in McMurdo Sound relative to 2006. A greater sea ice maximum area for Antarctica in 2007 may also contribute to the higher VCDs of the large–scale BrO clouds observed by SCIAMACHY in 2007. Another factor leading to the higher BrO VCDs both in McMurdo Sound and over the circumpolar sea ice, could be different meteorological conditions in 2007. Long term sea ice measurements in McMurdo Sound, together with an investigation into large scale meteorology, are needed to determine whether BrO observations in McMurdo Sound are correlated with satellite measurements and meteorological conditions from year to year.

Air mass back trajectories, calculated using HYSPLIT, indicated that the air masses from up to five days previously had almost always travelled over the Antarctic continent rather than making contact with extensive sea ice areas. This is consistent with the findings of Kottmeier and Fay (1998). In one case, during a partial ODE observed at Arrival Heights, the air mass at 500 m had travelled across sea ice three days previously. This could explain why lower ozone was observed at Arrival Heights than on the sea ice at Cape Evans, though the HYSPLIT model back trajectories should be interpreted with caution due to large uncertainties in the meteorology driving them (Kottmeier and Fay, 1998). The slow onset of the partial ODEs over several hours, also supports the hypothesis of local chemical destruction, as transport events typically result in rapid changes in boundary layer halogen and ozone concentrations on a timescale of a few minutes (Morin et al., 2005; Jones et al., 2006). It is concluded that the observed boundary layer BrO enhancement and ozone depletion in McMurdo Sound were locally produced rather than from transport.

Low boundary layer IO mixing ratios of ∼0.5–2.5 ppt were observed on several days each year but more frequently in 2007 than in 2006. This was the first time IO has been observed from ground–based measurements in McMurdo Sound, and so far very few IO measurements have been made in Antarctica. The IO mixing ratios are low compared to measurements at Halley and Neumayer Stations in the Weddell Sea region, and also lower than IO mixing ratios measured at coastal mid–latitude sites. A possible reason for this may be that most of the IO was present in the snow, and thus the zenith measurements also contain a significant

amount of IO absorption (Frieß et al., 2010). Therefore, to test this hypothesis, a reanalysis of the measurements should be undertaken using a single zenith reference from a clear day when no boundary layer IO was observed.

Snow mercury concentrations were significantly higher in 2007 than in 2006, and this could be related to the greater BrO concentrations in 2007, but several years of concurrent BrO and mercury measurements would be required to verify this.

Fourteen tethersonde profiles were measured in 2007 and surface ozone depletion was observed for one sounding up to a capping temperature inversion at ∼40 m. A positive or neutral potential temperature gradient was observed for all soundings, with a strong surface inversion layer ranging from ∼5–40 m. It is likely that these very shallow inversion layers during low wind conditions are typical for McMurdo Sound, as has been observed over the ice shelf at Halley Station (Jones et al., 2009).

Chapter 7

Conclusions

Ground–based Multi–Axis Differential Optical Absorption Spectroscopy (MAX–DOAS) measurements of BrO and IO were made from a portable instrument platform at three sites in McMurdo Sound during the Antarctic spring of 2006 and 2007. Surface ozone, temperature, pressure, humidity, and wind speed and direction were also measured, tethersonde soundings were performed and snow samples were collected for mercury analysis.

A linear maximum *a posteriori* (MAP) inversion of the differential slant column densities (DSCDs) was implemented to retrieve information on the vertical distribution of trace gases in the lowermost troposphere. Retrievals of artificial DSCDs, modelled from prescribed NO_2 profiles, demonstrated that the linear MAP retrieval of MAX–DOAS DSCDs in both the UV (360 nm) and visible (477 nm) regions can give reliable estimates of trace gas partial vertical column densities (VCDs) from the ground up to 2–3 km, depending on atmospheric conditions and instrumental errors, as long as realistic aerosol extinction profiles are used in the forward model calculations. Apart from blowing snow conditions, aerosol optical depths in Antarctica are typically very low (Shaw, 1980), and neglecting aerosols in the radiative transfer calculations is therefore expected to have only a small effect on the retrieved trace gas amounts (Frieß et al., 2010). Two to three independent pieces of vertical information are typically retrieved, depending on the measurement geometry, solar zenith angle (SZA), relative azimuth angle between the viewing direction and the Sun, aerosols, wavelength and the signal–to–noise ratio. The sensitivity of the measurements is reduced by aerosol scattering in the lowermost troposphere. The greatest information content is retrieved for the lowest 50–100 m of the atmosphere and the retrieved mixing ratios are a reasonable estimate of the true values for trace gas profiles that peak below 100 m. Therefore, this type of retrieval is ideally suited for the estimation of BrO and IO concentrations in a shallow inversion layer, which is commonly in the range of 10–100 m over sea ice and ice shelves (Jones et al., 2009, 2010).

The NIMO spherical multiple scattering Monte Carlo radiative transfer model (RTM), developed for the forward model DSCD and weighting function calculations used in the optimal estimation algorithm, was validated using a series of tests prescribed in Wagner et al. (2007a). Box–air–mass–factors (box–AMFs) and radiances for the simulated MAX–DOAS measurements showed good agreement

with nine other RTMs within the typical range of variability of ∼6% from the multi–model median values.

Boundary layer BrO was observed on several days in both 2006 and 2007, with a maximum retrieved surface mixing ratio of 14.4±0.3 ppt and a median of 7.5±0.5 ppt for 2007, which was significantly higher than the median of 5.2±0.5 ppt and maximum of 12.0±0.6 ppt observed in 2006. Similar, though slightly higher, boundary layer BrO concentrations have been observed at Halley in the Weddell Sea area (Saiz-Lopez et al., 2007b), and at coastal sites in the Arctic (Hausmann and Platt, 1994; Morin et al., 2005). The median partial VCDs up to 3 km were $9.7\pm0.07 \times 10^{12}$ molec cm^{-2} in 2007, with a maximum of 2.3×10^{13} molec cm^{-2}, consistent with mixing ratios of 1.2 ppt and 2.7 ppt respectively, if the layer is well–mixed. The median VCD in 2006 was $7.4\pm0.06 \times 10^{12}$ molec cm^{-2}, with a maximum of $1.05 \pm 0.07 \times 10^{13}$ molec cm^{-2}, with corresponding mixing ratios of 0.9 ppt and 1.25 ppt. The higher BrO VCDs and surface mixing ratios retrieved in 2007 may be related to more extensive areas of first year sea ice relative to 2006, which have higher concentrations of sea–salts than multi–year ice.

Enhanced boundary layer BrO, and one ODE out of a total of five, were observed during calm, cold weather, consistent with the traditionally accepted conditions leading to bromine explosion events (Barrie et al., 1988; Piot and von Glasow, 2008; Pöhler et al., 2010). Boundary layer BrO and four of the five ODEs were observed during high surface winds, blowing snow and often also poor visibility, consistent with recent findings (Yang et al., 2008, 2010; Jones et al., 2009, 2010).

Air mass back trajectories, calculated by the Hybrid Single–Particle Lagrangian Integrated Trajectory (HYSPLIT) model, indicated that the air–masses from the sea ice surface up to one kilometre arrived from inland Antarctica from 2–5 days previously. Kottmeier and Fay (1998) also confirmed the continental origin of air–masses in McMurdo Sound, which is due to the predominance of katabatic winds from the Antarctic plateau. It is therefore concluded that the source of the observed boundary layer BrO enhancement and ozone depletion was from the sea ice within McMurdo Sound. The slow onset of the observed partial ODEs over several hours also supports the hypothesis of local halogen activation and ozone depletion, as transport events typically result in rapid changes in boundary layer halogen and ozone concentrations on a timescale of a few minutes (Morin et al., 2005; Jones et al., 2006).

The higher observed levels of boundary layer BrO in 2007 relative to 2006 could be related to the higher VCDs observed by SCIAMACHY, but these large–scale BrO clouds are generally several hundred kilometres north of McMurdo Sound, and back trajectory calculations indicated that transport of air–masses from those regions was unlikely. The cause of the higher VCDs observed from SCIAMACHY may have been from stratospheric intrusions of BrO (Salawitch, 2010), or from storm events on the sea ice lifting BrO, sea salt aerosols, snow and ice crystals from the surface the free troposphere (Frieß et al., 2004; Jones et al., 2010; Begoin et al., 2010). As the southern–most coastal site, typically isolated from the large–

scale BrO clouds in the northern part of the Ross Sea, McMurdo Sound is ideally located to study locally–produced boundary layer bromine explosion events to compare the dynamics with the large–scale events observed over extensive sea ice regions.

Boundary layer IO mixing ratios of 0.5–2.5±0.5 ppt were observed on several days. These values are low compared to measurements at Halley (Saiz-Lopez et al., 2007b) and Neumayer (Frieß et al., 2010) Stations, as well as mid-latitudes (Alicke et al., 1999; Allan et al., 2000).

Snow mercury concentrations, with a maximum of 460 ng/L and a median of 111.2 ng/L in 2007, were significantly higher than the maximum of 120 ng/L and the median of 41.5 ng/L in 2006. This could be related to the higher BrO concentrations in 2007, but this needs to be verified with further measurements of boundary layer halogens and snow mercury concentrations over several years.

7.1 Outlook

In order to further investigate the patterns of bromine activation during cold, calm conditions versus high winds and blowing snow, as well as the relationship between first–year sea ice extent and boundary layer BrO mixing ratios in McMurdo Sound, a long–term sea ice measurement site is recommended. Additionally, this would allow the comparison of local bromine explosion events in McMurdo Sound with inter–annual variations in the large–scale BrO clouds observed by SCIAMACHY.

The instrumental platform would be a modification of the TARDIS, with lower power requirements, a larger battery bank, and possibly a second wind generator and more solar panels, to enable near–autonomous operation. Snow sampling for total mercury content and air sampling for gaseous elemental mercury (GEM) would help verify if individual bromine explosion events as well as inter–annual differences in boundary layer BrO amounts are correlated with total snow mercury concentrations and anti–correlated with GEM. Further boundary layer studies, using tethersondes and Sound Detection and Ranging (SODAR) could be used to investigate the potential relationship between the inversion height, wind speed and surface BrO mixing ratios. Aerosol mass spectrometer measurements would help investigate the relationship between aerosol counts and size distributions and bromine activation. In addition, the aerosol measurements could be used to construct appropriate aerosol extinction profiles for the radiative transfer model. Cape Evans would be an ideal site for ongoing measurements as it is typically within, or close to the edge of the first–year sea ice each year, and it is usually accessible from August through to November, when most bromine explosion events occur. Cape Bird is further inside the active sea ice zone, but it is only accessible from mid–October until February.

The retrieval algorithm, developed in this work, will be used to retrieve BrO

profiles from MAX–DOAS measurements made at Arrival Heights during the 2006 and 2007 sea ice campaigns. Since Arrival Heights is at ∼185 m above the sea ice, this will give some information about higher layers relative to what is observed on the sea ice. Due to the high surface albedo, as well as multiple scattering below the instrument, the Arrival Heights measurements also contain some information about the layers below the instrument. To accurately model the radiative transfer, surface topography should also be included for the forward model calculations. Retrieved BrO mixing ratios at Arrival Heights and the sea ice can then be compared to investigate a possible relationship between BrO and the differences in ozone concentrations between the sites.

To obtain information about stratospheric BrO, a retrieval of the zenith–sky measurements could be performed using the method described by Schofield et al. (2004). A set of five diurnal profiles, for example, could be simultaneously retrieved at different SZA describing the diurnal variation of stratospheric BrO. Initially, this could be done using the single–scattering model Schofield et al. (2004), but multiple scattering is important at high SZA, as demonstrated by Hendrick et al. (2006). The treatment of photochemistry in the NIMO multiple scattering RTM is currently possible using the direct Monte Carlo simulation, but the calculation of box–AMFs for high SZA is very inefficient. Therefore, the adjoint trajectory simulation technique needs to be modified to correctly include the effect of photochemistry along the light paths.

As aerosols have a major influence on the scattered light paths observed by MAX–DOAS, an important development for areas with significant aerosol optical depth would be the capability to retrieve aerosol profiles and properties using measurements of O_4, and the variation of intensity with viewing elevation angle and SZA as described by Frieß et al. (2006). This would require a modification of the NIMO backwards adjoint MC calculation, in order to analytically determine the weighting functions needed for the non–linear iterative aerosol retrievals. The aerosol optical depths in Antarctica are low and the precision of the MAX–DOAS aerosol retrieval of total optical depth is of a similar magnitude, so retrieving the aerosol properties using this method is not necessary or useful. However, Frieß et al. (2010) describes an effective systematic method for selecting conditions equivalent to clear sky days, by comparing the measured O_4 SCDs with modelled SCDs, which should be applied in future analyses of the Antarctic measurements.

Bibliography

Aben, I., Stam, D. M., Helderman, F., 2001. The Ring effect in skylight polarisation. Geophysical Research Letters 28 (3), 519–522.

Adams, J. W., Holmes, N. S., Crowley, J. N., 2002. Uptake and reaction of HOBr on frozen and dry NaCl/NaBr surfaces between 253 and 233 K. Atmospheric Chemistry and Physics 2, 79–91.

Alicke, B., Hebestreit, K., Stutz, J., Platt, U., 1999. Iodine oxide in the marine boundary layer. Nature 397 (6720), 572–573.

Aliwell, S. R., Jones, R. L., Fish, D. J., 1997. Mid-latitude observations of the seasonal variation of BrO .1. Zenith-sky measurements. Geophysical Research Letters 24 (10), 1195–1198.

Aliwell, S. R., Van Roozendael, M., Johnston, P. V., Richter, A., Wagner, T., Arlander, D. W., Burrows, J. P., Fish, D. J., Jones, R. L., Tornkvist, K. K., Lambert, J. C., Pfeilsticker, K., Pundt, I., 2002. Analysis for BrO in zenith-sky spectra: An intercomparison exercise for analysis improvement. Journal of Geophysical Research-Atmospheres 107 (D14), –.

Allan, B. J., McFiggans, G., Plane, J. M. C., Coe, H., 2000. Observations of iodine monoxide in the remote marine boundary layer. Journal of Geophysical Research-Atmospheres 105 (D11), 14363–14369.

Anderson, P. S., Neff, W. D., 2008. Boundary layer physics over snow and ice. Atmospheric Chemistry and Physics 8 (13), 3563–3582.

Anderson, T. L., Covert, D. S., Wheeler, J. D., Harris, J. M., Perry, K. D., Trost, B. E., Jaffe, D. J., Ogren, J. A., 1999. Aerosol backscatter fraction and single scattering albedo: Measured values and uncertainties at a coastal station in the Pacific Northwest. Journal of Geophysical Research-Atmospheres 104 (D21), 26793–26807.

Anlauf, K. G., Mickle, R. E., Trivett, N. B. A., 1994. Measurement of Ozone During Polar Sunrise Experiment 1992. Journal of Geophysical Research-Atmospheres 99 (D12), 25345–25353.

Ariya, P. A., Dastoor, A. P., Amyot, M., Schroeder, W. H., Barrie, L., Anlauf, K., Raofie, F., Ryzhkov, A., Davignon, D., Lalonde, J., Steffen, A., 2004. The

Arctic: a sink for mercury. Tellus Series B-Chemical and Physical Meteorology 56 (5), 397–403.

Arpag, K. H., Johnston, P. V., Miller, H. L., Sanders, R. W., Solomon, S., 1994. Observations of the stratospheric BrO column over Colorado, 40-degrees-N. Journal of Geophysical Research-Atmospheres 99 (D4), 8175–8181.

Ayers, G. P., Granek, H., Boers, R., 1997. Ozone in the marine boundary layer at Cape Grim: Model simulation. Journal of Atmospheric Chemistry 27 (2), 179–195.

Backus, G., Gilbert, F., 1970. Uniqueness in the Inversion of Inaccurate Gross Earth Data. Philosophical Transactions of the Royal Society of London. Series A, Mathematical and Physical Sciences 266 (1173), 123–192.

Barker, H. W., Goldstein, R. K., Stevens, D. E., 2003. Monte Carlo simulation of solar reflectances for cloudy atmospheres. Journal of the Atmospheric Sciences 60 (16), 1881–1894.

Barnes, R. A., Bandy, A. R., Torres, A. L., 1985. Electrochemical concentration cell ozonesonde accuracy and precision. Journal of Geophysical Research-Atmospheres 90 (ND5), 7881–7887.

Barret, B., De Maziere, M., Demoulin, P., 2003. Retrieval and characterization of ozone profiles from solar infrared spectra at the Jungfraujoch (vol 108, pg , 2002). Journal of Geophysical Research-Atmospheres 108 (D12).

Barrie, L., Platt, U., 1997. Arctic tropospheric chemistry: an overview. Tellus Series B-Chemical and Physical Meteorology 49 (5), 450–454.

Barrie, L. A., Bottenheim, J. W., Schnell, R., Crutzen, P., Rasmussen, R., 1988. Ozone destruction and photochemical reactions at polar sunrise in the lower Arctic atmosphere. Nature 334, 138–141.

Bates, D. E., Porter, J. N., 2008. AO3D: A Monte Carlo code for modeling of environmental light propagation. Journal of Quantitative Spectroscopy and Radiative Transfer 109 (10), 1802–1814.

Bates, D. R., 1984. Rayleigh-scattering by air. Planetary and space science 32 (6), 785–790.

Begoin, M., Richter, A., Weber, M., Kaleschke, L., Tian-Kunze, X., Stohl, A., Theys, N., Burrows, J., 2010. Satellite observations of long range transport of a large BrO plume in the Arctic. Atmospheric Chemistry and Physics 10, 6515–6526.

Berg, W. W., Heidt, L. E., Pollock, W., Sperry, P. D., Cicerone, R. J., Gladney, E. S., 1984. Brominated Organic-Species in the Arctic Atmosphere. Geophysical Research Letters 11 (5), 429–432.

Bernhard, G., Booth, C. R., Ehramjian, J. C., Nichol, S. E., 2006. UV climatology at McMurdo Station, Antarctica, based on version 2 data of the National Science Foundation's Ultraviolet Radiation Monitoring Network - art. no. D11201. Journal of Geophysical Research-Atmospheres 111 (D11), 11201–11201.

Bloss, W. J., Camredon, M., Lee, J. D., Heard, D., Plane, J., Saiz-Lopez, A., Bauguitte, S., Salmon, R. A., Jones, A., 2010. Coupling of HOx, NOx and halogen chemistry in the Antarctic boundary layer. Atmos. Chem. Phys. Discuss. 10, 15109–15165.

Bogumil, K., Orphal, J., Homann, T., Voigt, S., Spietz, P., Fleischmann, O. C., Vogel, A., Hartmann, M., Kromminga, H., Bovensmann, H., Frerick, J., Burrows, J. P., 2003. Measurements of molecular absorption spectra with the SCIAMACHY pre-flight model: instrument characterization and reference data for atmospheric remote-sensing in the 230-2380 nm region. Journal of Photochemistry and Photobiology a-Chemistry 157 (2-3), 167–184.

Bottenheim, J. W., Barrie, L. A., Atlas, E., Heidt, L. E., Niki, H., Rasmussen, R. A., Shepson, P. B., 1990. Depletion of Lower Tropospheric Ozone During Arctic Spring - the Polar Sunrise Experiment 1988. Journal of Geophysical Research-Atmospheres 95 (D11), 18555–18568.

Bottenheim, J. W., Chan, E., 2006. A trajectory study into the origin of spring time Arctic boundary layer ozone depletion - art. no. D19301. Journal of Geophysical Research-Atmospheres 111 (D19), 19301–19301.

Bottenheim, J. W., Gallant, A. G., Brice, K. A., 1986. Measurements of NOy Species and O-3 at 82-Degrees-N Latitude. Geophysical Research Letters 13 (2), 113–116.

Bottenheim, J. W., Netcheva, S., Morin, S., Nghiem, S. V., 2009. Ozone in the boundary layer air over the Arctic Ocean: measurements during the TARA transpolar drift 2006-2008. Atmospheric Chemistry and Physics 9 (14), 4545–4557.

Boucher, O., Moulin, C., Belviso, S., Aumont, O., Bopp, L., Cosme, E., von Kuhlmann, R., Lawrence, M. G., Pham, M., Reddy, M. S., Sciare, J., Venkataraman, C., 2003. DMS atmospheric concentrations and sulphate aerosol indirect radiative forcing: a sensitivity study to the DMS source representation and oxidation. Atmospheric Chemistry and Physics 3, 49–65.

Brandt, R. E., Warren, S. G., Worby, A. P., Grenfell, T. C., 2005. Surface albedo of the Antarctic sea ice zone. Journal of Climate 18 (17), 3606–3622.

Breider, T. J., Chipperfield, M. P., Richards, N. A. D., Carslaw, K. S., Mann, G. W., Spracklen, D. V., 2010. Impact of BrO on dimethylsulfide in the remote marine boundary layer - art. no. L02807. Geophysical Research Letters 37, 2807–2807.

Brewer, A. W., McElroy, C. T., Kerr, J. B., 1973. Nitrogen dioxide concentrations in the atmosphere. Nature 246 (5429), 129–133.

Brinkman, R., 1968. Rotational Raman scattering in planetary atmospheres. Astrophysical Journal 154 (3P1), 1087–1093.

Brooks, S., Lindberg, S., Southworth, G., Arimoto, R., 2008. Springtime atmospheric mercury speciation in the McMurdo, Antarctica coastal region. Atmospheric Environment 42 (12), 2885–2893.

Brooks, S. B., Saiz-Lopez, A., Skov, H., Lindberg, S. E., Plane, J. M. C., Goodsite, M. E., 2006. The mass balance of mercury in the springtime arctic environment - art. no. L13812. Geophysical Research Letters 33 (13), 13812–13812.

Bruns, M., Buehler, S. A., Burrows, J. P., Heue, K. P., Platt, U., Pundt, I., Richter, A., Rozanov, A., Wagner, T., Wang, P., 2004. Retrieval of profile information from airborne multiaxis UV-visible skylight absorption measurements. Applied Optics 43 (22), 4415–4426.

Bucholtz, A., 1995. Rayleigh-Scattering Calculations for the Terrestrial Atmosphere. Applied Optics 34 (15), 2765–2773.

Calvert, J. G., Lindberg, S. E., 2003. A modeling study of the mechanism of the halogen-ozone-mercury homogeneous reactions in the troposphere during the polar spring. Atmospheric Environment 37 (32), 4467–4481.

Calvert, J. G., Lindberg, S. E., 2004. Potential influence of iodine-containing compounds on the chemistry of the troposphere in the polar spring. I. Ozone depletion. Atmospheric Environment 38 (30), 5087–5104.

CamyPeyret, C., Bergqvist, B., Galle, B., Carleer, M., Clerbaux, C., Colin, R., Fayt, C., Goutail, F., NunesPinharanda, M., Pommereau, J. P., Hausmann, M., Platt, U., Pundt, I., Rudolph, T., Hermans, C., Simon, P. C., Vandaele, A. C., Plane, J. M. C., Smith, N., 1996. Intercomparison of instruments for tropospheric measurements using differential optical absorption spectroscopy. Journal of Atmospheric Chemistry 23 (1), 51–80.

Carpenter, L. J., Sturges, W. T., Penkett, S. A., Liss, P. S., Alicke, B., Hebestreit, K., Platt, U., 1999. Short-lived alkyl iodides and bromides at Mace Head, Ireland: Links to biogenic sources and halogen oxide production. Journal of Geophysical Research-Atmospheres 104 (D1), 1679–1689.

Carroll, M. A., Sanders, R. W., Solomon, S., Schmeltekopf, A. L., 1989. Visible and near-ultraviolet spectroscopy at McMurdo Station, Antarctica. 6. Observations of BrO. Journal of Geophysical Research-Atmospheres 94 (D14), 16633–16638.

Chance, K. V., Spurr, R. J. D., 1997. Ring effect studies: Rayleigh scattering, including molecular parameters for rotational Raman scattering, and the Fraunhofer spectrum. Applied Optics 36 (21), 5224–5230.

Chandrasekhar, S., 1950. Radiative Transfer. Courier Dover Publications, New York.

Ciddor, P. E., 1996. Refractive index of air: New equations for the visible and near infrared. Applied Optics 35 (9), 1566–1573.

Cota, G. F., Sturges, W. T., 1997. Biogenic bromine production in the Arctic. Marine Chemistry 56 (3-4), 181–192.

Davis, C., Emde, C., Harwood, R., 2005. A 3-D polarized reversed Monte Carlo radiative transfer model for millimeter and submillimeter passive remote sensing in cloudy atmospheres. Ieee Transactions on Geoscience and Remote Sensing 43 (5), 1096–1101.

de Beek, R., Vountas, M., Rozanov, V. V., Richter, A., Burrows, J. P., 2001. The Ring Effect in the cloudy atmosphere. Geophysical Research Letters 28 (4), 721–724.

Domine, F., Sparapani, R., Ianniello, A., Beine, H. J., 2004. The origin of sea salt in snow on Arctic sea ice and in coastal regions. Atmospheric Chemistry and Physics 4, 2259–2271.

Douglas, T. A., Sturm, M., Simpson, W. R., Brooks, S., Lindberg, S. E., Perovich, D. K., 2005. Elevated mercury measured in snow and frost flowers near Arctic sea ice leads. Geophysical Research Letters 32 (4), –.

Draxler, R. R., Hess, G. D., 1998. An overview of the HYSPLIT4 modeling system for trajectories, dispersion, and deposition. Aust. Meteorol. Mag. 47, 295–308.

Du, H., 2004. Mie-scattering calculation. Applied Optics 43 (9), 1951–1956.

Dubovik, O., Holben, B., Eck, T. F., Smirnov, A., Kaufman, Y. J., King, M. D., Tanre, D., Slutsker, I., 2002. Variability of absorption and optical properties of key aerosol types observed in worldwide locations. Journal of the Atmospheric Sciences 59 (3), 590–608.

Dyrssen, D., Fogelqvist, E., 1981. Bromoform Concentrations of the Arctic Ocean in the Svalbard Area. Oceanologica Acta 4 (3), 313–317.

Ebinghaus, R., Kock, H. H., Temme, C., Einax, J. W., Lowe, A. G., Richter, A., Burrows, J. P., Schroeder, W. H., 2002. Antarctic springtime depletion of atmospheric mercury. Environmental Science and Technology 36 (6), 1238–1244.

Emde, C., Buras, R., Mayer, B., Blumthaler, M., 2010. The impact of aerosols on polarized sky radiance: model development, validation, and applications. Atmospheric Chemistry and Physics 10 (2), 383–396.

Emde, C., Mayer, B., 2007. Simulation of solar radiation during a total eclipse: a challenge for radiative transfer. Atmospheric Chemistry and Physics 7 (9), 2259–2270.

Erle, F., Pfeilsticker, K., Platt, U., 1995. On the Influence of Tropospheric Clouds on Zenith-Scattered-Light Measurements of Stratospheric Species. Geophysical Research Letters 22 (20), 2725–2728.

Errera, Q., Fonteyn, D., 2001. Four-dimensional variational chemical assimilation of CRISTA stratospheric measurements. Journal of Geophysical Research-Atmospheres 106 (D11), 12253–12265.

Evans, K. F., 1998. The spherical harmonics discrete ordinate method for three-dimensional atmospheric radiative transfer. Journal of the Atmospheric Sciences 55 (3), 429–446.

Fan, S. M., Jacob, D. J., 1992. Surface Ozone Depletion in Arctic Spring Sustained by Bromine Reactions on Aerosols. Nature 359 (6395), 522–524.

Fickert, S., Adams, J. W., Crowley, J. N., 1999. Activation of Br-2 and BrCl via uptake of HOBr onto aqueous salt solutions. Journal of Geophysical Research-Atmospheres 104 (D19), 23719–23727.

Fiebig, M., Ogren, J. A., 2006. Retrieval and climatology of the aerosol asymmetry parameter in the NOAA aerosol monitoring network. Journal of Geophysical Research-Atmospheres 111 (D21).

Finlayson-Pitts, B. J., Livingston, F. E., Berko, H. N., 1990. Ozone Destruction and Bromine Photochemistry at Ground-Level in the Arctic Spring. Nature 343 (6259), 622–625.

Fish, D. J., Jones, R. L., 1995. Rotational Raman-Scattering and the Ring Effect in Zenith-Sky Spectra. Geophysical Research Letters 22 (7), 811–814.

Fitzgerald, W. F., Engstrom, D. R., Mason, R. P., Nater, E. A., 1998. The case for atmospheric mercury contamination in remote areas. Environmental Science and Technology 32 (1), 1–7.

Fleischmann, O. C., Hartmann, M., Burrows, J. P., Orphal, J., 2004. New ultraviolet absorption cross-sections of BrO at atmospheric temperatures measured by time-windowing Fourier transform spectroscopy. Journal of Photochemistry and Photobiology a-Chemistry 168 (1-2), 117–132.

Foster, K. L., Plastridge, R. A., Bottenheim, J. W., Shepson, P. B., Finlayson-Pitts, B. J., Spicer, C. W., 2001. The role of Br-2 and BrCl in surface ozone destruction at polar sunrise. Science 291 (5503), 471–474.

Frieß, U., 2001. Spectroscopic Measurements of Atmospheric Trace Gases at Neumayer Station, Antarctica. Phd, University of Heidleberg.

Frieß U., Deutschmann, T., Gilfedder, B. S., Weller, R., Platt, U., 2010. Iodine monoxide in the Antarctic snowpack. Atmospheric Chemistry and Physics 10 (5), 2439–2456.

Frieß U., Hollwedel, J., Konig-Langlo, G., Wagner, T., Platt, U., 2004. Dynamics and chemistry of tropospheric bromine explosion events in the Antarctic coastal region. Journal of Geophysical Research-Atmospheres 109 (D6), D06305.

Frieß U., Kreher, K., Johnston, P. V., Platt, U., 2005. Ground-based DOAS measurements of stratospheric trace gases at two Antarctic stations during the 2002 ozone hole period. Journal of the Atmospheric Sciences 62 (3), 765–777.

Frieß U., Monks, P. S., Remedios, J. J., Rozanov, A., Sinreich, R., Wagner, T., Platt, U., 2006. MAX-DOAS O4 measurements: A new technique to derive information on atmospheric aerosols: 2. Modeling studies - art. no. D14203. Journal of Geophysical Research-Atmospheres 111 (D14), 14203–14203.

Frieß U., Wagner, T., Pundt, I., Pfeilsticker, K., Platt, U., 2001. Spectroscopic measurements of tropospheric iodine oxide at Neumayer Station, Antarctica. Geophysical Research Letters 28 (10), 1941–1944.

Gerstl, S. A., Zardecki, A., 1985. Discrete-ordinates finite-element method for atmospheric radiative transfer and remote sensing. Applied Optics 24, 81–93.

Gouesbet, G., 2009. Generalized Lorenz-Mie theories, the third decade: A perspective. Journal of Quantitative Spectroscopy and Radiative Transfer 110 (14-16), 1223–1238.

Grainger, J. F., Ring, J., 1962. Anomalous Fraunhofer line profiles. Nature 193 (4817), 762.

Grannas, A. M., Jones, A. E., Dibb, J., Ammann, M., Anastasio, C., Beine, H. J., Bergin, M., Bottenheim, J., Boxe, C. S., Carver, G., Chen, G., Crawford, J. H., Domine, F., Frey, M. M., Guzman, M. I., Heard, D. E., Helmig, D., Hoffmann, M. R., Honrath, R. E., Huey, L. G., Hutterli, M., Jacobi, H. W., Klan, P., Lefer, B., McConnell, J., Plane, J., Sander, R., Savarino, J., Shepson, P. B., Simpson, W. R., Sodeau, J. R., von Glasow, R., Weller, R., Wolff, E. W., Zhu, T., 2007. An overview of snow photochemistry: evidence, mechanisms and impacts. Atmospheric Chemistry and Physics 7 (16), 4329–4373.

Greiner, M. A., Duncan, B. D., Dierking, M. P., 2009. Monte Carlo simulation of multiple photon scattering in sugar maple tree canopies. Applied Optics 48 (32), 6159–6171.

Grenfell, T. C., Perovich, D. K., 2004. Seasonal and spatial evolution of albedo in a snow-ice-land-ocean environment. Journal of Geophysical Research-Oceans 109 (C1).

Haley, C. S., Brohede, S. M., Sioris, C. E., Griffioen, E., Murtagh, D. P., McDade, I. C., Eriksson, P., Llewellyn, E. J., Bazureau, A., Goutail, F., 2004. Retrieval of stratospheric O-3 and NO2 profiles from Odin Optical Spectrograph and Infrared Imager System (OSIRIS) limb-scattered sunlight measurements. Journal of Geophysical Research-Atmospheres 109 (D16).

Hansen, A. D. A., Rosen, H., 1984. Vertical Distributions of Particulate Carbon, Sulfur, and Bromine in the Arctic Haze and Comparison with Ground-Level Measurements at Barrow, Alaska. Geophysical Research Letters 11 (5), 381–384.

Hansford, G. M., Freshwater, R. A., Bosch, R. A., Cox, R. A., Jones, R. L., Pratt, K. F. E., Williams, D. E., 2005. A low cost instrument based on a solid state sensor for balloon-borne atmospheric O-3 profile sounding. Journal of Environmental Monitoring 7 (2), 158–162.

Hausmann, M., Platt, U., 1994. Spectroscopic Measurement of Bromine Oxide and Ozone in the High Arctic During Polar Sunrise Experiment 1992. Journal of Geophysical Research-Atmospheres 99 (D12), 25399–25413.

Heckel, A., Richter, A., Tarsu, T., Wittrock, F., Hak, C., Pundt, I., Junkermann, W., Burrows, J. P., 2005. MAX-DOAS measurements of formaldehyde in the Po-Valley. Atmospheric Chemistry and Physics 5, 909–918.

Helmig, D., Oltmans, S. J., Carlson, D., Lamarque, J. F., Jones, A., Labuschagne, C., Anlauf, K., Hayden, K., 2007. A review of surface ozone in the polar regions. Atmospheric Environment 41 (24), 5138–5161.

Hendrick, F., Barret, B., Van Roozendael, M., Boesch, H., Butz, A., De Maziere, M., Goutail, F., Hermans, C., Lambert, J. C., Pfeilsticker, K., Pommereau, J. P., 2004. Retrieval of nitrogen dioxide stratospheric profiles from ground-based zenith-sky UV-visible observations: validation of the technique through correlative comparisons. Atmospheric Chemistry and Physics 4, 2091–2106.

Hendrick, F., Van Roozendael, M., Kylling, A., Petritoli, A., Rozanov, A., Sanghavi, S., Schofield, R., von Friedeburg, C., Wagner, T., Wittrock, F., Fonteyn, D., De Maziere, M., 2006. Intercomparison exercise between different radiative transfer models used for the interpretation of ground-based zenith-sky and multi-axis DOAS observations. Atmospheric Chemistry and Physics 6, 93–108.

Henyey, L. G., Greenstein, J. L., 1941. Diffuse radiation in the galaxy. Astrophysical Journal 93 (1), 70–83.

Hollwedel, J., Wenig, M., Beirle, S., Kraus, S., Kuhl, S., Wilms-Grabe, W., Platt, U., Wagner, T., 2004. Year-to-year variations of spring time polar tropospheric BrO as seen by GOME. Trace Constituents in the Troposphere and Lower Stratosphere 34 (4), 804–808.

Hönninger, G., Bobrowski, N., Palenque, E. R., Torrez, R., Platt, U., 2004a. Reactive bromine and sulfur emissions at Salar de Uyuni, Bolivia. Geophysical Research Letters 31 (4), –.

Hönninger, G., Platt, U., 2002. Observations of BrO and its vertical distribution during surface ozone depletion at Alert. Atmospheric Environment 36 (15-16), 2481–2489.

Hönninger, G., von Friedeburg, C., Platt, U., 2004b. Multi axis differential optical absorption spectroscopy (MAX-DOAS). Atmospheric Chemistry and Physics 4, 231–254.

Hoogen, R., Rozanov, V. V., Burrows, J. P., 1999. Ozone profiles from GOME satellite data: Algorithm description and first validation. Journal of Geophysical Research-Atmospheres 104 (D7), 8263–8280.

Hopper, J. F., Barrie, L. A., Silis, A., Hart, W., Gallant, A. J., Dryfhout, H., 1998. Ozone and meteorology during the 1994 Polar Sunrise Experiment. Journal of Geophysical Research-Atmospheres 103 (D1), 1481–1492.

Hu, R. M., Martin, R. V., Fairlie, T. D., 2007. Global retrieval of columnar aerosol single scattering albedo from space-based observations. Journal of Geophysical Research-Atmospheres 112 (D2).

Ishimoto, H., Masuda, K., 2002. A Monte Carlo approach for the calculation of polarized light: application to an incident narrow beam. Journal of Quantitative Spectroscopy and Radiative Transfer 72 (4), 467–483.

Iwabuchi, H., 2006. Efficient Monte Carlo methods for radiative transfer modeling. Journal of the Atmospheric Sciences 63 (9), 2324–2339.

Jacobi, H., Kaleschke, L., Richter, A., Rozanov, A., Burrows, J. P., 2006. Observation of a fast ozone loss in the marginal ice zone of the Arctic Ocean. Journal of Geophysical Research-Atmospheres 111 (D15), –.

Johnston, P. V., 2010a. Personal communication regarding the increased DOAS fitting errors that can result from using a wide spectral fitting window due changes in air-mass factor with wavelength.

Johnston, P. V., 2010b. Personal communication regarding the linearity of the dark spectrum over a range of integration times for the Hanamatsu C7042 detector.

Johnston, P. V., McKenzie, R. L., 1989. NO2 observations at 45-degrees-S during the decreasing phase of solar-cycle 21, from 1980 to 1987. Journal of Geophysical Research-Atmospheres 94 (D3), 3473–3486.

Johnston, P. V., McKenzie, R. L., Keys, J. G., Matthews, W. A., 1992. Observations of depleted stratospheric NO2 following the Pinatubo volcanic eruption. Geophysical Research Letters 19 (2), 211–213.

Jones, A., Anderson, P., Wolff, E., Roscoe, H., Marshall, G. J., Richter, A., Brough, N., Colwell, S., 2010. Vertical structure of Antarctic tropospheric ozone depletion events: characteristics and broader implications. Atmos. Chem. Phys. Discuss. 10, 8189–8246.

Jones, A. E., Anderson, P. S., Begoin, M., Brough, N., Hutterli, M. A., Marshall, G. J., Richter, A., Roscoe, H. K., Wolff, E. W., 2009. BrO, blizzards, and drivers of polar tropospheric ozone depletion events. Atmospheric Chemistry and Physics 9 (14), 4639–4652.

Jones, A. E., Anderson, P. S., Wolff, E. W., Turner, J., Rankin, A. M., Colwell, S. R., 2006. A role for newly forming sea ice in springtime polar tropospheric ozone loss? Observational evidence from Halley station, Antarctica. Journal of Geophysical Research-Atmospheres 111 (D8), –.

Jones, A. E., Weller, R., Wolff, E. W., Jacobi, H. W., 2000. Speciation and rate of photochemical NO and NO2 production in Antarctic snow. Geophysical Research Letters 27 (3), 345–348.

Kaleschke, L., Richter, A., Burrows, J., Afe, O., Heygster, G., Notholt, J., Rankin, A. M., Roscoe, H. K., Hollwedel, J., Wagner, T., Jacobi, H. W., 2004. Frost flowers on sea ice as a source of sea salt and their influence on tropospheric halogen chemistry. Geophysical Research Letters 31 (16), –.

Kalnajs, L. E., Avallone, L. M., 2006. Frost flower influence on springtime boundary-layer ozone depletion events and atmospheric bromine levels - art. no. L10810. Geophysical Research Letters 33 (10), 10810–10810.

Kattawar, G. W., Plass, G., Guinn, J., 1973. Monte Carlo Calculations of the Polarization of Radiation in the Earth's Atmosphere-Ocean System. Journal of Physical Oceanography 3 (4), 353–372.

Kattawar, G. W., Young, A. T., Humphreys, T. J., 1981. Inelastic-scattering in planetary-atmospheres .1. The Ring effect, wihtout aerosols. Astrophysical Journal 243 (3), 1049–1057.

Kottmeier, C., Fay, B., 1998. Trajectories in the Antarctic lower troposphere. Journal of Geophysical Research-Atmospheres 103 (D9), 10947–10959.

Kreher, K., 1996. Spectroscopic Measurements of Atmospheric OClO, BrO and NO2 and their Relation to Antarctic Ozone Depletion. Phd, University of Heidleberg.

Kreher, K., Johnston, P. V., Wood, S. W., Nardi, B., Platt, U., 1997. Ground-based measurements of tropospheric and stratospheric BrO at Arrival Heights, Antarctica. Geophysical Research Letters 24 (23), 3021–3024.

Kreher, K., Keys, J. G., Johnston, P. V., Platt, U., Liu, X., 1996. Ground-based measurements of OClO and HCl in austral spring 1993 at Arrival Heights, Antarctica. Geophysical Research Letters 23 (12), 1545–1548.

Kudo, R., Uchiyama, A., Yamazaki, A., Kobayashi, E., Nishizawa, T., 2008. Retrieval of aerosol single-scattering properties from diffuse and direct irradiances: Numerical studies - art. no. D09204. Journal of Geophysical Research-Atmospheres 113 (D9), 1–U43.

Langford, A. O., Schofield, R., Daniel, J. S., Portmann, R. W., Melamed, M. L., Miller, H. L., Dutton, E. G., Solomon, S., 2007. On the variability of the Ring effect in the near ultraviolet: understanding the role of aerosols and multiple scattering. Atmospheric Chemistry and Physics 7, 575–586.

Lee, J. S., Kim, Y. J., Kuk, B., Geyer, A., Platt, U., 2005. Simultaneous measurements of atmospheric pollutants and visibility with a long-path DOAS system in urban areas. Environmental Monitoring and Assessment 104 (1-3), 281–293.

Lee, R. L., 1998. Mie theory, Airy theory, and the natural rainbow. Applied Optics 37 (9), 1506–1519.

Lehrer, E., Honninger, G., Platt, U., 2004. A one dimensional model study of the mechanism of halogen liberation and vertical transport in the polar troposphere. Atmospheric Chemistry and Physics 4, 2427–2440.

Leser, H., Honninger, G., Platt, U., 2003. MAX-DOAS measurements of BrO and NO2 in the marine boundary layer. Geophysical Research Letters 30 (10), –.

Light, B., Eicken, H., Maykut, G. A., Grenfell, T. C., 1998. The effect of included particulates on the spectral albedo of sea ice. Journal of Geophysical Research-Oceans 103 (C12), 27739–27752.

Liley, J. B., Forgan, B. W., 2009. Aerosol optical depth over Lauder, New Zealand - art. no. L07811. Geophysical Research Letters 36, 7811–7811.

Lindberg, S. E., Brooks, S., Lin, C. J., Scott, K. J., Landis, M. S., Stevens, R. K., Goodsite, M., Richter, A., 2002. Dynamic oxidation of gaseous mercury in the Arctic troposphere at polar sunrise. Environmental Science and Technology 36 (6), 1245–1256.

Liou, K., 2002. An introduction to atmospheric radiation, 2nd Edition. Vol. 84 of International Geophysics Series. Elsevier Science, California.

Lu, J. Y., Schroeder, W. H., Barrie, L. A., Steffen, A., Welch, H. E., Martin, K., Lockhart, L., Hunt, R. V., Boila, G., Richter, A., 2001. Magnification of atmospheric mercury deposition to polar regions in springtime: the link to tropospheric ozone depletion chemistry. Geophysical Research Letters 28 (17), 3219–3222.

Mann, G. W., Anderson, P. S., Mobbs, S. D., 2000. Profile measurements of blowing snow at Halley, Antarctica. Journal of Geophysical Research-Atmospheres 105 (D19), 24491–24508.

Marchuk, G. I., Mikhailov, G. A., Nazaraliev, M. A., Dearbinjan, R., Kargin, B., Elepov, B., 1980. The Monte Carlo methods in atmospheric optics. Vol. 12 of Springer Series in Optical Sciences. Springer-Verlag, Berlin.

Marquard, L. C., Wagner, T., Platt, U., 2000. Improved air mass factor concepts for scattered radiation differential optical absorption spectroscopy of atmospheric species. Journal of Geophysical Research-Atmospheres 105 (D1), 1315–1327.

Marshak, A., Davis, A., 2005. 3D radiative transfer in cloudy atmospheres. Springer, Berlin, Heidelberg, New York.

Martinez-Cortizas, A., Pontevedra-Pombal, X., Garcia-Rodeja, E., Novoa-Munoz, J. C., Shotyk, W., 1999. Mercury in a Spanish peat bog: Archive of climate change and atmospheric metal deposition. Science 284 (5416), 939–942.

McConnell, J. C., Henderson, G. S., Barrie, L., Bottenheim, J., Niki, H., Langford, C. H., Templeton, E. M. J., 1992. Photochemical Bromine Production Implicated in Arctic Boundary-Layer Ozone Depletion. Nature 355 (6356), 150–152.

McElroy, C. T., McLinden, C. A., McConnell, J. C., 1999. Evidence for bromine monoxide in the free troposphere during the Arctic polar sunrise. Nature 397 (6717), 338–341.

McFiggans, G., Plane, J. M. C., Allan, B. J., Carpenter, L. J., Coe, H., O'Dowd, C., 2000. A modeling study of iodine chemistry in the marine boundary layer. Journal of Geophysical Research-Atmospheres 105 (D11), 14371–14385.

McKenzie, R. L., Johnston, P. V., 1984. Springtime stratospheric NO2 in Antarctica. Geophysical Research Letters 11 (1), 73–75.

McKenzie, R. L., Johnston, P. V., McElroy, C. T., Kerr, J. B., Solomon, S., 1991. Altitude Distributions of Stratospheric Constituents from Ground-Based Measurements at Twilight. Journal of Geophysical Research-Atmospheres 96 (D8), 15499–15511.

McKenzie, R. L., Kotkamp, M., Ireland, W., 1996. Upwelling UV spectral irradiances and surface albedo measurements at Lauder, New Zealand. Geophysical Research Letters 23 (14), 1757–1760.

Metropolis, N., Ulam, S., 1949. The Monte Carlo method. Journal of the American Statistical Association 44 (247), 335–341.

Michalowski, B. A., Francisco, J. S., Li, S. M., Barrie, L. A., Bottenheim, J. W., Shepson, P. B., 2000. A computer model study of multiphase chemistry in the Arctic boundary layer during polar sunrise. Journal of Geophysical Research-Atmospheres 105 (D12), 15131–15145.

Mie, G., 1908. Beitrge zur Optik trber Medien, speziell kolloidaler Metallsungen. Annalen der Physik 25 (4), 377–445.

Miller, H. L., Weaver, A., Sanders, R. W., Arpag, K., Solomon, S., 1997. Measurements of arctic sunrise surface ozone depletion events at Kangerlussuaq, Greenland (67 degrees N, to 51 degrees W). Tellus Series B-Chemical and Physical Meteorology 49 (5), 496–509.

Mishchenko, M. I., 2009. Electromagnetic scattering by nonspherical particles: A tutorial review. Journal of Quantitative Spectroscopy and Radiative Transfer 110 (11), 808–832.

Morin, S., Honninger, G. H., Staebler, R. M., Bottenheim, J. W., 2005. A high time resolution study of boundary layer ozone chemistry and dynamics over the Arctic Ocean near Alert, Nunavut. Geophysical Research Letters 32 (8), –.

Mozurkewich, M., 1995. Mechanisms for the Release of Halogens from Sea-Salt Particles by Free-Radical Reactions. Journal of Geophysical Research-Atmospheres 100 (D7), 14199–14207.

Nardino, V., Martelli, F., Bruscaglioni, P., Zaccanti, G., Del Bianco, S., Guzzi, D., Marcoionni, P., Pippi, I., 2008. McCART: Monte Carlo code for atmospheric radiative transfer. Ieee Transactions on Geoscience and Remote Sensing 46 (6), 1740–1752.

Noxon, J. F., 1975. Nitrogen-dioxide in the stratosphere and troposphere measured by ground-based absorption spectroscopy. Science 189 (4202), 547–549.

Noxon, J. F., Whipple, E. C., Hyde, R. S., 1979. Stratospheric NO2 .1. Observational method and behaviour at mid-latitude. Journal of Geophysical Research-Oceans and Atmospheres 84 (NC8), 5047–5065.

O'Hirok, W., Gautier, C., 1998a. A three-dimensional radiative transfer model to investigate the solar radiation within a cloudy atmosphere. Part I: Spatial effects. Journal of the Atmospheric Sciences 55 (12), 2162–2179.

O'Hirok, W., Gautier, C., 1998b. A three-dimensional radiative transfer model to investigate the solar radiation within a cloudy atmosphere. Part II: Spectral effects. Journal of the Atmospheric Sciences 55 (19), 3065–3076.

Oikarinen, L., Sihvola, E., Kyrola, E., 1999. Multiple scattering radiance in limb-viewing geometry. Journal of Geophysical Research-Atmospheres 104 (D24), 31261–31274.

Oltmans, S. J., Komhyr, W. D., 1986. Surface Ozone Distributions and Variations from 1973-1984 Measurements at the Noaa Geophysical Monitoring for Climatic-Change Base-Line Observatories. Journal of Geophysical Research-Atmospheres 91 (D4), 5229–5236.

Otten, C., Ferlemann, F., Platt, U., Wagner, T., Pfeilsticker, K., 1998. Groundbased DOAS UV/visible measurements at Kiruna (Sweden) during the SESAME winters 1993/94 and 1994/95. Journal of Atmospheric Chemistry 30 (1), 141–162.

Peck, E. R., Reeder, K., 1972. Dispersion of Air. J. Opt. Soc. Am. 62 (8), 958–962.

Perliski, L. M., Solomon, S., 1993. On the evaluation of air-mass factors for atmospheric near-ultraviolet and visible absorption-spectroscopy. Journal of Geophysical Research-Atmospheres 98 (D6), 10363–10374.

Perner, D., Platt, U., 1979. Detection of nitrous-acid in the atmosphere by differential optical-absorption. Geophysical Research Letters 6 (12), 917–920.

Perovich, D. K., Grenfell, T. C., Light, B., Hobbs, P. V., 2002. Seasonal evolution of the albedo of multiyear Arctic sea ice. Journal of Geophysical Research-Oceans 107 (C10).

Perovich, D. K., Richtermenge, J. A., 1994. Surface Characteristics of Lead Ice. Journal of Geophysical Research-Oceans 99 (C8), 16341–16350.

Piot, M., von Glasow, R., 2008. The potential importance of frost flowers, recycling on snow, and open leads for ozone depletion events. Atmospheric Chemistry and Physics 8 (9), 2437–2467.

Plane, J. M. C., Saiz-Lopez, A., 2006. UV-visible differential optical absorption spectroscopy (DOAS). In: Heard, D. (Ed.), Analytical techniques for atmospheric measurement. Blackwell, Oxford, pp. 147–188.

Plass, G. N., Kattawar, G. W., 1968. Monte Carlo calculations of light scattering from clouds. Applied Optics 7 (3), 415–419.

Platt, U., 1994. Differential Optical Absorption Spectroscopy (DOAS). In: Sigrist, M. (Ed.), Air Monitoring by Spectroscopic Techniques. Vol. 127 of Chemical Analysis: A series of monographs on analytical chemistry and its applications. John Wiley and Sons, Inc., New York, pp. 27–84.

Platt, U., Honninger, G., 2003. The role of halogen species in the troposphere. Chemosphere 52 (2), 325–338.

Platt, U., Marquard, L., Wagner, T., Perner, D., 1997. Corrections for zenith scattered light DOAS. Geophysical Research Letters 24 (14), 1759–1762.

Platt, U., Perner, D., Patz, H. W., 1979. Simultaneous measurement of atmospheric CH2O, O3, and NO2 by differential optical-absorption. Journal of Geophysical Research-Oceans and Atmospheres 84 (NC10), 6329–6335.

Platt, U., Stutz, J., 2008. Differential optical absorption spectroscopy. Physics of Earth and Space environments. Springer-Verlag, Heidelberg.

Pöhler, D., Vogel, L., Frieß U., Platt, U., 2010. Observation of halogen species in the Amundsen Gulf, Arctic, by active long-path differential optical absorption spectroscopy. Proceedings of the National Academy of Sciences, –.

Preston, K. E., Jones, R. L., Roscoe, H. K., 1997. Retrieval of NO2 vertical profiles from ground-based UV-visible measurements: Method and validation. Journal of Geophysical Research-Atmospheres 102 (D15), 19089–19097.

Pundt, I., Mettendorf, K. U., Laepple, T., Knab, V., Xie, P., Losch, J., Friedeburg, C. V., Platt, U., Wagner, T., 2005. Measurements of trace gas distributions using Long-path DOAS-Tomography during the motorway campaign BAB II: experimental setup and results for NO2. Atmospheric Environment 39 (5), 967–975.

Quack, B., Wallace, D. W. R., 2003. Air-sea flux of bromoform: Controls, rates, and implications. Global Biogeochemical Cycles 17 (1).

Rankin, A. M., Auld, V., Wolff, E. W., 2000. Frost flowers as a source of fractionated sea salt aerosol in the polar regions. Geophysical Research Letters 27 (21), 3469–3472.

Rankin, A. M., Wolff, E. W., Martin, S., 2002. Frost flowers: Implications for tropospheric chemistry and ice core interpretation. Journal of Geophysical Research-Atmospheres 107 (D23).

Rasmussen, R. A., Khalil, M. A. K., 1984. Gaseous Bromine in the Arctic and Arctic Haze. Geophysical Research Letters 11 (5), 433–436.

Richter, A., Wittrock, F., Eisinger, M., Burrows, J. P., 1998. GOME observations of tropospheric BrO in northern hemispheric spring and summer 1997. Geophysical Research Letters 25 (14), 2683–2686.

Rodgers, C. D., 1976. Retrieval of Atmospheric-Temperature and Composition from Remote Measurements of Thermal-Radiation. Reviews of Geophysics 14 (4), 609–624.

Rodgers, C. D., 1990. Characterization and Error Analysis of Profiles Retrieved from Remote Sounding Measurements. Journal of Geophysical Research-Atmospheres 95 (D5), 5587–5595.

Rodgers, C. D., 2000. Inverse Methods for Atmospheric Sounding: Theory and Practice, 1st Edition. Vol. 2 of Series on Atmospheric, Oceanic and Planetary Physics. World Scientific Publishing, Singapore.

Rodgers, C. D., Connor, B. J., 2003. Intercomparison of remote sounding instruments. Journal of Geophysical Research-Atmospheres 108 (D3), –.

Roscoe, H. K., Fish, D. J., Jones, R. L., 1996. Interpolation errors in UV-visible spectroscopy for stratospheric sensing: Implications for sensitivity, spectral resolution, and spectral range. Applied Optics 35 (3), 427–432.

Roscoe, H. K., Kreher, K., Frieß, U., 2001. Ozone loss episodes in the free Antarctic troposphere, suggesting a possible climate feedback. Geophysical Research Letters 28 (15), 2911–2914.

Rozanov, V. V., Rozanov, A. V., 2007. Relationship between different approaches to derive weighting functions related to atmospheric remote sensing problems. Journal of Quantitative Spectroscopy and Radiative Transfer 105 (2), 217–242.

Saiz-Lopez, A., Chance, K., Liu, X., Kurosu, T. P., Sander, S. P., 2007a. First observations of iodine oxide from space - art. no. L12812. Geophysical Research Letters 34 (12), 12812–12812.

Saiz-Lopez, A., Mahajan, A. S., Salmon, R. A., Bauguitte, S. J. B., Jones, A. E., Roscoe, H. K., Plane, J. M. C., 2007b. Boundary layer halogens in coastal Antarctica. Science 317 (5836), 348–351.

Saiz-Lopez, A., Notario, A., Martinez, E., Albaladejo, J., 2006a. Seasonal evolution of levels of gaseous pollutants in an urban area (Ciudad Real) in central-southern Spain: A DOAS study. Water Air and Soil Pollution 171 (1-4), 153–167.

Saiz-Lopez, A., Plane, J. M. C., 2004. Novel iodine chemistry in the marine boundary layer. Geophysical Research Letters 31 (4), –.

Saiz-Lopez, A., Plane, J. M. C., Mahajan, A. S., Anderson, P. S., Bauguitte, S. J. B., Jones, A. E., Roscoe, H. K., Salmon, R. A., Bloss, W. J., Lee, J. D., Heard, D. E., 2008. On the vertical distribution of boundary layer halogens over coastal Antarctica: implications for O-3, HOx, NOx and the Hg lifetime. Atmospheric Chemistry and Physics 8 (4), 887–900.

Saiz-Lopez, A., Plane, J. M. C., McFiggans, G., Williams, P. I., Ball, S. M., Bitter, M., Jones, R. L., Hongwei, C., Hoffmann, T., 2006b. Modelling molecular iodine emissions in a coastal marine environment: the link to new particle formation. Atmospheric Chemistry and Physics 6, 883–895.

Saiz-Lopez, A., Shillito, J. A., Coe, H., Plane, J. M. C., 2006c. Measurements and modelling of I-2, IO, OIO, BrO and NO3 in the mid-latitude marine boundary layer. Atmospheric Chemistry and Physics 6, 1513–1528.

Salawitch, R. J. e. a., 2010. A New Interpretation of Total Column BrO during Arctic Spring. Geophysical Research Letters Submitted.

Sander, R., Burrows, J., Kaleschke, L., 2006. Carbonate precipitation in brine - a potential trigger for tropospheric ozone depletion events. Atmospheric Chemistry and Physics 6, 4653–4658.

Sander, R., Keene, W. C., Pszenny, A. A. P., Arimoto, R., Ayers, G. P., Baboukas, E., Cainey, J. M., Crutzen, P. J., Duce, R. A., Honninger, G., Huebert, B. J., Maenhaut, W., Mihalopoulos, N., Turekian, V. C., Van Dingenen, R., 2003.

Inorganic bromine in the marine boundary layer: a critical review. Atmospheric Chemistry and Physics 3, 1301–1336.

Sander, R., Vogt, R., Harris, G. W., Crutzen, P. J., 1997. Modeling the chemistry ozone, halogen compounds, and hydrocarbons in the arctic troposphere during spring. Tellus Series B-Chemical and Physical Meteorology 49 (5), 522–532.

Sanders, R. W., Solomon, S., Mount, G. H., Bates, M. W., Schmeltekopf, A. L., 1987. Visible spectroscopy at McMurdo Station, Antarctica. 3. Observations of NO3. Journal of Geophysical Research-Atmospheres 92 (D7), 8339–8342.

Sanders, R. W., Solomon, S., Smith, J. P., Perliski, L., Miller, H. L., Mount, G. H., Keys, J. G., Schmeltekopf, A. L., 1993. Visible and near-ultraviolet spectroscopy at McMurdo Station, Antarctica. 9. Observations of OClO from April to October 1991. Journal of Geophysical Research-Atmospheres 98 (D4), 7219–7228.

Sarkissian, A., Roscoe, N. K., Fish, D. J., 1995. Ozone Measurements by Zenith-Sky Spectrometers - an Evaluation of Errors in Air-Mass Factors Calculated by Radiative-Transfer Models. Journal of Quantitative Spectroscopy and Radiative Transfer 54 (3), 471–480.

Schofield, R., 2003. The Vertical Distribution of Atmospheric BrO from Ground-Based Measurements. Ph.D. thesis, University of Auckland.

Schofield, R., Connor, B. J., Kreher, K., Johnston, P. V., Rodgers, C. D., 2004. The retrieval of profile and chemical information from ground-based UV-visible spectroscopic measurements. Journal of Quantitative Spectroscopy and Radiative Transfer 86 (2), 115–131.

Schofield, R., Johnston, P. V., Thomas, A., Kreher, K., Connor, B. J., Wood, S., Shooter, D., Chipperfield, M. P., Richter, A., von Glasow, R., Rodgers, C. D., 2006. Tropospheric and stratospheric BrO columns over Arrival Heights, Antarctica, 2002. Journal of Geophysical Research-Atmospheres 111 (D22), –.

Schönhardt, A., Richter, A., Wittrock, F., Burrows, J., 2007. First observations of atmospheric iodine oxide columns from satellite. Geophysical Research Abstracts 9, 592.

Schönhardt, A., Richter, A., Wittrock, F., Kirk, H., Oetjen, H., Roscoe, H. K., Burrows, J. P., 2008. Observations of iodine monoxide columns from satellite. Atmospheric Chemistry and Physics 8 (3), 637–653.

Schroeder, W. H., Anlauf, K. G., Barrie, L. A., Lu, J. Y., Steffen, A., Schneeberger, D. R., Berg, T., 1998. Arctic springtime depletion of mercury. Nature 394 (6691), 331–332.

Seitz, K., Buxmann, J., Pohler, D., Sommer, T., Tschritter, J., Neary, T., O'Dowd, C., Platt, U., 2010. The spatial distribution of the reactive iodine

species IO from simultaneous active and passive DOAS observations. Atmospheric Chemistry and Physics 10 (5), 2117–2128.

Shannon, C., Weaver, W., 1949. The Mathematical Theory of Communication. University of Illinois Press, Urbana.

Shaw, G. E., 1980. Optical, chemical and physical properties of aerosols over the antarctic ice sheet. Atmospheric Environment (1967) 14 (8), 911–921.

Simpson, W. R., Alvarez-Aviles, L., Douglas, T. A., Sturm, M., Domine, F., 2005. Halogens in the coastal snow pack near Barrow, Alaska: Evidence for active bromine air-snow chemistry during springtime. Geophysical Research Letters 32 (4), –.

Simpson, W. R., Carlson, D., Honninger, G., Douglas, T. A., Sturm, M., Perovich, D., Platt, U., 2007a. First-year sea-ice contact predicts bromine monoxide (BrO) levels at Barrow, Alaska better than potential frost flower contact. Atmospheric Chemistry and Physics 7, 621–627.

Simpson, W. R., von Glasow, R., Riedel, K., Anderson, P., Ariya, P., Bottenheim, J., Burrows, J., Carpenter, L. J., Frieß U., Goodsite, M. E., Heard, D., Hutterli, M., Jacobi, H. W., Kaleschke, L., Neff, B., Plane, J., Platt, U., Richter, A., Roscoe, H., Sander, R., Shepson, P., Sodeau, J., Steffen, A., Wagner, T., Wolff, E., 2007b. Halogens and their role in polar boundary-layer ozone depletion. Atmospheric Chemistry and Physics 7 (16), 4375–4418.

Sinreich, R., Frieß U., Wagner, T., Platt, U., 2005. Multi axis differential optical absorption spectroscopy (MAX-DOAS) of gas and aerosol distributions. Faraday Discussions 130, 153–164.

Sioris, C. E., Evans, W. F. J., 1999. Filling in of Fraunhofer and gas-absorption lines in sky spectra as caused by rotational Raman scattering. Applied Optics 38 (12), 2706–2713.

Solberg, S., Schmidbauer, N., Semb, A., Stordal, F., Hov, O., 1996. Boundary-layer ozone depletion as seen in the Norwegian Arctic in Spring. Journal of Atmospheric Chemistry 23 (3), 301–332.

Solomon, S., Garcia, R. R., Ravishankara, A. R., 1994a. On the Role of Iodine in Ozone Depletion. Journal of Geophysical Research-Atmospheres 99 (D10), 20491–20499.

Solomon, S., Sanders, R. W., Carroll, M. A., Schmeltekopf, A. L., 1989. Visible and near-ultraviolet spectroscopy at McMurdo Station, Antarctica. 5. Observations of the diurnal variations of BrO and OClO. Journal of Geophysical Research-Atmospheres 94 (D9), 11393–11403.

Solomon, S., Sanders, R. W., Jakoubek, R. O., Arpag, K. H., Stephens, S. L., Keys, J. G., Garcia, R. R., 1994b. Visible and near-Ultraviolet Spectroscopy at Mcmurdo-Station, Antarctica .10. Reductions of Stratospheric No2 Due

to Pinatubo Aerosols. Journal of Geophysical Research-Atmospheres 99 (D2), 3509–3516.

Solomon, S., Schmeltekopf, A. L., Sanders, R. W., 1987. On the interpretation of zenith sky absorption measurements. Journal of Geophysical Research-Atmospheres 92 (D7), 8311–8319.

Sommersten, E. R., Lotsberg, J. K., Stamnes, K., Stamnes, J. J., 2010. Discrete ordinate and Monte Carlo simulations for polarized radiative transfer in a coupled system consisting of two media with different refractive indices. Journal of Quantitative Spectroscopy and Radiative Transfer 111 (4), 616–633.

Spada, F., Krol, M. C., Stammes, P., 2006. McSCIA: application of the equivalence theorem in a Monte Carlo radiative transfer model for spherical shell atmospheres. Atmospheric Chemistry and Physics 6, 4823–4842.

Spicer, C. W., Plastridge, R. A., Foster, K. L., Finlayson-Pitts, B. J., Bottenheim, J. W., Grannas, A. M., Shepson, P. B., 2002. Molecular halogens before and during ozone depletion events in the Arctic at polar sunrise: concentrations and sources. Atmospheric Environment 36 (15-16), 2721–2731.

Spietz, P., Martin, J. C. G., Burrows, J. P., 2005. Spectroscopic studies of the I-2/O-3 photochemistry - Part 2. Improved spectra of iodine oxides and analysis of the IO absorption spectrum. Journal of Photochemistry and Photobiology a-Chemistry 176 (1-3), 50–67.

Spurr, R., 2008. LIDORT and VLIDORT: Linearized pseudo-spherical scalar and vector discrete ordinate radiative transfer models for use in remote sensing retrieval problems. In: Kokhanovsky, A. A. (Ed.), Light scattering reviews. Vol. 3. Springer, pp. 229–275.

Spurr, R., de Haan, J., van Oss, R., Vasilkov, A., 2008. Discrete-ordinate radiative transfer in a stratified medium with first-order rotational Raman scattering. Journal of Quantitative Spectroscopy and Radiative Transfer 109 (3), 404–425.

Spurr, R. J. D., 2006. VLIDORT: A linearized pseudo-spherical vector discrete ordinate radiative transfer code for forward model and retrieval studies in multilayer multiple scattering media. Journal of Quantitative Spectroscopy and Radiative Transfer 102 (2), 316–342.

Stam, D. M., Aben, I., Helderman, F., 2002. Skylight polarization spectra: Numerical simulation of the Ring effect. Journal of Geophysical Research-Atmospheres 107 (D20).

Sturges, W. T., Sullivan, C. W., Schnell, R. C., Heidt, L. E., Pollock, W. H., 1993. Bromoalkane Production by Antarctic Ice Algae. Tellus Series B-Chemical and Physical Meteorology 45 (2), 120–126.

Stutz, J., Hebestreit, K., Alicke, B., Platt, U., 1999. Chemistry of halogen oxides in the troposphere: Comparison of model calculations with recent field data. Journal of Atmospheric Chemistry 34 (1), 65–85.

Stutz, J., Platt, U., 1996. Numerical analysis and estimation of the statistical error of differential optical absorption spectroscopy measurements with least-squares methods. Applied Optics 35 (30), 6041–6053.

Stutz, J., Platt, U., 1997. Improving long-path differential optical absorption spectroscopy with a quartz-fiber mode mixer. Applied Optics 36 (6), 1105–1115.

Tang, T., McConnell, J. C., 1996. Autocatalytic release of bromine from Arctic snow pack during polar sunrise. Geophysical Research Letters 23 (19), 2633–2636.

Tarasick, D. W., Bottenheim, J. W., 2002. Surface ozone depletion episodes in the Arctic and Antarctic from historical ozonesonde records. Atmospheric Chemistry and Physics 2, 197–205.

Temme, C., Einax, J. W., Ebinghaus, R., Schroeder, W. H., 2003. Measurements of atmospheric mercury species at a coastal site in the Antarctic and over the south Atlantic Ocean during polar summer. Environmental Science and Technology 37 (1), 22–31.

Theys, N., Van Roozendael, M., Hendrick, F., Fayt, C., Hermans, C., Baray, J. L., Goutail, F., Pommereau, J. P., De Maziere, M., 2007. Retrieval of stratospheric and tropospheric BrO columns from multi-axis DOAS measurements at Reunion Island (21 degrees S, 56 degrees E). Atmospheric Chemistry and Physics 7 (18), 4733–4749.

Thomas, G., Stammes, K., 1999. Radiative transfer in the atmosphere and ocean. Atmospheric and Space Science Series. Cambridge University Press, Cambridge.

Tornkvist, K. K., Arlander, D. W., Sinnhuber, B. M., 2002. Ground-based UV measurements of BrO and OClO over Ny-Alesund during winter 1996 and 1997 and Andoya during winter 1998/99. Journal of Atmospheric Chemistry 43 (2), 75–106.

Toublanc, D., 1996. Henyey-Greenstein and Mie phase functions in Monte Carlo radiative transfer computations. Applied Optics 35 (18), 3270–3274.

van de Hulst, H., 1980. Multiple Light Scattering. Academic Press, New York.

Van Roozendael, M., 2003. Personal communication of O4 cross-sections based on O4 spectra at 296 K (335-666 nm) from Hermans et al, unpublished results.

Van Roozendael, M., Hermans, C., Demaziere, M., Simon, P. C., 1994. Stratospheric NO2 observations at the Jungfraujoch Station between June 1990 and May 1992. Geophysical Research Letters 21 (13), 1383–1386.

Vandaele, A. C., Fayt, C., Hendrick, F., Hermans, C., Humbled, F., Van Roozendael, M., Gil, M., Navarro, M., Puentedura, O., Yela, M., Braathen, G., Stebel, K., Tornkvist, K., Johnston, P., Kreher, K., Goutail, F., Mieville, A., Pommereau, J. P., Khaikine, S., Richter, A., Oetjen, H., Wittrock, F., Bugarski, S., Frieß U., Pfeilsticker, K., Sinreich, R., Wagner, T., Corlett, G., Leigh, R., 2005. An intercomparison campaign of ground-based UV-visible measurements of NO2, BrO, and OClO slant columns: Methods of analysis and results for NO2. Journal of Geophysical Research-Atmospheres 110 (D8), –.

Vandaele, A. C., Hermans, C., Fally, S., Carleer, M., Colin, R., Merienne, M. F., Jenouvrier, A., Coquart, B., 2002. High-resolution Fourier transform measurement of the NO2 visible and near-infrared absorption cross sections: Temperature and pressure effects. Journal of Geophysical Research-Atmospheres 107 (D18).

Veitel, H., Kromer, B., Mossner, M., Platt, U., 2002. New techniques for measurements of atmospheric vertical trace gas profiles using DOAS. Environmental Science and Pollution Research, 17–26.

Vogt, R., Sander, R., Von Glasow, R., Crutzen, P. J., 1999. Iodine chemistry and its role in halogen activation and ozone loss in the marine boundary layer: A model study. Journal of Atmospheric Chemistry 32 (3), 375–395.

Voigt, S., Orphal, J., Bogumil, K., Burrows, J. P., 2001. The temperature dependence (203-293 K) of the absorption cross sections of O-3 in the 230-850 nm region measured by Fourier-transform spectroscopy. Journal of Photochemistry and Photobiology a-Chemistry 143 (1), 1–9.

von Clarmann, T., Glatthor, N., Grabowski, U., Hopfner, M., Kellmann, S., Kiefer, M., Linden, A., Tsidu, G. M., Milz, M., Steck, T., Stiller, G. P., Wang, D. Y., Fischer, I., Funke, B., Gil-Lopez, S., Lopez-Puertas, M., 2003. Retrieval of temperature and tangent altitude pointing from limb emission spectra recorded from space by the Michelson Interferometer for Passive Atmospheric Sounding (MIPAS). Journal of Geophysical Research-Atmospheres 108 (D23), –.

von Glasow, R., Sander, R., 2001. Variation of sea salt aerosol pH with relative humidity. Geophysical Research Letters 28 (2), 247–250.

von Glasow, R., Sander, R., Bott, A., Crutzen, P. J., 2002. Modeling halogen chemistry in the marine boundary layer - 2. Interactions with sulfur and the cloud-covered MBL. Journal of Geophysical Research-Atmospheres 107 (D17).

Voulgarakis, A., Yang, X., Pyle, J. A., 2009. How different would tropospheric oxidation be over an ice-free Arctic? - art. no. L23807. Geophysical Research Letters 36, 23807–23807.

Vountas, M., Rozanov, V. V., Burrows, J. P., 1998. Ring effect: Impact of rotational Raman scattering on radiative transfer in earth's atmosphere. Journal of Quantitative Spectroscopy and Radiative Transfer 60 (6), 943–961.

Wagenbach, D., Ducroz, F., Mulvaney, R., Keck, L., Minikin, A., Legrand, M., Hall, J. S., Wolff, E. W., 1998. Sea-salt aerosol in coastal Antarctic regions. Journal of Geophysical Research-Atmospheres 103 (D9), 10961–10974.

Wagner, T., Beirle, S., Deutschmann, T., 2009. Three-dimensional simulation of the Ring effect in observations of scattered sun light using Monte Carlo radiative transfer models. Atmos. Meas. Tech. 2 (1), 113–124.

Wagner, T., Burrows, J. P., Deutschmann, T., Dix, B., von Friedeburg, C., Frieß U., Hendrick, F., Heue, K. P., Irie, H., Iwabuchi, H., Kanaya, Y., Keller, J., McLinden, C. A., Oetjen, H., Palazzi, E., Petritoli, A., Platt, U., Postylyakov, O., Pukite, J., Richter, A., van Roozendael, M., Rozanov, A., Rozanov, V., Sinreich, R., Sanghavi, S., Wittrock, F., 2007a. Comparison of box-air-mass-factors and radiances for Multiple-Axis Differential Optical Absorption Spectroscopy (MAX-DOAS) geometries calculated from different UV/visible radiative transfer models. Atmospheric Chemistry and Physics 7 (7), 1809–1833.

Wagner, T., Dix, B., von Friedeburg, C., Frieß U., Sanghavi, S., Sinreich, R., Platt, U., 2004. MAX-DOAS O-4 measurements: A new technique to derive information on atmospheric aerosols - Principles and information content. Journal of Geophysical Research-Atmospheres 109 (D22), –.

Wagner, T., Erle, F., Marquard, L., Otten, C., Pfeilsticker, K., Senne, T., Stutz, J., Platt, U., 1998. Cloudy sky optical paths as derived from differential optical absorption spectroscopy observations. Journal of Geophysical Research-Atmospheres 103 (D19), 25307–25321.

Wagner, T., Ibrahim, O., Sinreich, R., Frieß U., von Glasow, R., Platt, U., 2007b. Enhanced tropospheric BrO over Antarctic sea ice in mid winter observed by MAX-DOAS on board the research vessel Polarstern. Atmospheric Chemistry and Physics 7 (12), 3129–3142.

Wagner, T., Leue, C., Wenig, M., Pfeilsticker, K., Platt, U., 2001. Spatial and temporal distribution of enhanced boundary layer BrO concentrations measured by the GOME instrument aboard ERS-2. Journal of Geophysical Research-Atmospheres 106 (D20), 24225–24235.

Wagner, T., von Friedeburg, C., Wenig, M., Otten, C., Platt, U., 2002. UV-visible observations of atmospheric O-4 absorptions using direct moonlight and zenith-scattered sunlight for clear-sky and cloudy sky conditions. Journal of Geophysical Research-Atmospheres 107 (D20), –.

Wahner, A., Ravishankara, A. R., Sander, S. P., Friedl, R. R., 1988. Absorption cross-section of BrO between 312 and 385nm at 298 and 223K. Chemical Physics Letters 152 (6), 507–512.

Wahner, A., Tyndall, G. S., Ravishankara, A. R., 1987. Absorption cross-sections for OClO as a function of temperature in the wavelength range 240-480nm. Journal of Physical Chemistry 91 (11), 2734–2738.

Wallace, J., Hobbs, P., 2006. Atmospheric science: an introductory survey, 2nd Edition. Vol. 92 of International Geophysics Series. Elsevier Inc., London.

Wark, D. O., Fleming, H. E., 1966. Indirect measurements of atmospheric temperature profiles from satellites: I. Introduction. Monthly Weather Review 94 (6), 351–362.

Warwick, N. J., Pyle, J. A., Carver, G. D., Yang, X., Savage, N. H., O'Connor, F. M., Cox, R. A., 2006a. Global modeling of biogenic bromocarbons - art. no. D24305. Journal of Geophysical Research-Atmospheres 111 (D24), 24305–24305.

Warwick, N. J., Pyle, J. A., Shallcross, D. E., 2006b. Global modelling of the atmospheric methyl bromide budget. Journal of Atmospheric Chemistry 54 (2), 133–159.

Wessel, S., Aoki, S., Winkler, P., Weller, R., Herber, A., Gernandt, H., Schrems, O., 1998. Tropospheric ozone depletion in polar regions - A comparison of observations in the Arctic and Antarctic. Tellus Series B-Chemical and Physical Meteorology 50 (1), 34–50.

Wilmouth, D. M., Hanisco, T. F., Donahue, N. M., Anderson, J. G., 1999. Fourier transform ultraviolet spectroscopy of the A (2)Pi(3/2) ¡- X (II3/2)-I-2 transition of BrO. Journal of Physical Chemistry A 103 (45), 8935–8945.

Wiscombe, W. J., 1980. Improved Mie scattering algorithms. Applied Optics 19 (9), 1505–1509.

Wittrock, F., Muller, R., Richter, A., Bovensmann, H., Burrows, J. P., 2000. Measurements of iodine monoxide (IO) above Spitsbergen. Geophysical Research Letters 27 (10), 1471–1474.

Wittrock, F., Oetjen, H., Richter, A., Fietkau, S., Medeke, T., Rozanov, A., Burrows, J. P., 2004. MAX-DOAS measurements of atmospheric trace gases in Ny-Alesund - Radiative transfer studies and their application. Atmospheric Chemistry and Physics 4, 955–966.

Wofsy, S. C., McElroy, M. B., Yung, Y. L., 1975. The Chemistry of Atmospheric Bromine. Geophysical Research Letters 2 (6), 215–218.

Wolff, E. W., Rankin, A. M., Rothlisberger, R., 2003. An ice core indicator of Antarctic sea ice production? Geophysical Research Letters 30 (22).

Wuttke, S., Seckmeyer, G., Konig-Lang, G., 2006. Measurements of spectral snow albedo at Neumayer, Antarctica. Annales Geophysicae 24 (1), 7–21.

Wyputta, U., 1997. On the transport of trace elements into Antarctica using measurements at the Georg-von-Neumayer station. Tellus Series B-Chemical and Physical Meteorology 49 (1), 93–111.

Yang, X., Pyle, J. A., Cox, R. A., 2008. Sea salt aerosol production and bromine release: Role of snow on sea ice - art. no. L16815. Geophysical Research Letters 35 (16), 16815–16815.

Yang, X., Pyle, J. A., Cox, R. A., Theys, N., Van Roozendael, M., 2010. Snow-sourced bromine and its implications for polar tropospheric ozone. Atmos. Chem. Phys. Discuss. 10, 8135–8164.

Yokouchi, Y., Machida, T., Barrie, L. A., Toom-Sauntry, D., Nojiri, Y., Fujinuma, Y., Inuzuka, Y., Li, H. J., Akimoto, H., Aoki, S., 2000. Latitudinal distribution of atmospheric methyl bromide: Measurements and modeling. Geophysical Research Letters 27 (5), 697–700.

Yokouchi, Y., Toom-Sauntry, D., Yazawa, K., Inagaki, T., Tamaru, T., 2002. Recent decline of methyl bromide in the troposphere. Atmospheric Environment 36 (32), 4985.

Yung, Y. L., Pinto, J. P., Watson, R. T., Sander, S. P., 1980. Atmospheric Bromine and Ozone Perturbations in the Lower Stratosphere. Journal of the Atmospheric Sciences 37 (2), 339–353.

Yurganov, L. N., 1990. Surface-Layer Ozone above the Weddell Sea During the Antarctic Spring. Antarctic Science 2 (2), 169–174.